Laser-driven heavy ion acceleration

Florian Lindner

München 2021

Laser-driven heavy ion acceleration

Florian Lindner

DISSERTATION

an der Fakultät für Physik der
Ludwig–Maximilians–Universität München

vorgelegt von
Florian H. Lindner
aus Tirschenreuth

München, den 14.01.2021

Erstgutachter: Prof. Dr. Peter G. Thirolf
Zweitgutachter: Prof. Dr. Jörg Schreiber
Tag der mündlichen Prüfung: 09.03.2021

Zusammenfassung

Der schnelle Neutroneneinfangprozess (r-Prozess) ist verantwortlich für die Erzeugung von ungefähr der Hälfte aller Elemente im Universum mit einer höheren Masse als Eisen. Während sich seit der ersten multimodalen Beobachtung einer Neutronensternverschmelzung durch die LIGO-Virgo-Kollaboration im Jahr 2017 die Erkenntnisse über die vieldiskutierten astrophysikalischen Schauplätze des r-Prozesses unlängst verdichteten, bleiben die nuklearen Eigenschaften der beteiligten Isotope, insbesondere um den Wartepunkt bei der magischen Neutronenzahl von N = 126, noch immer unzugänglich für die konventionelle Beschleunigertechnologie. In Folge dessen entwickelten Habs et al. vor etwa einem Jahrzehnt die Idee des 'Fission-Fusion'-Reaktionsmechanismus, welche das Potenzial birgt, neutronenreiche r-Prozess-Isotope in der Nähe dieses Wartepunkts bei N = 126 mittels ultradichter, laserbeschleunigter Pulse schwerer, spaltbarer Ionen im Massenbereich von A $\geq$ 200 und mit kinetischen Energien um 7 MeV/u zu erzeugen.

Zum Beginn dieser Arbeit lagen lediglich zwei Veröffentlichungen vor, die über die Messung laserbeschleunigter Schwerionen im relevanten Energiebereich berichteten, mit kinetischen Energien von maximal 2 MeV/u. Diese Dissertation präsentiert die Ergebnisse zweier Experimentierkampagnen, die darauf abzielten, das Wissen über lasergetriebene Goldionenbeschleunigung zu erweitern und Ionenpulse zu erzeugen, welche die energetischen Voraussetzungen des 'Fission-Fusion'-Reaktionsmechanismus erfüllen. In beiden Experimenten wurden die Schwerionenenergien erfolgreich nach oben getrieben, was schlussendlich in der Detektion von laserbeschleunigten Schwerionen mit Energien jenseits des 'Fission-Fusion'-Schwellenwerts von etwa 7 MeV/u resultierte.

Um den Beitrag von Kohlenwasserstoffverunreinigungen auf den Goldfolienoberflächen zu den laserbeschleunigten Schwerionenpulse zu reduzieren, wurde eine Targetreinigung mittels optischer Laserstrahlung implementiert. Für die Messung von Schwerionen wurde ein Thomson-Parabel-Spektrometer konstruiert, dessen Parameter ideal auf diesen Zweck abgestimmt wurden. Mit Hilfe dieser Diagnostik konnten zum ersten Mal einzelne Gold-

ladungszustände aufgelöst werden, wodurch eine bemerkenswerte Abhängigkeit von der Targetdicke ans Licht kam, die nicht auf einfache Art und Weise durch die gewöhnlichen Ionisationsmechanismen erklärt werden können. Die Daten aus dieser Doktorarbeit stellen daher einen sehr wertvollen Beitrag für künftige theoretische Betrachtungen der Ionisationsprozesse von Schwerionen in lasererzeugten Plasmen dar.

Abstract

The rapid neutron capture process (r-process) is responsible for the generation of about half of the heavy elements beyond iron in the Universe. While knowledge about its long-debated astrophysical sites converged recently by the first multi-modal observation of neutron-star mergers by the LIGO-Virgo collaboration in 2017, the nuclear properties of the involved isotopes, especially around the waiting point at the magic neutron number N = 126, still remain inaccessible using conventional accelerator techniques. As a consequence, Habs et al. proposed about one decade ago the fission-fusion reaction mechanism, which offers the potential to produce neutron-rich r-process isotopes close to this waiting point at N = 126 applying ultra-dense, laser-accelerated bunches of heavy, fissile ions in the mass range of A $\geq$ 200 with kinetic energies around 7 MeV/u.

Only two publications had reported on the measurement of laser-accelerated heavy ions in the relevant energy range at the beginning of this work, with maximum kinetic energies of 2 MeV/u. This dissertation presents the results from two experimental campaigns dedicated to advance the knowledge about laser-driven gold ion acceleration and to generate an ion bunch which meets the energy requirements of the fission-fusion reaction mechanism. In both experiments, the heavy ion energies have been successfully pushed towards higher limits, finally resulting in the detection of laser-accelerated heavy ions with energies beyond the fission-fusion threshold of 7 MeV/u.

A radiative target cleaning has been implemented in order to reduce the contribution of hydrocarbon contaminants on the gold foil surfaces to the laser-accelerated heavy ion bunches. A Thomson parabola spectrometer has been designed with parameters that ideally support the detection of heavy ions. With that diagnostics, individual gold ion charge states could be resolved for the first time, showing a remarkable target thickness dependency, which cannot be explained with the common ionization mechanisms in a straight-forward way. Thus, the data presented in this thesis is highly valuable as input for future theoretical considerations on the ionization processes of heavy ions in laser-generated plasmas.

Contents

Chapter 1

Introduction

The demonstration of the technique of chirped pulse amplification (CPA) by D. Strickland and G. Mourou in 1985 [1] paved the way for the development of a new generation of high-power laser systems. Laser pulses with peak intensities exceeding 1.37×10^{18} W/cm^2 became available at which electrons are accelerated to relativistic energies within one laser cycle. These high intensities laid the foundations for the field of laser-driven ion acceleration, introduced by the first observation of laser-accelerated fast protons in 2000 [2, 3].

Laser-accelerated ion bunches exhibit very unique features that fundamentally differ from conventionally generated ion sources [4–6]. For instance, they have quite broad energy distributions at initially very short bunch durations and they are, in general, highly divergent but originate from a remarkably small source. Moreover, multiple ion species like protons and carbons can be instantaneously accelerated from the very same source, accompanied by X-rays, neutrons and relativistic electrons. These special bunch characteristics turn out to be very promising for a whole range of applications in various fields of research [7]. The short ion bunch durations, for example, are advantageous for the study of fast reaction dynamics in radiation chemistry [8] or for the investigation of DNA defect creation as a consequence of ion irradiation in radiobiology [9]. Considerable efforts have been invested into the still ongoing examination of the suitability of laser-accelerated ion bunches for medical radiotherapy [10, 11], especially regarding the cellular response to the pulsed high doses [12–14], theoretical considerations about ion beam and dose delivery [15, 16] as well as first attempts towards in-vivo irradiation of vertebrates [17]. High potential for laser-driven ion acceleration in radiotherapy is particularly seen in the possible ultra-fast dose delivery (being especially interesting for the concept of FLASH irradiation which requires dose rates above 100 Gy/s [18]) and in the feasibility of the instantaneous

production of more than one ion species [19], although there still remains a long path towards clinical application.

Another high-potential application for laser-driven ion acceleration is related to medical imaging and radiography in general, which exploits especially two properties of this unique ion source [20]: on the one hand, the generated mixed radiation field can be used for bi-modal imaging, for example employing both protons and X-rays from the very same particle source, and, on the other hand, the extremely small source size can be used for phase contrast imaging along a very short distance. In material science, laser-accelerated ion bunches are, for example, of great interest for non-destructive material characterization using ion beam analysis [21], which could benefit from reduced efforts for radiation protection, an easily tunable energy spectrum (by modification of the laser energy) and reduced facility sizes compared to the typically employed conventional accelerators. Laser-based ion acceleration may also serve for the production of bright, ultra-short neutron bunches with extremely high peak fluxes [22–24], which are generated by nuclear reactions when protons or deuterons impinge on a converter material like beryllium or lithium fluoride.

The present dissertation work achieved essential milestones towards the realization of an application idea for laser-driven ion acceleration regarding nuclear astrophysics, which is aiming at deepening the understanding of the nucleosynthesis of the heaviest elements in the Universe. Fig. 1.1 shows the chart of nuclides with the stable nuclei (in black) and the hitherto known isotopes (in yellow). Besides, the most important nucleosynthesis processes are indicated. Right after the big bang, the primordial abundance structure has been formed within the first $3 - 20$ minutes [27, 28]. During the big bang nucleosynthesis, only light elements (^{4}He, D, ^{3}He and ^{7}Li) have been produced (light blue line in Fig. 1.1), with dominating contributions of hydrogen and ^{4}He, having a primordial abundance of about 75 % and 25 %, respectively [29]. Fusion processes in stars are responsible for the generation of heavier elements up to iron (green line in Fig. 1.1) [30], where the nuclear binding energy reaches a maximum, which inhibits the fusion to heavier nuclei.

Above iron, nucleosynthesis is dominated by neutron capture processes, which in turn are balanced by radioactive β^--decay [31–33]. As indicated by the arrows on the bottom right part of Fig. 1.1, neutron capture leads to an increase of the isotope's neutron number (towards the right in the chart of nuclides), while the β^--decay subsequently converts neutrons to protons (diagonally towards the top left). By this, nuclei with higher proton number Z are generated while preserving the mass number A, which then can further capture neutrons, repeating this whole process and leading to the production of heavier

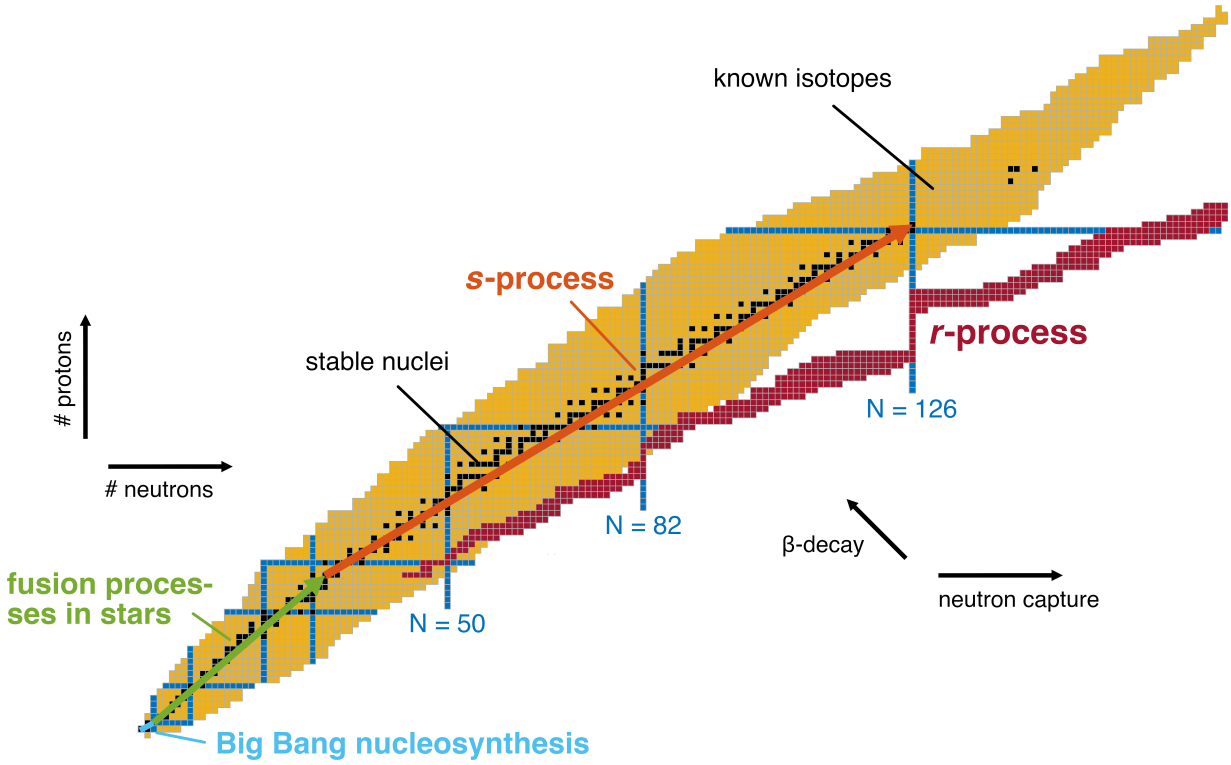

Figure 1.1: Chart of nuclides with visualized nucleosynthesis processes. The stable nuclei are shown in black and the known isotopes are displayed in yellow (data taken from the Karlsruhe Nuclide Chart of 2018 [25]). The magic proton and neutron numbers are shown as blue horizontal and vertical lines, respectively. The r-process path is illustrated in red (pathway taken from reference [26]).

and heavier elements.

While the β^--decay rate is solely an isotope-specific property, the rate of neutron capture strongly relates to the astrophysical environment, namely on the neutron density. At relatively low neutron densities of about $10^6 - 10^{10}$ cm^{-3}, the neutron capture is slow compared to the β^--decay (i.e. the average time between two neutron capture events τ_n is much larger than the mean β^--decay lifetime τ_β: $\tau_n \gg \tau_\beta$) and the nucleosynthesis process follows the valley of stability in the chart of nuclides. This is denoted as the slow neutron capture (s-)process [34], which is indicated by the orange line in Fig. 1.1. The s-process occurs predominantly at late evolutionary stages of low- and intermediate-mass stars ($\leq 8\,\mathrm{M}_\odot$, with $\mathrm{M}_\odot$ being the solar mass). Lighter isotopes with mass numbers of $\mathrm{A} \leq 90$ are also produced by a weak s-process component during neutron-releasing fusion processes at massive stars ($> 8\,\mathrm{M}_\odot$). The s-process terminates at polonium (^{210}Po), which decays into lead (^{206}Pb) by α-decay before it captures further neutrons, resulting in a cycle

around lead, bismuth and polonium [30]. Heavier naturally abundant elements like thorium (^{232}Th) and uranium (^{235}U, ^{238}U) cannot be generated by the s-process. Instead, they result from the rapid neutron capture (r-)process [33], which proceeds on the neutron-rich side of the chart of nuclides, as displayed by the red-coloured isotopes in Fig. 1.1. The r-process occurs at astrophysical sites with extremely high neutron densities of around 10^{23} cm^{-3}. At these neutron densities, neutron capture is fast compared to the β^--decay ($\tau_n \ll \tau_\beta$) and the nuclei capture multiple neutrons before they decay to the next higher-Z element, leading the r-process nuclei away from the valley of stability towards neutron-rich isotopes.

Both s- and r-process contribute approximately equally to the abundances of heavy elements above iron in the Universe [31–35], as demonstrated in Fig. 1.2 showing the elemental abundances in the solar system. Obviously, there are elements that are predominantly generated by either the s-process (like strontium or barium) or the r-process (like xenon, europium or platinum), while others are equally produced by both processes. It is apparent that each process exhibits three distinct maxima in the abundance distribution which are indicated by the respective arrows in Fig. 1.2. These abundance peaks can be ascribed to so-called waiting points in the nucleosynthesis processes at the magic neutron numbers N = 50, 82 and 126. The magic neutron numbers are associated with closed neutron shells in the nuclei, which result in a reduction of the neutron capture cross sections. Thus, the further nucleosynthesis of heavier elements is slowed down, which leads to the

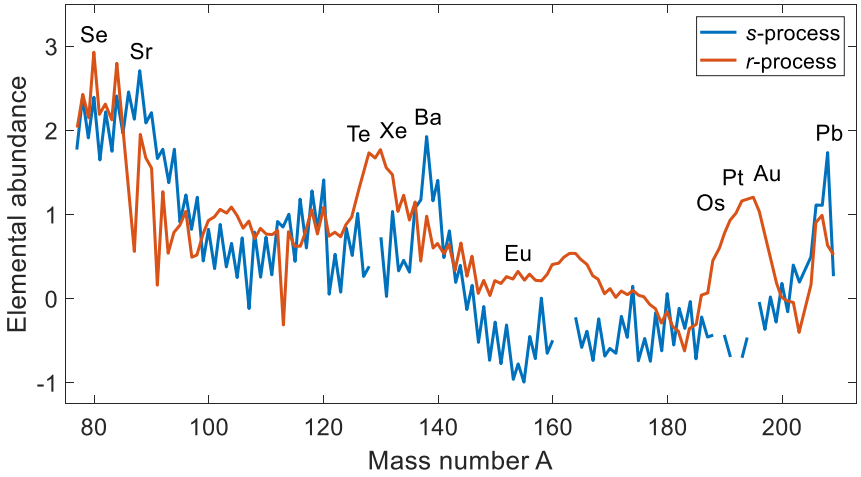

Figure 1.2: Abundances of heavy elements in the solar system generated by the s-process (blue) and the r-process (orange). The y-axis shows the common logarithm of the elemental abundances relative to hydrogen with an offset of 12. The arrows indicate peaks in the abundance distribution associated with the waiting points at the magic neutron numbers. Figure adapted from reference [32].

accumulation of elemental abundances around the waiting points. The r-process nuclei reach the magic neutron numbers far off the valley of stability on the neutron-rich side of the chart of nuclides (i.e. at a lower proton number) and undergo β^--decay until stable isotopes are generated. Therefore, their peaks in the abundance structure are shifted towards lower mass numbers compared to the s-process.

While knowing that the r-process proceeds in explosive, high-neutron-density environments, the exact astrophysical sites have been debated for decades [35]. Possible candidates are especially neutrino winds of core-collapse type II supernovae and mergers of two neutron stars. Evidence is growing that the latter are indeed a prime source for the r-process nucleosynthesis, at least for the heavier isotopes. Together with the groundbreaking detection of gravitational waves caused by a binary neutron star merger by the LIGO-Virgo collaboration in 2017 [36], the spectroscopic signatures of a kilonova have been detected [37, 38]. Kilonovae are thermal afterglows which are powered by the energy released by the radioactive β-decay of the r-process nuclei, which proves the occurrence of the r-process in merging neutron star binaries beyond any doubt.

Still, the dynamics and physical conditions of the r-process as well as the role of alternative r-process sites prompt yet unanswered questions [39]. This is because the understanding and simulations of the involved nuclear physics lack precise experimental data about the nuclear properties (e.g. masses, decay half-lives and β-delayed neutron emission probabilities) of the neutron-rich isotopes especially close to the waiting point at the magic neutron number N = 126. The nuclide chart in Fig. 1.1 illustrates the gap between the known nuclear isotopes as of 2018 and the nuclei which are expected to be involved in the r-process around the waiting point at N = 126. Up to now, the generation of neutron-rich isotopes in this region has not been realized with conventional acceleration concepts. Considerable effort is being made in the design and construction of new rare-isotope facilities with larger-scale accelerators (e.g. FRIB at the Michigan State University in the USA [40], RIBF at the RIKEN Nishina Center in Japan [41] or FAIR at GSI in Germany [42]), which aim at the production of neutron-rich isotopes close to the N = 126 waiting point [39].

Laser-driven ion acceleration offers the potential for two alternative, eventually more cost-effective approaches for gaining knowledge about the nuclear physics involved in the r-process. One of them, suggested by Chen et al. [43], employs the above mentioned high-brightness neutron bunches generated by irradiation of a converter material with laser-accelerated protons or deuterons, which are directed towards a heavy element target. This offers the potential of the direct measurement of (double) neutron captures and β-

decay rates, which are of relevance for the r-process, possibly even in laser-generated hot plasma conditions. The second laser-based approach is the so-called fission-fusion reaction mechanism, proposed by Habs et al. [26], which is the long-term goal of the research project this dissertation work is associated with. The fission-fusion reaction mechanism directly aims at the generation – and the subsequent measurement of the nuclear properties – of neutron-rich isotopes in reach of the N = 126 waiting point. The idea behind this reaction scenario is the laser-driven acceleration of heavy, fissile ions which impinge afterwards onto a solid foil out of the same fissile material, which leads to fission of both heavy projectile and target ions. After that, the light neutron-rich fission fragments can fuse with each other and form thereby extremely neutron-rich isotopes close to the desired magic neutron number (more details are provided in Sec. 2.4).

The fission-fusion reaction mechanism requires the usage of laser-accelerated ion bunches, as they have an unprecedentedly high, almost solid-state-like density. The usage of a conventional ion source would not yield a detectable amount of fission-fusion products due to the low cross sections of the involved processes. At the beginning of this thesis work in 2016, little was known about the laser-driven acceleration of heavy ions in the required mass range of A $\geq$ 200. Only two experiments had been documented which delivered reasonable heavy ion energies: Clark et al. accelerated in 2000 lead ions to energies of about 2 MeV/u [44] and Braenzel and colleagues reported in 2015 on the acceleration of gold ions up to energies of 1 MeV/u [45]. Both results were still far away of the kinetic energies which are required to overcome the fission barrier (e.g. $\approx$ 7 MeV/u in case of thorium), which motivated this thesis work dealing with the investigation of laser-driven heavy (gold) ion acceleration as preparatory study for the realization of the fission-fusion reaction mechanism.

In the past years, the interest in the study of laser-driven heavy ion acceleration and in understanding the underlying ionization dynamics has been growing. Petrov et al. published in 2016 and 2017 two simulation papers theoretically investigating the acceleration of gold ions from varying foil thicknesses and implementing diverse pulse parameters from three different laser systems [46, 47]. In 2019, the results presented in Sec. 4.1 have been published with improved gold ion energies up to 5 MeV/u [48], being a factor of 2.5 higher than the above mentioned results from Clark et al. for lead ions. In 2020, an additional simulation of the acceleration of gold ions with long (500 fs) laser pulses has been published by Domanski et al. [49]. Furthermore, two experimental papers have been released: one by Nishiuchi et al. [50] dealing with the acceleration of silver ions including a detailed dis-

cussion of potentially involved ionization mechanisms and one by Wang et al. [51], further pushing the gold ion energies to about 6.1 MeV/u and showing for the first time experimentally measured charge state distributions for gold ions above 1 MeV/u, however, still with limited resolution. The results presented in Sec. 4.2 advance this work showing the acceleration of gold ions to energies beyond 7 MeV/u, which are required for – and can thus be judged as the accomplishment of a major milestone towards – the realization of the fission-fusion reaction mechanism. Additionally, individual gold ion charge states could be resolved for the first time, providing insight into a remarkable dependency of the charge state distributions on the target foil thicknesses. As none of the dominant ionization processes provides a straight-forward explanation for the occurring charge states, this data is very valuable for future theoretical investigations of the ionization dynamics.

Outline of the dissertation

The dissertation starts in Chapter 2 with a brief theoretical discussion of laser-driven ion acceleration, beginning with a description of the dominant ionization mechanisms. Basic equations for the laser plasma interaction are provided as well as a short overview of the processes which lead to the absorption of the laser energy by the plasma electrons. The two most prominent laser-based ion acceleration methods will be introduced before this chapter ends with a description of the fission-fusion reaction mechanism, being the long-term goal of this research project.

Chapter 3 provides an overview of the technology essential for the later-on presented laser-driven heavy ion acceleration experiments. It starts with a brief description of high-power laser systems, followed by the detectors employed for the detection of the accelerated charged particles. The principles of the detection with magnetic spectrometers will be introduced together with details about a specifically designed heavy ion diagnostics. The chapter closes with a discussion of the radiative target cleaning method which has been employed for the removal of surface contaminants on the gold target foils.

Chapter 4 is the main part of this dissertation presenting two experimental campaigns dedicated to the laser-driven acceleration of heavy (gold) ions. The first one has been conducted at the Texas Petawatt laser (TPW) at the University of Texas at Austin, USA, resulting in kinetic heavy ion energies which have been a factor of 2.5 higher than published before. The second one has been conducted at the PHELIX laser of the GSI Helmholtzzentrum für Schwerionenforschung (GSI) in Darmstadt, Germany. During this beamtime, the previously measured heavy ion energies could be overtaken and gold ion charge state dis-

tributions with a yet unprecedented resolution have been detected.

Chapter 5 summarizes the results obtained by this thesis work and provides an outlook on the next steps towards the realization of the fission-fusion reaction mechanism.

Chapter 2

Theoretical Background: Laser-Driven Ion Acceleration

The principle of laser-driven ion acceleration is very simple: a high-power laser pulse is focused down to a small spot on a solid target. Above certain laser threshold intensities, the target atoms are ionized and the freed electrons form a plasma. In the following, the laser interacts with this plasma, which absorbs part of the laser energy resulting in higher electron velocities. Consequently, some energetic plasma electrons will leave the target, while the ionized target atoms will initially remain at their original positions. Thus, immense electric dipole fields in the order of MV/μm emerge that accelerate the target ions to high energies. This chapter briefly reviews the mechanisms of target ionization (Sec. 2.1), the principles of laser plasma interaction and the heating of plasma electrons (Sec. 2.2) as well as the methods of the subsequent acceleration of ions to high energies (Sec. 2.3). The targeted application of this thesis work, the fission-fusion reaction mechanism, is described in Sec. 2.4.

2.1 Plasma Generation and Target Ionization

The understanding of the ionization mechanisms of solid targets by high-intensity lasers is essential for the control of laser-driven heavy ion acceleration, as the realized ion charge states fundamentally influence the heavy ion bunch characteristics. The relevance of the ionization dynamics becomes conceivable considering that, on the one hand, the strength and the spatial extent of the accelerating charge separation field depends on the number and

the distribution of the freed electrons. On the other hand, the strength of the accelerating force itself, which acts on the heavy ion, is depending on the particle charge as well.

A major outcome of this thesis is the highly-resolved detection of the charge state distributions of laser-accelerated gold ion bunches, as will be discussed in the end of Chapter 4. Therefore, the direct ionization by the electromagnetic field of the laser pulse and – as a direct consequence of the field ionization – the ionization by collisions of the freed electrons with target atoms are reviewed as expected predominant ionization mechanisms in more detail in this section.

2.1.1 Optical Field Ionization

The foundations for the theoretical description of the ionization of atoms by high-intensity laser fields have been laid by L. V. Keldysh in 1964 [52]. He combined the two different field ionization processes (multiphoton ionization and tunnel ionization) as limiting cases of the same nonlinear photoionization theory. Both mechanisms can be distinguished by the Keldysh parameter γ,

$$\gamma = \frac{\omega_0 \sqrt{2 m_e I_Z}}{eE}, \tag{2.1}$$

with e being the elementary charge, E the field strength of the laser, m_e the electron mass and I_Z the ionization potential of the ion with charge state Z. For $\gamma \gg 1$, *multiphoton ionization (MPI)* is predominant. This process is illustrated by Fig. 2.1(a), which shows in blue the potential of the atomic nucleus and the electron as black circle. The electron absorbs multiple photons (red) in order to be lifted above the atomic potential. For $\gamma \ll 1$, *tunnel ionization* dominates, which is shown in Fig. 2.1(b). The external laser potential (dashed orange line) modifies the ionic potential in blue and a potential barrier is formed, here on the right side of the electron, through which the electron can tunnel (green dashed line).

The meaning of the Keldysh parameter for the differentiation of both mechanisms can be understood intuitively if one considers classically the time that an electron needs to tunnel through the potential barrier. We assume that the electron has a kinetic energy of the order of the ionization potential I_Z and has to pass through a potential barrier of width $l = I_Z/(eE)$ [52, 53]. The classical time of flight through the potential barrier (tunneling time) is then

$$\tau_T = \frac{l}{\sqrt{2 I_Z / m_e}} = \frac{\sqrt{m_e I_Z / 2}}{eE}.$$

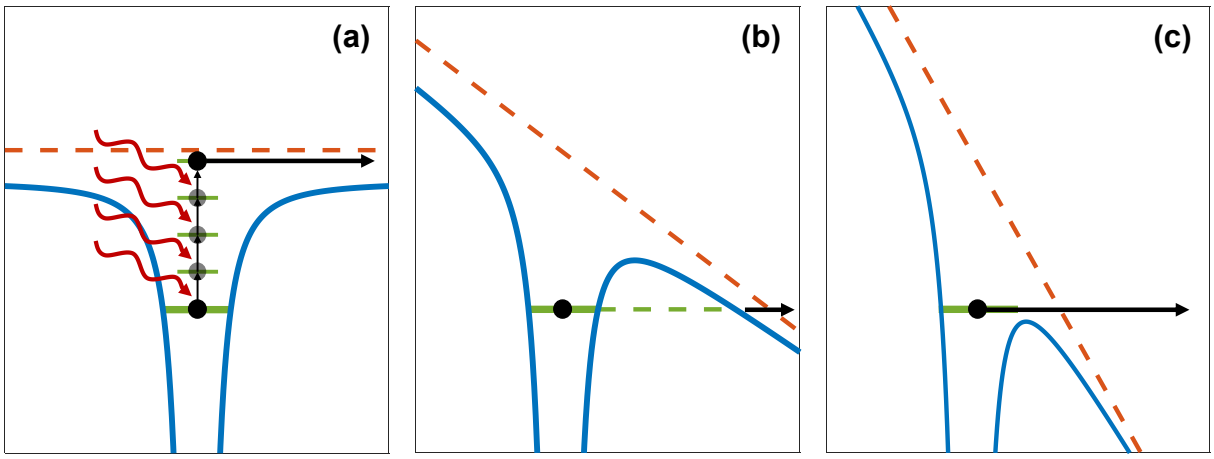

Figure 2.1: The electron (black circle) is shown in the electric potential of the ion (blue), that was modified by an external field (potential plotted as orange dashed lines), for three cases:
(a) multiphoton ionization with very fast oscillating electric field (i.e. $\gamma \gg 1$, the electron sees on average the non-modified ion potential); the electron can be lifted over the potential barrier by the absorption of multiple laser photons (red),
(b) tunneling ionization with a slowly oscillating, quasi-static electric field (i.e. $\gamma \ll 1$). The modification of the ion potential lasts long enough that the electron can tunnel through the potential barrier (green dashed line),
(c) barrier suppression ionization, similar case to (b) but with a higher electric field that suppresses the potential barrier sufficiently, such that the electron can escape the ionic potential without tunneling.

The potential barrier is formed by superposition of the atomic potential and the laser field. As the laser field oscillates, this barrier is only maintained for the duration of half of a laser cycle, $\tau_L/2 = 1/2\omega_0$, before laser field changes its polarity and the surmountable potential barrier becomes a potential wall. Relating τ_T with $\tau_L/2$ delivers [53]

$$\frac{\tau_t}{\tau_L/2} = \frac{\omega_0\sqrt{2m_e I_Z}}{eE} = \gamma,$$

which is the Keldysh parameter. Thus, in the regime of MPI, for $\gamma \gg 1$, the polarity of the laser field changes too fast (which means that the potential barrier is not maintained sufficiently long) for the electron to tunnel through the potential barrier. Calculating the Keldysh parameter for laser-driven heavy ion acceleration delivers $\gamma \ll 1$[1], which means

[1] A conservative calculation: A nowadays easily realizable laser peak intensity of $I = 1 \times 10^{20}$ W/cm^2 delivers an electric field strength of $E = \sqrt{2I/c\epsilon_0} = 2.74 \times 10^{13}$ V/m, with c denoting the vacuum speed of light and ϵ_0 the vacuum permittivity. Taking a rather high ionization potential of 21920 eV for 74-fold ionized gold (which corresponds to the highest gold charge state detected in the scope of this thesis, compare Chapter 4), and a laser wavelength of 1 μm, the Keldysh parameter can be computed to be $\gamma = 0.03 \ll 1$.

that MPI is only of minor relevance for the ionization of a target exposed to a high-intensity laser pulse used for laser ion acceleration.

For $\gamma \ll 1$, the oscillation of the laser field is slow compared to the electron tunneling time. The potential barrier is maintained sufficiently long for the electron to tunnel through. If the laser field strength is further increased, the potential barrier is suppressed to values even below the electron energy level and the electron can simply leave the Coulomb field of the atomic nucleus, as shown in Fig. 2.1(c). This is called *barrier-suppression ionization (BSI)* and can be easily calculated in one dimension [54, 55]: the potential experienced by the electron is the superposition of the Coulomb potential of the ion with charge state Z, which is created by the ionization, and the potential caused by the laser field E, which oscillates very slowly and is thus assumed to be quasi-static,

$$V(x) = -\frac{Ze^2}{4\pi\epsilon_0 |x|} - eEx.$$

The required laser field strength for the electron to overcome the potential barrier can be calculated by equating the maximum of the potential, $V_{\max} = -\sqrt{e^3 ZE/\pi\epsilon_0}$, to the ionization potential I_Z, which delivers a threshold laser field for the BSI of

$$E_{\text{th}}^{\text{bsi}} = \frac{\pi\epsilon_0 I_Z^2}{Ze^3}.$$

This delivers a threshold laser intensity for the onset of ionization of

$$I_{\text{th}}^{\text{bsi}} = \frac{\pi^2 c\epsilon_0^3 I_Z^4}{2Z^2 e^6},$$

which reads in an easier usable notation [56]

$$I_{\text{th}}^{\text{bsi}} = \frac{2.2 \times 10^{15}}{Z^2} \left(\frac{I_Z}{27.21\,\text{eV}}\right)^4 \text{W/cm}^2. \tag{2.2}$$

This simple model describes surprisingly well the measured ionization rates of noble gases exposed to high-intensity laser pulses [54, 55] and delivers fair estimates for the threshold intensity. According to Gibson et al. [57] this can be attributed to the opposing influence of different error sources that cancel out each other.

A physically more accurate description including electron tunneling can be found by taking the ionization rate W_Z (= tunneling rate through the atomic potential barrier) of a three-dimensional hydrogenlike atom, a "simple atom", with charge state Z in a static

electric field E [58, 59],

$$W_Z^{\mathrm{sa}} = 6\omega_0 E_Z \left(\frac{\frac{2}{3}E_Z^{3/2}}{E} \right) \cdot \exp\left[-\frac{\frac{2}{3}E_Z^{3/2}}{E} \right], \tag{2.3}$$

with $\omega_0 = 4.1 \times 10^{16}\,\mathrm{s}^{-1}$ denoting the atomic frequency unit, $E_Z = 2I_Z/E_h$ the ionization potential of the ion in atomic units and $E_h = 27.2$ eV being the atomic energy unit, defined as twice the Rydberg constant. This ionization rate can be applied to oscillating laser fields by averaging over one laser cycle. Based on this cycle-averaged ionization rate, Chang et al. derived an expression for the threshold laser field strength for the sequential ionization of an ion with charge state Z to the charge state $Z+1$, which they defined as the field strength at which the ionization probability is equal to 1 % [59],

$$E_{\mathrm{th}}^{\mathrm{sa}} = \frac{2}{3} E_Z^{3/2} E_{au} \cdot \ln\left[\frac{(6\omega_0 E_Z)(2\tau/1.76)}{0.01} \right]^{-1},$$

with $E_{au} = 5.1 \times 10^{-11}$ V/m being the atomic unit of the electric field and τ denoting the full width at half maximum of the laser pulse. The cycle-averaged threshold intensity for the ionization of a hydrogenlike, simple atom with charge state Z to charge state $Z+1$ is thus

$$I_{\mathrm{th}}^{\mathrm{sa}} = \frac{2c\epsilon_0}{9} E_Z^3 E_{au}^2 \cdot \ln\left[\frac{(6\omega_0 E_Z)(2\tau/1.76)}{0.01} \right]^{-2}. \tag{2.4}$$

Ammosov, Delone and Krainov [61] developed an expression for the ionization rate for complex atoms in static electric fields based upon a quasi-classical approximation [57, 59],

$$W_Z = \omega_0 \widetilde{C}_{nl}^2 G_{lm} \frac{E_Z}{2} \left(\frac{2E_Z^{3/2}}{E} \right)^{2n-|m|-1} \cdot \exp\left[-\frac{2/3 \cdot E_Z^{3/2}}{E} \right], \tag{2.5}$$

where n, m and l are the standard quantum numbers of the electron's valence shell and [59]

$$\widetilde{C}_{nl}^2 = \left(\frac{2e}{n} \right)^{2n} \frac{3^{2n-1}}{(2\pi n)},$$

$$G_{lm} = \frac{(2l+1)(l+|m|)!}{2^{|m|}(|m|)!(l-|m|)!3^{|m|}},$$

with e being Euler's number. This model is also referred to as ADK model in literature and is the most accepted model for the photoionization of complex atoms, as it includes

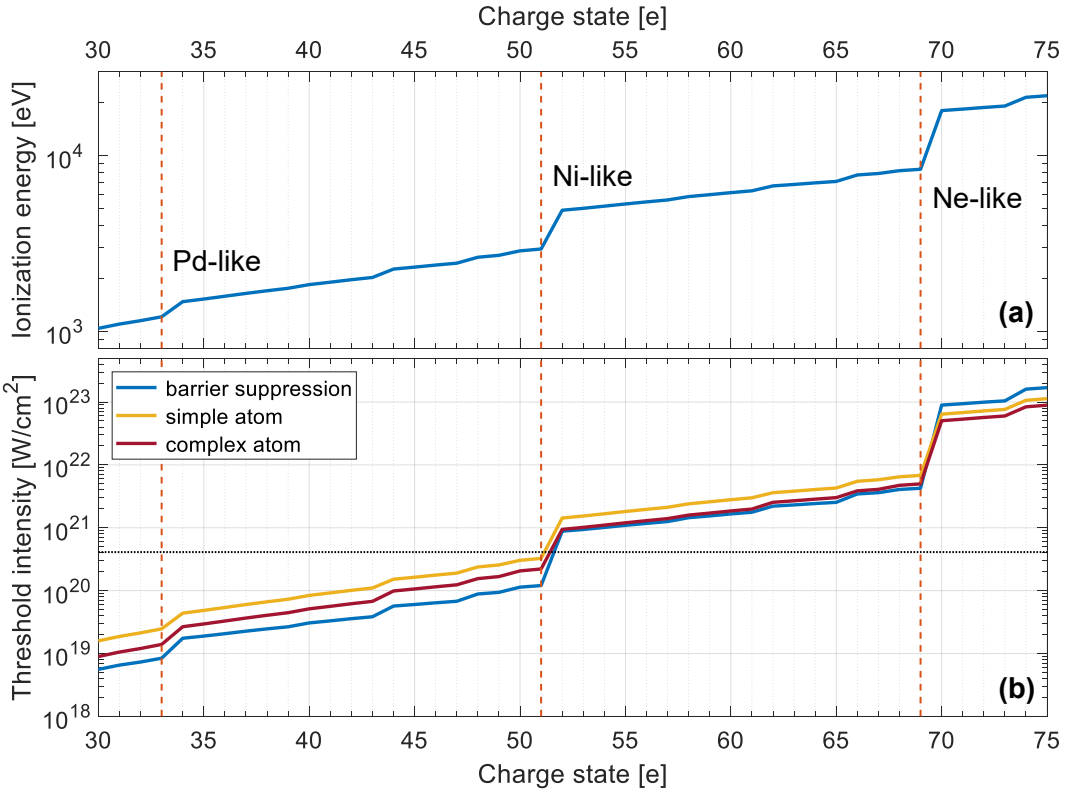

Figure 2.2: (a) Ionization potentials for the sequential ionization of gold ions, taken from reference [60]. The dashed orange lines show charge states at which further ionization requires a relatively large amount of energy compared to the surrounding charge states. These configurations can be assigned to closed atomic shells: 33^+ is palladium-like with a closed 4d shell ([Kr].4d10), 51^+ is nickel-like with a closed 3d shell ([Ar].3d10) and 69^+ is like the noble gas neon with a closed 2p shell.
(b) Laser threshold intensity for the case of gold for the barrier suppression ionization (blue, Eq. (2.2)), the simple atom tunneling ionization (yellow, Eq. (2.4)) and the complex atom tunneling ionization (red, Eq. (2.6)). The black dotted line indicates the cycle-averaged peak intensity of the experiment at the GSI using the PHELIX laser (see Sec. 4.2), for which consequently gold ions with charge states up to 51^+ would be expected from optical field ionization.

with the quantum numbers also a species dependency. For the calculation of the ionization rates, the G_{lm} factor is averaged over degenerate quantum states. Based on the ADK model, Chang et al. found the cycle-averaged threshold field strength for complex atoms to be [59]

$$E_{\mathrm{th}}^{\mathrm{ca}} = \frac{2}{3} E_Z^{3/2} E_{au} \cdot \ln\left[\frac{(\omega_0 \widetilde{C}_{nl}^2 G_{lm} \frac{E_Z}{2})(2\tau/1.76)}{0.01}\right]^{-1} .$$

Thus, the corresponding cycle-averaged threshold intensity for *complex atoms* can be cal-

culated by

$$I_{\mathrm{th}}^{\mathrm{ca}} = \frac{2c\epsilon_0}{9} E_Z^3 E_{au}^2 \cdot \ln\left[\frac{(\omega_0 \widetilde{C}_{nl}^2 G_{lm} \frac{E_Z}{2})(2\tau/1.76)}{0.01}\right]^{-2}. \tag{2.6}$$

Fig. 2.2(a) shows in blue the ionization potentials, E_Z, for the sequential ionization of gold [60], which was the material of choice for the laser-driven heavy ion acceleration experiments in this thesis. The dashed orange lines show positions in the charge state spectrum with significant steps in the ionization potential that occur for closed atomic shells: 33^+ is palladium-like with a closed 4d shell ([Kr].4d10), 51^+ is nickel-like with a closed 3d shell ([Ar].3d10) and 69^+ is like the noble gas neon with a closed 2p shell. These ionization energies have been inserted into Eqs. (2.2), (2.4) and (2.6). The results are plotted in Fig. 2.2(b), in blue for the BSI, in yellow for the hydrogenlike, simple atom model and in red for the ADK-based model of complex atoms. The overall behaviour is very similar for all formulas. Clearly, the large steps in the ionization potential at the closed shell electron configurations for the gold atoms can also be seen in the threshold intensity. It is striking that the simple barrier suppression ionization model indeed describes the laser threshold intensities very well, especially in the charge state range between 52^+ and 69^+. The dotted black line indicates the cycle-averaged peak intensity, which has been achieved during the experiment at the GSI Helmholtzzentrum für Schwerionenforschung in Darmstadt, Germany, using the PHELIX laser, which is presented in Sec. 4.2. It can be seen, that 51^+ is the maximum charge state of gold ions which would be expected for optical field ionization by all three presented models.

2.1.2 Electron Impact Ionization

The second relevant ionization mechanism is the so-called collisional or *electron impact ionization*. An electron e^-, that has been liberated by the optical laser field, collides with a Z-fold ionized atomic nucleus, A^{Z+}, which results in further ionization,

$$\mathrm{e}^- + \mathrm{A}^{Z+} \rightarrow \mathrm{A}^{(Z+1)+} + 2\,\mathrm{e}^-. \tag{2.7}$$

Generally, this problem of electrons interacting with atomic nuclei requires a quantum-mechanical treatment [62]. However, there are (semi-)empirical approaches that estimate the ionization cross sections in reasonable agreement with experimental data. Most widely used for cross section estimations is the Lotz formula [63], which formed also the basis for the collisional ionization calculations for the simulations of laser-driven gold ion accelera-

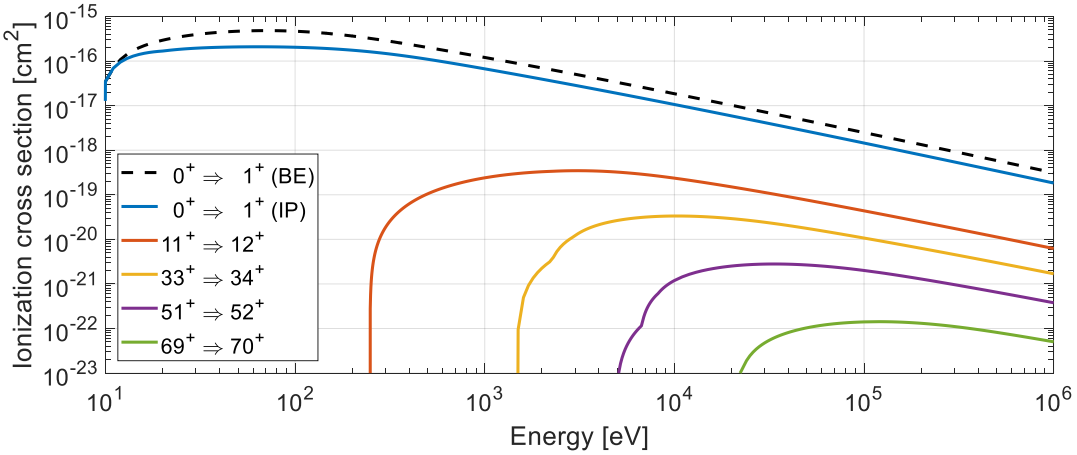

Figure 2.3: Eq. (2.8) has been evaluated for different ionization steps. Instead the binding energies, the ionization potentials [60] have been taken for the calculations. The black dashed line has been determined by calculation with the binding energies for neutral gold from reference [64] and agrees with the cross section curve for neutral gold in reference [65]. A comparison with the calculation using the ionization energies shows differences up to a factor of 2.3, but agrees in the overall shape.

tion by Petrov et al. [46,47], which are of relevance for this thesis. The total cross section σ for the single ionization of an atom or ion is the summation over the individual ionization cross sections σ_{ei} of all electrons, which are bound to the atom or ion [63],

$$\sigma = \sum_{i=1}^{N} q_i \, \sigma_{ei},$$

with q_i denoting the number of all electrons in a subshell i, which are assumed to exhibit the same individual ionization cross sections. According to Lotz, the total ionization cross section then reads [63]

$$\sigma = \sum_{i=1}^{N} q_i a_i \frac{\ln(E/P_i)}{EP_i} \left(1 - b_i \exp\left[-c_i(E/P_i - 1)\right]\right), \tag{2.8}$$

with a_i, b_i and c_i being empirical subshell-specific constants, P_i the binding energies of the electrons in the i-th subshell (P_1 is the ionization potential of the valence electron) and $E \geq P_i$ the kinetic energy of the impacting electron. The underlying assumptions for the calculation of collisional heavy ion ionization cross sections are given in reference [65], where also the constants a_i, b_i and c_i are tabulated, which have been "determined by experiment,

theory, or reasonable guesswork". For the calculation of the total cross sections $N = 3$ is chosen (i.e. only the cross sections of the three outermost subshells are summed up) [66].

The electron impact ionization cross sections for gold ions have been calculated using the Lotz formula (Eq. (2.8)) for electron configurations with closed shells (33^+, 51^+ and 69^+ as in Fig. 2.2 and 11^+ for [Xe].4f14]) and plotted in Fig. 2.3. As the binding energies for highly charged gold ions were not available, the calculations have been done using the ionization potentials from reference [60], assuming that this will still be sufficient to get estimates for the order of magnitude of the ionization cross sections. In order to confirm this assumption, the cross sections of the neutral gold atom have been calculated once with the ionization potentials (blue line) and once with the binding energies for neutral gold given by reference [64] (black dashed line), which results in the cross section curve for gold in reference [65]. Both curves differ by a maximum factor of 2.3, and are thus in reasonable agreement with each other. Therefore, it is assumed that the calculations with the ionization potentials provide decent ballpark estimates for the electron impact ionization cross sections for highly charged gold.

2.2 Laser Plasma Interaction

The ionization processes from the preceding section create a plasma of free electrons within the solid target foil. A plasma in general contains charged particles, exhibits collective behaviour and is quasi-neutral in charge [67]. Collective behaviour means that the particle motion in a plasma is not dominated by collisions but by long-range electromagnetic forces. If a charge is inserted into the plasma, its Coulomb field acts on all surrounding plasma particles. A direct consequence of the collective characteristics is that the plasma particles rearrange in the presence of this charge and, by that, shield regions further away from the charge from the disturbing influence of its Coulomb field, which is also known as Debye shielding. Thus, despite possible variations in the electric or magnetic fields, leading to a local accumulation or dispersion of electric charges, the overall plasma stays neutral – it is quasi-neutral. The width of this neutralizing plasma particle cloud, the so-called sheath, is called Debye length and reads [67]

$$\lambda_{\mathrm{D}} = \sqrt{\frac{T_e}{4\pi n_e e^2}}, \tag{2.9}$$

with T_e being the electron temperature[2], n_e the electron density and e the elementary charge. An inserted charge leads to a rearrangement of the plasma particles within a radius corresponding to the Debye length, while particles outside of this sheath are not influenced.

The presence of the electromagnetic field of a high-power laser pulse leads to a displacement of the plasma electrons, while the ions remain at their initial position due to their high mass. As a consequence, a neutrality-restoring electric charge separation field acts on the electrons. This redirects the electrons to their equilibrium position close to the positive ion charge. As the electrons experience an accelerating force towards this equilibrium position, they will overshoot and start to oscillate around that point with the plasma frequency [67, 68],

$$\omega_p = \sqrt{\frac{4\pi n_e e^2}{m_e}}. \tag{2.10}$$

As long as the oscillation frequency of the plasma electrons is lower than the laser frequency (i.e. $\omega_p < \omega_0$), the electrons cannot compensate for the incoming electromagnetic field and the laser can penetrate the plasma. This is reflected in a real refractive index [68],

$$n_\mathrm{r} = \sqrt{1 - \frac{\omega_p^2}{\omega_0^2}}. \tag{2.11}$$

Consequently, if the plasma oscillations are faster than the laser field oscillations (i.e. $\omega_p > \omega_0$), the refractive index becomes complex and the laser is reflected at the plasma surface. The turning point, when $\omega_p = \omega_0$, defines the critical density of the plasma,

$$n_{cr} = \frac{m_e \omega_0^2}{4\pi e^2}. \tag{2.12}$$

The plasma is denoted as overdense for $n_e > n_{cr}$ (i.e. when the laser cannot penetrate and is reflected back) and as underdense for $n_e < n_{cr}$.

The kinetic energy of the oscillating plasma electrons can be approximated by the ponderomotive potential [69, 70],

$$E_{pon} = m_e c^2 (\gamma - 1), \tag{2.13}$$

[2]It is worth mentioning, that the plasma temperature is usually given in units of eV. The actual temperature in units of K can be calculated by division with the Boltzmann constant k_B (1 eV corresponds to $\approx$ 11600 K). The electron temperature corresponds to the mean electron energy in a two-dimensional plasma [67].

where γ is the relativistic Lorentz factor, which can be calculated using [69, 70]

$$\gamma = \sqrt{1 + I\lambda_\mu / 1.37 \times 10^{18}\ \mathrm{W\,cm^{-2}}}, \tag{2.14}$$

with I being the mean laser intensity in $\mathrm{W\,cm^{-2}}$ and λ_μ the laser wavelength in μm.

The plasma electrons absorb the energy of the laser pulse, before it is transferred to the target ions, as will be briefly outlined in Sec. 2.3. In the following, the dominating mechanisms for the energy transfer from laser pulses with intensities of $I\lambda^2 > 10^{15}\ \mathrm{W\,\mu m^2/cm^2}$ to the plasma electrons will be shortly sketched based upon reference [71], which offers a more detailed description.

Resonance Absorption

Resonance absorption [72, 73] requires a component of the electric laser field parallel to the plasma density gradient of an overdense target. The laser field leads to electron oscillations, which result in slight density fluctuations along the density gradient. At the critical density, the plasma electron oscillations are in resonance with the laser frequency and drive a plasma wave coupling the laser energy into the plasma. This mechanism usually requires obliquely incident, p-polarized lasers [74].

Brunel Heating

Like resonance absorption, vacuum or Brunel heating [75] requires p-polarized laser pulses that are obliquely incident on overdense targets. For Brunel heating, the plasma vacuum interface has to be very sharp, i.e. a plasma density gradient scale length of well below a laser wavelength is required. Electrons at the target surface are pulled out by the laser field and get initially accelerated into the vacuum. Following the laser cycle with the alternating polarity of the accelerating electric field, the electrons turn around and reenter the plasma. Due to the steep density gradient, the critical density layer is very close to the target surface. Thus, the laser cannot penetrate the plasma and leaves the reentered electrons with their gained kinetic energy in the plasma.

Relativistic $\mathbf{j} \times \mathbf{B}$ Heating

The relativistic $\mathbf{j} \times \mathbf{B}$ heating [76] originates from the $\mathbf{v} \times \mathbf{B}$ term of the Lorentz force (see Eq. (3.5)), which leads at relativistic laser intensities to longitudinal oscillations of the electrons with twice the laser frequency along the laser propagation direction. Analogous

to the Brunel heating, a steep plasma density gradient is required, which prevents the laser from penetrating the target. Thus, it cannot influence the electrons anymore once they have been accelerated into the target, such that the kinetic electron energy is transferred to the plasma. As the $\mathbf{v} \times \mathbf{B}$ term leads to an electron movement along the laser propagation direction – contrary to the two previously presented mechanisms which are due to the electrical laser field component – $\mathbf{j} \times \mathbf{B}$ heating is most efficient for normally incident lasers. This mechanism requires linearly polarized lasers, which can lead to a significant suppression of electron heating for a circular laser polarization.

2.3 Mechanisms for Laser-Driven Ion Acceleration

At presently achievable laser intensities, laser-driven ion acceleration requires electrons as intermediate step for the energy transfer to the ions. Electron heating as described in the previous section will always occur when a high-intensity laser interacts with a solid-foil target. These hot electrons are responsible for the well known mechanism of target normal sheath acceleration (TNSA), which is introduced in Sec. 2.3.1 and explains the measured heavy-ion energy spectra in Chapter 4. Another wide-spread acceleration technique called radiation pressure acceleration (RPA), which is briefly addressed in Sec. 2.3.2, exploits the light pressure for the direct laser acceleration of electrons, leading to the subsequent generation of fast ions. The development of heavy ion bunches, accelerated in the RPA regime, is a prerequisite for the successful realization of the fission-fusion reaction mechanism, which will be addressed in Sec. 2.4. A detailed description of these two laser-based ion acceleration mechanisms and others, like Coulomb explosion, collisionless shock acceleration or the breakout afterburner regime, which are not of particular relevance for this dissertation, can be found in the respective review papers (e.g. references [4] and [5]).

2.3.1 Target Normal Sheath Acceleration (TNSA)

Answering new experimental findings of the production of high energetic proton bunches with maximum kinetic energies up to 58 MeV and a high particle number of up to 3×10^{13} particles by the interaction of high-power laser pulses, focused down to intensities in the range of about 10^{20} W/cm^2, with thin solid foil targets [2, 3], Wilks et al. developed in 2001 the concept of target normal sheath acceleration (TNSA) [77].

The working principle of TNSA is visualized in Fig. 2.4. A high-power laser pulse is focused onto a solid foil target with a thickness ranging from some tens of nm up to some

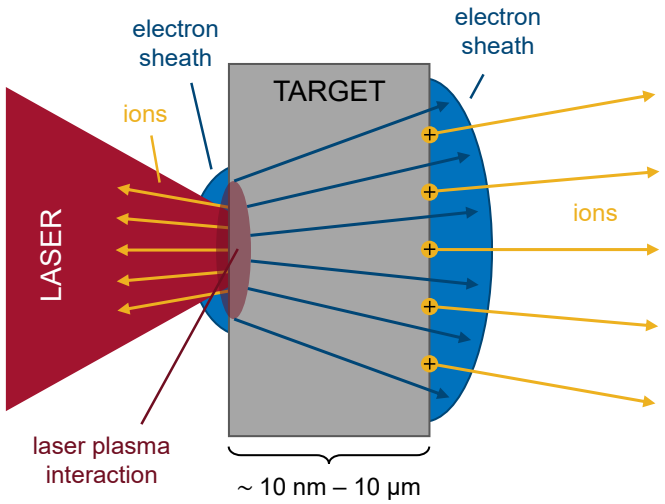

Figure 2.4: Schematic working principle of target normal sheath acceleration (TNSA).

tens of μm. As the target is overdense, the laser only interacts with the foil surface, where consequently a plasma is generated. The plasma electrons get heated by the laser pulse as described in the previous section and leave, due to their gained kinetic energy, the location of laser plasma interaction. A fraction of the heated electrons traverses the target and exits at its rear side. The hereby emerging electric fields ionize the atoms at the target rear side, leading to a charge separation field and to the formation of an electron sheath of a thickness corresponding to the Debye length λ_D, which is given by Eq. (2.9). While some electrons are continuously retracted into the target by the charge separation field, the sheath is maintained by the arrival of new electrons that have been heated by the laser plasma interaction at the target front surface. As a consequence of the electron sheath, a very strong quasi-static electric field acts on the ions at the target rear surface, which are accordingly accelerated roughly along the target normal direction. The strength of this sheath field is in the order of TV/m and can be estimated by [4]

$$E_\mathrm{sheath} = \sqrt{\frac{2T_e^2}{e_N e^2 \lambda_\mathrm{D}^2}} = \sqrt{\frac{8\pi n_e T_e}{e_N}}, \tag{2.15}$$

with e_N being Euler's number. Thus, the strength of the accelerating field and the achievable kinetic ion energies, correspondingly, are strongly depending on the density and temperature of hot electrons in the plasma. This motivates the investigation of correlations between laser-accelerated ions and electrons, as will be suggested by the simultaneous electron and ion diagnostics presented in Secs. 3.3.1 and 3.3.2. As visible in Fig. 2.4, an

electron sheath generally emerges also at the target front side, which, however, usually results in lower energetic ion bunches accelerated in opposite direction of the ions from the rear side.

Ion bunches that have been accelerated in the TNSA regime exhibit characteristics that fundamentally differ from any conventional particle acceleration source [4–6]. For instance, these ion bunches have very broad, exponentially decaying kinetic ion energy spectra up to a sharp maximum energy cutoff. At the same time, the ion bunch duration is very low in the order of some picoseconds at the moment of production. Naturally, the bunch duration broadens already after short propagation distances of some meters to values in the order of nanoseconds due to the energy-caused bunch dispersion. However, the ions are highly correlated in time and energy with a very low longitudinal emittance of 1×10^{-4} eV s [78], which in principle allows for a tight refocusing in the time domain.

Similarly, the position and divergence angle of the particles in the bunch are highly correlated, which is expressed in the normalized transverse emittance, which has been measured to be below 0.004 mm mrad [78] and, thus, at least two orders of magnitude superior to conventional accelerators. Hence, despite large divergence half-angles, which range from some tens down to two degrees (and are generally decreasing with increasing ion energies) [79, 80], such laser-accelerated ion bunches are due to their small source sizes very well suitable for a tight spatial refocusing [17, 81]. Another fundamental difference to conventional acceleration techniques is that mixed radiation fields are produced when high-intensity lasers interact with solid-density plasmas. Relativistic electrons, neutrons and X-rays accompany the ion bunch, which may consist of one or even several ion species, depending on the choice and preparation of the target.

2.3.2 Radiation Pressure Acceleration (RPA)

Radiation pressure acceleration (RPA) is based on direct laser acceleration by the light pressure acting on the particles. This mechanism was first proposed in 2004 by Esirkepov et al. [82], predicting a required minimum intensity of around 10^{23} W/cm^2 for linearly polarized lasers, which still is challenging to be realized for modern high-power laser systems. For circularly polarized and normally incident laser pulses, when the electron heating described in Sec. 2.2 is suppressed, it has been shown theoretically [83] and experimentally (e.g. [84, 85]) that RPA can occur even at lower laser intensities.

In RPA, the electrons at the surface of the target foil are pushed in forward direction by the radiation pressure of the laser pulse, while the target ions initially remain at their

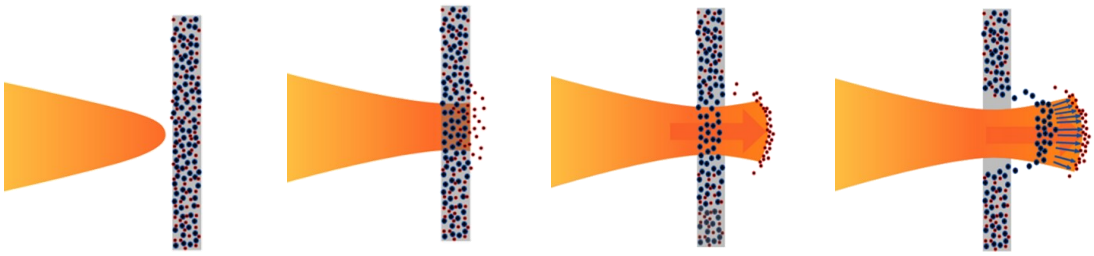

Figure 2.5: Schematic working principle of radiation pressure acceleration (RPA) in the light sail regime. Figure taken from reference [86].

original positions[3]. As a consequence, a charge separation field emerges that balances the radiation pressure, which in turn results in an acceleration of the target ions. This process is schematically illustrated in Fig. 2.5 for a thin target foil.

Generally, it can be distinguished between two different regimes of RPA. The first one is the so-called *hole boring* regime, which occurs for thick target foils. In this case, the laser 'bores' into the target like a piston, continuously pushing a compressed layer of electrons further and further into the foil and by this accelerating also ions from deeper target layers. The second regime is called the *light sail* regime, which either occurs for thin ($\sim$ 10 nm) target foils as in Fig. 2.5 or for long laser pulses, which still continue after the hole boring phase has been finished (i.e. after the rear side of the target foil has been reached). In this case, the compressed electron layer acts as relativistic mirror, that is pushed forward by the laser pulse, thereby absorbing the laser energy and transferring it to the co-moving ions.

The acceleration in the RPA regime exhibits three major advantages compared to TNSA. First, the energy bandwidth is much lower. While TNSA usually results in broad, exponential decaying energy spectra with high particle numbers at lower energy, RPA promises an acceleration that ends up in a narrow kinetic energy band at higher energies (in TNSA: $E \propto \sqrt{I}$, in RPA: $E \propto I$). The final kinetic energy of the ions (independent of the ion species!) is strongly connected to the velocity at which the laser bores into the material and/or at which it pushes the electron 'light-sail' layer after it has left the target foil. Second, the conversion efficiency of the laser energy to kinetic ion energy is much higher in RPA. While for TNSA the maximum hitherto measured conversion efficiency is around 15 % [87], it has been predicted that a transfer of almost all of the laser energy to the ions is theoretically possible in the case of RPA [82]. Moreover, both light and

[3] A direct acceleration of the ions in the target foil by the radiation pressure of the laser pulse is also conceivable, however, requires laser intensities of $I = 4.6 \times 10^{24}$ W/cm$^2 \times (1\,\mu\text{m}/\lambda)^2$ and above due to the high ion mass [82].

heavy ions are accelerated together with the electron layer and will end up with the same velocity. Compared to TNSA, where light ions are favourably accelerated, the efficiency of heavy ion acceleration in RPA is considerably higher. Third, in principle, the foil as a whole is pushed in forward direction by the laser in RPA. Thus, ion bunches with a very high, almost solid-state-like density are generated, which is up to 14 orders of magnitude higher than what is achievable with conventional accelerators [86]. This high density is the major prerequisite for the fission-fusion reaction mechanism, an application of laser-accelerated heavy ion bunches related to nuclear astrophysics, which will be covered in the following section. It should be noted that the laser-driven acceleration of ion bunches can be dominated by a certain acceleration mechanism, however, the occurrence of other mechanisms cannot be completely suppressed. Therefore, the generation of ion bunches based purely upon acceleration in the RPA regime, as would be desirable for the fission-fusion reaction mechanism, is virtually impossible.

2.4 The Fission-Fusion Reaction Mechanism

A promising application idea for laser-accelerated heavy ion bunches is the fission-fusion reaction mechanism [26], which aims at the production of extremely neutron-rich isotopes in close vicinity to the astrophysical r-process waiting point at the magic neutron number N = 126, still being inaccessible using conventional accelerators. As discussed in the previous section, this nuclear reaction scheme exploits the unprecedented high density of laser-accelerated ion bunches. The idea is that such a high-density, laser-accelerated bunch consisting of heavy, fissile ions like thorium (^{232}Th) hits a target of the same fissile material, which triggers the two-step fission-fusion reaction mechanism: first, the heavy ions from the incident ion bunch and from the fissile target will both undergo fission, which results in an asymmetric mass distribution with light and heavy fission products, as typical for actinide fission [88]. In a second step, the light fission products fuse with each other and form the desired neutron-rich isotopes. This fusion stage requires an extremely high density of light fission products, which can only be provided due to the nearly solid-state-like density of the incident ion bunch.

A schematic view of a possible target design for the fission-fusion reaction mechanism is shown in Fig. 2.6 [89, 90]. It basically consists of a production target, onto which the laser is focused in order to generate the required laser-accelerated, high-density ion bunch, and a reaction target, that is positioned very closely to the production target

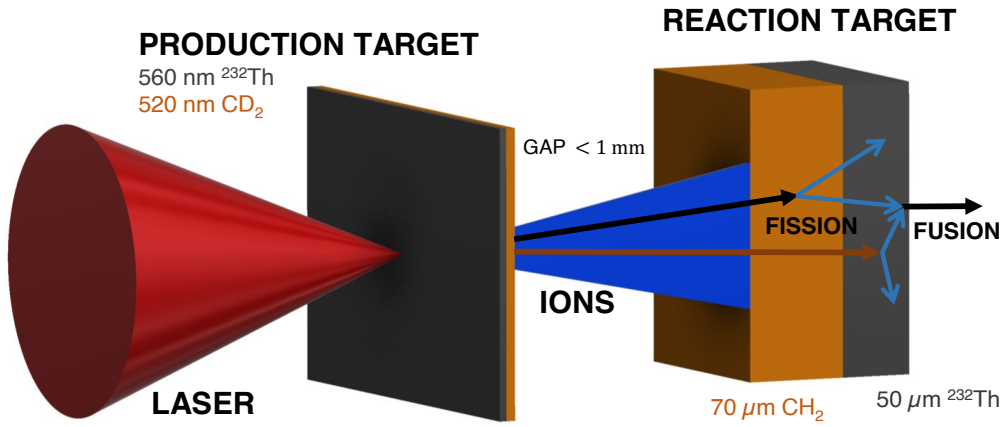

Figure 2.6: Fission-fusion reaction scheme. Figure similarly published in reference [90].

(at a distance of 100 μm up to a maximum of 1 mm), where incident ions induce the fission-fusion reaction process. Both targets consist of a thorium layer and, to increase the fission yield, an additional polyethylene layer. From the production target, thorium ions as well as deuterium and carbon ions are accelerated towards the reaction target. There, the laser-accelerated thorium ions fission during the interaction with the light particles in the polyethylene layer and the incident deuterons and carbons induce fission of the heavy thorium ions in the subsequent thorium layer. The fission barrier for thorium ions lies around 7 MeV/u, which necessitates the laser acceleration of the particles from the production targets to kinetic energies around this value.

The thicknesses of the two layers in the production target, which are proposed in Fig. 2.6, are based on estimations of the available and required number of laser-accelerated particles. The thickness of the polyethylene layer in the reaction target (70 μm) is chosen such that the fission products are decelerated on their way towards the thorium layer to kinetic energies which optimize the cross section for the fusion of the fission fragments ($\sim$ 3 MeV/u). In the thorium layer of the reaction target, the light fission products of the projectile thorium ions from the production target and of the thorium ions from the reaction target fuse with each other. Hereby, extremely neutron-rich isotopes in reach of the r-process waiting point at the neutron number N = 126 are generated, which can be diagnosed behind the reaction target. The here proposed thickness of the thorium layer (50 μm) covers the energy range of the incident light projectiles from the production target above the fission barrier in order to maximize the fission yield.

A more detailed description and quantitative considerations about the fission-fusion

reaction mechanism are provided by the authors of reference [26]. Assuming conventional, Bethe-Bloch-based stopping of the laser-accelerated ion bunch in the reaction target, they predict a yield of $1-2$ fusion products per laser shot, which is only reachable due to the ultra-high density of the ion bunch. However, considering these unprecedented ion bunch densities, collective effects may gain in importance, that could significantly influence the stopping behaviour of the incident ions. In case of the interaction of such a high-density ion bunch with a solid target foil, a reduction of electronic stopping power is expected, as the foremost ions in the incident bunch, arriving first at the target foil, act like a snowplough and remove the electrons in the target material. The following ions, representing the major part of the bunch, are afterwards screened from the electrons, allowing them to penetrate the target much deeper compared to conventional stopping. This results in a highly increased number of fission events, therefore delivering much more light fission products that are available for fusion. The authors of reference [26] predicted a much higher yield of the fission-fusion reaction mechanism in the order of 10^4 fusion products per laser pulse, assuming a reduction of the stopping power by a factor of 100. However, the influence of collective effects on the stopping behaviour in general has hitherto not been shown experimentally and depicts one of the major milestones that have to be accomplished on the way towards the realization of the fission-fusion reaction mechanism.

Besides the investigation of the impact of collective effects, a laser-driven heavy ion source needs to be developed that matches the requirements of the fission-fusion reaction scenario. Two main goals can be identified in this context: first, the feasibility of the laser-based acceleration of heavy ions to kinetic energies required to overcome the fission barrier has to be shown. This could be accomplished with gold ions in the scope of this thesis, as will be shown in Chapter 4. These developments enable in general the investigation of the first step of the reaction mechanism, the fission stage. Second, for the maximization of the fission-fusion yield, the acceleration in the RPA regime has to be pursued in order to realize the required high, almost solid-state-like density of the ion bunch as well as the efficient acceleration of heavy ions, predominantly to energies around the fission barrier.

Chapter 3

Laser Technology and Charged Particle Diagnostics

This chapter presents the technologies and methods which have been used for the generation of this dissertation's experimental results. The relevant high-power laser systems are briefly introduced in Sec. 3.1, followed by a discussion of the employed detector systems in Sec. 3.2. The detection principle using magnetic spectrometers is explained in Sec. 3.3, including the example of a simultaneous electron and ion wide-angle spectrometer, which serves to demonstrate the data analysis in magnetic spectrometers. Additionally, the design of a new Thomson parabola spectrometer for the dedicated measurement of heavy ions is presented. This chapter concludes with a description of the radiative target cleaning mechanism in Sec. 3.4, employed for the removal of hydrocarbon contaminants on the target surfaces, which affect adversely the acceleration of heavy ions.

3.1 High-Power Laser Systems

The laser-based acceleration of particles requires the application of short, high-intensity laser pulses, which became accessible with the invention of chirped pulse amplification (CPA) in 1985 [1]. CPA circumvents the major limitation for the generation of high-power laser pulses posed by the damage thresholds of optical components, which get destroyed above certain laser fluences [91]. It exploits the broad frequency band $\Delta\nu_L$ of laser pulses which comes along with short pulse durations τ_L (necessary to maximize the laser intensity), resulting from the time-bandwidth product, e.g. $\Delta\nu_L\,\tau_L \geq 0.44$ for Gaussian-shaped laser

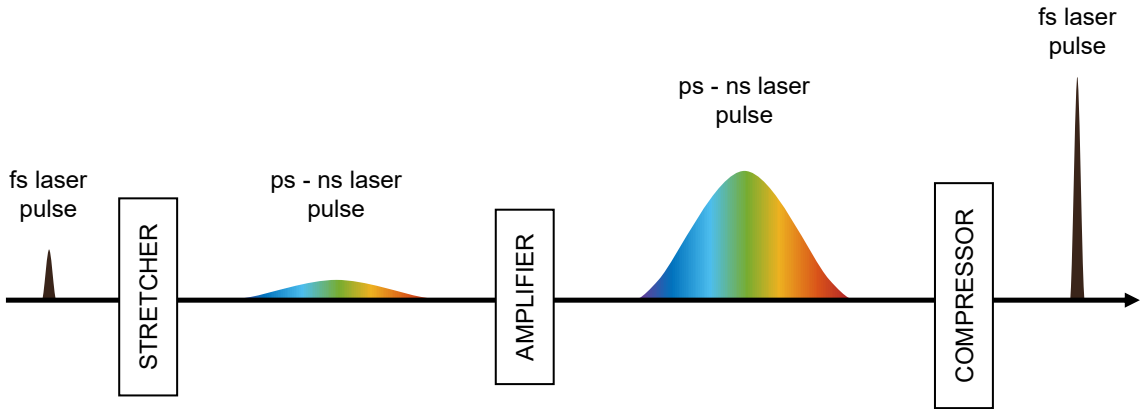

Figure 3.1: Working principle of chirped pulse amplification (CPA): A short laser pulse is stretched in a first step, resulting in a pulse with a temporally separated wavelength sequence. The resulting flux is well below the damage thresholds of optical components (e.g. amplifier crystals), which allows in a next step for the amplification of the pulse to higher energies. In a last step, the laser pulse is recompressed to short pulse durations, delivering a high-power laser pulse that can be focused to high intensities.

pulses [92]. The working principle of CPA is illustrated in Fig. 3.1. In a first step, an initially short fs laser pulse is stretched, for instance by a pair of optical gratings. These introduce a frequency-dependent variation of the optical path length, resulting in a laser pulse with a spatial sequence of different wavelengths. For example, in the case of so-called positive group velocity dispersion, the optical path of shorter wavelengths is elongated compared to that of longer wavelengths [93]. This means that in a positively chirped laser pulse, longer wavelengths arrive first, as illustrated in the example of Fig. 3.1 (negatively chirped pulses behave vice versa). Thus, the stretcher generates a temporal separation of the individual wavelengths in a laser pulse. Consequently, the laser energy is distributed over a longer period of time, allowing in a next step the amplification of the laser pulse to higher energies, within the tolerated values for the damage thresholds of the optical components. In a last step, this higher-energy laser pulse is recompressed to the fs level, for example by applying an inverted configuration of optical gratings, delivering the required high-power laser pulses, which can subsequently be focused down to high intensities.

The laser-driven heavy ion acceleration experiments presented in this dissertation have been performed at two different laser systems: at the Texas Petawatt laser (TPW) [94] at the Center for High Energy Density Science of the University of Texas at Austin, USA, and at the Petawatt High Energy Laser for heavy Ion eXperiments (PHELIX laser) [95] at the GSI Helmholtzzentrum für Schwerionenforschung (GSI) in Darmstadt, Germany.

	TPW	PHELIX	ATLAS-300	ATLAS-3000
Maximum pulse energy [J]	140	200	6	60
Minimum pulse duration [fs]	140	500	20 – 30	20 – 30
Repetition rate [Hz]	1/3600	1/5400	5	1
Wavelength [nm]	1057	1053	800	800
Main amplification medium	Nd:glass	Nd:glass	Ti:sapphire	Ti:sapphire

Table 3.1: Overview of fundamental parameters of the laser systems which are of relevance to this dissertation.

Both laser systems rely on flashlamp-pumped neodymium-doped glass disks for their main amplification stage, limiting the repetition rate to about one shot every 60 – 90 minutes, which is the time period required for cooling down the system.

The TPW delivers laser pulses at a central wavelength of 1057 nm with energies up to 140 J within durations down to 140 fs [96]. It is a hybrid system with an optical parametric chirped pulse amplification (OPCPA) [97] stage prior to the main amplification by two Nd:glass amplifiers, which replaces the conventional amplification medium with a nonlinear optical parametric amplifier (OPA) [98][1]. The TPW can be delivered into two different target chambers (TCs): in TC1 with a short-focus f/3 off-axis parabola (used for the experiment presented in Sec. 4.1) and in TC2 with an f/40 focusing optics.

The PHELIX laser system operates at a central wavelength of 1053 nm. Depending on the choice of the frontend, it provides two different types of laser pulses: the usage of the ns-frontend results in pulses with an energy of 0.3 – 1 kJ within durations of 1 – 10 ns, while the fs-frontend delivers pulses with an energy of up to 200 J within durations of down to 500 fs [99]. The latter was used for the experiment presented in Sec. 4.2. The laser pulse passes in the fs-frontend through an ultrafast OPA stage, which is optionally used for contrast enhancement [100], and two Ti:sapphire amplifiers, before it is further amplified by several Nd:glass modules in the pre- and main amplifiers. The PHELIX laser can either be directed into the Z6 experimental area, which provides the possibility of the laser interaction with a heavy ion beam accelerated with the universal linear heavy ion accelerator UNILAC of the GSI [101], or into a dedicated petawatt target chamber, which is used for laser plasma experiments as that discussed in Sec. 4.2.

Table 3.1 summarizes the pulse parameters from the different laser systems of rel-

[1] In optical parametric amplification (OPA), a photon of a pump beam with higher frequency ω_P than the signal beam is nonlinearly converted into two photons, one at the frequency of the signal ω_S, which amplifies the incident signal beam, and one at the difference of both frequencies, $\omega_I = \omega_P - \omega_S$, which forms the so-called idler beam, a byproduct of this process.

evance for this thesis work. Additionally to the Nd:glass laser systems used for the experiments discussed in Chapter 4, the Advanced Ti:Sapphire Laser (ATLAS) system in Garching near Munich [102] is presented, which is based upon the amplification by titanium-sapphire (Ti:sapphire) crystals and operates at a central wavelength of 800 nm. The ATLAS-300 was located at the Laboratory for Extreme Photonics (LEX Photonics) from 2014 – 2016, before it was upgraded to the ATLAS-3000 and moved to the Centre for Advanced Laser Applications (CALA), adjacent to LEX Photonics. The ATLAS-300 was designed to deliver laser pulses with a peak power of up to 300 TW at a maximum energy of 6 J within minimum durations of 20 fs at a repetition rate of 5 Hz. It was used for the generation of the experimental data presented in Sec. 3.3.2. The ATLAS-3000 is designed to provide laser pulses up to 3 PW (= 3000 TW) at a repetition rate of 1 Hz with pulse energies up to 60 J within pulse durations down to 20 fs. At CALA, a dedicated beamline for the investigation of laser-driven heavy ion acceleration and preparatory studies for the fission-fusion reaction mechanism is available. Future experiments applying the ATLAS-3000 will complement the results presented in Chapter 4 and finalize the study of laser-driven heavy ion acceleration, initiated with this dissertation work, based upon three laser systems with different pulse parameters (TPW, PHELIX and ATLAS-3000).

3.2 Relevant Charged Particles Detectors

The interaction of high-power laser pulses with solid matter creates a quite harsh environment for all involved experimental equipment. In particular, the occurrence of electromagnetic pulses (EMPs) [103,104] impedes the operation of electronic devices close to the point of laser plasma interaction, but sometimes also at a supposedly safe distance outside the vacuum chamber. Thus, state-of-the-art technology is difficult to apply for the detection of laser-accelerated charged particles.

Imaging plates and CR-39 are offline diagnostics elements without any electronical components. They have been used as ion detectors for decades and are, owing to their obvious resistance to EMPs, still firmly established in the laser plasma community. They were also the detectors of choice during the two experimental campaigns dedicated to the investigation of laser-driven heavy ion acceleration, which are presented as main part of this dissertation in Chapter 4. Both diagnostics components are briefly described in the following two Secs. 3.2.1 and 3.2.2.

The mentioned beamtimes were conducted at the TPW and the PHELIX laser. Both

are glass laser systems with repetition rates of one hour or even below, where the usage of an offline diagnostics is reasonable. However, regarding statistical investigations and applications of laser plasma interaction, higher repetition rates are gaining rapidly in importance. The usage of offline detectors at high-repetition-rate Ti:sapphire laser systems like the ATLAS-3000 is inconceivable, as they require replacement after each shot, which implies time-consuming venting and re-evacuation on a regular basis. Handling the processing of the offline diagnostics is prohibitive regarding the high number of shots at laser systems with repetition rates around 1 Hz, like the ATLAS-3000. Therefore, technological solutions have been found that withstand the restricting effects of EMPs to a certain degree.

In Sec. 3.2.3, the CMOS-based RadEye detector is introduced, which has proven to be quite EMP-resistant and operates as standard diagnostics for laser-accelerated protons at the Centre for Advanced Laser Applications (CALA) in Garching. Another approach for online detectors is using a combination of highly sensitive cameras and scintillators, which is shown in Sec. 3.2.4. Both online diagnostics approaches have not yet been tested with laser-accelerated heavy ions, but are firmly included in the design of the dedicated experimental setup in the High Field (HF) beamline at CALA.

3.2.1 Imaging Plates

Imaging plates (IPs) or storage phosphors can store energy deposited by ionizing radiation in lattice defects in the structure of their materials [105]. By irradiation with a red laser, this energy be can released long after the initial exposure in form of violet light. This effect is called photostimulated luminescence (PSL).

For the experiments reported in this work, we applied GE Storage Phosphor Screens BAS-IP TR 2040 E. The individual layers of the detection screen with the respective

Layer name	**Thickness** [μm]	**Density** [g/cm^3]
Surface layer	–	–
Phosphor layer	50	3.3
Back layer	10	1.4
Base layer	250	1.4
Ferrite layer	80	3.0
Back protective layer	25	1.4

Table 3.2: Composition of GE Storage Phosphor Screens BAS-IP TR 2040 E [106].

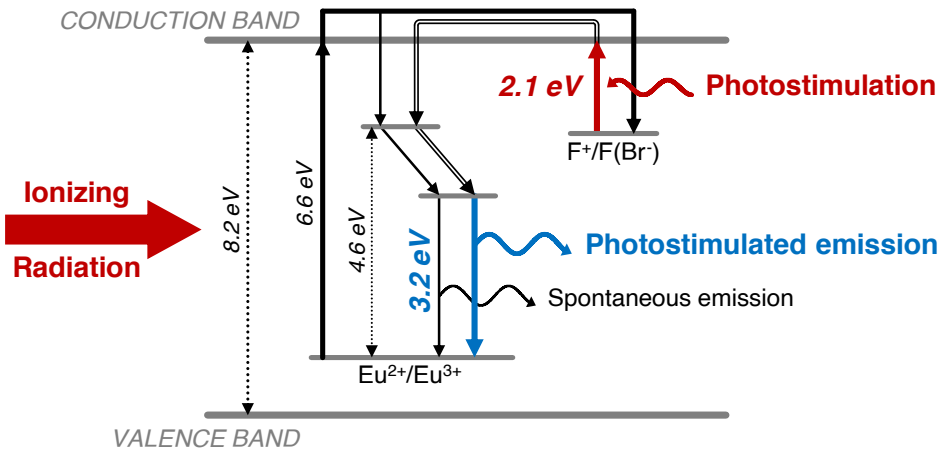

Figure 3.2: Working principle of photostimulated luminescence in IPs, explained with the aid of the energy level diagram of the IP material BaFBr:Eu^{2+}: electron-hole pairs are created by incident ionizing radiation. The holes and electrons are trapped in Eu^{3+} ions and F-centres, respectively. Red laser light frees the trapped electrons from the F-centres, which can recombine with Eu^{3+} under emission of photons with an energy of 3.2 eV, corresponding to a wavelength of 387 nm.

densities are shown in Table 3.2. The peculiarity about the TR-type IP is the absence of any protective coating covering the photoluminescent layer. Even though the IPs need to be handled very carefully for this reason, especially because of the required shot-to-shot replacement, the detection of heavy ions is possible even at low energies, which makes these TR-type IPs to suitable detectors for the measurement of heavy ions at yet unknown energies.

The photoluminescent material in the phosphor layer of the IP is europium-doped barium fluorobromide (BaFBr:Eu^{2+}) [107]. The working principle of PSL can be easily understood considering the energy level diagram shown in Fig. 3.2. Incident ionizing radiation creates electron-hole pairs in the photoluminescent material, whereby their number is directly proportional to the deposited energy. The electrons are elevated to the conduction band, while the holes get trapped by Eu^{2+} ions, forming Eu^{3+}. A number of the freed electrons immediately recombines and does not contribute to the PSL mechanism. The remaining electrons may be trapped by F^+ colour centres. F^+-centres are halogen ion vacancies, that were introduced as lattice defects during the manufacturing process of the photoluminescent material. The energy of the original ionizing radiation is stored in the F-centre[2] and the corresponding hole.

[2] An F-centre is an F^+-centre trapping an electron. F-centres are so called colour centres. This name

Later, the signal can be extracted by illumination with red light. The electrons trapped by the F^+-centres absorb this light and are thereby elevated to the conduction band. From there, they recombine with Eu^{3+} and fall into an excited state of Eu^{2+}. During the transition to the ground state, photons with an energy of 3.2 eV are emitted, corresponding to the violet wavelength 387 nm. The spatial information is preserved by the fixed positions of the Eu^{2+} holes, which are not freed by the red light.

For this readout process, special scanners are necessary, which incorporate, on the one hand, a red laser that enables a targeted excitation of the F-centres while maintaining the spatial information. On the other hand, a readout module is needed, that is sensitive to the emitted violet wavelength but not to the incident laser light. In the scope of this work, IP scanners of the type GE Typhoon FLA 7000 were used. In order to minimize the influence of fading effects [108] on the comparability between shots from the same beamtime, the IPs were all read out with the same time delay of 20 – 30 minutes after each exposure.

3.2.2 Solid-State Nuclear Track Detectors: Columbia Resin #39

Solid-state nuclear track detectors (SSNTDs) are thin slices of solid insulators like crystals, glasses or plastic polymers [109]. In contrast to IPs, the ion detection with a SSNTD is based on radiation-induced damage of the detector material. Thus, SSNTDs are single-use detectors, that in addition need laborious processing after being irradiated. However, they usually have three advantageous features: they provide an outstanding spatial resolution, they are capable of detecting single ion impacts and they are insensitive to light, X-rays and electrons.

Columbia Resin #39 (CR-39)[3] [111] is one of the most commonly used SSNTDs. CR-39 is a clear plastic polymer made out of polyallyl diglycol carbonate ($C_{12}H_{18}O_7$). Ions traversing the detector material break polymeric bonds along their tracks and thus remove electrons. The trajectory of an ion forms a cylindrical path containing positively charged ions, which strongly repel and move away from each other. It remains a depleted cylindric region with a diameter of a few tens of Å, that in principle can already be viewed in an electron microscope. By etching the CR-39 sheets in sodium hydroxide solution (NaOH), the tracks

originates from the fact that naturally colourless alkali metal halides absorb in the visible spectrum after introduction of lattice vacancies, the colour centres. By the way, the term F-centre originates from the German word “Farbe” - colour [68].

[3] During World War II, the *Columbia Southern Chemical Company* investigated 180 different compounds while looking for a new plastic material. “Columbia Resins” was chosen to be the name of this project. Trial 39 was the most promising – CR-39 [110].

can be enlarged until they become visible in an optical microscope [109, 112].

For our measurements, we employed 1 mm thick CR-39 sheets, manufactured by *Track Analysis Systems Ltd. (TASL)*[4]. The sheets were etched in 6-molar NaOH for time periods between 40 and 60 minutes at a controlled temperature of 80 °C. After the etching process, the sheets were scanned by an autofocus Zeiss Axiotron II microscope, equipped with an IDS UI-6280SE-M-GL R3 camera. The automatic scanning process is controlled by the pattern recognition software SAMAICA, programmed by *Elbek-Bildanalyse GmbH* in Siegen. The software fits an ellipsis to each identified track, providing its absolute position, together with information about the enclosed area (size) of the track, its central brightness (when being perpendicularly illuminated) and its ellipticity, for further data processing.

A major advantage of CR-39 is that the dimensions of the impact pits are strongly related to the projectile ions. For example, their ellipticity provides information about the angle of incidence of the impinging ion [113]. Moreover, their size is depending on the ion energy [114] as well as on the projectile species [115]. Fig. 3.3(a) shows exemplarily a microscope image with black dots originating from gold and carbon impacts. They have been recognized by SAMAICA, which fitted green ellipses around the dots. The pits originating from heavy gold ions have larger diameters than impacts from the lighter carbon ions, which is confirmed by the inset showing lineouts through several pits from both species (in this specific example, the carbon impact diameter is about 15 % smaller than that of the gold ions). Thus, the two ion species can be distinguished from each other.

The relevance of this can be seen from Fig. 3.3(b), which shows a scanned CR-39 image from a detector in a Thomson parabola spectrometer. As will be explained in Sec. 3.3, this is a type of magnetic spectrometer that deflects ions with different charge-to-mass ratios on separate curves. The colourmap refers to the size of the individual ion pits: red pits have large diameters, while blue pits correspond to smaller diameters. In the present case, three curves originating from carbon ions with charge states 4^+ to 6^+ and an additional gold curve (with no resolvable charge information) are visible. The C^{4+} line in green overlaps with the gold ion pits (in red), which is in more detail shown in the inset. The carbon impacts can still be differentiated from gold ions, which is not possible when employing an IP or the detectors introduced in the following sections. Furthermore, the dependence of the ion pit sizes on the kinetic energy can be seen from the figure as well. The spectrometer is energy selective and deflects carbon ions with a higher charge state more than carbons with a lower charge state but the same velocity. In case of Fig. 3.3(b), all three carbon lines

[4] http://www.tasl.co.uk/

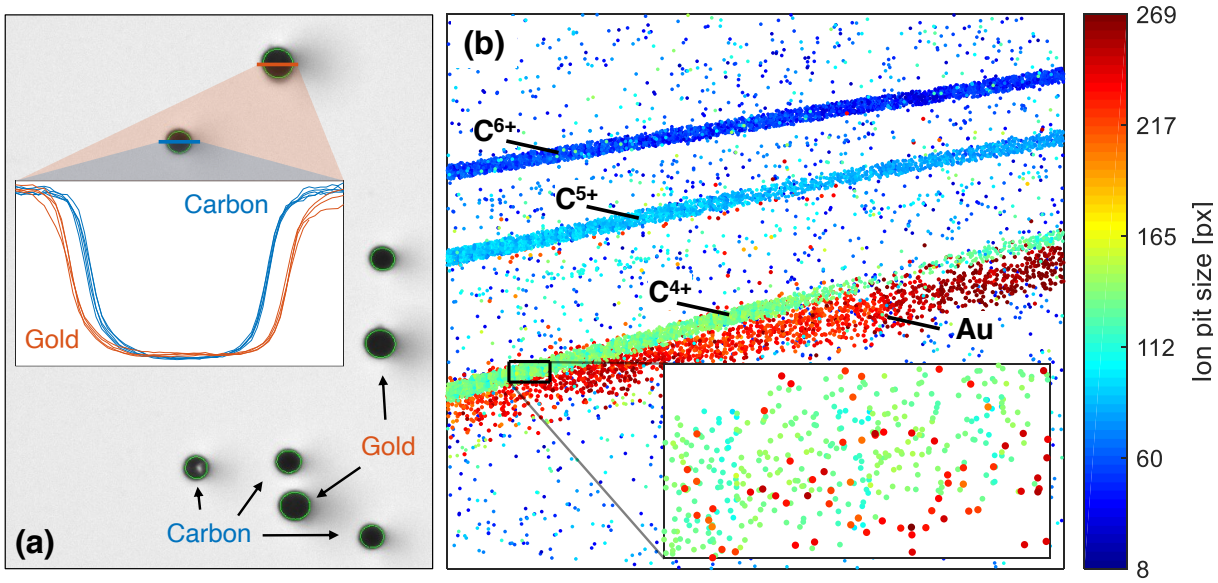

Figure 3.3: (a) Microscope image of an irradiated CR-39 sheet. The black dots originate from gold and carbon impacts and have been registered by the software SAMAICA, which fitted ellipses around the dots (in green). Carbon and gold ion impacts can be discriminated by their size, which is confirmed by the inset showing lineouts through several pits of the respective ion species. The FWHM of the carbon and gold ion impacts in this specific example are about 32 and 38 px, respectively (not shown in the figure).
(b) Scanned CR-39 image from a detector in a Thomson parabola spectrometer, taken at the beamtime at the PHELIX laser, which is presented in Chapter 4. Each point corresponds to an ion impact. The colourmap visualizes the ion pit size in form of the enclosed area (number of enclosed pixels). The visible structures can be assigned to C^{6+}, C^{5+}, C^{4+} and gold ions, respectively. This image shows the dependency of the ion pit size both on ion species (carbons in green and gold ions in red can be distinguished even in their overlapping region, see inset) and on the particles' kinetic energies (see text for explanation).

show different energy ranges. The carbon ions from the C^{6+} (C^{5+}) line have higher kinetic energies than the carbons from the C^{5+} (C^{4+}) curve. As a consequence, they deposit less energy on the CR-39 surface, which generally results in smaller pit diameters, which can be seen from the colour code.

3.2.3 RadEye Detectors

The RadEye large area image sensors [116,117] are pixelated silicon detectors based on the technology of complementary metal oxide semiconductors (CMOS) [118]. Originally, they have been developed by *Rad-icon Imaging Corp* for usage in biomedical X-ray radiography,

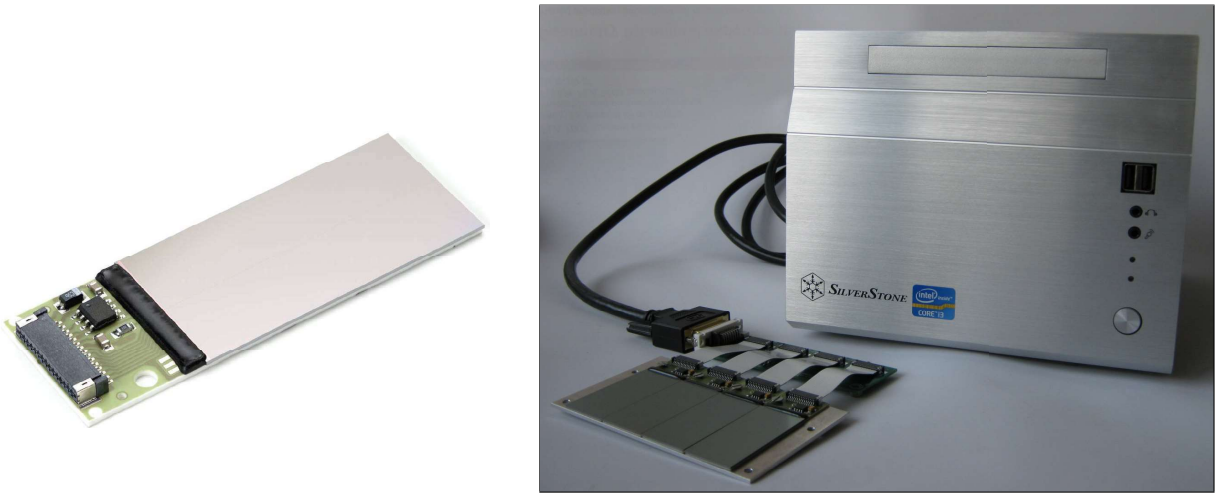

(a) (b)

Figure 3.4: Photographs of the RadEye detection system. (a) Image of a single RadEye1 detector chip, which incorporates the active area (grey) and the corresponding electronics. The active area can be enlarged by tiling additional detectors to the free three sides. Image taken from [116]. (b) Remote RadEye detection system with four RadEye detectors prepared for the usage in laser-ion-acceleration experiments. Image taken from [119].

in combination with scintillators[5] directly coupled to their surface. However, they have proven their suitability as diagnostics for laser-accelerated ions [119–123], thereby directly exposed to the radiation without any supplementary scintillation screen. In the scope of this thesis, the RadEye detectors have also been employed as electron detectors, inspired by the original application with the support of a scintillation screen (see Sect. 3.3.1).

Fig. 3.4(a) shows a photograph of a single RadEye1 detector, which incorporates a smaller electronics part (green) and the active detection region (gray). The active area consists of 512×1024 quadratic pixels with side lengths of 48 μm and a pixel fill factor of above 80 % [117]. Therefore, the total detection area in a single RadEye chip spans 24.6×49.2 mm^2. Additional sensors can be added to up to three sides of a RadEye1 detector chip, thus further enlarging the detection screen. The active layer is made of 2 μm thick silicon, covered by a silicon dioxide (SiO_2) passivation layer of approximately the same thickness [119].

The RadEye detectors have shown a linear response over a large dynamic range, from single proton impacts up to the saturation flux of about 10^7 protons/cm^2/ns at a proton energy of 20 MeV. The detectors have proven to reasonably withstand fluences of up

[5]Scintillating materials absorb the energy of incident radiation, by this elevating electrons to higher energy levels in the material. The absorbed energy is afterwards converted to visible light by the transition of these electrons to lower energy levels, which results in a signal proportional to the absorbed energy.

to 10^{10} protons/cm^2, while still comparably responding to incident protons. The detectors have been calibrated for protons by Reinhardt et al. [120]. The conversion of the detector-specific analog-to-digital units (ADUs) to proton energy loss in the active layer of the RadEye chip can be performed using the factor 1.09 ± 0.12 ADU/keV.

The RadEye1 detectors are operated with the Remote RadEye module, which allows to simultaneously connect four individual detector chips, as shown in Fig. 3.4(b). Hence, the maximum active area achievable with one Remote RadEye detection system has a size of about 10×5 cm^2. The detector system is operated by an in-house developed software called CamOuFlage [124].

3.2.4 sCMOS Camera and Scintillators

Scintillators in combination with cameras have been used for the detection of laser-accelerated ions for example in stacked configurations [123, 125–127] or as detectors in a Thomson parabola spectrometer[6] [128], which is also the intended application in our heavy-ion-acceleration setup at CALA [129]. As camera, we chose the back-illuminated scientific CMOS camera KURO-1200B, developed by *Princeton Instruments, Inc.* [130] and equipped with a zoom objective from *TAMRON Europe GmbH*[7]. The KURO-1200B consists of 1200×1200 pixels, each having a size of 11×11 μm with a pixel fill factor of 100 %. It has a selectable bit depth of 12 or 16 bit with a corresponding frame rate of 82 and 41 frames per second, respectively. The quantum efficiency curve, provided by *Princeton Instruments, Inc.*, is shown in blue in Fig. 3.5.

The camera images the plastic scintillator BC-400B [132], manufactured by *Saint-Gobain Ceramics & Plastics, Inc.* The scintillator has a size of 250×150 mm and a thickness of 200 μm, which is thick enough to completely stop gold ions up to 11.9 MeV/u [133]. This is well above the energy range of interest around the fission-fusion barrier of 7 MeV/u (see the description of the fission-fusion reaction scenario in Sec. 2.4), while the scintillator is still thin enough to provide a satisfying spatial resolution. The relative light output spectrum of the scintillator is plotted in orange in Fig. 3.5. The spectrum has a peak at 423 nm, where the KURO-1200B has still a very high quantum efficiency of about 75 %. The light output of the scintillator in general is quite high with 65 % of the output of anthracene[8]. As Fig. 3.5 shows, a spectral output at high wavelengths is desirable, as the

[6] See Sec. 3.3.3 for an explanation of a Thomson parabola spectrometer.

[7] We employ a TAMRON zoom objective SP 24-70mm F/2.8 Di VC USD [131].

[8] The light output is traditionally given as percentage of anthracene, which is an organic scintillator with one of the highest light outputs [134].

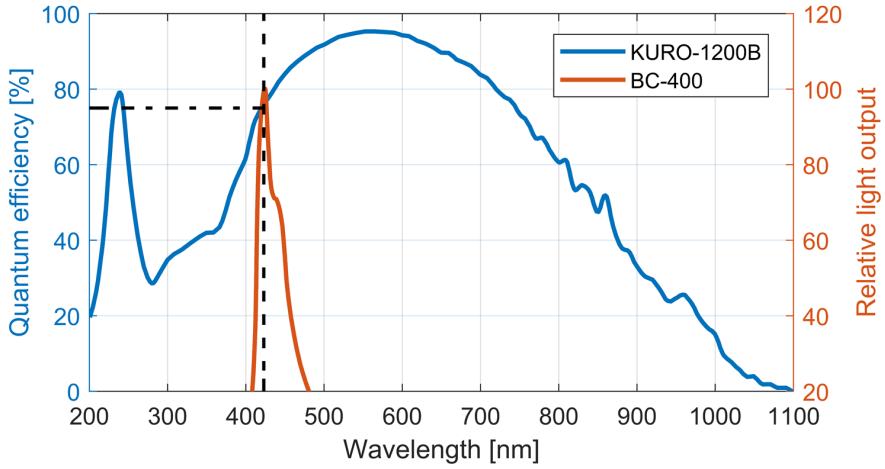

Figure 3.5: Quantum efficiency curve of the sCMOS camera KURO-1200B (blue, data from reference [130]) and relative light output spectrum of the employed plastic scintillator BC-400B (orange, data from reference [132]). The quantum efficiency of the KURO-1200B at the position of the peak of the output spectrum (423 nm) is still very high with 75 %, as indicated by the black dotted lines.

	BC-400	**BC-404**	**BC-408**	**BC-412**	**BC-416**
Light Output [% anthracene]	65	68	64	60	38
Output peak [nm]	423	408	425	434	434
Rise Time [ns]	0.9	0.7	0.9	1.0	–
Decay Time [ns]	2.4	1.8	2.1	3.3	4.0
Base material	polyvinyltoluene				
Density [g/cm^3]	1.023				
Refractive index	1.58				

Table 3.3: Properties of BC-400 in comparison to other plastic scintillators [132].

quantum efficiency increases with the wavelength in this range. On the other hand, the scintillator's light output should be maximized, as a weak signal from the laser-accelerated gold ions is expected. Table 3.3 shows the scintillator material properties in comparison to other candidates, indicating why we chose BC-400 as the appropriate detector material, especially considering the scintillator light output and output peak wavelength.

3.3 Spectrometric Detection Principles

Charged particles traversing a magnetic field **B** undergo a deflection perpendicular to their direction of movement and to the orientation of the magnetic field lines. The amount of

this deflection is depending on the kinetic energies of the particles and can be deduced from the Lorentz force,

$$\mathbf{F}_\mathrm{L} = q\,(\mathbf{v} \times \mathbf{B})\,, \tag{3.1}$$

with $q = Z{\cdot}e$ being the particle charge, Z the charge number, e the elementary charge and $\mathbf{v}$ the particle velocity, that directly relates to the kinetic energy. Adequate two-dimensional detectors, as presented in the preceding section, can measure both the amount of deflection and the number of particles following the same trajectory. Hence, combined with these detectors, magnetic fields can be employed for the indirect measurement of the kinetic energy spectra of laser-accelerated charged particles, which is the parameter of utmost interest in the laser-ion-acceleration community.

The simplest design of such a magnetic spectrometer consists of a magnetic dipole field, which is oriented perpendicular to the direction of particle motion. Fig. 3.6 shows this case schematically. A small fraction of a diverging charged particle bunch, originating from laser matter interaction, enters a magnetic dipole field of length l_B through a thin pinhole. At the end of the field, particles with the same velocity v_0 and mass m have been deflected according to Eq. (3.1) by $y_\mathrm{L} = qB/(2mv_0)\cdot l_\mathrm{B}^2$ in the non-relativistic case. After a drift length d_B, the particles hit a two-dimensional detector measuring the particles' total deflection y from their original direction of motion,

$$y = \frac{q}{m}\frac{l_\mathrm{B}B}{v_0}\left(d_\mathrm{B} + \frac{l_\mathrm{B}}{2}\right), \tag{3.2}$$

that determines the kinetic energy $E_\mathrm{kin} = mv_0^2/2$ beyond all doubt. The corresponding particle number per energy bin is provided by the employed areal detectors.

Two different types of magnetic charged particle spectrometers have been of relevance for this work. In Sec. 3.3.1, a wide-angle spectrometer (WASP) is introduced, that was designed to simultaneously detect electrons and ions with automated online detectors. Being applicable to all magnetic spectrometers, the method of spectrometric data analysis will be shown using the example of the proton-detecting WASP. Furthermore, in the scope of this work, we developed an own approach for electron background separation (Sec. 3.3.2) in order to acquire more precise electron spectra. The main ion diagnostics component in the experiments in chapter 4, dedicated to the laser-driven acceleration of heavy ions, were Thomson parabola spectrometers. Their working principle will be explained in Sec. 3.3.3, which will also include our design of a TPS dedicated to highly-charged heavy ion detection.

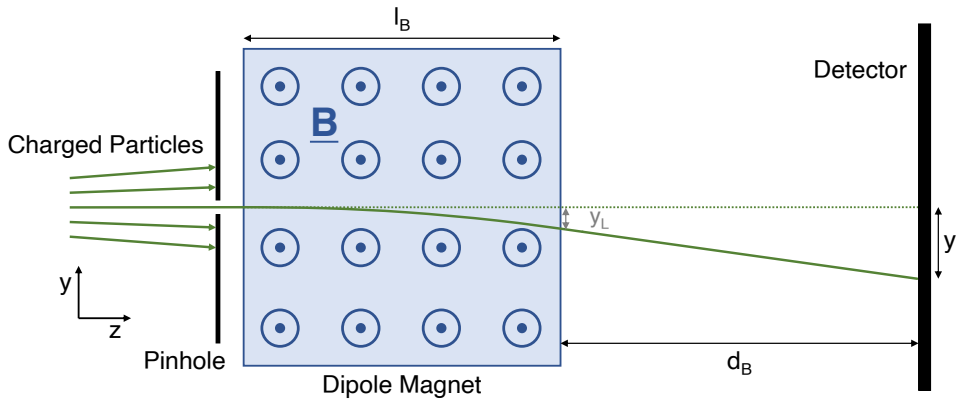

Figure 3.6: Basic working principle of the simplest magnetic spectrometer design. A charged, collimated particle bunch enters a magnetic dipole field, perpendicularly oriented to the direction of particle motion and gets deflected. The amount of deflection y at the detector position is an indirect measure of the particle energy.

3.3.1 Wide-Angle Spectrometer (WASP) for Electrons and Ions

A wide-angle spectrometer (WASP) directly applies the simple magnetic detection principle introduced at the beginning of this section. A thin entrance slit parallel to the magnetic field lines (instead of a pinhole) cuts out a line from the incoming divergent particle bunch, which enters the magnetic dipole field like a fan beam (instead of a pencil beam). The replacement of the entrance pinhole by a thin slit allows to measure the charged-particle energy spectra along different angles, providing the particle bunch profile along one dimension as additional information.

In its common configuration, a WASP is solely used for the detection of ions which leave the laser plasma interaction always positively charged and, therefore, are all deflected in one direction in the magnetic field. However, we make use of the fact that positively and negatively charged particles are deflected in opposite directions and can be detected separately. Equipped with RadEye detectors, our WASP design allows for the first time for a simultaneous, automatic online detection of angularly resolved energy spectra of both laser-accelerated electrons and ions [121].

Laser-driven ion acceleration is a consequence of immense charge separation fields, that emerge when target electrons leave the target foil due to the preceding laser plasma interaction. A direct correlation between the laser-accelerated electron and ion bunch is thus not surprising and has been predicted by various theoretical models [135, 136] for TNSA and has also been proven experimentally [137]. An online, high-repetition-rate measurement of electron and ion spectra at the same solid angle on a single shot basis

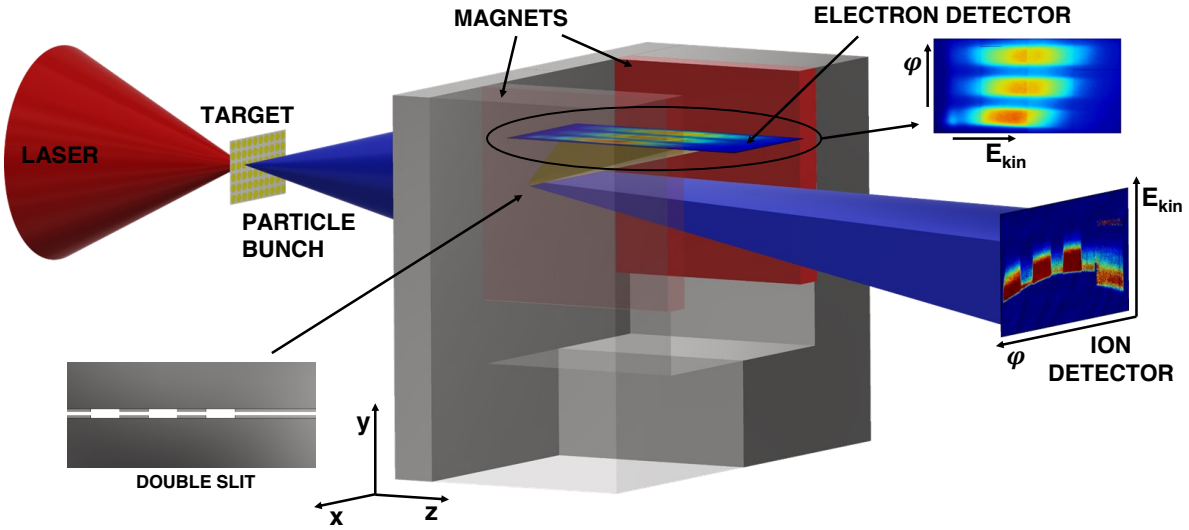

Figure 3.7: Schematic sketch of the electron and ion wide-angle spectrometer [121]. A high-power laser pulse interacts with a solid foil target and a bunch of negatively charged electrons and positively charged ions is emitted. After entering the magnetic spectrometer through a thin slit entrance, the electrons are deflected upwards (yellow) and the oppositely charged ions downwards (blue). A double slit design is chosen as slit entrance (2 cm thick steel blocks in dark grey, separated by 1.5 mm, followed by a tooth-like array of 250 μm broad, 1.5 mm thick aluminum slits in light gray) for electron background separation, see Sec. 3.3.2.

enables the investigation of this correlation in more detail. Full understanding of this relationship and the identification of reliable, correlating experimental parameters would pave the way for a non-invasive characterization of ion bunch parameters by detecting solely laser-accelerated electrons. Such diagnostics is vitally important for a high number of applications waiting for an unperturbed but well-characterized laser-accelerated ion bunch.

Fig. 3.7 shows a schematic sketch of our WASP design. Diverging electron and ion bunches are generated by a high-power laser interacting with a solid foil target. A horizontal slit entrance cuts a line out of the two-dimensional bunch profile, that further propagates into the magnetic field. We employed a tooth-like double slit configuration for electron background separation (see Sec. 3.3.2), as shown in the figure: the first component consists of two 2 cm thick steel blocks, separated by a 1.5 mm gap. The steel blocks are thick enough to stop electrons up to 40 MeV [138]. After the steel blocks, a tooth-like, 250 μm broad slit out of 1.5 mm thick aluminum plates follows, which provides a fair energy resolution for ion detection.

The magnetic dipole field is formed by two $100 \times 100 \times 15$ mm^3 neodymium permanent magnet blocks, that are separated by a gap of 105 mm. The magnetic field distribution

was measured with a three-axis Hall magnetometer and roughly amounts to 150 mT in the center. Entering the magnetic field, the electrons are deflected upwards and detected within the gap of the magnet yoke. The ions turn downwards and are registered behind the magnet after an arbitrary drift length. Both particle species are detected by four RadEye detectors, respectively, that are tiled together in order to form a large detection area of approximately 5×10 cm^2. The electron detection is supported by a Kodak BioMax MS intensifying screen, which has been directly attached to the RadEye surface. Appropriate aluminum housings have been designed for EMP protection of the detectors [139].

3.3.2 Energy Spectra Generation and Electron Background Separation in the Electron and Ion WASP

The generation of charged particle energy spectra in a WASP is basically a two-step process [121, 139], which is similar for protons and electrons. In this section, the concept is first explained for protons and afterwards applied to electrons, which require a more sophisticated approach regarding the background signal separation. In the first step, each coordinate point on the employed two-dimensional detector needs to be matched with both the corresponding particle energy and the respective angle, at which the particle has left its source. For this, trajectories of protons with predefined energies and angles have been modeled based on the previously measured magnetic field distribution. Intersecting these trajectories with the detection plane delivers the desired iso-energy, iso-angle map, which can be overlaid with the detector raw image, as done in Fig. 3.8(a). For ion detection, materials of different arbitrary thickness can be introduced in front of the detector in order to generate energy cutoff lines, as ions below this energy are not able to get through the material. In case of the data shown here, we used aluminum foils with thicknesses of 45 μm on the left side, 75 μm in the middle and 275 μm on the right side to achieve cutoff lines for proton energies of 2.1, 2.9 and 6.2 MeV, respectively. These energy cutoff lines can be used for a precise overlay of the energy-angle map with the raw data as well as for a calibration of the magnetic field.

The energy-angle map subdivides the detector image into many tetragons, each of them enclosed by two adjacent iso-energy and iso-angle lines, respectively. In the second step of the particle spectra generation, the signal within these tetragons is summed up. For the generation of the energy spectrum, this signal needs to be divided by the energy difference between the neighbouring iso-energy lines and by the solid angle, which is enclosed in one dimension by the iso-angle lines and in the other one by the WASP entrance slit. Using

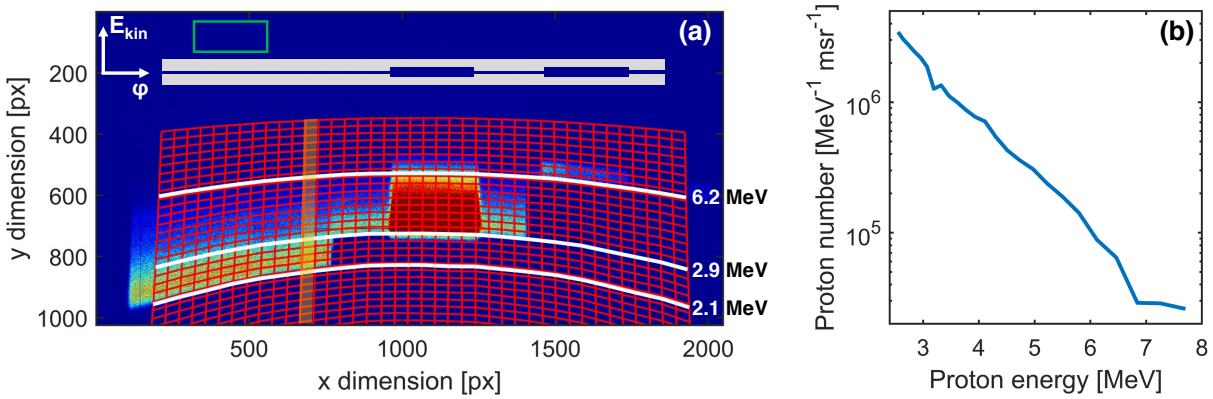

Figure 3.8: (a) Overlay of a calculated iso-energy, iso-angle mesh (red) with proton raw data measured with the RadEye detectors. The y-axis shows the deflection due to the magnetic field and, thus, corresponds to the proton energy. The x-axis lies parallel to the WASP entrance slit, thus, giving information about the angle at which the protons left the source. Aluminum foils of three different thicknesses (from left to right: 45, 75 and 275 μm) were introduced in front of the detector to generate proton energy cutoffs (2.1, 2.9 and 6.2 MeV) for energy calibration. The tooth-like entrance slit with the two different thicknesses (250 μm and 1.5 mm) is sketched in gray for better understanding of the raw image. The rectangle in green shows a region unexposed to protons, which has been used for the spectral background determination with the *constant background value* method. (b) Proton energy spectrum taken at an angle of -0.85° (indicated by the transparent orange region in (a)). Figure similarly published in [121].

the RadEye detectors, the signal needs to be converted from ADU to the absolute number of protons using

$$N_\mathrm{p} = \frac{\mathrm{signal}}{\Delta E \cdot 1.09} \frac{\mathrm{keV}}{\mathrm{ADU}}, \tag{3.3}$$

with ΔE being the energy loss of a single proton in the active layer of the RadEye detector. This energy loss $\Delta E\,(E)$ was simulated with the software SRIM (Stopping and Range of Ions in Matter) [133].

For the calculation of proton energy spectra, the background signal needs to be determined that originates from different particle species released during the laser matter interaction or as secondary particles generated by collisions with experimental equipment, especially the WASP entrance slit and the front plate of the magnet yoke. The background signal may be assumed to be homogeneously distributed over the proton detector surface, as this is far away from the magnet yoke and directly facing the front plate, enabling a homogeneous irradiation. The spectral background information is gained by applying the same analysis to an artificial detector image, with each pixel having the same *constant*

background value, taken as an average from an unexposed region in the original raw image (green rectangle in Fig. 3.8(a)). The angularly resolved energy spectra can be taken along iso-angle intervals, as indicated by the transparent orange area. After subtraction of the corresponding background spectrum, the desired proton energy spectrum is finally obtained, as shown in Fig. 3.8(b).

In principle, the generation of electron energy spectra is identical to the proton case, but with two exceptions. First, the angle of incidence, at which the particles impinge on the detector surface, is much larger for electrons compared to protons. Due to the large angle, the distance which the electrons travel in the active medium is enlarged. This effect is corrected for by multiplication of the raw data with the sine of the angle of incidence at the respective position on the detector surface. The angles result as a byproduct from the trajectory calculations for the generation of the iso-energy, iso-angle map.

Second, the constant background value method used for the spectral background determination of the protons cannot be applied to electrons. The assumption of a homogeneous background signal is not valid for the electron detector, as it is positioned within the magnet yoke, much closer to the front plate, where secondary particles are generated. This is aggravated by the fact that, contrary to protons, which have a comparably high energy deposition in the active layer, the electron detector is similarly sensitive to both primary and secondary particles.

Instead of using a constant background value, we consider the influence of entrance slits with varying width d on the electron signal at a position z. Assuming ideal conditions, this position z corresponds to exactly one specific kinetic energy defined by magnetic deflection. A prerequisite for the validity of this relation is the possibility to employ an infinitesimal thin entrance slit, to ensure that only particles with one certain angle ϑ may enter the spectrometer. Otherwise, electrons with the same energy enter the magnetic field at different angles, which means that they follow different trajectories and hit the detector screen at slightly different z values, which is in contradiction with the initial assumption. Furthermore, a detector with an infinitely small spatial resolution is necessary, in order to precisely determine the position z (meaning the electron energy E) and not merely measure a finitely broad range Δz (meaning an electron energy interval ΔE).

Of course, such ideal diagnostic conditions are unrealistic. A detector signal $S(z)$ measured with the spatial resolution Δz will always correspond to a signal $S(\vartheta, E)$ that

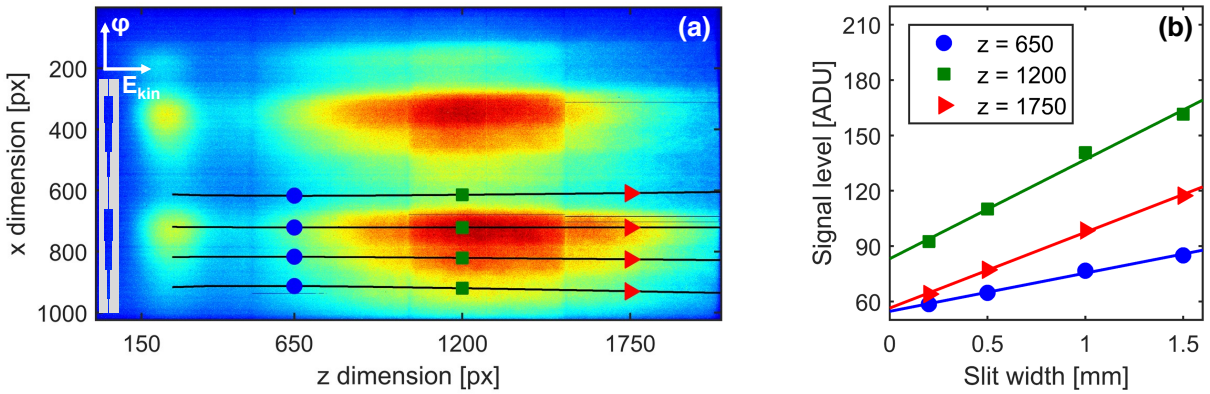

Figure 3.9: The figure confirms the linear dependency of the electron signal to the width of the entrance slit. (a) Electron data measured with a slit with four different widths (0.2, 0.5, 1.0 and 1.5 mm). The electrons are incident from the left, where the entrance slit configuration with the four different widths is sketched. The black lines show the iso-angle lines in the center of each slit step. The markers indicate, where the data from (b) is taken from. (b) The signal levels at three z positions are plotted in dependency of the slit width and confirm the linear behaviour stated in Eq. (3.4). Figure similarly published in [121].

was emitted into an angular interval $\Delta\vartheta_d \approx d/L$ with a certain energy range ΔE,

$$S(z) \cdot \Delta z = S(\vartheta, E) \cdot \Delta\vartheta_d \cdot \Delta E \approx S(\vartheta, E) \cdot \frac{d}{L} \cdot \Delta E, \tag{3.4}$$

where L denotes the distance from the particle source to the WASP entrance slit. This equation shows a linear dependency on the entrance slit width d, which can be exploited for the extraction of the electron primary signal, assuming that the electron spectra for adjacent slits with different widths vary very slowly. This linear dependency is confirmed by the electron data shown in Fig. 3.9(a). Unlike the setup description in Sec. 3.3.1, we employed a slit not only with two but with four different slit widths (0.2, 0.5, 1.0 and 1.5 mm), as is indicated for better understanding in gray of the left side of the figure. The black curves are the iso-angle lines in the centre of the respective slits. The measured signal levels $S(z)$ at three z positions (indicated by the markers on the iso-angle lines) have been plotted against the corresponding slit widths in Fig. 3.9(b), clearly confirming the linear dependency stated in Eq. (3.4). For pragmatic reasons, we have reduced the number of different widths in the entrance slit from four to two for all further measurements.

The slope of the linear fits in Fig. 3.9(b) is proportional to $S(\vartheta, E) \cdot \frac{\Delta E}{\Delta z}$ and, thus, contains the wanted electron energy distribution $S(\vartheta, E)$. Fig. 3.10(a) shows the extracted

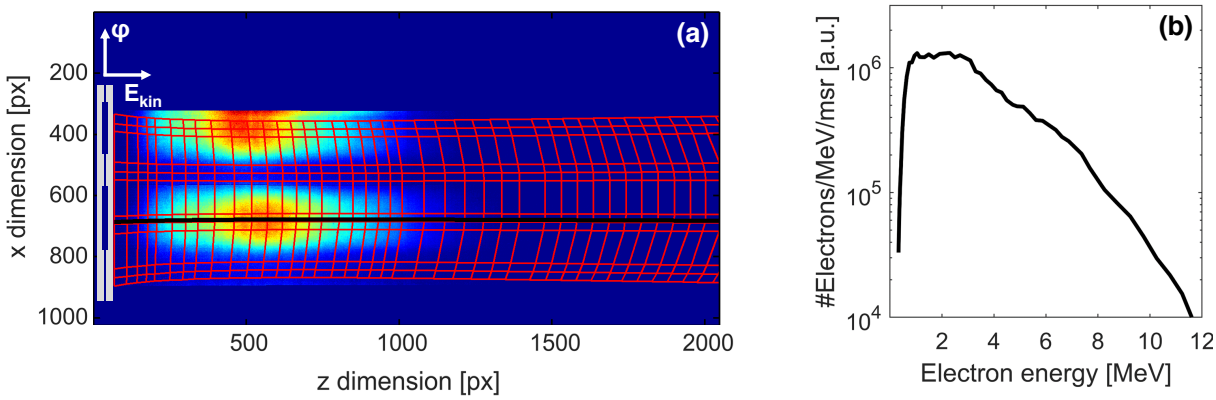

Figure 3.10: (a) Electron primary data extracted from the slope after correction for the angular incidence on the detector surface. The electrons enter the spectrometer from the left, where the entrance slit with the two widths is illustrated. An energy-angle map is generated (red) and overlaid with the primary data. The black line indicates the iso-angle line, along which the spectrum in (b) is taken. (b) Electron energy spectrum from the electron detector at an angle of 0.875°. Figure similarly published in [121].

electron primary signal (meaning the original raw data minus the corresponding y-intercept from the discussed linear fit, which contains the information about the background signal) from an exemplary shot. Again, the used slit configuration (this time the one described in Sec. 3.3.1) is illustrated on the left side for a better understanding of the shown signal. The generation of the electron energy spectra follows from now on the same principles as for the proton case: an iso-energy, iso-angle grid (red) is generated and overlaid with the detector image. Summation of the signal within each grid voxel and division by the energy interval and solid angle delivers the electron energy spectra, as shown in Fig. 3.10(b). Although the electron detector has not been calibrated for absolute numbers yet, it may be assumed that the shape of the spectrum is correct, as the electron energy deposition is constant for energies between 1 and 100 MeV [140, 141]. Hence, the spectrum can already be used for drawing fair comparisons between different laser shots and for the determination of important electron parameters, for example the electron temperatures (mean energies).

Application example and impact of the new electron background separation approach

The WASP presented here was implemented as the standard electron and proton diagnostics for all experiments dealing with laser-driven ion acceleration at the Laboratory

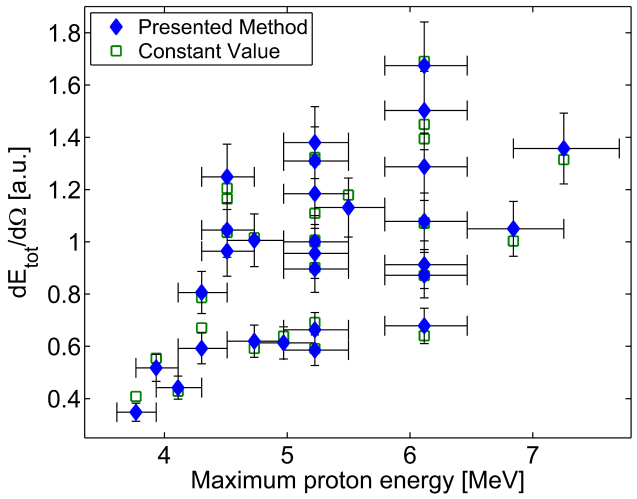

Figure 3.11: Differential total electron energies, integrated from 1 to 25 MeV, plotted versus the maximum proton energy. The blue diamonds are evaluated with our background separation approach, while the constant value method was applied for the green rectangles. The error on the x-axis originates from the spectrometer energy resolution. For the error on the y-axis, an uncertainty of 20 % was assumed. Figure published in [121].

for Extreme Photonics (LEX Photonics). The 300 TW Advanced Ti:Sapphire Laser 300 Terawatt (ATLAS-300) laser system delivered laser pulses with energies up to 6 J within durations down to 20 fs with a repetition rate up to 5 Hz. A first example of a measured correlation between laser-accelerated electrons and protons is shown in Fig. 3.11. The total differential electron energy (in arbitrary units due to the missing electron number calibration), which has been integrated from 1 to 25 MeV, is plotted versus the maximum proton energy for a number of shots on plastic targets with thicknesses between 250 and 1500 nm. A general trend is observable, that higher maximum proton energies come along with higher total differential electron energies. This encourages to investigate the electron proton correlation in more detail with more statistics, which becomes possible with our electron and ion WASP.

The novel approach for background separation does not show any substantial influence on the electron proton correlation presented here, as shown by the green, unfilled rectangles. However, the spectral shape and important electron bunch parameters like the total electron number will be extracted more correctly by our method. A direct comparison with the constant background value method is shown in Fig. 3.12 for three arbitrary shots. Especially for high electron energies, the difference between both background extraction methods is evident, where the primary electron signal is comparable to the noise level.

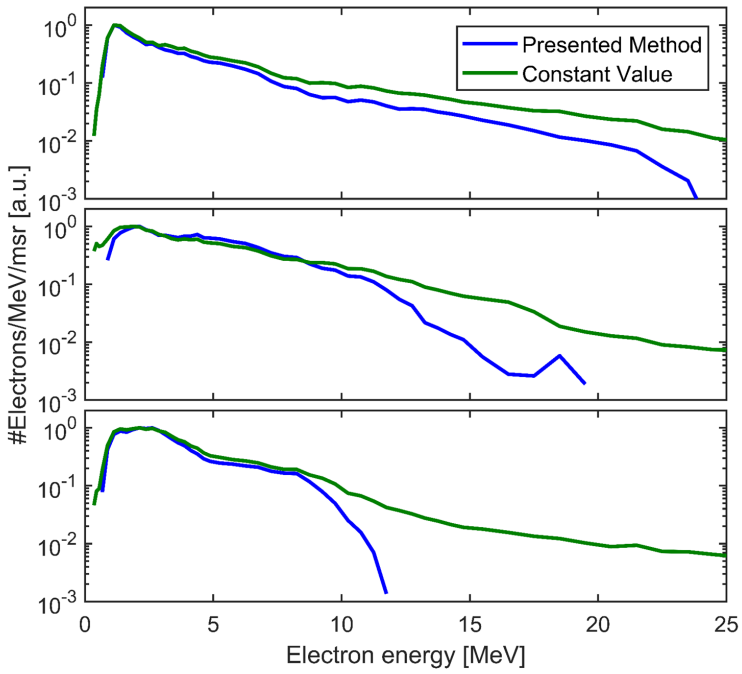

Figure 3.12: Comparison of the three arbitrary electron spectra evaluated with the method presented in this section (blue) with the constant background value approach (green). Figure similarly published in [121].

As this influences electron parameters, in particular the electron temperature, we think that the application of our background separation approach is essential for the precise determination of electron energy spectra in future experiments.

3.3.3 Thomson Parabola Spectrometer

A drawback of the WASP presented in the previous section is the difficulty in distinguishing between particles with different charge-to-mass ratios. When aiming at laser-driven acceleration of protons, where only a single charge-to-mass ratio is expected (1 for protons), or – if any – only one additional ion species (C^{6+}) appears, the usage of a WASP is totally sufficient. Though, when accelerating heavy ions, the differentiation between a high number of charge states is necessary. This can be achieved by adding the Coulomb force to Eq. (3.1). The Lorentz force reads then

$$\mathbf{F}_\mathrm{L} = q\left(\mathbf{E} + \mathbf{v} \times \mathbf{B}\right), \tag{3.5}$$

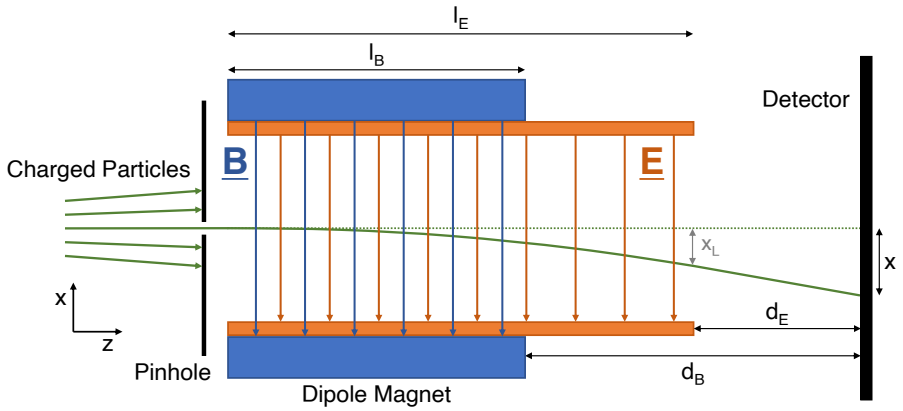

Figure 3.13: Working principle of a Thomson parabola spectrometer. A charged, collimated particle bunch enters through a thin pinhole a region with parallel magnetic and electrical fields, both oriented perpendicularly to the direction of particle motion. The particles get deflected due to the magnetic field, which is not shown here but in Fig. 3.6, which shows the perpendicular y-z plane, and due to the electric field. The amount of deflection x at the detector position, which occurred due to the electrical field, is an indirect measure of the particle's charge-to-mass ratio.

with **E** denoting an electrical field. Clearly, the magnetic fields deflects particles depending upon their charge and energy, while the deflection due to the electrical field is only dependent on the particle charge. If the particle deflection caused by the different fields can be oriented into different directions, the effects due to charge and energy can be separated. Hence, the energy spectra for particle species with different charge-to-mass ratios become attainable.

A Thomson parabola spectrometer (TPS) [142, 143] makes use of parallelly oriented electric and magnetic fields. The deflection due to the magnetic field is perpendicular to the field lines and independent of the electric field. Thus, Eq. (3.2) is still valid. The deflection due to the electrical field is parallel to the field lines and is likewise independent of the magnetic field. Analogous to Eq. (3.2), the deflection due to the electric field can be described as

$$x = \frac{q}{m}\frac{l_\mathrm{E} E}{v_0^2}\left(d_\mathrm{E} + \frac{l_\mathrm{E}}{2}\right), \tag{3.6}$$

where l_E is the length of the electric field and d_E the drift distance afterwards. Fig. 3.13 schematically shows the TPS working principle with all involved parameters.

Eqs. (3.2) and (3.6) can be combined, which results in the eponymous parabolic equation

$$x = \frac{m}{q}\frac{l_\mathrm{E} E\left(d_\mathrm{E} + \frac{l_\mathrm{E}}{2}\right)}{l_\mathrm{B}^2 B^2 \left(d_\mathrm{B} + \frac{l_\mathrm{B}}{2}\right)^2} \cdot y^2. \tag{3.7}$$

Hence, a TPS deflects particles with different charge-to-mass ratios onto parabolic traces, while the position y within these parabolas defines the corresponding kinetic energy, according to Eq. (3.2).

Heavy Ion Thomson Parabola Spectrometer Measuring charge-resolved energy spectra of heavy ions in the mass range of $A \approx 200$ is relatively difficult, since the deflection of these heavy ions caused by magnetic and electric fields is – due to their high mass – low compared to light ions. To compensate the influence of the higher ion mass, the impact of the respective fields needs to be increased. According to Eqs. (3.2) and (3.6), this can be done by increasing either the field strength or the field length. However, both parameters are limited and cannot be arbitrarily enhanced. When using permanent magnets, which is desirable for the given hostile experimental conditions especially regarding EMPs, the maximum achievable field strength is 1.4 T for neodymium-based materials. The limited dielectric strength of electrode materials, even in high vacuum environments, impedes the application of electric fields of the desired high values. Moreover, the geometry of experimental setups and vacuum chambers, as well as demands on handiness, constrain the size of magnets and electrodes, thus limiting the field lengths.

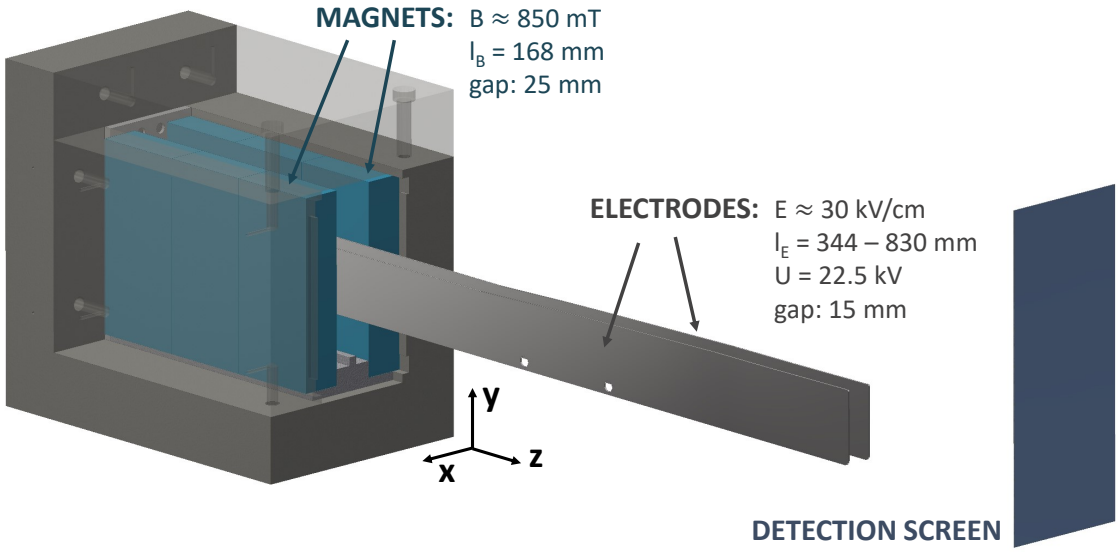

Figure 3.14: Design of a heavy ion TPS. The neodymium magnets create a dipole field over a length of 168 mm with a design average field of 850 mT in the center of the gap. The polarity of the magnetic field ensures an upward deflection of positively charged ions. The electrodes start at a distance of 1 cm from the front plate and stick out of the magnets. After a certain drift length, a detection screen measures the expected charge-separated curves. The total length of the electrodes and the drift length afterwards is setup dependent.

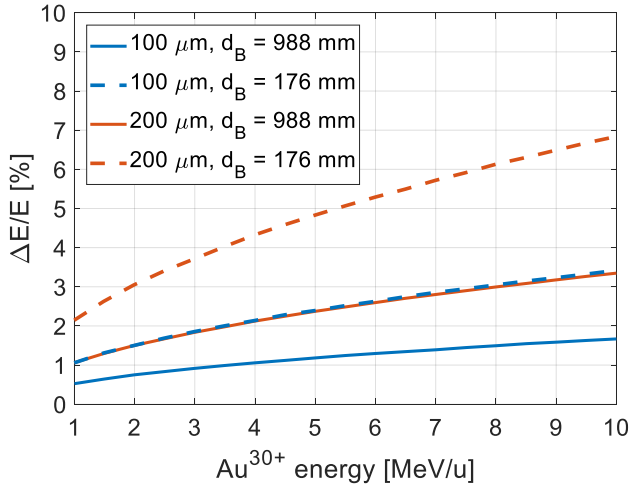

Figure 3.15: Hypothetical energy resolution of the TPS, provided the magnetic field is exactly known, for two different pinhole sizes (100 and 200 μm in blue and red) and two different drift lengths (176 and 988 mm in dashed and solid lines, respectively). Data taken from reference [129].

We have developed a TPS with field parameters which are optimized for the detection of gold ions with charge states above 30^+ and energies ranging from 1 to 10 MeV [129]. Fig. 3.14 shows the design of this TPS. The magnetic field is formed by two times three adjacent VACODYM 753 TP magnet blocks from the company *VACUUMSCHMELZE GmbH & Co. KG* with dimensions of 116 × 56 × 24 mm^3 and a magnetization of above 1.4 T, which are separated by a gap of 25 mm. Thus, the total magnetic dipole field spans over a length of 168 mm. The magnetic design was based on an average design field strength of 0.85 T. The polarity of the magnetic field ensures an upward deflection of positively charged ions. Fig. 3.15 shows the energy resolutions for 30-fold charged gold ions, which could be hypothetically achieved (provided an exact knowledge of the magnetic field) for two different pinhole diameters of 100 and 200 μm in blue and red, respectively, and for two different design drift lengths of 176 and 988 mm (dashed and solid lines). Employing a 100 μm thin pinhole, an energy resolution of below 4 % can be achieved at 10 MeV/u, even for a very short drift length of 176 mm [129]. As higher charged particles undergo a stronger deflection due to Eq. (3.5), the energy resolution is expected to further improve for increasing charge states.

For the electrodes, a design field strength of 30 kV/cm was chosen. This value gave the best compromise between the resulting necessary electrode length and physical feasibility of voltage application, while still keeping the system simple with two conventional electrodes, directly connected to DC high voltage power supplies[9]. In order to save space, the

[9]We used two HCP 140-35000 modules produced by *FuG Elektronik GmbH* as high voltage power

electrodes start already within the gap between the dipole magnets at a distance of 1 cm from the yoke's front plate and stick out of the magnets.

The improvement of the charge state resolution at a given energy, either by increasing the electric field strength or the electrode length, is always associated with a loss of dynamic range for the energy detection. For the optimization of the charge state resolution at high gold ion energies like 10 MeV/u, the gold ion deflection caused by the electric field must be strengthened. As this deflection is generally larger for lower energies and occurs parallelly to the electric field lines, lower energetic particles will crash into the electrodes at some point. Hence, while the charge state resolution is optimized for 10 MeV/u, the detection of lower energetic ions is not possible anymore. This can be circumvented by shaping the electrodes such, that lower energetic particles of a certain minimum charge state can just pass the electrode edges. In case of the experiment at the PHELIX laser, described in Sec. 4.2, we chose a positive charge state of 35 as minimum and calculated the shape of the curve, which is formed by intersecting the trajectories of 35-fold positively charged gold ions with energies ranging from 1 to 10 MeV/u with the y-z plane at the x-position of the electrode based upon theoretical simulations of the fields. The electrodes were adapted to the shape of this intersection, as shown in Fig. 3.16. The ions impinge from the left along the z direction and are deflected upwards in y direction by the magnetic field, while they are accelerated in x direction (towards the electrode) due to the electric field. At the point (z = 333.2 mm | y = 27.4 mm), 35-fold charged gold ions with energies of 1 MeV/u arrive at the electrode plane and can just pass the electrode. Higher energetic particles arrive at the plane of the electrode at higher z values, which goes along with higher y values, as they drifted a longer distance. Thus, the electrode can be shaped following this (z | y) curve, which enables that the electric field acts on the higher energetic ions for a longer distance. By this, the highest desired charge state resolution for fast gold ions is ensured, while the slower ions can still escape the electric field and do not crash into the electrodes. Employing such shaped electrodes, two adjacent gold charge states around 60^+ can be theoretically separated up to energies of above 8 MeV/u, when using a pinhole with a diameter of 100 μm and the longest electrodes, which we have designed for the heavy ion detection, with a length of 830 mm, followed by a drift distance of 326 mm [129].

For the mentioned beamtime at the PHELIX laser, conventional circuit boards (copper coating on FR-4 substrates[10]) were redesignated as electrodes. The calculated shape was

supplies.

[10] We used circuit boards manufactured by *IBR Leiterplatten GmbH & Co. KG* with a 1 mm thick substrate material FR-4 TG135 and a 35 μm thick copper layer.

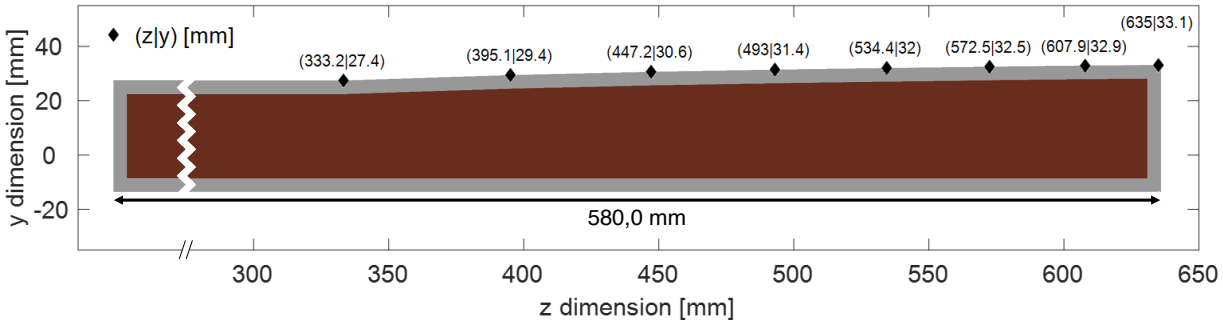

Figure 3.16: Electrode design for the heavy ion TPS using copper-coated FR-4 circuit boards. The outer shape of the top edge was adapted to the intersect of Au^{35+} trajectories with the electrode plane (according to the sketched points, with the beginning of the magnet yoke's front plate denoting z = 0 and y = 0 being the height of the laser target interaction point). A 5 mm margin was freed from the copper material around the substrate. The final electrode is formed by two FR-4 plates glued together, thus enclosing and insulating the copper electrode.

adapted to the FR-4 circuit board material. An electrode is formed by two accordingly shaped copper-coated FR-4 plates, which are glued together. One plate is completely etched (freed from the copper), while the other plate is etched on a 5 mm broad margin around the substrate, as shown in Fig. 3.16. Thus, the copper electrode is enclosed (and insulated) by two FR-4 plates with one cable connecting the electrode to the high voltage power supply. The electrodes have a total length of 580 mm. The field of 30 kV/cm is formed by a pair of such electrodes with the two copper layers separated by a distance of 15 mm from each other. Thus, a voltage of ± 22.5 kV needs to be applied to each electrode in order to achieve the design field strength.

3.4 Radiative Target Cleaning

Particles with high charge-to-mass ratio are preferentially accelerated in the sheath fields generated by the laser plasma interaction. The ever-present hydrocarbon contaminant layers on high-Z target foil surfaces provide a large pool of light particles that consequently experience a more efficient acceleration than the heavy particles from subjacent target layers. It has been found by numerous experiments (e.g. [48,144–149]) that the efficiency of laser-driven heavy ion acceleration increases (i.e. higher heavy ion energies and/or numbers) when the contaminant layers are removed before the laser interacts with the target foil.

There are various methods of cleaning the target foil surfaces. The most frequently used methods are resistive target heating, where a current is applied to the conducting target

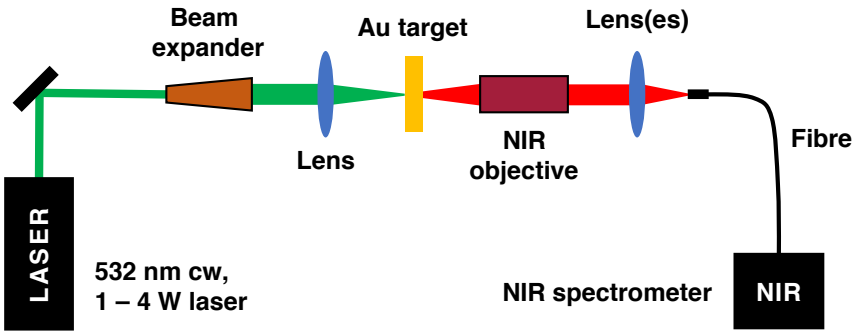

Figure 3.17: Basic setup for radiative target heating with thermal radiation measurement.

foil [144–146] (or to wires attached to the target foil [150]), and radiative target heating, where a continuous-wave (cw) heating laser with an output power in the range of several 100 mW up to same watts is focused onto the target surface [48, 147–149]. There have also been several experiments using pulsed laser beams for laser ablation [151–153], but also for laser desorption [154], removing the surface contaminants by exciting electrons which induce chemical reactions. Successful target cleaning has also been shown by exploitation of the rising edge of the accelerating main laser pulse [50], which blows off the surface contaminants before the pulse peak arrives, and by the usage of an argon-ion sputter gun [155], which enables the efficient cleaning of either the target front or rear side.

We have chosen to clean our targets by a cw laser, which we judge to be the best controllable and easiest-to-realize target cleaning method, especially regarding high-repetition-rate laser accelerators. Fig. 3.17 shows the basic setup for radiative target heating, which has been implemented in the experiments for laser-driven heavy ion acceleration presented in Chapter 4. A green cw laser with a wavelength of 532 nm has been selected, being the best compromise between the optical absorption properties of gold [156] and the availability of reasonably-priced commercial lasers. For the experiments in this dissertation, diode-pumped solid-state lasers (DPSSLs) from *Beijing Viasho Technology Co.,Ltd.* with output powers of 1 and 4 W have been chosen[11], which turned out to not provide a sufficient quality of the beam profile for the heating process, as will be discussed in Chapter 4. Consequently, an opus 532 3000 from *Laser Quantum GmbH*[12] with an output power of up to 3 W and a considerably superior beam profile has been acquired for future beamtimes and characterised during a master thesis [157], which still was in preparation at the time of finishing this dissertation. The laser is focused on the gold target foils (drawn in yellow)

[11] VA-II-N-532-1W and VA-II-N-532-4W, http://www.viasho.com/
[12] http://www.laserquantum.com

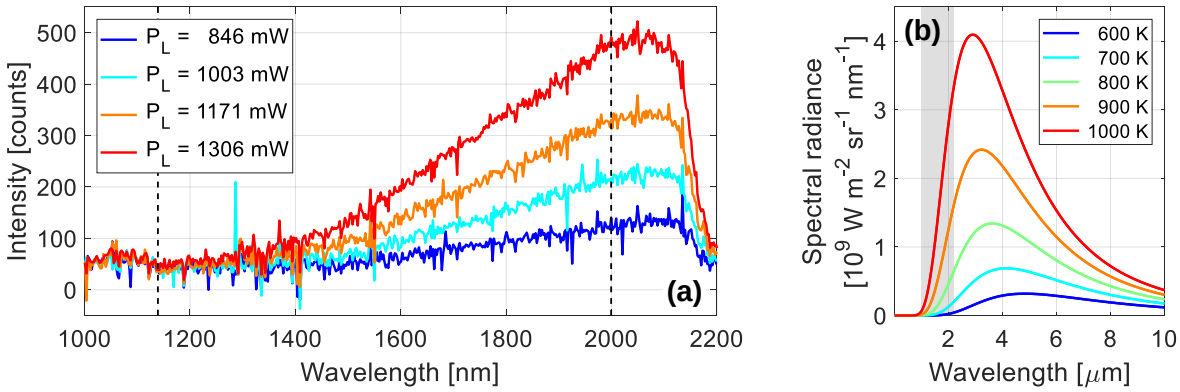

Figure 3.18: (a) Raw signal from a heated, 130 nm thick gold foil measured with the NIR spectrometer for increasing laser power. The signal has been collected by an optical lens instead of a NIR objective. The signal outside of the dashed black lines is physically not meaningful and is thus not used for the temperature determination. Data taken from reference [129].
(b) Theoretical Planck curves, calculated with Eq. (3.10), for various temperatures. The grey region visualizes the location of the spectra shown in (a). The colours in (a) do not refer to the same temperatures as in (b).

by ordinary bi-convex, uncoated UV fused silica lenses, once it has been expanded by a zoom beam expander[13] to simplify the adjustment of the focal spot size on the target foil. For the temperature control of the heated target, the thermal radiation is collected and collimated by a NIR objective[14], before it is focused by one or two optical lenses into a glass fibre with 400 μm core diameter[15], which directs the thermal radiation into a NIR spectrometer[16]. Alternatively to the NIR objective, the thermal radiation can also be collected by an optical lens, as was done during the TPW beamtime, see Sec. 4.1. However, the usage of an objective allows to use the same optical path for both the optical focus diagnostics and the thermal radiation detection. This simplifies the setup and ensures a more stable alignment of the temperature diagnostics.

An example for the raw data signal in the NIR spectrometer is provided in Fig. 3.18(a) for different laser output powers [129]. Clearly, for higher laser powers (corresponding to higher target foil temperatures), the thermal radiation signal measured by the spectrometer rises as well, as is expected from Planck's law [158],

[13] Zoom Beam Expander (1x – 8x) for 532 nm from *Eksma Optics*, http://www.eksmaoptics.com
[14] M Plan Apo NIR B 20x Objective from *Mitutoyo*, https://www.mitutoyo.com/.
[15] QP400-2-VIS-BX from *Ocean Insight*, http://www.oceaninsight.com.
[16] NIRQuest NQ512-2.2 from *Ocean Insight*, http://www.oceaninsight.com.

$$u_\nu \mathrm{d}\nu = \frac{8\pi h\nu^3}{c^3} \cdot \frac{\mathrm{d}\nu}{\exp\left(\frac{h\nu}{k_\mathrm{B}T}\right) - 1}, \tag{3.8}$$

with u_ν being the energy density, ν the frequency of the radiation, h the Planck constant, c the vacuum speed of light, k_B the Boltzmann constant and T the temperature. A typical representation of Planck's law is in the form of the spectral radiance B_ν in units of $\mathrm{W\,m^{-2}\,sr^{-1}\,Hz^{-1}}$ [159],

$$B_\nu = \frac{2h\nu^3}{c^2} \cdot \frac{1}{\exp\left(\frac{h\nu}{k_\mathrm{B}T}\right) - 1}, \tag{3.9}$$

which is the energy density given by Eq. (3.8) normalized to the solid angle 4π and multiplied with c, which considers that the energy density of the emitted thermal radiation spreads over the full solid angle and that the radiation travels at the speed of light. Eq. (3.9) can also be expressed in terms of the wavelength λ and reads then [159]

$$B_\lambda = -B_\nu \frac{\mathrm{d}\nu}{\mathrm{d}\lambda} = \frac{2hc^2}{\lambda^5} \cdot \frac{1}{\exp\left(\frac{hc}{\lambda k_\mathrm{B}T}\right) - 1} \tag{3.10}$$

in units of $\mathrm{W\,m^{-3}\,sr^{-1}}$, which corresponds to the typical wavelength-dependent Planck curves, which are exemplarily shown in Fig. 3.18(b), confirming an increasing signal level for higher temperatures. The grey region visualizes the location of the spectra shown in panel (a), which demonstrates a reasonable agreement in the spectral shape with increasing temperature.

However, the shape of the spectrometer raw data necessarily deviates from the theoretical Planck curves, as optical components in the thermal radiation beam path (for instance the objective, the lenses and the fibre), which can deviate from setup to setup, exhibit a wavelength-dependent transmission and, thus, distort the signal shape. While the spectrum shown in Fig. 3.18(a) has been detected without the usage of a NIR objective, this was included in the optical path for the measurement of the spectrometer raw data shown in Fig. 3.19(a) [129]. It is evident that the transmission characteristics differ. Therefore, the temperature detection setup needs to be calibrated prior to each measurement, for example using a calibrated light source[17]. The application of the calibration procedure delivers a spectrum that can be used for the temperature determination, as can be seen in Fig. 3.19(b). The orange curve corresponds to the calibrated spectrum from which the

[17] We use a HL-3P-CAL light source from *Ocean Insight*, http://www.oceaninsight.com.

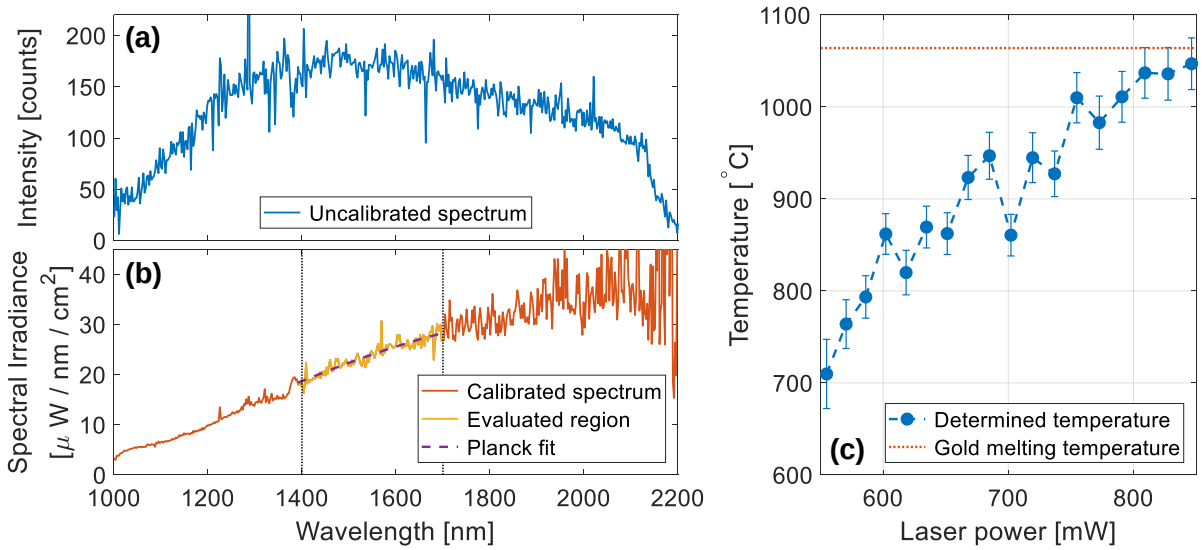

Figure 3.19: (a) Raw data collected and collimated by a NIR objective and measured with the NIR spectrometer. (b) Calibrated spectrometer data (orange). Only a part of the spectrum (yellow) has been analyzed for the temperature evaluation by fitting a theoretical Planck curve to the data (dashed violet line). (c) Calculated temperature values as a function of the heating laser power. All data originate from the same gold target with a thickness of 150 nm and are taken from reference [129].

yellow part was taken for the temperature evaluation (the inclusion of the remaining parts of the spectrum did not deliver physically meaningful temperature values; for more details see reference [129]). For this, Eq. (3.10) has been fitted to the data, delivering temperature values, that have been plotted as a function of the heating laser power in Fig. 3.19(c) for the example of a 150 nm thick gold foil. For this plot, the laser power has been increased until the foil melted, which is well represented in the temperature data that approaches the melting temperature of gold (1064 °C) for the highest laser power values.

The setup and temperature evaluation method presented so far is the status during the experiments discussed in Chapter 4. The correct determination of the temperature was highly depending on the choice of the evaluated spectral range (e.g. yellow part in Fig. 3.19(b)), which differed from foil to foil. Hence, a reliable temperature evaluation was not feasible for these experiments and the heating laser power was adjusted empirically by carefully observing the evolution of the measured thermal radiation spectrum in order to heat the gold foil, based on experience, as close as possible to the melting point.

Problems connected to the temperature evaluation were especially the poor signal-to-noise ratio, as the measured signal level was generally very low, and a necessary, back

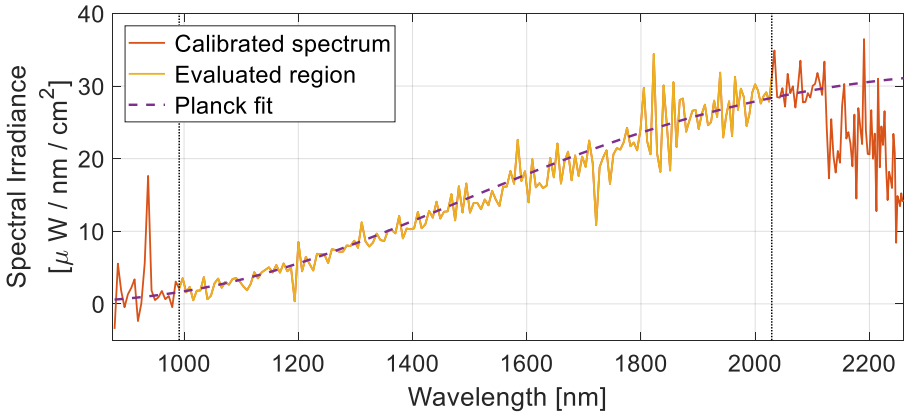

Figure 3.20: Calibrated thermal radiation spectrum for a 400 nm thick gold foil (orange), which is irradiated by the green heating laser with an output power of 2.4 W. The yellow part is used for the Planck curve fit (violet), which yields a temperature of $(879 \pm 4)\,^{\circ}\mathrm{C}$. Data from reference [157].

then unknown, additional empirical factor in Eq. (3.10), considering setup- or material-dependent characteristics. A subsequent, at the time of completion of this dissertation still ongoing master thesis work considerably improved the efficiency of the radiative target heating by optimizing the diameter of the heating laser focus as well as that one of the freestanding target foil on the target mount. Moreover, the newly developed temperature evaluation method now enables a controlled target cleaning and a reliable online temperature determination, as will be presented in reference [157]. Fig. 3.20 exemplarily shows such a thermal spectrum for a 400 nm thick gold foil (orange), which has been recorded in the scope of the mentioned ongoing master thesis. A much larger part of the spectrum (yellow) could be included into the temperature determination compared to Fig. 3.19(b). The evaluated spectral range stays the same for different foils and only the outer spectral margins are neglected, at which the signal obviously is not physically meaningful. The Planck fit to the central part of the spectrum (violet) yields a temperature of $(879 \pm 4)\,^{\circ}\mathrm{C}$ for this example of a 400 nm thick gold foil, which was heated by a 532 nm cw laser with an output power of 2.4 W. The stated uncertainty results from the mathematical fitting process of the Planck curve and does not account for experienced fluctuations of the overall spectral shape from measurement to measurement, which increases the uncertainty for about half an order of magnitude. These fluctuations are expected to originate from instabilities in the spectrometer background level and the heating laser output power [157].

Chapter 4

Study of Laser-Driven Acceleration of Gold Ions

The main goal of this thesis is the investigation of laser-driven gold ion acceleration as preparatory study for the realization of the fission-fusion reaction mechanism, described in detail in Sec. 2.4. This mechanism requires highly-dense heavy ion bunches in the mass range of $A \geq 200$ with energies around 7 MeV/u. As outlined in Chapter 1, little was known about laser-driven heavy ion acceleration in the desired energy range at the beginning of this work. Only two papers presented experimental results demonstrating the successful acceleration of gold and lead ions up to 1 and 2 MeV/u, respectively [44, 45]. This chapter presents two experimental campaigns, dedicated to extend the availability of data regarding laser-driven acceleration of gold ions.

4.1 Experiment at the Texas Petawatt Laser

The campaign at the Texas Petawatt laser (TPW) at the University of Texas at Austin in the United States of America was the first gold ion acceleration experiment in the scope of this thesis. Besides the realization of a new energy record for laser-accelerated gold ions of around 5 MeV/u, we identified several aspects regarding target cleaning and ion diagnostics, which were improved for the follow-up experiment at the PHELIX laser, presented in Sec. 4.2. The key results of this experiment were published in reference [48]. This section intends to provide access to data beyond the mentioned publication, in order to deliver a full impression of the data analysis and results regarding the laser-based acceleration of heavy ions obtained by this experiment.

4.1.1 Experimental Setup

The main experimental components are sketched in Fig. 4.1. The TPW is incident from the right with a pulse energy of about 110 J within pulse durations around 140 fs at a central wavelength of 1057 nm. An f/3 off-axis parabolic mirror focused the laser down to a spot size of about 10 μm. Antireflectively coated, UV fused silica windows from *Altechna UAB*[1] with a diameter of one inch with a substrate thickness of 5 mm functioned as single inline plasma mirrors for contrast enhancement. They were positioned by a standard mirror holder placed on a kinematic base, which enabled an easy and precise replacement of the plasma mirror after each laser shot, preserving the alignment. An intensity of $(8 \pm 2) \times 10^{20}$ W cm^{-2} was achieved on target.

Gold foils with thicknesses of 50, 100 and 300 nm were employed as laser targets. The gold foils were produced by the target factory of the Ludwig-Maximilians-Universität München in Garching by physical vapor deposition. Afterwards, the foils were floated on conventional silicon wafers, which were previously cut into small pieces of an area of 25×3 mm^2. Each piece has two 500 μm diameter holes separated by 1 cm, providing

[1] http://www.altechna.com

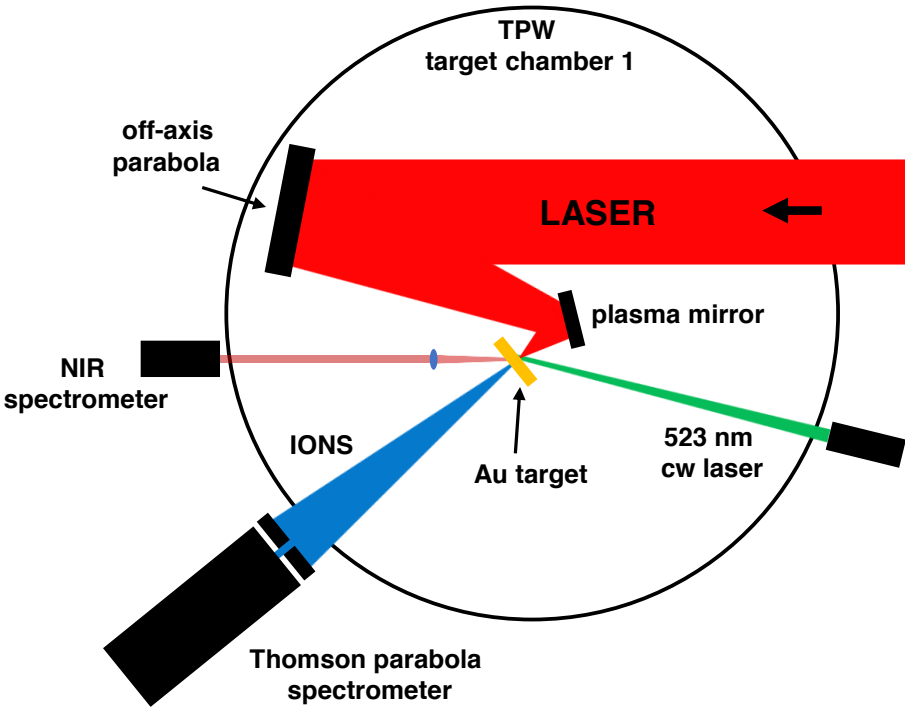

Figure 4.1: Experimental setup of the experiment at the TPW. Figure published in reference [48].

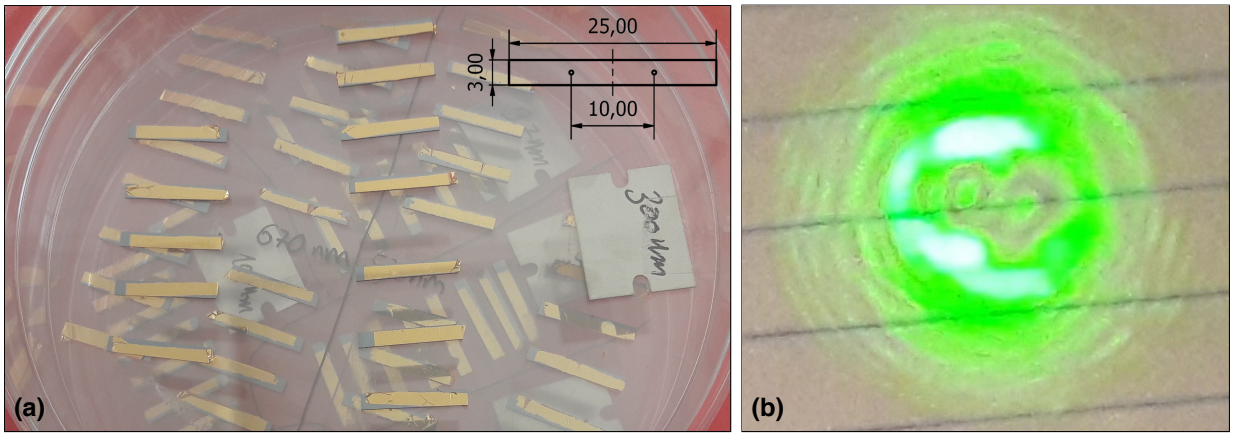

Figure 4.2: (a) Gold foil targets for the TPW experiment packed in the transportation box. The gold foils are floated on pieces of conventional silicon wafers, each having two 500 μm holes, providing the free-standing laser target. The dimensions of the target holder (in units of mm) are sketched on the top right corner.
(b) Expanded heating laser profile after a few laser shots on target. Damaged spots in the center of the laser profile are evident, degrading the total heating laser output power.

the freestanding foil, onto which the laser is focused. Fig. 4.2(a) shows the gold foil targets packed and stacked in their transportation box for the delivery to the United States. It also shows the dimensions of the target holder in the top right corner (in units of mm). The targets (as well as the plasma mirrors) had to be replaced after each laser shot, which required venting and re-evacuation of the target chamber. This process took about one hour, which matches approximately the repetition rate of the TPW.

The surface contaminants were removed as described in Sec. 3.4 by radiative heating using a 532 nm continuous-wave (cw) laser[2] with an adjustable output power of up to 1 W. The emitted heat spectrum, detected by a near infrared (NIR) spectrometer[3], was used as rough measure for the heating efficiency. The corresponding temperature has not been determined, however, the gold foils were heated up to the melting point (1064 °C) as close as possible. Hence, it is assumed that temperatures well above 500 °C have been achieved. After a few laser shots on target, damaged spots in the center of the laser beam profile appeared, as shown in Fig. 4.2(b), which resulted in a degraded heating laser power. As the heating laser was not shuttered before each shot in the beginning, we suppose focusing of scattered light from the main laser pulse into the heating laser optics as most likely reason for this degradation. As a consequence, we employed a locally available blue laser

[2]VA-II-N-532-1W by *Beijing Viasho Technology Co.,Ltd* (http://www.viasho.com/)
[3]NIR-Quest512-2.2 by *Ocean Optics, Inc.* (now: *Ocean Insight*) [160]

pointer[4] with an output power of 1 W and a wavelength of 445 nm as support for the green heating laser. As the blue laser's output power was not controllable and its focusability was very poor, it was only used to establish a basic constant heating power level, before the main heating process and the fine adjustment was done with the green laser.

As ion diagnostics, a TPS in target normal direction (corresponding to an angle of 0°) was employed. The employed diagnostics was *not* the TPS presented in Sec. 3.3.3, specially designed for heavy ion detection. The need for such a diagnostics was one of the outcomes of this experiment. An entrance pinhole with a diameter of 200 μm collimated the ion bunch, accepting a solid angle of 2×10^{-5} msr at a distance of 1.12 m from the target. After passing the entrance pinhole, the ions are deflected by a magnetic field with an average field strength of 0.55 T over a length of 10 cm and an electric field of about 11 – 12 kV/cm over a distance of 33 cm. The drift lengths after the magnetic and the electric field were 28.8 cm and 5.0 cm, respectively. CR-39 sheets with a thickness of 1 mm have been used for the detection of gold and carbon ions. IPs have been positioned directly behind the CR-39 sheets for the detection of protons. The exact value for the magnetic field has been determined using the spectrometer's zero point and the proton energy cut-off point after passage through the CR-39 at 10.4 MeV [133], as will be described in Sec. 4.1.3. The value of the electric field has been determined for each shot separately by adapting the theoretical ion curves to the measured data. The IPs were scanned 20 minutes after each laser shot using a GE Typhoon FLA 7000 IP scanner.

4.1.2 Processing and Digitization of CR-39 Data

Following the procedure written in Sec. 3.2.2, the CR-39 sheets have been etched for 40 minutes. A first visual inspection by eye revealed parabolic curves as expected from a TPS, as shown in Fig. 4.3. In the region towards higher charge-to-mass ratios (towards the top right corner of the figure), most CR-39 sheets showed one to three curves, which were thin and clearly separable. In the lower charge-to-mass-ratio region (towards the bottom left corner in the figure), only one broad parabolic curve appeared, consistently for all shots. It stands to reason that the thin curves can be attributed to light ions like carbons (protons traversed the CR-39 sheets and were detected in the IPs). The thick curves can accordingly be associated with heavy ions like gold, whose charge states are not resolved with the used TPS, which explains the broad lines.

[4] S3 Arctic Series by *wicked lasers* (http://www.wickedlasers.com/arctic)

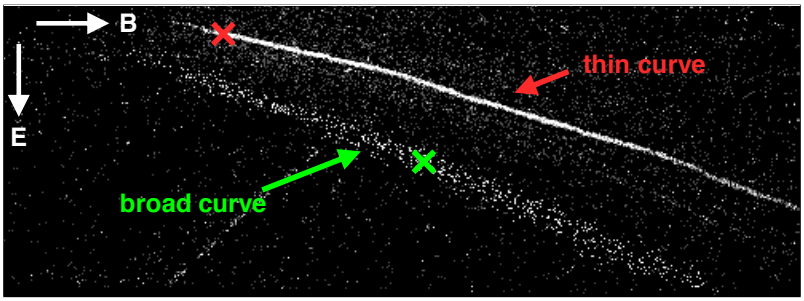

Figure 4.3: A first glance on the CR-39 sheets revealed up to three thin parabolic curves (here only one is visible, marked by the red arrow) and one broad curve (green arrow). The magnetic field deflected to the right, while the electric field deflected downwards. The thin parabola is closer to the top right corner, which means that it has a higher charge-to-mass ratio than the broad curve. The figure shows data from a shot on an unheated 300 nm gold foil, which has been visualized following the procedure described in Sec. 4.1.2. The red and green crosses mark the positions where the microscope images with the carbon and gold ion pits shown in Fig. 4.4 where taken from.

The CR-39 sheets were studied with a Zeiss Axiotron II autofocusing microscope. Unlike stated in Sec. 3.2.2, the pattern recognition software SAMAICA was not available for the processing of the detectors of this beamtime, which made the track identification more difficult. The pits from the different types of curves have been examined separately in order to validate the above assignments to light and heavy ions, respectively. A direct comparison of pits from the different curves is shown in Fig. 4.4. Clearly, the pits from the narrow curve, which are presented on the left-hand side of the figure, are much smaller compared to the pits on the right, originating from the broad curve. This first impression is confirmed quantitatively by determining the pit diameters. For this, Gaussian curves have been fitted to ten different pits of the same kind, respectively. This resulted in an averaged standard deviation of $2\sigma = 14 \pm 3$ pixels for the large pits, which are therefore more than twice as big as the smaller pits with $2\sigma = 6.5 \pm 0.4$ pixels. This verifies the initial assumption that the narrow curves are formed by lighter ions, which will in the following be referred to as carbon ions, and the broad curves are made by heavy ions, subsequently called gold ions, which deposit much more energy in the CR-39 material and, thus, create larger pits.

Lacking the automatic pattern recognition software SAMAICA[5], which directly processes the collected information, the microscope images had to be postprocessed differently in order to digitize the information stored in the CR-39 sheets. Therefore, an auto-

[5]The software SAMAICA became only available for the experiment at the PHELIX laser, presented in Sec. 4.2.

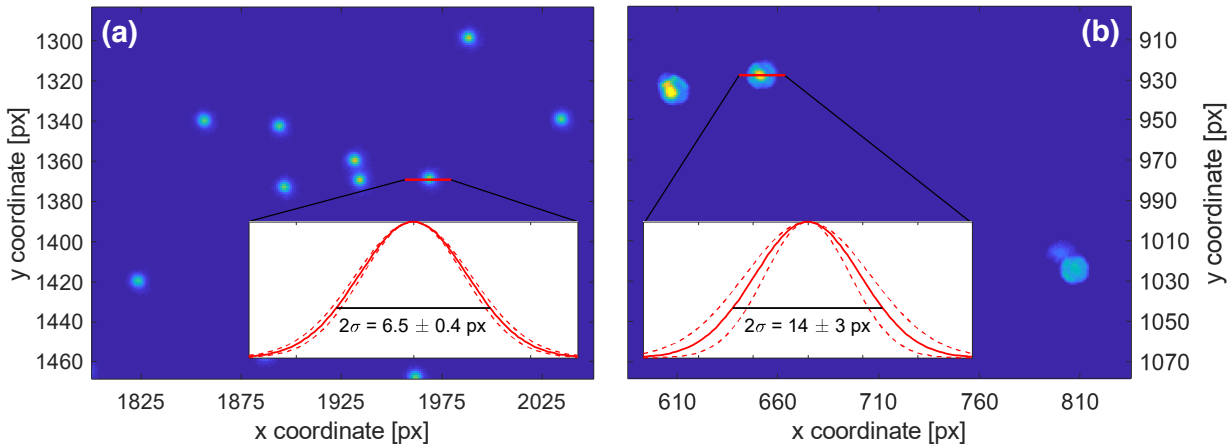

Figure 4.4: Microscope image details showing a comparison of pit sizes from (a) a narrow parabolic curve, which has been attributed to light ions and (b) a broad curve, which was assigned to heavy ions. The insets show Gaussian fits to the diameter of the ion pits. The standard deviations σ for the shown Gaussian curves have been averaged over the fits to ten different pits of the same kind. Clearly, the pits from the thick curve with $2\sigma = 14 \pm 3$ pixels are more than twice as wide as pits from the thin curves with $2\sigma = 6.5 \pm 0.4$ pixels. Variations of the pit sizes along the same parabolic curves (meaning for ions of the same type but with different energy) have turned out to be negligible compared to the shown difference of pits from the thin and thick curves. The microscope images in (a) and (b) have the same scale and are from the same unheated shot on a 300 nm thick gold foil. The positions from which the images were taken are indicated by the crosses in Fig. 4.3.

matic pattern recognition was implemented using the Trainable Weka Segmentation plugin [161] for the ImageJ-based image processing software Fiji[6]. Weka stands for **W**aikato **e**nvironment for **k**nowledge **a**nalysis and is an open-source machine learning tool, developed at the University of Waikato in New Zealand [162]. With this tool, it is possible to train the software which structures in the image can be associated with ions due to their size and shape and which structures are not of relevance for the further analysis, like scratches or dust particles or simply the image background, and can thus be discarded[7]. For this training process, the relevant areas in the image have to be marked manually, as shown in Fig. 4.5(a). Two different classes have been defined: one class for the carbon ions and one background class for all of the remaining image. The user tells the software that small blue points correspond to the class of carbon ions and marks it in red colour (for the reader – to get a visual impression – the user has not yet marked all blue carbon ions in the image), while the remaining area shall be accounted to the background class and is

[6]Fiji is short for "**F**iji **i**s **j**ust **I**mageJ", http://www.fiji.sc/

[7]The author acknowledges T. M. Ostermayr for the idea and implementation of the main part of the Weka-based analysis.

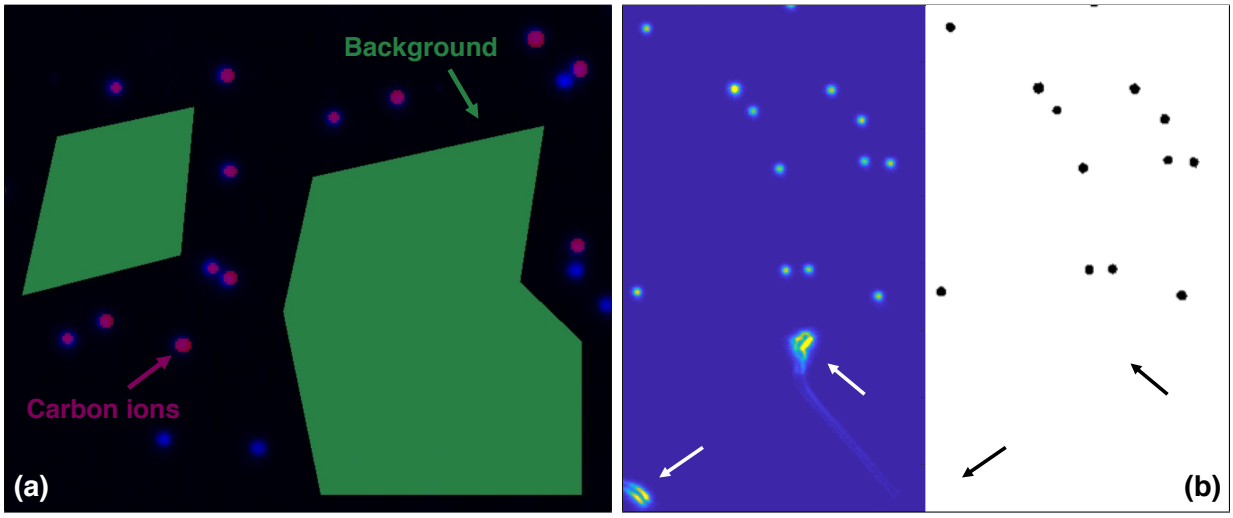

Figure 4.5: (a) The machine learning software has to be trained manually, which structures can be associated with carbon ions and which parts of the image correspond to a background class, not related to carbon ion hits. The user marks the respective structures with red, if they are related to carbon ions and parts of the remaining image with green. Some carbon ion impacts (in blue) are not registered yet in this image by the user.
(b) An example of a microscope image on the left and the corresponding image after the Weka tool has been applied to this image. Scratches and other structures, which cannot be assigned to carbon ions (black), are discarded and assigned to the background class (here in white), as indicated by the arrows. The scale in (b) is not comparable to (a).

marked in green. The different sizes of the red marks are due to the manual process and may not be mistaken to correspond to different pit sizes (which would mean different ion species/energies).

This is repeated with several microscope images, until the machine learning tool can reliably and independently distinguish between carbon ion pits and unwanted structures. Afterwards, the program is applied to all microscope images, creating masks showing the value 0 for pixels, where a carbon ion was registered, and 1 for all other pixels. This is exemplarily shown in Fig. 4.5(b). The original microscope image is on the left side with two structures that cannot be assigned to carbon ions, indicated by the arrows. This image is transferred into a carbon ion mask, where the unwanted structures have been discarded. In a further step, all objects (black spots) in this mask are located and listed together with their centre of mass coordinates and their enclosed area using the Mathematica function `ComponentsMeasurements`. The final image is generated with a $50 \times 50\ \mu\mathrm{m}^2$ pixel size, which corresponds to the resolution of the IP images, whereby each object having centre of mass coordinates within the respective pixel increments the pixel count

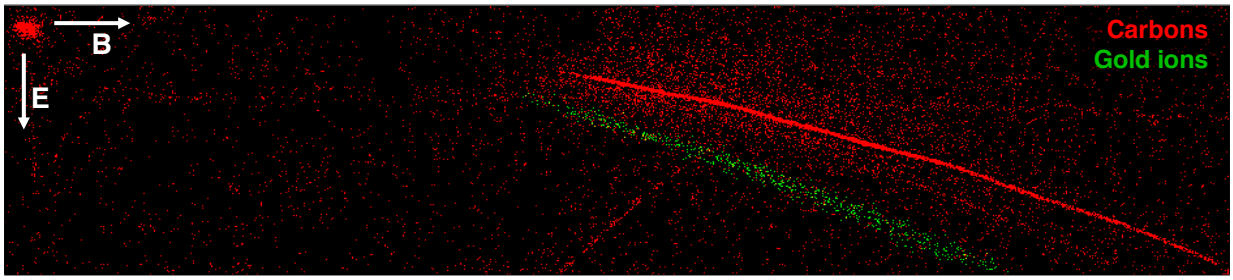

Figure 4.6: Digitized information from a CR-39 sheet, which was exposed to an ion bunch from a shot on an unheated 300 nm thick gold foil. The result from the carbon ion registration using the Weka machine learning tool is shown in red. The parabolic C^{6+} curve is prominent, as well as the zero point on the top left side. All over the image, structures have been falsely identified as carbon ions, resulting in the presented red noisy image. The manually registered gold ions are shown in green. As indicated on the top left, the magnetic field deflected the ions to the right (energy-dependent axis), while the electric field deflected in downward direction.

by 1. An example for the result of this procedure for the carbon ion registration is shown in red in Fig. 4.6. The expected TPS curve – in this case only C^{6+} – is identified sufficiently well. However, a lot of structures have been wrongly associated with carbon ions, resulting in the shown noisy image in red colour.

Unfortunately, the presented method using the WEKA machine learning tool could not be applied to gold ions. As can be seen from Fig. 4.4(b), the shape and internal structure of the gold ion pits differ from each other. It was not possible to train the software to consistently recognize the gold ion impacts. Therefore, the gold ion pits on the CR-39 sheet have been registered manually on the microscope images, which was feasible thanks to the limited total amount of gold particles. The gold ion distribution is shown in green in Fig. 4.6, which represents the previously mentioned broad parabolic curve, associated with heavy ions.

4.1.3 Determination of Gold Ion Energy Spectra

For the determination of the gold ion energy spectra, the magnetic and electric field values must be known very precisely. The protons were detected on IPs, positioned directly behind CR-39 sheets, and can be used for a calibration of the magnetic field. A typical proton parabola from an unheated shot is shown in white in Fig. 4.7(a). The protons are deflected to the right by the magnetic field. The further right they are detected, the lower is their energy. At a certain point, the proton trace terminates. This point corresponds to an energy of 10.4 $\pm$ 0.1 MeV, which protons need in order to penetrate the 1 mm thick

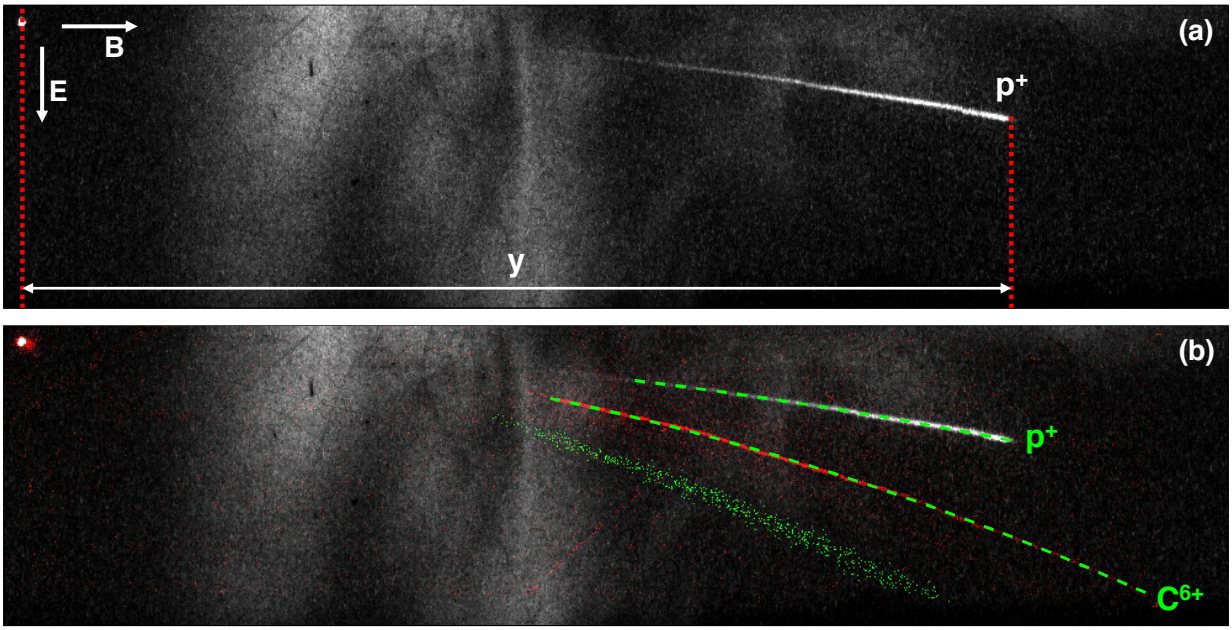

Figure 4.7: (a) Proton raw data on an IP from an unheated shot on a 300 nm gold foil. As indicated, the magnetic field deflected the protons to the right (energy-dependent axis), while the electric field deflected in downward direction. The distance y between the proton energy cutoff and the zero point (visible on the top left) can be used to determine the magnetic field strength. The widespread, irregular white structure in the background appeared on almost all IPs from shots which had problems with sparking TPS electrodes. Thus, it originates most likely from radiation emitted during the sparking process of the electrodes and is no real signal from the laser matter interaction. (b) Final raw data image after coregistration and rotation of the IP and CR-39 sheet. The calculated parabolas perfectly match the measured data.

CR-39 layer in front of the IP [133]. Protons with lower energies, which would appear further right on the IP, are stopped within this CR-39 layer. Inserting the distance y between this proton cutoff point and the zero point, which is visible on the top left, into Eq. (3.2), directly provides the average magnetic field B that deflected the protons to this cutoff point. The distance y has been measured to be 4.02 $\pm$ 0.03 cm, including a rotational uncertainty of $\pm\,2°$ due to slight positioning errors of the IP and an uncertainty of up to $\pm\,3$ pixels for the determination of the exact coordinates of the zero and cutoff points. Together with the TPS dimensions given in Sec. 4.1.1[8], the average magnetic field strength amounts to

$$B = 0.550 \pm 0.025 \text{ T}.$$

In contrast to the magnetic field, which is generated by permanent dipole magnets, the

[8] An uncertainty of $\pm\,0.1$ cm was assumed for the measurement of the TPS dimensions.

electric fields can vary from shot to shot, as the TPS electrode voltage needed to be turned off and re-applied after each shot due to the venting and re-evacuation process for target replacement. Thus, the exact value has to be determined for each shot separately. This requires an iterative process, which involves the coregistration of CR-39 and IP images and the overlay with the theoretical TPS curves defined by Eq. (3.7). The zero point, which is visible on both detector types, serves as fix point for the image coregistration and is the intersection point for the individual parabolas. As the detectors were facing each other and the parabolas are plotted in the detection plane, only one degree of freedom is left: the rotation around the zero point. Knowing now the magnetic field strength, the parabolic TPS curves can be calculated using Eq. (3.7) with an initial assumption for the electric field ($\approx 11-12$ kV/cm). The calculated lines were chosen to be fixed, as this scenario corresponds to a horizontal deflection by the magnetic field. For the identification of the electric field value, the CR-39 image was rotated around the zero point and the electric field parameter was iteratively adapted, until the overlay of the theoretical parabolas with the measured carbon lines was optimized[9]. Afterwards, the rotation of the IP was adapted, until the proton curve matched its theoretical prediction as well, as shown in Fig. 4.7(b).

With the magnetic and electric field strengths, all relevant parameters for the calculation of the gold ion parabolas using Eq. (3.7) are known. These parabolas are needed for the generation of a mesh which can be overlaid with the measured data, like it was done in Sec. 3.3.2. As a TPS resolves energy and charge states, instead of energy and angle of emission, the mesh in this case is formed by iso-energy and iso-charge-state lines. Fig. 4.8 shows the resulting mesh, which is overlaid with the gold data. The two red lines correspond to the minimum and maximum charge states between which the gold signal has been detected. The green dashed lines indicate the energy intervals, which are defined by equidistant steps on the detector surface. The width of these steps is given by the geometric size of the projection of the TPS entrance pinhole on the detection screen (in this case about 350 μm). The blue lines enclose exemplarily the area between two adjacent charge states, the yellow lines enclose the area corresponding to one specific energy interval. As the inset visualizes in orange colour, tetragons are formed by two adjacent charge states and the energy interval boundaries. The signal within these tetragons is summed up and saved together with the corresponding energy and charge state information.

As the parabolas overlap and are not separable from each other, the gold ion energy

[9]The available number of carbon lines varied from shot to shot. In Fig. 4.7(b), only the C^{6+} line appeared. Up to three lines (C^{4+} – C^{6+}) were visible in other shots, as can be seen in Figs. 4.9 to 4.11 in the following section.

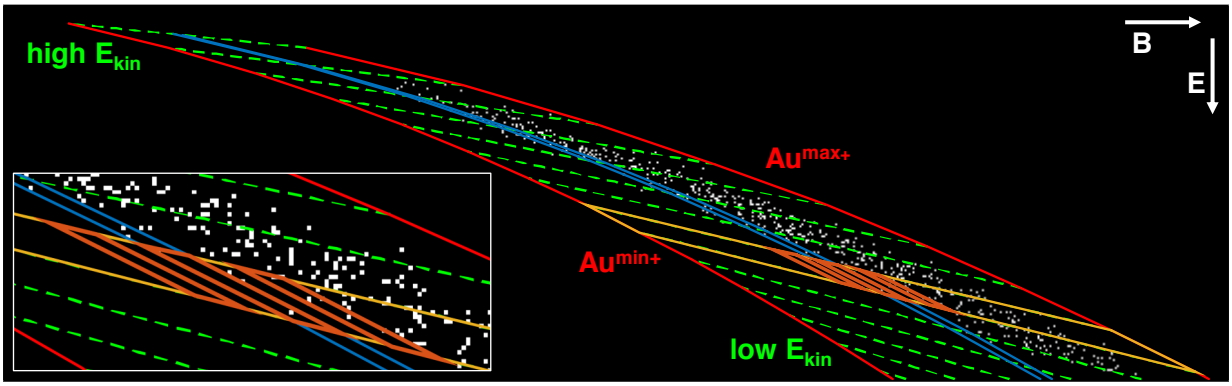

Figure 4.8: The gold ion raw data is overlaid with an iso-energy, iso-charge-state mesh for the determination of the gold energy spectra. The red lines correspond to the minimum and maximum charge states, between which the gold ions have been detected. The green dashed lines depict to the energy intervals, defined by equidistant steps on the detector surface with a width given by the projection of the entrance pinhole. As enlarged in the inset, tetragons are formed by neighbouring charge state lines and the energy interval boundaries. The signal within the tetragons is saved together with the information about the respective charge state and energy. As indicated, the magnetic field deflected the ions to the right (energy-dependent axis), while the electric field deflected in downward direction.

spectra for one distinct charge state cannot be extracted from the data. Therefore, the spectra shown and discussed in the following section are integrated over all charge states, meaning the summation of all tetragons within one energy interval (area enclosed by yellow lines in Fig. 4.8). However, it is still possible to extract charge-dependent information from the intensity distribution of the signal across the gold ion parabola band, even if single charge states are not distinguishable. Hence, the following section will show such charge state distributions. This information needs to be interpreted very carefully, always considering the shown error bars, which result again from the projection of the entrance pinhole onto the detection screen. As the gold parabolas get closer towards higher energies, these error bars naturally increase.

4.1.4 Experimental Results and Discussion

In total, seven shots on gold foils were recorded on CR-39 during this beamtime: two on 50 nm, three on 100 nm and two on 300 nm thick gold foils. For each thickness, one unheated shot is available, allowing to draw conclusions about the influence of the target heating. In Figs. 4.9 to 4.11, the raw data of the seven shots is shown. The data has been prepared as discussed in Secs. 4.1.2 and 4.1.3. The green data points correspond to gold

Thickness	**heated**	$\mathbf{S_C}$ [#carbons]	$\mathbf{S_p}$ [a.u.]	$\mathbf{E_{kin}}$ $\mathbf{p^+}$ [MeV]	$\mathbf{E_{kin}}$ $\mathbf{C^{6+}}$ [MeV/u]	$\mathbf{E_{kin}}$ $\mathbf{C^{5+}}$ [MeV/u]	$\mathbf{E_{kin}}$ $\mathbf{C^{4+}}$ [MeV/u]
50 nm	no	1.3×10^4	–	–	$4-10$	$3-8$	–
100 nm	no	1.6×10^4	41	$10-37$	$3-10$	$3-7$	–
300 nm	no	1.9×10^4	109	$10-31$	$2-9$	–	–
50 nm	yes	5.7×10^3	–	–	$6-12$	$5-9$	$5-5$
100 nm	yes (a)	6.0×10^3	6	$16-23$	$6-11$	$5-8$	–
100 nm	yes (b)	7.9×10^3	3	$16-20$	$5-13$	$5-10$	$5-6$
300 nm	yes	7.5×10^3	6	$16-22$	$6-14$	$6-12$	–

Table 4.1: The table documents the total number of registered carbon ions S_C and the proton signal on the IP, S_p, which has been measured between 16 and 20 MeV in a narrow region of ± 7 pixels around the centre of the protons trace. Additionally, the proton and carbon energy ranges are shown in MeV/u and with an uncertainty of at least 10 %.

ion impacts, while the red data points represent the carbon data. The proton data on IPs, where available, is plotted in white. The proton and carbon signal has been modified for each shot individually in order to achieve an optimal illustration of the geometric ion curves. Thus, the signal levels of protons and carbon ions may not be directly compared in Figs. 4.9 to 4.11.

A first glance at the raw data images immediately reveals that the heating indeed has an influence on the measured ion distributions. All gold traces from heated shots extend further left compared to data from unheated shots, meaning that the target cleaning results in higher energies. The gold ion energy spectra and – as much as possible due to the limited resolution – their charge distributions will be discussed below in more detail.

The proton and carbon ion data will not be quantitatively analyzed in detail, as they are only a byproduct of this experiment. However, the effect of heating is obvious for those two ion species as well. In order to get a rough measure of the ion fluence, the proton and carbon signals, S_P and S_C, have been summed up, respectively. The results are documented in Table 4.1. For the carbon ions, all as such identified pits have been counted all over the CR-39. Thus, the summation delivers the total number of detected carbon ions for a shot. As discussed in Sec. 4.1.2, a relatively large amount of structures have been falsely assigned to the class of carbon ions by the machine learning tool. Therefore, the carbon numbers are overestimated, however, in a comparable way for all shots.

For the protons, the unheated shots are superpositioned with a background structure caused by sparking electrodes. Thus, only a narrow region of ± 7 pixels around the centre of the parabolic trace on the IP has been taken into account to minimize the effect of this

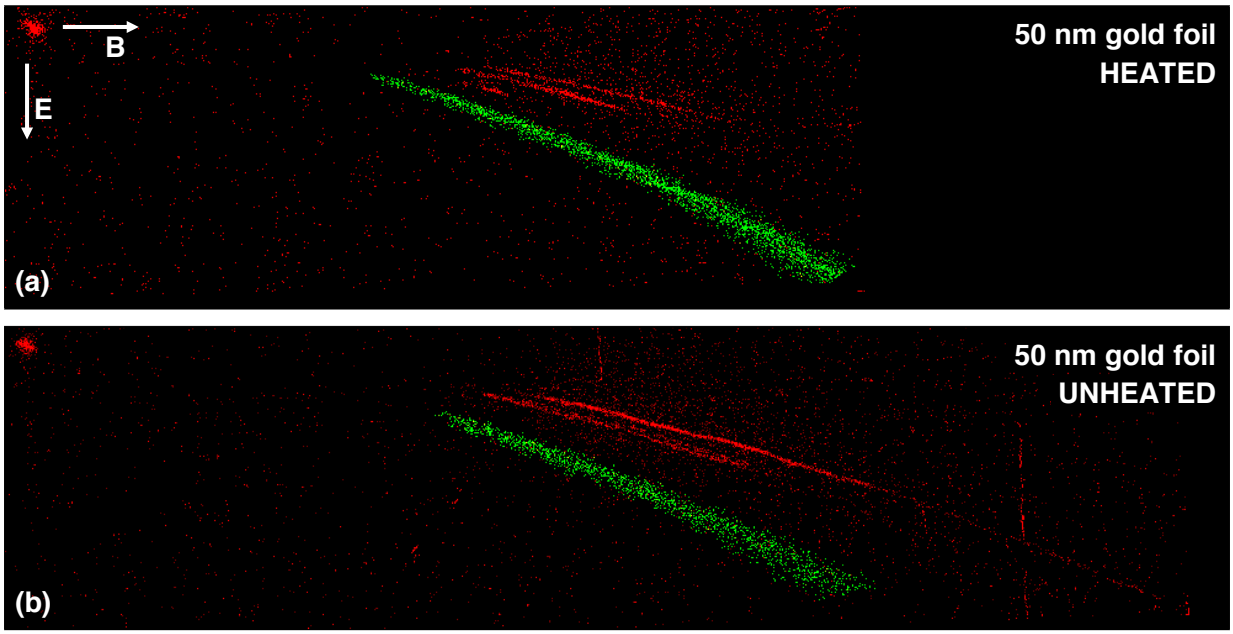

Figure 4.9: Raw data from (a) heated and (b) unheated shots on 50 nm thick gold foils. The green data points correspond to gold ions, the red data points to carbon ion data. For the shots on 50 nm, no IP data is available. The carbon ion signal levels have been adjusted for each image separately, in order to achieve a better illustration.

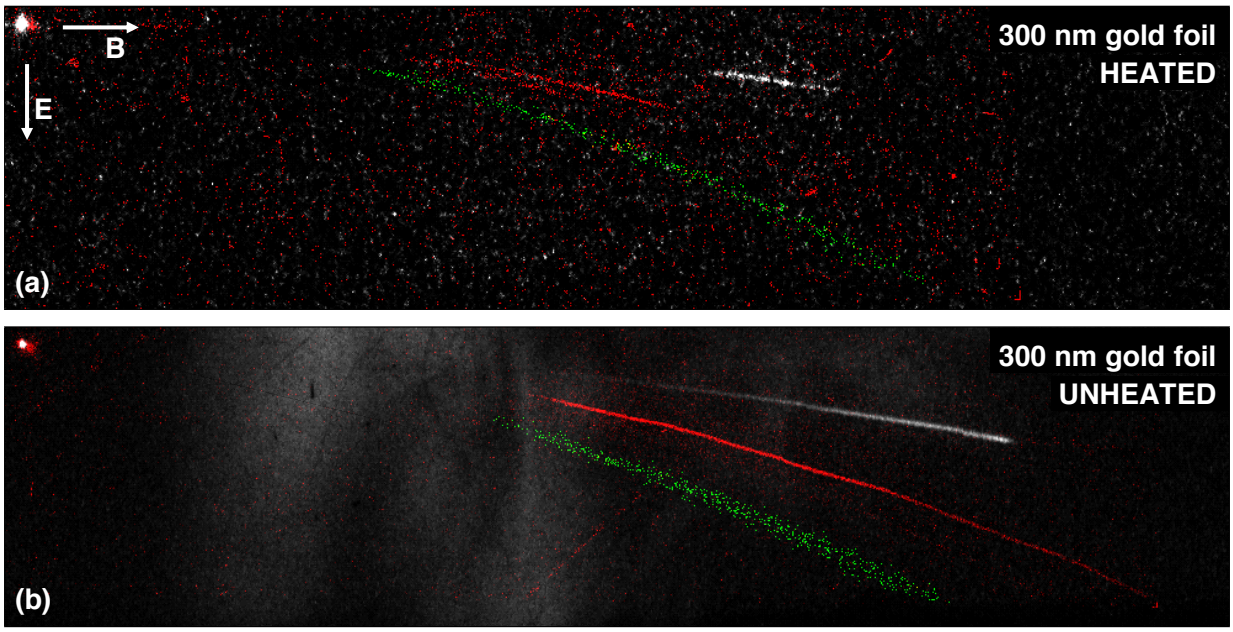

Figure 4.10: Raw data from (a) heated and (b) unheated shots on 300 nm thick gold foils. The green data points correspond to gold ions, the red data points to carbon ion data. The proton signal, detected by IPs, is shown in white. The proton and carbon ion signal levels have been adjusted for each image separately, in order to achieve a better illustration.

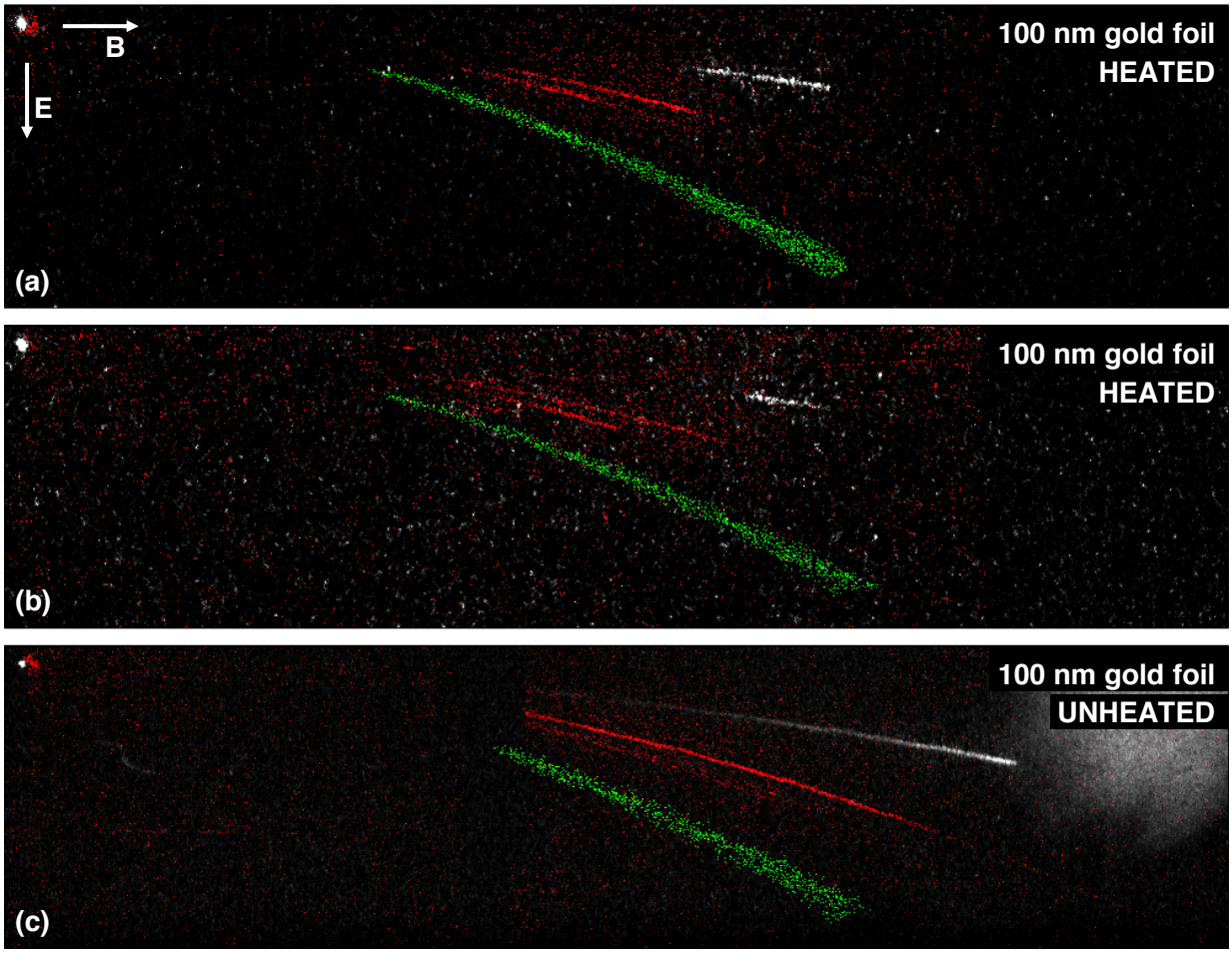

Figure 4.11: Raw data from (a), (b) heated and (c) unheated shots on 100 nm thick gold foils. The green data points correspond to gold ions, the red data points to carbon ion data. The proton signal, detected by IPs, is shown in white. The proton and carbon ion signal levels have been adjusted for each image separately, in order to achieve a better illustration.

radiation background. Since the signal was not transferred into absolute proton numbers, the energy dependency needs to be considered. To reduce this influence, only the region between 16 and 20 MeV was included, as in this energy range (which corresponds to a specific geometric region on the detector) proton signal was measured for all shots. Despite these uncertainties, it is evident that the proton signal from unheated shots is much higher than that from shots on heated foils. Also the carbon numbers are at least a factor of two higher for unheated shots. This points out that, apparently, the proton and carbon numbers are much lower for heated shots than for unheated ones. This demonstrates the efficiency of the heating, even though the proton and carbon numbers have not been decreased to zero.

Noteworthy are also the energy ranges for the protons and carbon ions, which are documented in Table 4.1 as well. The respective energy cutoff positions have been identified by eye and not algorithm-based, as it was shown in Sec. 4.1.3. Hence, the energy values have to be interpreted with an uncertainty of at least 10 %. The maximum proton energies for the heated shots are observed to be lower than for unheated shots. This initially appears contradictory, as the accelerating field remains the same and only the proton number is reduced, but has also been observed in several former experiments (e.g. references [144, 145, 148]). This observation possibly indicates an effective heating at the laser target interaction point, where protons indeed might have been completely removed, as they would be accelerated to the same energies. It has been shown that protons with lower energies originate from rings surrounding the central laser interaction spot with diameters of several hundreds of μm [163], where in this case the heating might not have been sufficient enough to remove all protons.

The gold ion energy spectra, which have been calculated following the procedure in Sec. 4.1.3, are presented in Fig. 4.12. Shots on unheated gold foils are displayed in blue, while the red and yellow lines are spectra from heated shots. Obviously, the target cleaning had indeed the desired effect and heated shots have achieved higher gold ion energies than unheated ones. The energy range appears to be independent of the target thickness. The achieved maximum gold ion energy of about 5 MeV/u was at the time of data publication the highest hitherto measured laser-accelerated heavy ion energy that was reported in literature [48]. Compared to the light ion energies in Table 4.1, it is striking that the carbon ion energies start at $5-6$ MeV/u for the heated shots, right at the gold ion energy cutoff point. The carbon ions achieve energies of up to $11-14$ MeV/u, where soon the protons take turns at energies of 16 MeV up to $20-23$ MeV. The energy spectra of the

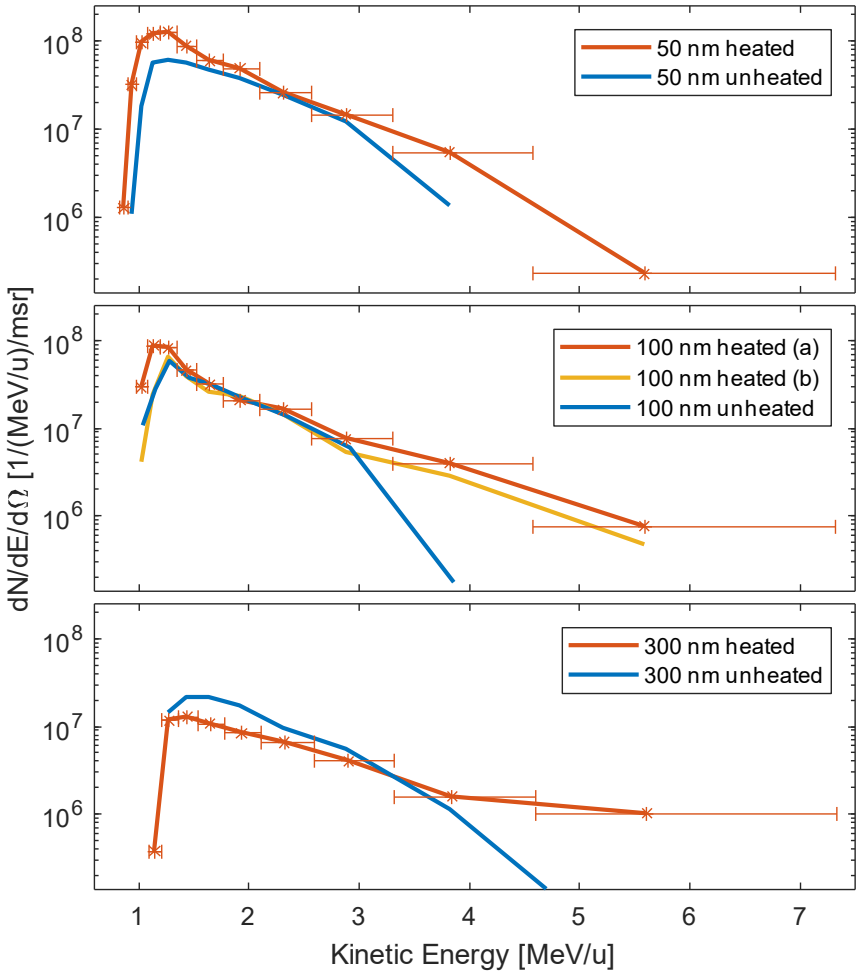

Figure 4.12: Gold ion energy spectra for shots on heated (red, yellow) and unheated (blue) target foils of thickness 50, 100 and 300 nm (from top to bottom). The energy spectra are integrated over all charge states. Figure published in reference [48].

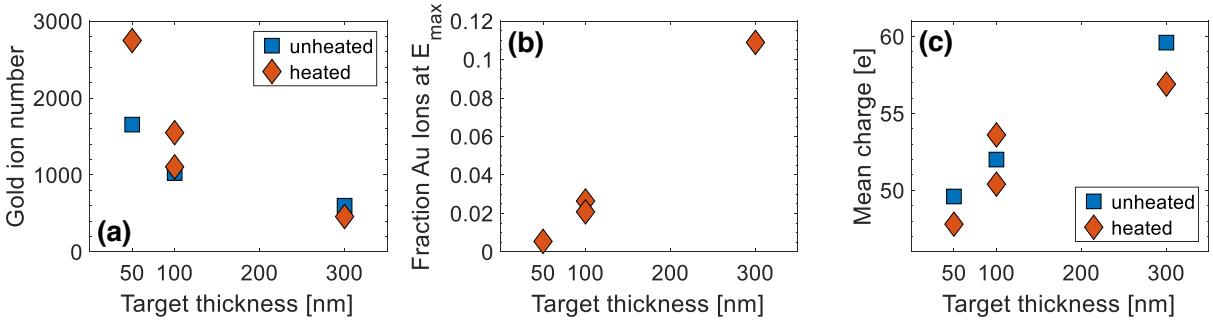

Figure 4.13: (a) Number of recorded gold ions that have been accelerated in target normal direction, plotted versus the target thickness. Red diamonds are from heated, blue squares from unheated shots. (b) Fraction of measured gold ions which were accelerated into the highest energy interval around 5 MeV/u, plotted versus the target thickness. (c) Mean charge state of detected gold ions plotted versus the target thickness.

light ions exhibit a pretty narrow bandwidth and it seems as if the ion species alternate with one another.

Comparable ion energy distributions with a spectral separation of the individual ion species have been shown experimentally and in simulations for circularly polarized, short laser pulses ($30 - 40$ fs, 1 J) on Formvar targets [164, 165], but also for linearly polarized, long laser pulses ($700 - 900$ fs, 200 J) on copper foils [85]. All target foils had a thickness of a few tens of nanometers. The authors of the respective studies concluded that the spectrally separated, narrow-bandwidth features, which they observed in their energy distributions, indicate the predominant acceleration in the (light sail) RPA regime, after an initial separation of the ion species due to their different charge-to-mass ratios in an early acceleration phase. The heaviest of three simultaneously accelerated ion species showed an exponentially decaying, TNSA-like spectrum [85, 165], which is also seen in Fig. 4.12 for the gold ions of this experiment.

The number of gold ions that are accelerated in the target normal direction decreases with increasing target thickness, which is shown in Fig. 4.13(a): for 50 nm thick gold foils, ion numbers between 1600 and 2700 have been accelerated in target normal direction. For 100 nm, this number dropped to $1000 - 1600$ and, for 300 nm, only $450 - 600$ gold ions have been registered in the TPS. At the same time, the slopes of the spectra from the heated gold targets seem to flatten with increasing target thickness. This means, that the fraction of gold ions that have been accelerated to maximum energy increases, as depicted in Fig. 4.13(b), while the total gold ion number declines. For 50 nm, this fraction is 0.5 % (15 gold ions within the highest energy interval). For 100 nm, it is 2.1 % and 2.6 % (23

and 41 gold ions) and for 300 nm 10.9 % (50 gold ions), showing that not only the relative fraction but also the total number of gold ions, that have been accelerated to maximum energies in target normal direction, increases with the target thickness.

The energy-dependent charge state distributions are plotted in Fig. 4.14, exemplarily for one heated shot on each target thickness. The charge state distributions did not differ for heated and unheated shots. The charge state distributions are plotted for each energy interval separately, starting from lower energies on the bottom towards higher energies in the upward direction. The corresponding energy interval and the uncertainty of the individual charge states are annotated next to each curve. The mean charge state for each energy interval is indicated together with the uncertainty of the individual charge states. The total mean charge state, averaged over all gold ions of a shot, independent of their energies, is depicted by the orange dotted line. The "S"-like fluctuation of the energy-dependent mean charge states around this line (the total mean charge state) has been observed for all shots. It is most likely a systematic error introduced during data analysis and not a real fluctuation in the charge state distributions. Apparently, thicker foils delivered gold ions with higher charges, which is also shown in Fig. 4.13(c). This could possibly be an explanation for the larger fraction of gold ions at higher energies, which has been observed for thicker foils, as higher charged particles generally experience a stronger acceleration in electromagnetic fields. However, the limited data statistics and spectrometer resolution do not allow for more than those coarse interpretations.

4.1.5 Concluding Remarks

The presented campaign at the TPW laser was the first experiment of our group dedicated to the investigation of laser-driven heavy ion acceleration. The detected maximum gold ion energy around 5 MeV/u marks an important step towards the envisaged realization of the fission-fusion reaction mechanism. The gap between the energy threshold for this reaction scheme at about 7 MeV/u and formerly achieved heavy ion energies of up to 2 MeV/u could be significantly reduced by a factor of 2.5. Beyond that, it is difficult to draw reliable empirical conclusions about the properties of the laser-accelerated gold ions, as the resolution of the employed TPS was very limited. A general trend towards higher charge states for thicker target foils could be observed. However, the exact distribution of charge states and the potential observation of any specially pronounced charge states, like Au^{51+} in the simulations shown in references [46, 47], cannot be extracted from the data. This information would be crucial for an understanding of the underlying ionization processes

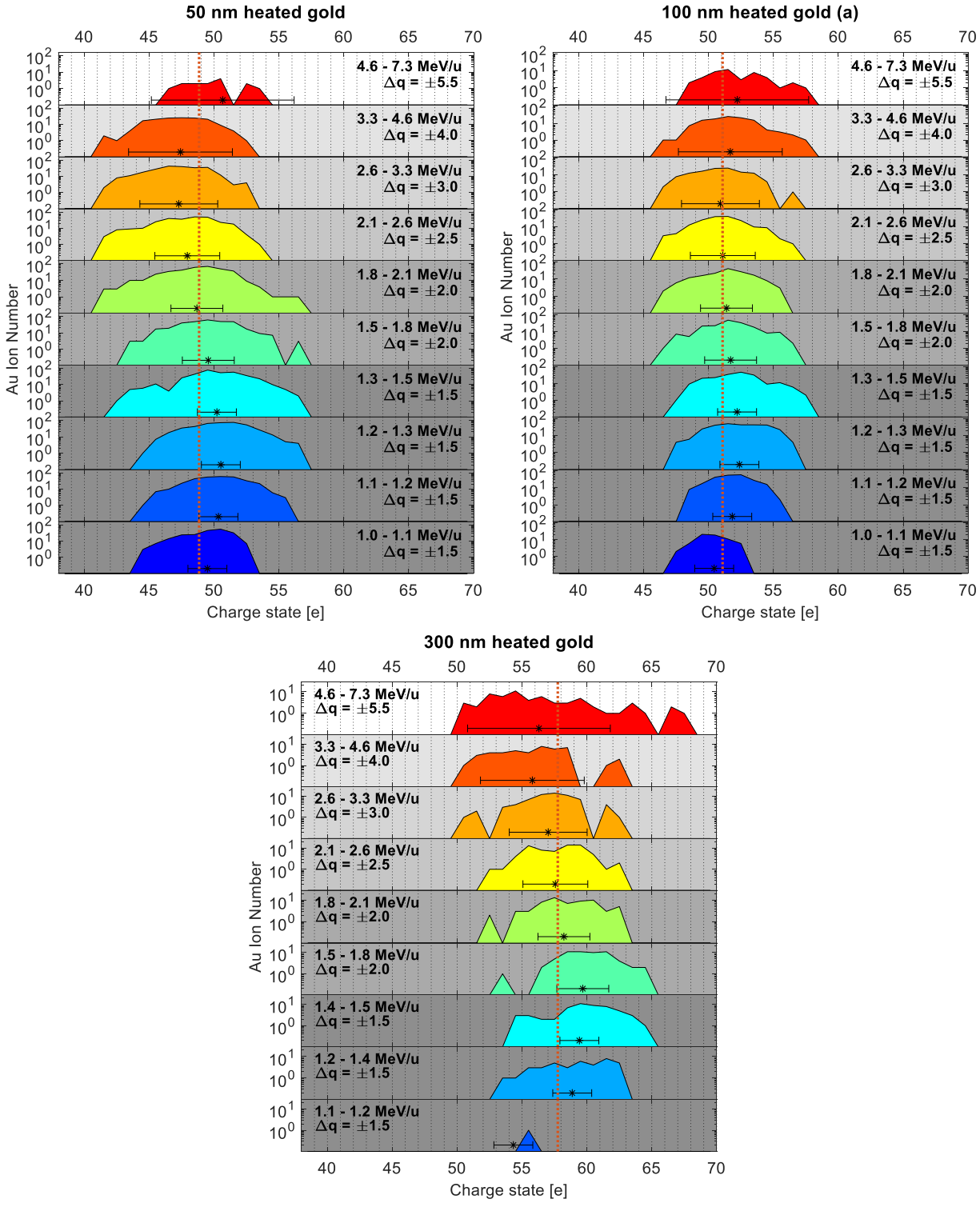

Figure 4.14: Charge state distributions for heated shots on 50, 100 and 300 nm targets as a function of the ions' kinetic energy (rising from bottom to top). The respective mean charge state for one energy interval is indicated together with the corresponding uncertainty of the charge states. The overall mean charge state, averaged over all energies, is indicated by the orange dotted line.

and, hence, the mechanisms of laser-driven heavy ion acceleration. As a consequence, a TPS has been developed, whose magnetic and electric fields have been designed with careful consideration of the heavy ion deflection properties, as presented previously in Sec. 3.3.3.

Furthermore, the beamtime revealed the need for an improvement of the target cleaning mechanism. Indeed, as has been shown, the heating of the target foils had the desired effect of proton signal reduction and an increase in the gold ion energies. However, the protons could not be entirely removed. It was discussed in the previous section that the still existent protons might originate from outer regions surrounding the laser matter interaction region. It stands to reason that heating a larger area could further reduce the proton number, potentially even to zero. For the irradiation of a larger area, a more powerful laser is needed in order to achieve the same heating intensity. Therefore, a new laser was acquired after the beamtime, which could deliver light up to 4 W at a wavelength of 532 nm[10].

A major issue during this experiment was the damage of the heating laser as shown in Fig. 4.2(b). As a direct optical path between the interaction point of the main laser with the target and the heating laser exists, scattered light from the laser matter interaction is most likely focused into the heating laser head. This can be prevented by blocking this beam path prior to each shot on a target. For this purpose, a fast shutter has been purchased[11] for the usage in future beamtimes. A rapid closing time of below 2 ms ensures that the heating can be maintained as long as possible before the target is shot. Thus, the time is minimized for any residual particles and/or molecules in the vacuum to re-accumulate on the target surface.

Room for improvement is also in the surveillance of the heating procedure itself, as it was only controlled by watching the shape and amplitude of the measured NIR spectra. The actual behaviour and condition of the gold foil has not been monitored. An optical control would provide information about the deformation of the foil, which is an inevitable side effect of the targeted application of heat. This becomes essential, once the deforming target would move out of the laser focus, which needs to be corrected. Besides, such an optical target control could be used for the identification of good quality foil surface spots with little wrinkles or dirt, which might differ from the initial, unheated target. Hence, an additional optical surveillance of the target surface during the heating process for example by including the focus diagnostics in the design of the heat spectrum measurement, would be beneficial for a better target control and to establish reproducible conditions.

[10] VA-II-N-532-4W by *Beijing Viasho Technology Co.,Ltd* (http://www.viasho.com/)
[11] Uniblitz Laser Shutter LS6S2Z1 by *Vincent Associates Inc.* (http://www.uniblitz.com)

4.2 Experiment at the PHELIX Laser

The second experiment dedicated to laser-driven gold ion acceleration, which is presented in this thesis, was performed at the PHELIX laser at the GSI in Darmstadt, Germany. The improvements suggested in Sec. 4.1.5 have been implemented and resulted indeed in higher gold ion energies and in individually resolvable gold ion charge states. After the description of the experimental setup and procedure and the data processing and analysis, the results will be shown and discussed in detail at the end of this section.

4.2.1 Experimental Setup and Procedure

A schematic overview of the experimental setup is provided in Fig. 4.15. The PHELIX laser delivered pulses with energies ranging between $170 - 200$ J and within durations of 500 fs at a central wavelength of 1054 nm. The beam is focused down by an f/1.6 off-axis parabolic mirror to a spot size of about $14 - 15$ μm^2 (FWHM), which contained around 23 % of the laser energy. As done for the experiment at the TPW, antireflectively coated, UV fused silica windows from *Altechna UAB*[12] with a diameter of one inch and a substrate thickness of 5 mm have been used as single inline plasma mirrors for contrast enhancement. Again, they have been mounted on a mirror holder positioned on a kinematic base, enabling an alignment-preserving plasma mirror replacement after each laser shot. The cycle-averaged intensity on target is estimated to be about $(2.9 \pm 0.6) \times 10^{20}$ W cm^{-2} within the FWHM area and around $(4.1 \pm 0.9) \times 10^{20}$ W cm^{-2} at the peak value[13].

Gold targets with thicknesses of 100, 300 and 500 nm (± 10 %) have been prepared by the LMU target factory using physical vapor deposition. Steel frames with holes of 3 mm diameter served as target holder for the gold foils. Additionally, the target laboratory of the GSI provided gold foils with thicknesses of 25 nm ($45 - 50\,\mu$g/cm^2) and 45 nm ($85 - 95\,\mu$g/cm^2) on steel frames with larger diameters. The targets have been cleaned radiatively by two green cw lasers at a wavelength of 532 nm. The very poor beam profile of the heating laser with a power of 4 W, which was acquired as a consequence of the findings of the TPW beamtime, cancelled out the advantage gained by the higher output power compared to the previously used 1 W heating laser. Therefore, the latter has also been installed as support for the target heating. The laser with the higher output power

[12] http://www.altechna.com, Product ID: CM-1-OS-2-0254-5-[6R27-63]

[13] A transmission of (72 ± 1) % through the beamline [166], a reflectivity of (70 ± 5) % of the plasma mirror [167] and an uncertainty of ± 5 % for the laser pulse duration have been assumed for the intensity calculation.

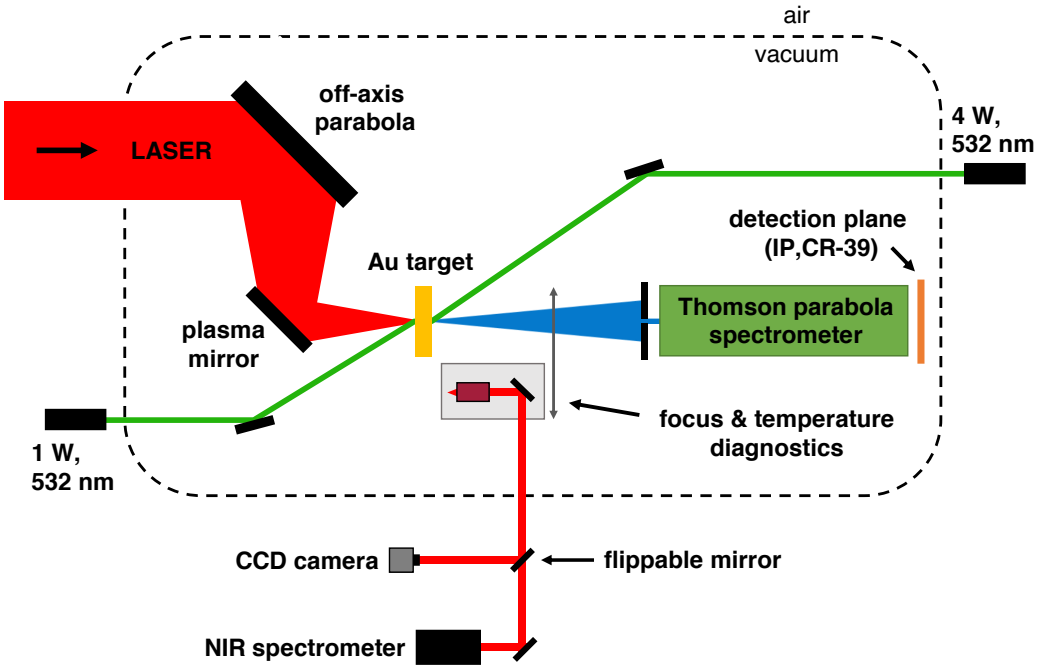

Figure 4.15: Schematic of the experimental setup at the PHELIX laser.

was focused onto the front side of the foil, facing towards the ion diagnostics, while the laser with the lower output power was heating the rear side. A simultaneous irradiation of both front and rear side turned out to provide the best heating efficiency, which led for two shots even to the desired total removal of the proton signal in the energy range detectable by the applied ion diagnostics.

As suggested in Sec. 4.1.5, the thermal spectrum measurement was included in the focus diagnostics. A Mitutoyo 20x Plan Apo NIR objective collected the thermal radiation from the irradiated target. The signal was guided to the outside of the vacuum chamber through a vacuum window. By means of a flippable mirror, it could be selected either to measure the thermal radiation emitted from the target with the NIR spectrometer or to inspect the target surface with a CCD camera, which was also used for focus diagnostics. As could be observed by using this camera, an increase in the laser power led to a flattening of the gold foils and a substantial removal of dust particles on the foil surface. Drifts of the foil position out of the focal plane of several tens of μm due to the deformation/flattening of the gold foil could be monitored and corrected by this optical surveillance. The point of melting was clearly recognizable on the camera images, when the laser heating exceeded the melting point of gold (1064 °C), as the foil surface started swirling until small, fast-growing holes have been formed. A reliable online calculation of the temperature values

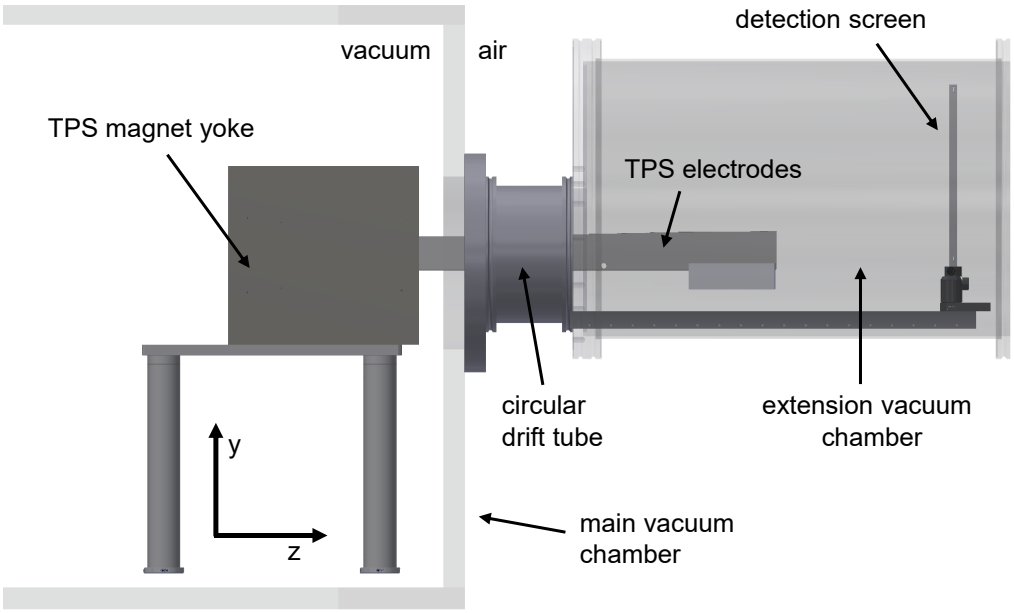

Figure 4.16: An extension vacuum chamber has been connected to the main vacuum chamber of the PHELIX laser via a 100 mm long drift tube with a diameter of 160 mm in order to fit the heavy ion TPS into the vacuum. The electrodes reach from the TPS magnet yoke in the main chamber into the extension chamber, where also the detection screen is placed. The extension chamber has been accessed through a blank flange after each laser shot for the replacement of the used offline detectors (CR-39 and IP). The dimensions of the vacuum chambers and the distances shown in the image are not to scale.

from the heat spectrum was not feasible during the beamtime. However, the shape and amplitude of the thermal spectrum reacted similarly on an increase of the laser power for different foils with varying thickness. Thus, the targets were heated empirically as close as possible to the melting point by carefully increasing the laser power, while watching the thermal spectrum and regularly checking the surface images using the microscope camera.

As ion diagnostics, the newly developed heavy ion TPS described in Sec. 3.3.3 has been installed at the direction of target normal. It has been equipped with a pinhole of 100 μm diameter at a distance of 72.2 cm to the target, resulting in a detected solid angle of 1.5×10^{-5} msr. The detection screen has been positioned at a distance of 86.4 cm to the pinhole, which ensured a sufficiently long drift distance while optimally using the size of the detection screen. The length of the PHELIX laser vacuum chamber was not sufficient for the TPS due to the length of the electrodes and the required drift distance for the ions before their registration in the detection screen. Therefore, as displayed in Fig. 4.16, an extension vacuum chamber was connected to the main chamber via a circular

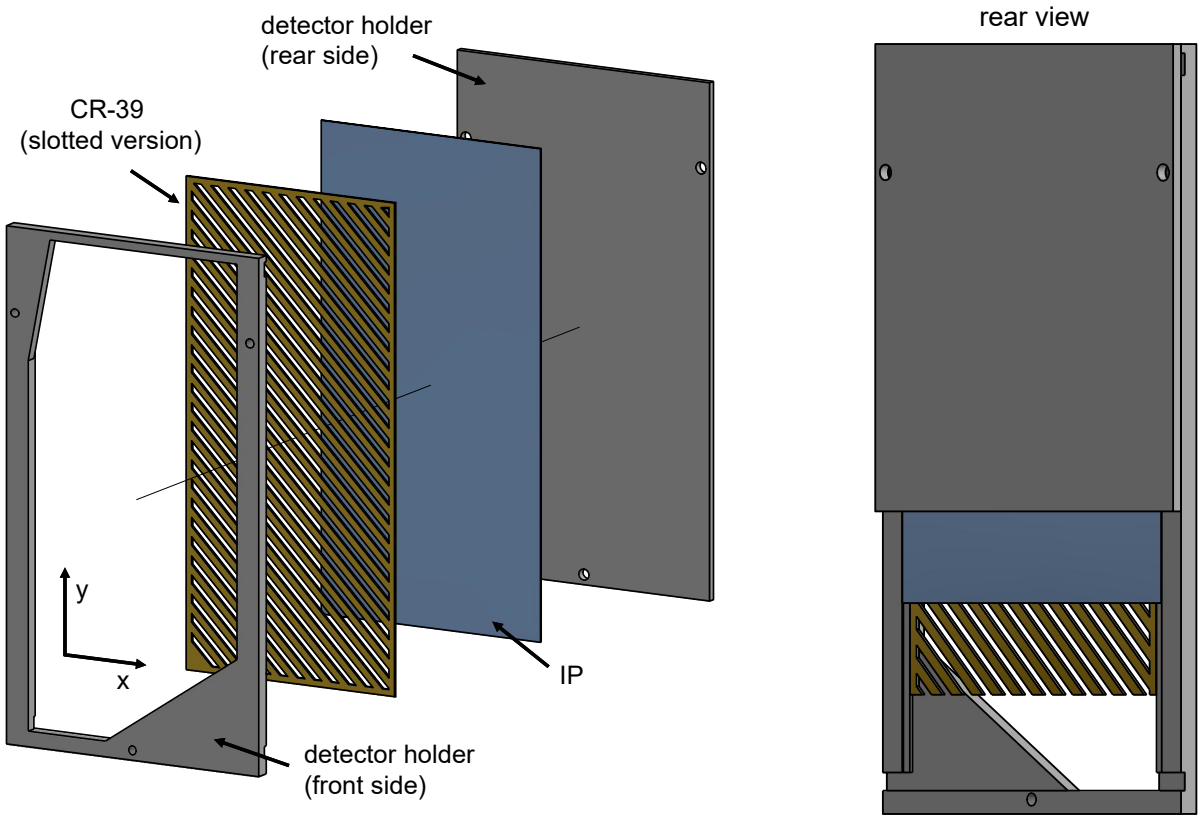

Figure 4.17: Detector unit used as ion diagnostics in the heavy ion TPS. Left: view from the front, right: view from the rear. IP (blue) and CR-39 sheets (yellow) are used as passive detectors. The skew edges in the left top and right bottom corners (view from the front) serve no other purpose than to support the CR-39 sheets. Tilting of the detectors within the detector holder is prevented by indentations, which exactly fit the detector dimensions, visible in the bottom of the rear view on the right side of the figure.

drift tube with a diameter of 160 mm and a length of 100 mm. The TPS electrodes start within the magnet yoke and reach into this extension chamber, where also the detection screen is placed. The positively charged ions will be deflected upward by the magnetic field of the TPS. Hence, ions with higher energies will hit the detection screen at lower y positions, while the trajectories of lower energetic ions, which generally experience a stronger deflection, will end up at the detector at higher y positions. Below a certain kinetic energy (depending on the respective particle species and charge state), the ion trajectories start to intersect with the drift tube. Thus, the circular shape of the rear edge of the drift tube will be projected onto the detector images. This will be of relevance in Sec. 4.2.2 for the consistent alignment of CR-39 nuclear track detector sheets from different

laser shots along the y dimension.

Fig. 4.17 shows the detection screen used in the heavy ion TPS with IPs[14] and 1 mm thick CR-39 track detectors[15] as passive ion detectors. The IPs have been scanned 30 minutes after irradiation with a GE Typhoon FLA 7000 IP scanner. The IPs and CR-39 sheets have been positioned by the shown detector holder, which consists of an aluminum plate at the rear and an aluminum frame at the front side. The detector holder was positioned with two kinematic bases, which enabled the reproducible placement of the detector holder after the passive diagnostics have been exchanged. The IPs have a size of 10×20 cm^2, while the CR-39 sheets are slightly smaller with a size of 9.5×20 cm^2. Two versions of CR-39 detectors have been used in the experiment: a conventional, simple sheet without any modifications and a slotted version (see Fig. 4.17) with 2.5 mm broad slots without material, that are separated by 3 mm broad stripes of CR-39 material. The latter version has the advantage that gold ions can be alternately detected by both CR-39 and IP, which enables the calibration of IPs for the detection of gold ions, which is, however, beyond the scope of this thesis. The detectors are aligned by indentations with the respective widths in the front side of the detector holder (see the rear view of the detector holder at the right side of Fig. 4.17), which prevents a tilt of the detectors within the holder. As can be seen in the figure, the only left degree of freedom is a displacement along the y dimension. The skew edges at the bottom right and top left corners (seen from the front) of the front side of the detector holder serve as locating surfaces, on which the CR-39 sheets rest. In contrast to the CR-39 sheets, the IPs have been wrapped in 12 μm thick aluminum foil for the protection from ambient light, which is why they did not fit exactly into the dedicated indentation, leading to slight tilts of the IP with respect to the intended position in the detector holder. A further rotational error could have been introduced by the positioning of the IPs in the IP scanner. For this reason, the shadow of the "rails" in the front plate supporting the IPs and the mentioned locating surfaces for the IP detectors are used for a rectification of the IPs, as will be described in Sec. 4.2.2.

[14]Storage Phosphor Screen BAS-IP TR 2040 E from Cytiva, formerly GE Healthcare Life Sciences, http://www.cytivalifesciences.com

[15]The CR-39 nuclear track detectors have been manufactured by Track Analytics Systems Ltd. (TASL), http://www.tasl.co.uk

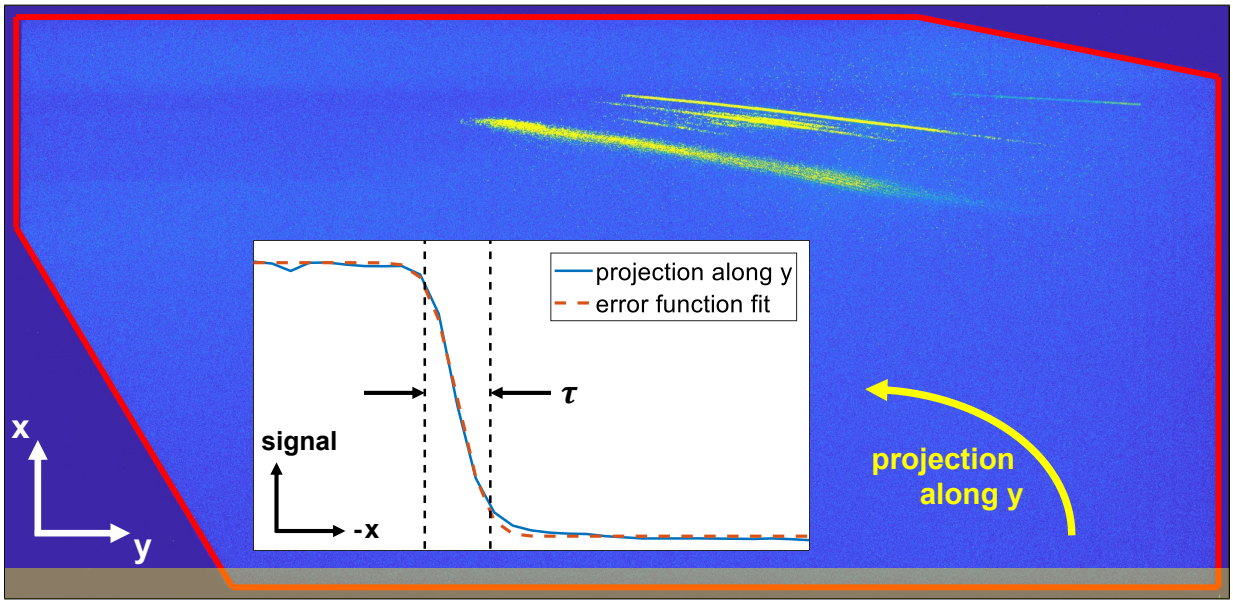

Figure 4.18: The IP images are rectified using the shadow of the detector holder (red polygon). The region inside this polygon was exposed to the signal plus background radiation. The latter was blocked by the holder in the outside area (dark blue area). The alignment of the IP images along the direction of magnetic (y) and electric (x) deflection, respectively, is ensured by fitting an error function to the projection along a clearly visible, horizontal edge (here the bottom edge, as indicated by the orange region) and minimizing the width τ of the error function.

4.2.2 Data Processing

Rectification of Image Plates

For a consistent data analysis of the various diagnostics elements (IP, CR-39 track detectors), the signals from different shots, and thus different passive detection media, need to be aligned in the same, comparable way. While the detector holder is mounted on two kinematic bases, ensuring its precise, reproducible positioning, the orientation of the IPs in this holder as well as in the IP scanner for the subsequent signal readout may vary slightly from shot to shot, as discussed in the previous section. Hence, the IPs need to be rectified before using them for data analysis. Typically, as described in Sec. 4.1.3 for the TPW experiment, the zero point serves as fixed rotation point and the detector is finally aligned by superposition of the measured TPS curves with the predicted theoretical parabolas. However, for this beamtime, the zero point could not be identified on the detector screens. The occurrence of the zero point was actually expected, as a free optical path from the TPS pinhole to the detection screen was ensured. Its absence complicates the rectification of the IPs.

As the detector holder is precisely positioned by kinematic bases, the shadow of its frame may be used to align the IP detector images. Fig. 4.18 shows an IP image, which was recorded without CR-39 in front of it. The red polygon corresponds to the detector holder frame, which encloses the irradiated area. Almost no background signal was detected outside of this region, since any kind of radiation was blocked by the detector holder frame. The detector holder was aligned such, that the vertical red lines on the left and right side in the figure (which corresponds to the bottom and top edge of the detector holder frame) matched the horizontal orientation of the magnetic and electric fields of the TPS. Thus, the IPs need to be rotated until the edges of the detector holder frame shadow, which is always visible on the images, are in vertical (for the left und right red lines) or horizontal (for the top and bottom red lines) orientation. Then it is ensured, that the deflection due to the magnetic field is (only) along the y dimension and the deflection due to the electric field (only) along the x dimension.

In order to align the IP images in the respective orientation, the projection along a clearly visible, horizontal edge has been taken. In Fig. 4.18, the projection along the bottom edge was chosen, as indicated by the yellow area on the bottom, and displayed in the inset graph. An error function,

$$\text{signal} = a \cdot \text{erf}\left(\frac{x-b}{\tau/2}\right) + c, \tag{4.1}$$

was fitted to this projection and its width, here defined by τ, was minimized. In this case, the transition from the irradiated region towards the unexposed area is as short as possible, meaning that the edge is oriented along the direction of the projection. By this, all analyzed IP images have been rotated into the same orientation. In a last step, they are moved into the same position. This is done by fitting error functions to the projections of a horizontal and a vertical edge and correcting for the respective axial displacement b from Eq. (4.1). As a result, the absolute x and y coordinates of all IP images are the same and directly comparable, within an estimated uncertainty of ± 1 pixel.

Digitization of CR-39 detector sheets

The CR-39 sheets have been etched in six-molar NaOH for 45 minutes and 80 °C and afterwards scanned with the autofocus Zeiss Axiotron II microscope and the pattern recognition software SAMAICA. The software fits ellipses to the registered structures and returns the coordinates of the pit positions. Additionally, information about the ellipses' central bright-

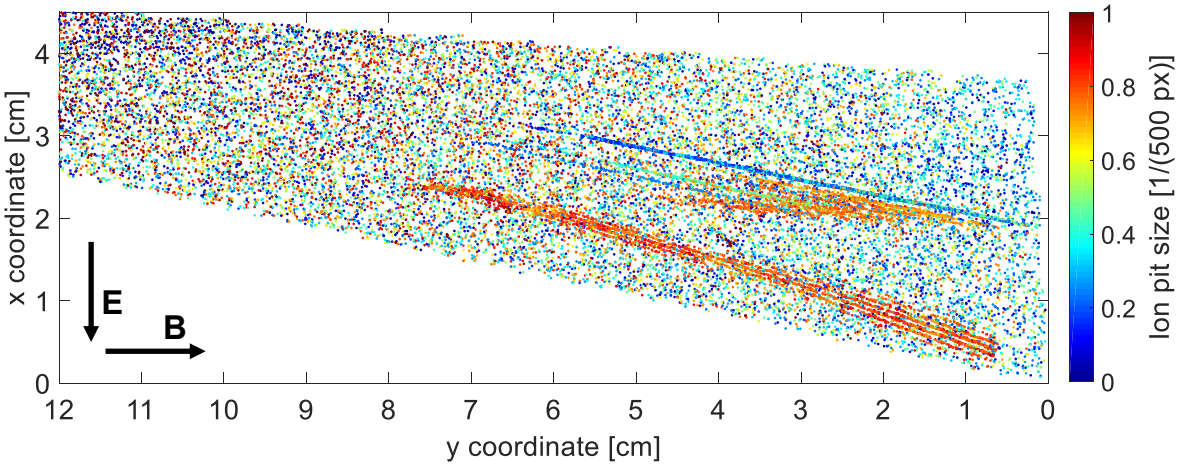

Figure 4.19: Result of the scanning process with the autofocus Zeiss Axiotron II microscope and the pattern recognition software SAMAICA. The colourmap refers to the size of the ion pits. The data is taken from a shot on an unheated 500 nm thick gold foil. The directions of deflection due to the electric field **E** and the magnetic field **B**, respectively, are indicated by the arrows.

ness, about their ratio of minor to major semi-axis and about the area which is enclosed by the ellipses is saved. The result of such a scan with SAMAICA is exemplarily shown in Fig. 4.19. The colourmap in the figure refers to the enclosed area and, hence, visualizes the ion pit size. Clearly, individual curves are visible on the scanned CR-39 image, which can be attributed to ions with different charge-to-mass ratios, as typical for TPS measurements. However, the signal is superimposed by a noisy background all over the image, which impedes the data analysis.

To minimize this background, the various fit result parameters of the CR-39 scan can be exploited as filter conditions. The fit parameters are expected to behave comparable for ion pits of the same species. Histograms of the three parameters (enclosed area, central brightness and semi-axis ratio) are plotted exemplarily for a shot on a 500 nm thick, unheated gold foil in Fig. 4.20(a)-(c). Both the central brightness and the ratio of minor to major semi-axis show one distinct peak, which contains the majority of the ion signal. As expected for almost normally incident ions, the peak for the ratio of minor to major semi-axis approaches 1, which means that the ion pit ellipses are close to perfect circles. The enclosed area exhibits four peaks. The lowest one around zero originates most likely from very small, noisy structures, which are not related to particle impacts. The other three peaks suggest the occurrence of three different ion species, as the pit size is dependent on the particle mass. The peaks are broadened due to the expected poly-energetic,

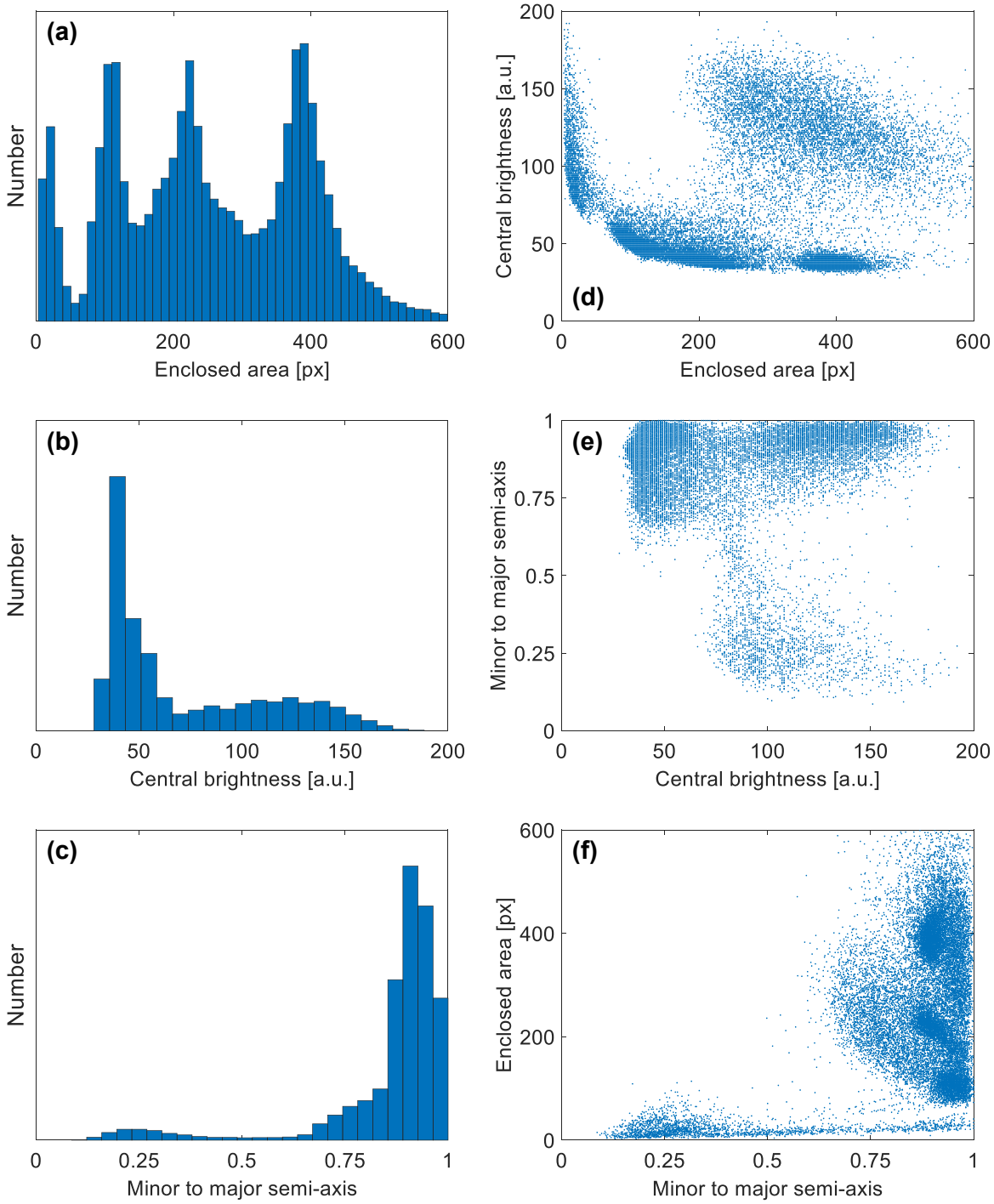

Figure 4.20: (a) - (c) Histograms of three selected pit parameters resulting from automatic elliptic fits applied by SAMAICA to scanned CR-39 data. (d) - (f) Correlations can be identified when the pit parameter are plotted versus each other. The data is taken from a shot on an unheated 500 nm thick gold foil.

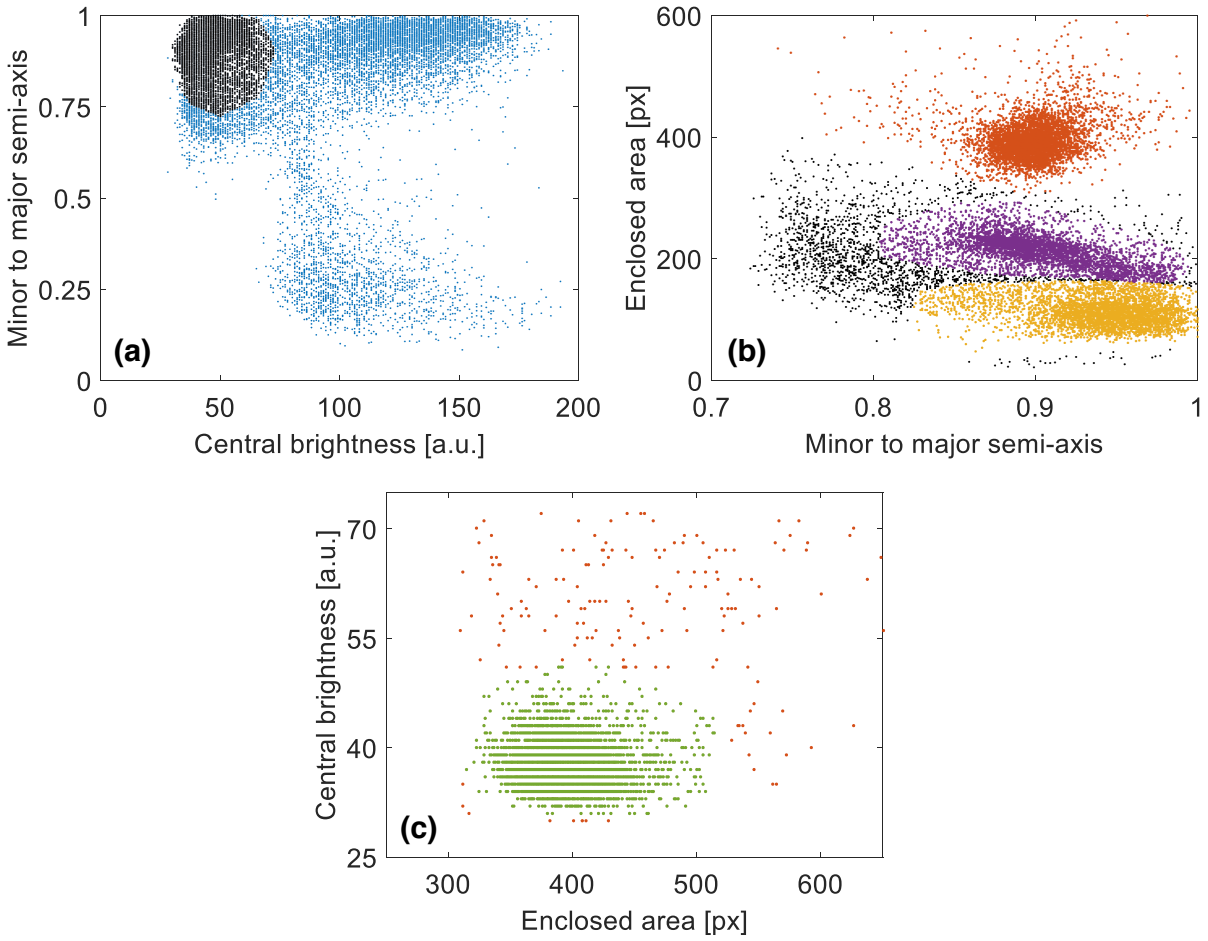

Figure 4.21: The background of the scanned CR-39 detector data can be reduced if only pits are accepted, whose ellipse parameters lie within certain boundaries, that can be attributed to ion signal. In total, three filtering stages have been applied to the CR-39 data. The accepted data points in (a) are drawn in black. In (b), the ion species can be separated by their pit sizes: orange refers to gold ions, violet to oxygens and yellow to carbons. (c) shows the last filtering step for the example of gold ions. The accepted data points are displayed in green. The two-dimensional gate conditions in each step have been defined by hand. The selected regions around the parameter correlations were chosen as small as possible in order to exclude a maximum number of background data points, but large enough that no correlated patterns related to the observed ion curves – especially for heavy ions – appeared in the discarded data (see Fig. 4.22(a)).

exponential ion energy distribution, resulting in slightly different pit sizes, but also due to small uncertainties of the ellipse fit parameters.

In Fig. 4.20(d)-(f), correlations between the parameters are plotted in order to identify different signal signatures and enable efficient filtering. Clearly, visible correlations confirm the accumulation of signal in certain parameter regions. Filtering these correlations by two-dimensional gate conditions in the offline analysis significantly reduces the background

signal, as exemplarily shown by Figs. 4.21 and 4.22. All analyzed CR-39 images have been filtered in a three-fold sequential procedure as described in the following for the example of the 500 nm thick, unheated gold foil. First, in Fig. 4.21(a), the semi-axis ratio is plotted against the central brightness. The region containing all ion signals is identified by hand (drawn in black) and the respective data points within this region are extracted. Thereby, the boundaries have been chosen as small as possible to exclude a maximum number of background data points. However, the selected region has to be large enough that no correlated patterns related to the observed ion curves – in particular for heavy ions – appeared in the discarded data, which would indicate the false identification of good ion data as background events. After this first filtering stage, the corresponding enclosed area parameters are plotted against the minor-to-major semi-axis ratios, as shown in Fig. 4.21(b). Doing this, a separation of different ion species is possible: the heavy gold ion data points can be identified as the data points drawn in orange, while the oxygen ion data is contained in the area marked by violet points and carbon ion data are localized in the region showing the yellow points. Such a clear separation between oxygen and carbon ion parameters, as displayed here, was not observed for all shots. Therefore, it was usually only differentiated between light and heavy ions. In a last filtering step, shown in Fig. 4.21(c) for gold ions, the enclosed area is plotted against the central brightness and, again, the data points identified nearby the correlated area were extracted.

All discarded data points, representing the identified background contribution, are shown in Fig. 4.22(a). The control of the discarded data points after each filtering stage was essential for the manual choice of the boundaries, as these were chosen as close as possible around the correlation regions, however, without discarding real ion data points. The resulting light ion signal is plotted in Fig. 4.22(b) and the heavy ion signal, which is lateron used for the determination of the quantitative gold ion spectra, is displayed in Fig. 4.22(c). It is striking that, besides the expected gold ion curves in the lower part of the image, large-sized pits have been measured in the higher charge-to-mass ratio region (towards larger x coordinates), where exclusively light ions would be expected. This has been observed for all shots and will be further discussed in Sec. 4.2.7. However, a convincing and consistent explanation for this phenomenon still has to be found.

After the ion signal has been discriminated from the background, the correct superposition of the scanned CR-39 data with the IP images has to be ensured. The orientation and x position was already defined by the design of the detector holder, as the x dimension of the CR-39 sheets fitted exactly into the detector holder (top and bottom red lines in

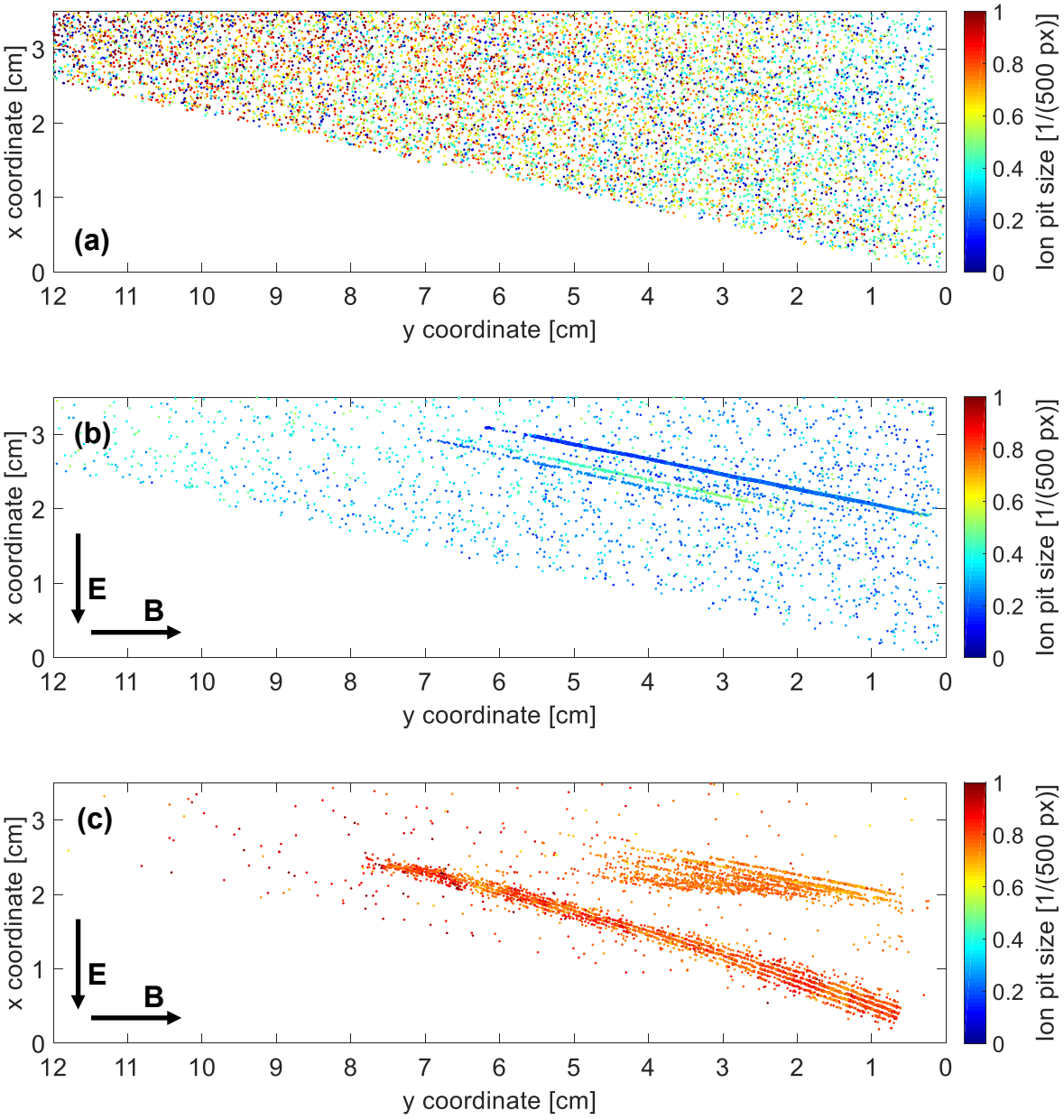

Figure 4.22: CR-39 data points from an unheated shot on a 500 nm thick gold foil after the filtering process as displayed in Fig. 4.21. After each filter stage, the discarded pits are inspected. In (a), all rejected data points are shown, clearly indicating the uncorrelated distribution of ion tracks. (b) shows the filtered light ion signal and (c) the heavy ion signal originating from large-sized pits. The directions of deflection due to the electric field **E** and the magnetic field **B**, respectively, are indicated by the arrows.

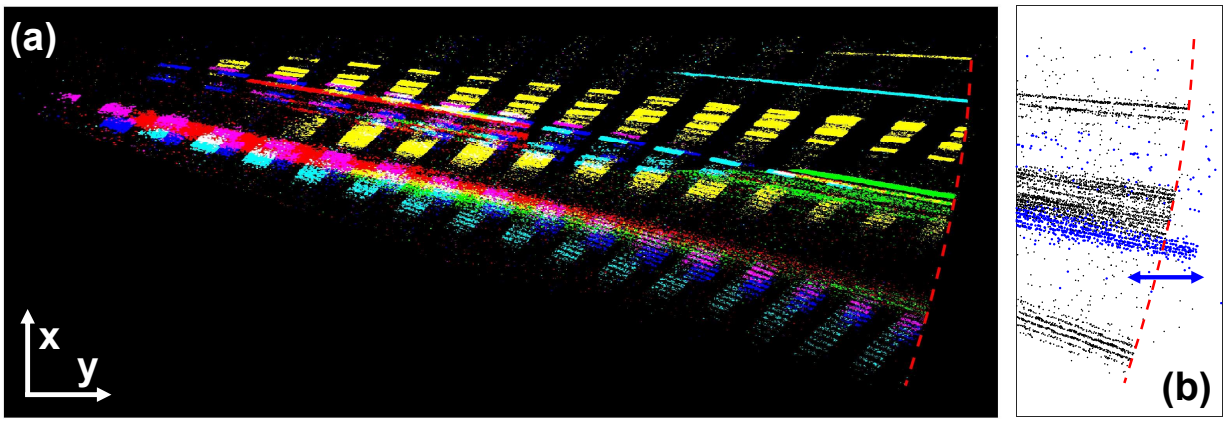

Figure 4.23: (a) Cumulated ion signal from six different laser shots measured on IP. Each shot is displayed in different colour. The laser-accelerated ions traversed a short drift tube before they hit onto the detection screen. Below certain energies, the trajectories of the ions, which are upward deflected by the magnetic field of the TPS, intersect with the drift tube. Thus, the circular shape of the tube's rear edge was projected onto the detector. This can be used for an exact positioning of the CR-39 sheets along the y dimension. The slotted structure for some shots is due to CR-39, which was partly covering the IP. The circular cutoff is clearly visible and has been traced by hand (red dashed line).
(b) Heavy ion data points from six different shots on CR-39. The data from five shots (black) have already been aligned to the circular cutoff curve. One shot still needs to be shifted to its correct position (blue). The y shift of the shown data in blue is slightly exaggerated for a better illustration.

Fig. 4.18). Since the detector holder was precisely and reproducibly positioned by kinematic bases, it can safely be assumed that the x position and the orientation of the CR-39 sheets match sufficiently well with the projection of the detector holder on the IPs. The only remaining degree of freedom is the positioning along the y-axis. The detection screen was mounted in an extension vacuum chamber, that was attached to the main chamber using a tube with a diameter of 160 mm and a length of 100 mm. The magnetic field of the TPS deflected the ions in upward direction. Naturally, below certain ion energies, the deflection causes the ion trajectories to intersect with the drift tube. Thus, the circular shape of the edge of this tube was projected by the ions onto the detector as a round, geometric cutoff curve. In Fig. 4.23(a), the ion signal from six different laser shots on IPs is shown, each shot is plotted in a different colour. The periodic structure, which is visible for some shots, is due to slotted CR-39, which was partly covering the IPs. The red, curved dashed line visualizes the cutoff curve, which was traced manually from the data on the IPs. This cutoff curve can be used to find the correct position of the CR-39 data by shifting along the y-axis, as shown in Fig. 4.23(b). The black points correspond

to the heavy ion data from five different shots on CR-39 that already have been shifted to their correct y position. The blue points visualize the data from a sixth shot on CR-39, which is not yet on its correct y position. By this, the CR-39 sheets can be aligned with an accuracy of about ± 5 pixels along the y dimension.

4.2.3 Energy Calibration

The magnetic dipole field of the TPS is calibrated using two different proton energy cutoffs by introducing differently thick copper layers in front of the detector for two consecutive shots. The magnetic field strength can be concluded from the distance between the positions of these proton energy cutoffs along the energy-dependent dimension y. In panels (a) and (b) of Fig. 4.24, the respective parts of the proton traces behind 998 ± 1 μm and 793 ± 1 μm copper are shown. The respective energies, that protons need to pass through the copper material and the subsequent aluminium foil with a thickness of 12 μm, that was wrapped around the IPs for ambient light protection, have been determined using the Monte-Carlo-based software TRIM [168]. By simulating 99999 particles each, it was found that protons with energies of 22.73 and 19.92 MeV reached on average to the end of the aluminium foil. Therefore, these energies are taken as proton energy cutoffs for the energy calibration. Regarding the respective average straggling of 37 and 31 μm for protons with these kinetic energies, the thickness uncertainties of the copper layers have been neglected in the following.

The proton traces are broadened due to scattering in the copper, which complicates the identification of the exact cutoff positions. Hence, the images of these traces were projected along the non-energy-dependent x dimension, as illustrated in blue colour in Figs. 4.24(c) and (d). Error functions as in Eq. (4.1) have been fitted to the relevant parts of the projections (yellow) and are drawn in orange in the figures. The proton energy cutoff positions are defined to be at the inflection points of the fitted error functions, where the signal has decreased to a level of 50 % of the maximum signal with respect to the background level. These cutoff positions are indicated as black dotted lines in the figure. The amplitude of the error function fit strongly depends on the arbitrarily chosen data range (yellow in the figure): if more (less) data points toward lower (higher) pixel values are included into the fit, the amplitude will be lower (higher). Nevertheless, the level of the background signal will not change by varying the data range and the error function will still resemble the shape of the decaying signal. If the amplitude is increased (decreased) by a different choice of the data point range, the position of the inflection point moves

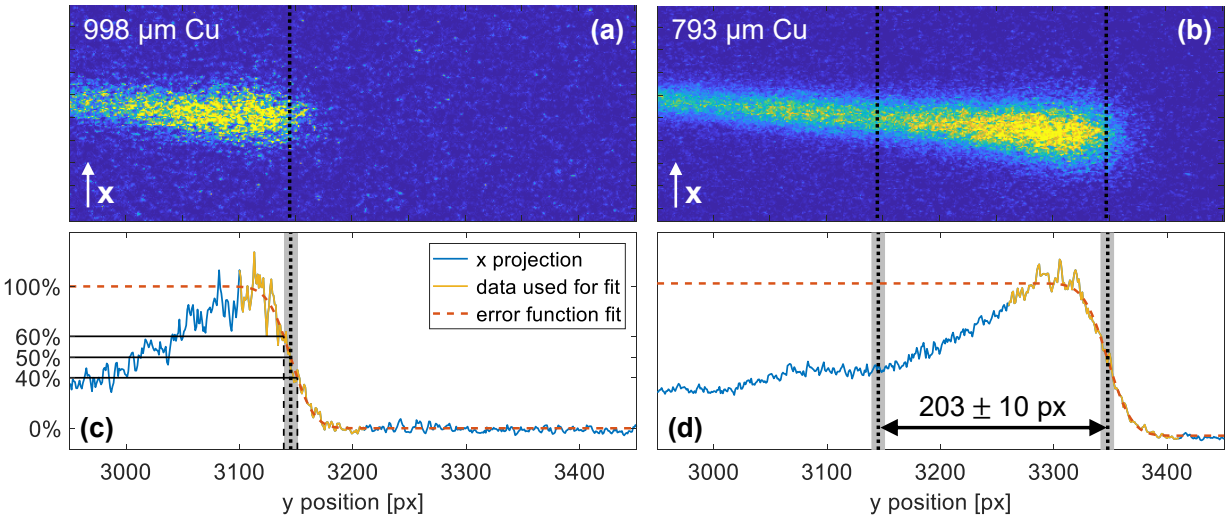

Figure 4.24: Panels (a) and (b) show the proton traces after passage through 998±1 and 793±1 μm thick copper layers, respectively. They have been recorded by IPs without preceding CR-39 sheets and aligned as described in Sec. 4.2.2. The corresponding projections onto the y-axis are plotted in blue in (c) and (d). The data shown in yellow has been used to fit an error function (orange) in order to define the energy-dependent y position of the proton cutoff, which is defined as the inflection points of the error functions (black dotted lines). This position is highly dependent on the data range used for the error function fit (yellow). Therefore, an error margin is defined for the inflection points and shown here by the grey bars. As indicated in (c), this error margins are defined by the y positions, at which the error function fits are between 40 and 60 % of the maximum signal. In (d), the cutoff position from (c) is also indicated, in order to visualize the distance along the energy-dependent axis y between the two proton energy cutoff points, which is used for the energy calibration of the TPS.

leftwards (rightwards), which needs to be accounted for. Therefore, the actual position of the inflection point is assumed to be within the range between $40 - 60\,\%$ of the maximal signal level (see Fig. 4.24(c)). Including the IP positioning uncertainty of ± 1 pixels, as stated in Sec. 4.2.2, the cutoff positions of protons with energies of 22.73 and 19.92 MeV have been by that determined to be at 3144 ± 5 and 3347 ± 5 pixels, respectively. Thus, the distance between the intersection points of the two proton trajectories with the detection plane is

$$d = 203 \pm 10 \text{ px} \tag{4.2}$$

in the direction of magnetic, energy-dependent deflection (along the y-axis).

Knowing the distance d, a calibration factor for the magnetic field distribution, which has already been simulated during the design of the heavy ion TPS (see Sec. 3.3.3), can be determined. Protons with the two energy values have been tracked using the tracking code from reference [139] based on the MATLAB function `ode23` applying the Runge-Kutta

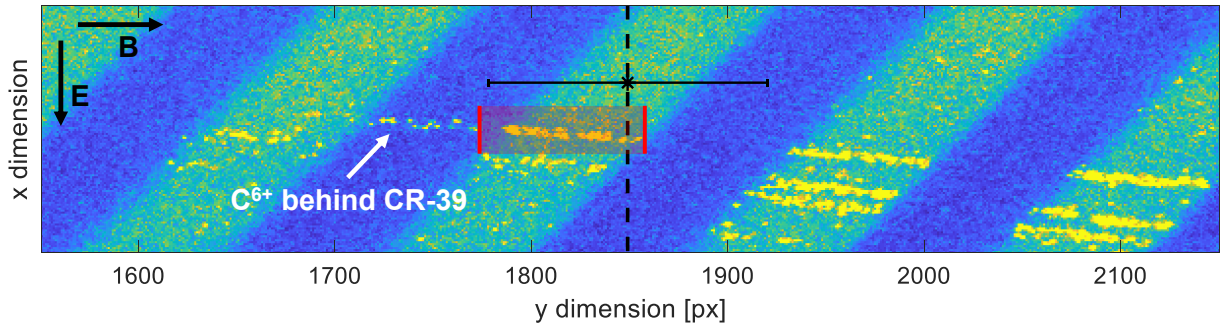

Figure 4.25: Section of a raw data image taken with an IP. The dark blue stripes are from a slotted CR-39 sheet in front of the IP. Ion signals are visible in form of yellow stripes. The topmost trace could be identified as C^{6+}. Special about this shot is, that the carbon ions were energetic enough to penetrate the 1 mm thick layer of CR-39, which requires a minimum energy of 18.87 MeV/u. The red area illustrates the range (1775 to 1857 pixels), in which the position of this carbon ion energy cutoff could be. This can serve as an additional data point for the energy calibration. The vertical dashed black line indicates the y position, at which carbon ions with the stated cutoff energy would impinge when tracking using the calibration value given by Eq. (4.3), which is well within the allowed y range. However, the error bar for this position towards higher y values exceeds this allowed range. Therefore, the error margin of the calibration factor b may be adapted for physical reasons, as carbon ions with these energies would be visible behind the CR-39. As indicated on the top left, the magnetic field deflected the ions to the right (energy-dependent axis), while the electric field deflected in downward direction.

algorithm. A calibration factor b for the magnetic field has been introduced and iteratively changed, until the distance between the two intersection points of the respective proton trajectories with the detection plane was equal to the value from Eq. (4.2). It was found that the magnetic field needed to be corrected by a factor of

$$b = 0.903 \pm 0.040. \tag{4.3}$$

This calibration factor can be confirmed by an additional shot, for which carbon ions were detected on an IP after passage through a 1 mm thick layer of CR-39, as shown in Fig. 4.25. The IP was covered by a slotted sheet of CR-39, which explains the stripes without ion signal in the figure. Dark blue parts were covered by CR-39, the remaining parts were directly exposed to the impinging ions (except for a 12 μm thick aluminum foil protecting the IP from ambient light). The yellow lines are ion traces, with the topmost being the C^{6+} curve, which starts to appear even behind CR-39 at a certain energy (the energy increases towards the left of the figure, with decreasing y). The cutoff energy for carbon ions for the passage through 1 mm of CR-39 (and a subsequent layer of 12 μm thick

aluminium) has been simulated as described above with TRIM [168] and was determined to be at 18.87 MeV/u [133]. The exact cutoff point cannot be determined on Fig. 4.25, as it might be at a position, where the IP was not covered by CR-39. Therefore, as indicated in red in the figure, only a range can be defined, within which this carbon energy cutoff must be located: 1775 to 1857 pixels.

This additional data point can be used for a validation of the calibration factor b, as carbon ions with the cutoff energy must impinge at y positions within the indicated red region. For this, the C^{6+} energy cutoff position is calculated via the tracking code and extracted as relative distance to the y position of the 19.92 MeV proton energy cutoff. The absolute y position of the C^{6+} energy cutoff on the detector plane can be calculated knowing the position of this proton cutoff, which was given above. Indeed, as indicated by the black dashed line in the figure, which shows the impact position of carbon ions, the tracking through the magnetic field distribution, which has been calibrated using the factor b delivers plausible results. However, the error bar towards increasing y exceeds the allowed range for the impact position of these carbons ions. This is physically meaningless, as carbon ions would have been detected at these positions behind the CR-39. Therefore, the error for the calibration factor b may be adapted and reads now

$$b = 0.903^{+0.040}_{-0.007}. \tag{4.4}$$

Based on this calibration factor and the y position of the 19.92 MeV proton cutoff, the gold ion trajectories have been tracked for charge states ranging from 30 to 79 and for energies between 0.5 and 10 MeV/u. For each charge state, all energy values can be assigned to distinct y coordinates on the detector plane, which is fundamental for the determination of the gold ion energy spectra, once the charge states have been identified. This calculation has been repeated for the outside margins of the error range ($b = 0.943$ and $b = 0.896$). This will be used to determine the spectral error due to the magnetic field uncertainty. The uncertainty of the proton energy cutoff point, which is used as fixpoint for the superposition of the calculated y positions with the experimental data, will be accounted for as additional positioning error, as will be described in Sec. 4.2.5.

4.2.4 Identification of Gold Charge States

Usually, the TPS ion traces are theoretically calculated using Eq. (3.7) and are afterwards superimposed with the measured data in order to identify the mass-to-charge ratios of the

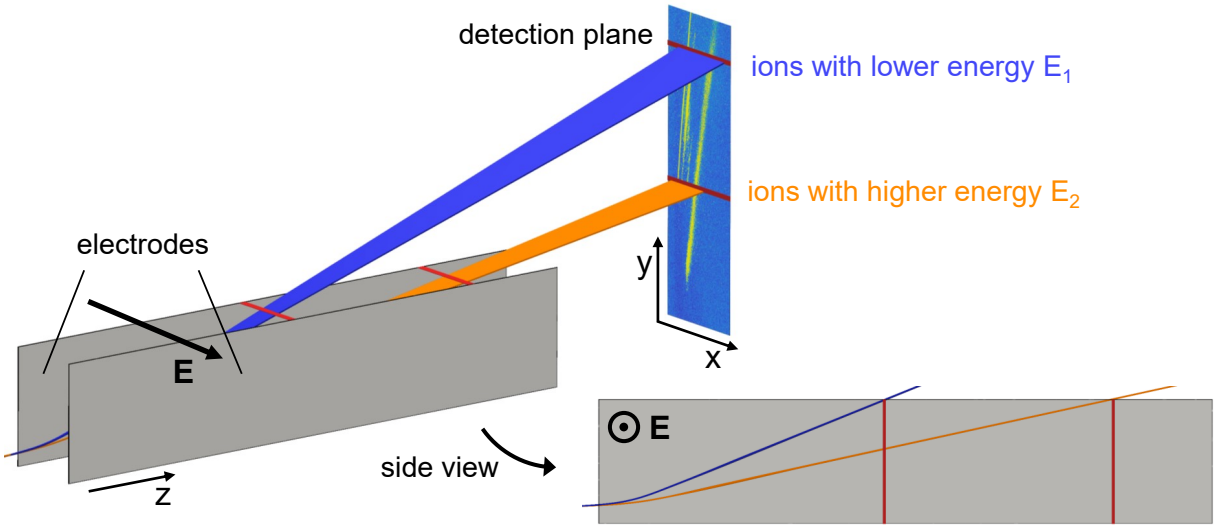

Figure 4.26: Schematic drawing of the ion deflection in the heavy ion TPS. Lower-energetic ions leave the electric field earlier than higher-energetic ions. Therefore, the parabolic TPS equation Eq. (3.7), which requires that all ions have experienced the same fields along the same lengths, is not applicable to this situation. However, this prerequisite is fulfilled for all ions impinging at the detector at a certain y coordinate (meaning they leave the electric field at the same position z). The deflection x due to the electric field is thus linearly dependent on the mass-to-charge ratio m/q, assuming a constant electric field E.

individual parabolas, as it was done in Sec. 4.1.3. The computed parabolas form also the basis for the two-dimensional iso-energy, iso-charge-state mesh, which is necessary for the generation of the ion energy spectra. Due to the electrode geometry of our heavy ion TPS, which allows some ions to escape from the electric field earlier than others, Eq. (3.7) cannot be directly applied anymore. In case of inhomogeneous field distributions, the particles need to be tracked through the simulated and/or measured magnetic and electric fields before the ion curves can be overlaid with the detector image, as discussed in Sec. 3.3.1 for a WASP. However, this approach failed for the analysis of this experiment's data, which motivated a closer look into the behaviour of the ion curves recorded on the detectors.

As mentioned above, the inhomogeneity in case of our heavy ion TPS is due to ions with lower energy leaving the electric field earlier than higher-energetic ions, as drawn schematically in Fig. 4.26. Thus, the distance l_E in the electric field as well as the subsequent drift length d_E are depending on the respective ion energy, which is why Eq. (3.7) is clearly not applicable to this case. However, all ions registered at a specific y coordinate on the detection plane, independently of their mass and charge state, traversed both the same length of the electric field, as demonstrated by the side view in Fig. 4.26, followed by the for both

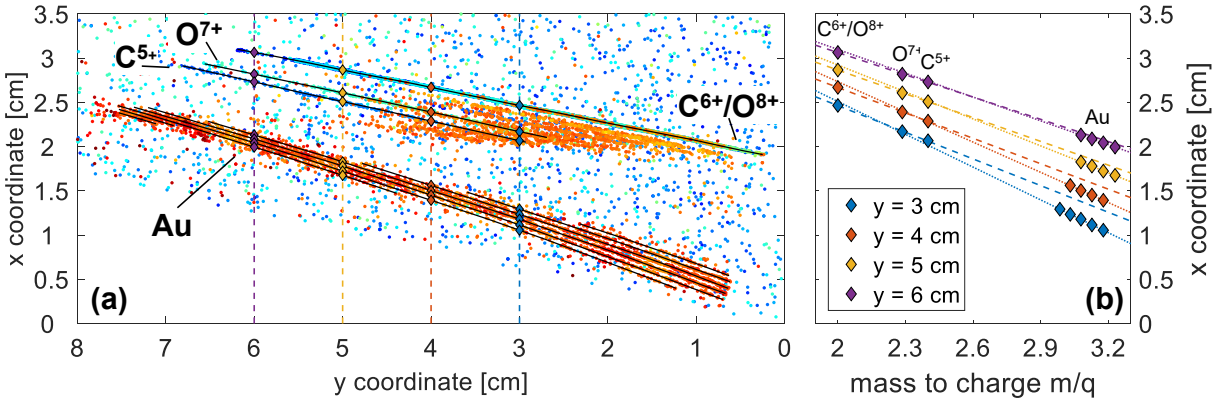

Figure 4.27: (a) Data acquired with CR-39 track detectors from a laser shot onto a 500 nm thick, unheated gold foil. The individual ion curves have been traced by hand, generating the solid black lines. The light ions can directly be assigned to distinct mass-to-charge ratios, supported by the different sizes of the carbon and oxygen ion pits on the CR-39 sheets. The x coordinate, which relates to the deflection x_{defl} due to the electric field, has been plotted in (b) versus the mass-to-charge ratio for four selected y positions marked by vertical dashed lines in panel (a), which should result in a linear relationship according to Eq. (4.5). However, linear fits through light (dashed) and heavy (dotted) ion points show significantly different slopes, which is in contradiction to the theoretical prediction.

same drift length. Also, the experienced magnetic field and the corresponding distances l_{B} and d_{B} are approximately the same for all ions at a given y coordinate. Assuming a constant electric field E between the electrodes, Eq. (3.7) reduces to a linear dependency of the ion deflection due to the electric field, x_{defl}, merely on the mass-to-charge ratio m/q,

$$x_{\mathrm{defl}} = \left(\frac{y_{\mathrm{defl}}^2 \cdot l_{\mathrm{E}} E \left(d_{\mathrm{E}} + \frac{l_{\mathrm{E}}}{2} \right)^2}{l_{\mathrm{B}}^2 B^2 \left(d_{\mathrm{B}} + \frac{l_{\mathrm{B}}}{2} \right)^2} \right) \cdot \left(\frac{m}{q} \right) = c \cdot \left(\frac{m}{q} \right) \tag{4.5}$$

with c being constant.

This simple relation is tested with the shot on a 500 nm thick, unheated gold foil, which is already known from Sec. 4.2.2. In Fig. 4.27(a), the individual ion curves have been traced by hand (black lines). The light ions could be assigned to distinct mass-to-charge ratios, supported by the different sizes of carbon and oxygen ion pits on the CR-39 sheets. The x coordinate has been taken at four different, equidistant y positions (marked in panel (a) by vertical dashed lines) and plotted against the mass-to-charge ratio in Fig. 4.27(b). It is important to note, that the x coordinate may not be mistaken with the deflection due to the electric field, $x_{\mathrm{defl}} = x_0 - x$, with x_0 being the offset of the x coordinate from the unknown zero point. Still, x is expected to behave linearly with the mass-to-charge ratio

m/q. The dotted lines are linear fits through the gold data points and the dashed lines visualize linear fits through the light ions data points. The mass-to-charge range for the gold ions, which are not known yet, has been chosen arbitrarily around the expected region, as the exact charge state values are not relevant for the main message of this figure: light and heavy ion data points are apparently not in a common linear relationship, which is in contradiction to Eq. (4.5). Instead, the deflection towards higher mass-to-charge ratios reduces. The most likely reason for this behaviour lies in the electric field, which collapsed after each laser shot, probably due to the negative influence of the EMP. The reduced deflection in the x direction is more pronounced for lower y values, which depict lower energetic ions in this case. As particles with lower energies experience the electric field for a longer period of time, they see on average lower fields than higher energetic particles and are less deflected, which is in agreement with the assumption of a collapsing field.

In order to compensate this and to identify the corresponding gold ion charge states, we allow for an additional nonlinear term and use the updated equation,

$$x = a \cdot \left(\frac{m}{q}\right)^2 + c \cdot \left(\frac{m}{q}\right) + d, \tag{4.6}$$

as a fit function for the data points in Fig. 4.27(b). The charges, which are assigned to the traced gold ion curves on the detector, are varied until the overall deviation of the data points from the fitted curve is minimized. As fits are naturally best for a high number of included data points, especially the regions with the maximum available information were considered. Fig. 4.28(a) shows as solid lines the R-squared parameter[16] from the Goodness-of-fit statistics provided by the employed MATLAB function `fit` for the y positions with the highest number of available data points. Additionally, the R-squared parameters are plotted for the y positions at which all light ion curves are accessible (dashed lines). For an R-squared value close to 1, the fitted curves resemble the data point distributions

[16]The R-squared parameter or coefficient of determination is the ratio of the sum of the '*S*um of S*q*uares *E*xplained', $SQE = \sum_{i=1}^{n} (\hat{y}_i - \bar{y})$, which describes the sum of the squares of the deviations of the points $\hat{y}$ of the fitted function from the mean value of the observed data points $\bar{y}$ and the '*S*um of S*q*uares *T*otal', $SQT = \sum_{i=1}^{n} (y_i - \bar{y})$, which is proportional to the variance of the data und describes the deviation of the measured data points y_i from their mean value. As the SQT is the sum of the SQE and the '*S*um of S*q*uares *R*esiduals', $SQR = \sum_{i=1}^{n} (y_i - \hat{y}_i)$, the coefficient of determination,

$$R^2 = \frac{SQE}{SQT} = \frac{SQE}{SQE + SQR},$$

can only take values between 0 and 1. A model fits the data points best for R^2 values as close as possible to 1, as the residuals are minimal for this case [169].

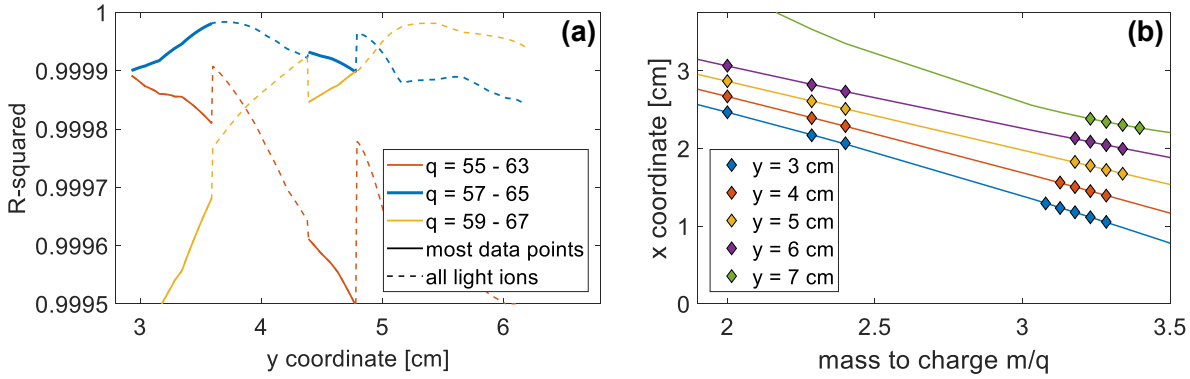

Figure 4.28: (a) R-squared factors that describe the deviation of the data points from the fitted function (Eq. (4.6)) are plotted versus the y coordinate. Each y position corresponds to an individual fit of Eq. (4.6) to the x coordinate as a function of the mass-to-charge ratio. Only y positions are plotted at which a sufficient amount of data points is available, meaning either the maximum number of data points (solid line) or at least all light ion curves (dotted). The shown lines correspond to three different charge ranges that have been assigned to the manually traced gold ion curves from Fig. 4.27: $55^+ - 63^+$ (orange), $57^+ - 65^+$ (blue) and $55^+ - 63^+$ (blue). (b) Data points and fit functions at different y positions. As expected, the fit fails if not enough data points are available, as is the case at $y = 7$ cm with no light ion data. This hinders the reconstruction of the ion traces in this region, which is necessary for the generation of the iso-energy, iso-charge-state mesh for the spectral analysis.

best. Three different cases are drawn: orange colour corresponds to an assignment of the manually traced gold ion curves in Fig. 4.27(a) to the positive charge state range of $55 - 63$, blue corresponds to the charge state range of $57 - 65$ and yellow to $59 - 67$, respectively. Although all three cases exhibit quite high R-squared values, the most favourable behaviour is observed for the blue line. Therefore, the charge states of the traced gold ion curves are considered to be most likely between 57^+ and 65^+, which will be confirmed further below.

Fig. 4.28(b) shows the quadratic fits resulting from Eq. (4.6). The fits represent the data very well for y positions with a high number of available data points. However, if the amount of data points is reduced, as in the low mass-to-charge region, the nonlinear fit function does not allow for an extrapolation into the region where no data points are available, as can be seen from the green line, which is taken at a y position of 7 cm. This is also visible in the fit parameters a, c and d, plotted in blue in Fig. 4.29 as a function of the y coordinate. In regions with little information, for $y < 3$ cm and $y > 6$ cm, the curve of fit parameters exhibits discontinuities, which is contradictory to the continuous ion traces observed on the detector. Using these fit parameters, the reconstruction of the ion traces, which is needed for the generation of the iso-energy, iso-charge-state mesh for

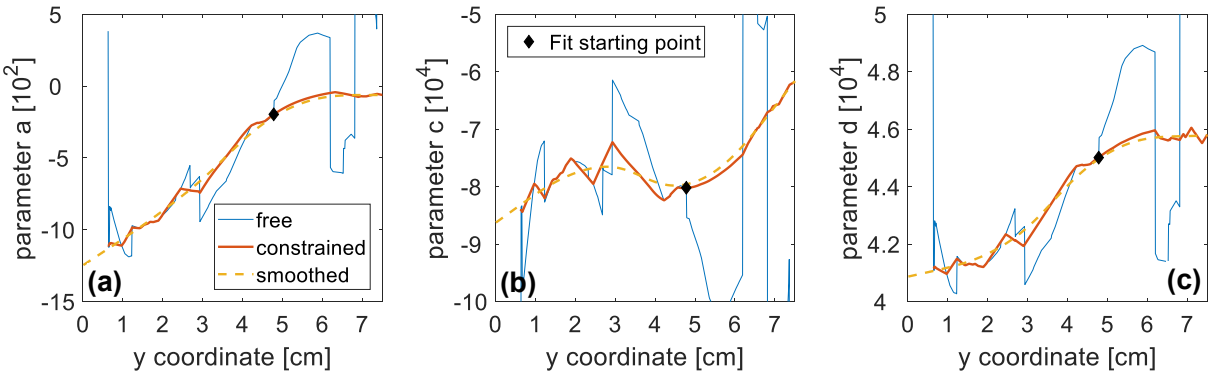

Figure 4.29: (a) Fit parameter a, (b) fit parameter c and (c) fit parameter d from Eq. (4.6) for different y positions. The blue curves are the parameters from the free fit, shown in Fig. 4.28. Especially in regions without a sufficient amount of data points (here for $y < 3$ cm and $y > 6$ cm), the fit parameters are quite discontinuous. As the ion curves are continuous along the y coordinate, this discontinuity is due to insufficiently well fits. Therefore, a y position with a large number of data points is chosen as fit starting point. The fit parameters of adjacent y positions are bounded and only small variations are allowed. The orange curves show the result of this fitting process, which is much more continuous than the free fit. For the reconstruction of the ion traces for the iso-energy, iso-charge-state mesh, the fit parameter curves have been smoothed by applying a Gaussian filter (yellow dashed lines).

the determination of the ion energy spectra, does not deliver the actually measured traces.

Therefore, it needs to be ensured that also fits at y positions with little information can profit from fits with a high amount of data points. Hence, the fit parameters are stabilized by allowing only small deviations between fit parameters derived at adjacent y positions. In order to achieve this, an initial fit is performed at a starting point providing the maximum number of available data points, indicated in Fig. 4.29 by the black trapezoid. Beginning from there, the function shown in Eq. (4.6) is fitted consecutively to all other y positions. When proceeding along the y direction, only small variations of the fitting parameters from adjacent y positions are allowed. The maximum accepted deviation of the parameters differs from shot to shot (between $10^{-2} - 10^{-5}$) and has to be chosen as small as possible in order to avoid discontinuities, but still large enough that the fit parameter curves still resemble their original appearance. The resulting parameters are plotted in orange in Fig. 4.29. For the reconstruction of the ion traces, the smoothed, yellow dashed lines have been used. The outcome of this reconstruction procedure is shown in Fig. 4.30(a) for the charge state range $57^+ - 65^+$, which matches the measured ion traces best. The detailed views in Figs. 4.30(b) – (d) confirm the very good overlay between reconstructed und recorded curves.

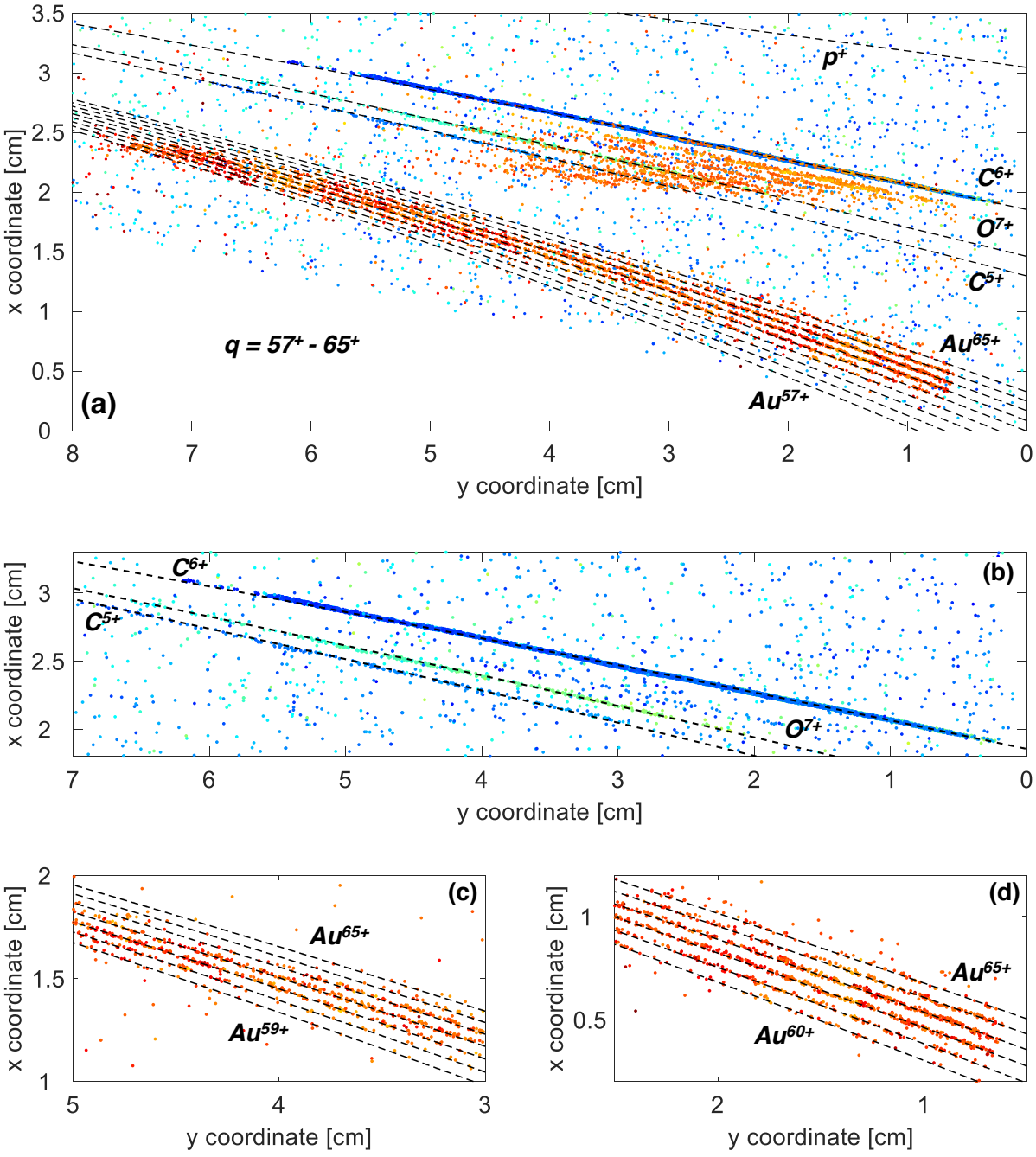

Figure 4.30: Reconstructed ion curves for the assignment of the manually traced curves (see Fig. 4.28(a)) to the charge state range of $57^+ - 65^+$. (a) shows the complete CR-39 detector image with the superimposed curves. (b) shows only the light ion data and (c) and (d) show details of the heavy ion data.

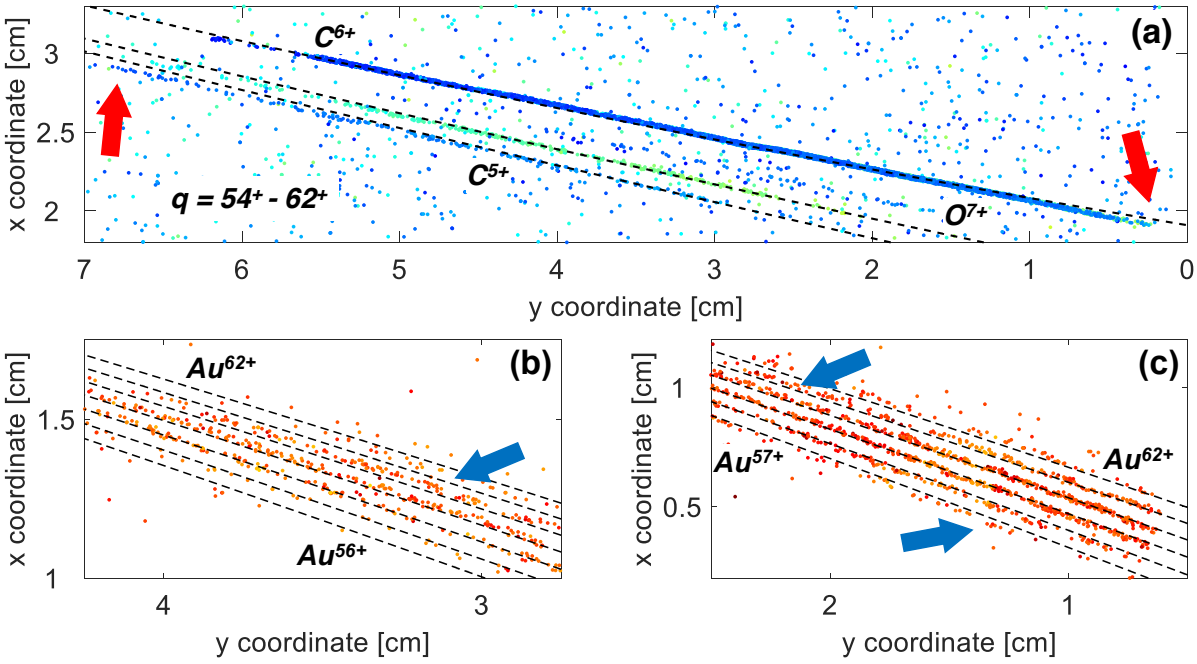

Figure 4.31: Details of the reconstructed curves for the assignment of the manually traced ion curves to the charge state range of $54^+ - 62^+$, which does not fit the measured data sufficiently well, as is highlighted at prototypical cases by the red and blue arrows. (a) shows the light ion data only, (b) and (c) show heavy ion data.

However, as shown in Fig. 4.28(a), the assignment of the charge state range $57^+ - 65^+$ might not be unambiguously correct. Slightly different charge state ranges result as well in fits of comparable quality according to their R-squared factors. In order to determine their uncertainty, the charge state ranges are varied until the reconstructed curves obviously do not fit the recorded traces anymore. Figs. 4.31 and 4.32 show the resulting lower and upper cases for the charge state ranges $54^+ - 62^+$ and $61^+ - 69^+$, respectively. The arrows indicate some exemplary positions, where the trace reconstructions obviously do not fit the measured curves anymore. Thus, it is assumed that these charge state intervals are just outside the error margins of the actual charge state distribution. As a result, the manually traced curves are assigned to the charge state interval $57^+ - 65^+$ with an uncertainty of $\Delta q = ^{+3}_{-2}$ for this shot on a 500 nm thick, unheated gold foil.

4.2.5 Generation of Gold Ion Spectra

The reconstruction of the gold ion traces in the preceding section enables the transformation of each pair of $(x \,|\, y)$ coordinates to a pair of $(y \,|\, q)$, the y positions with the corresponding charge state q. Using the information from Sec. 4.2.3 about the charge-dependent energy

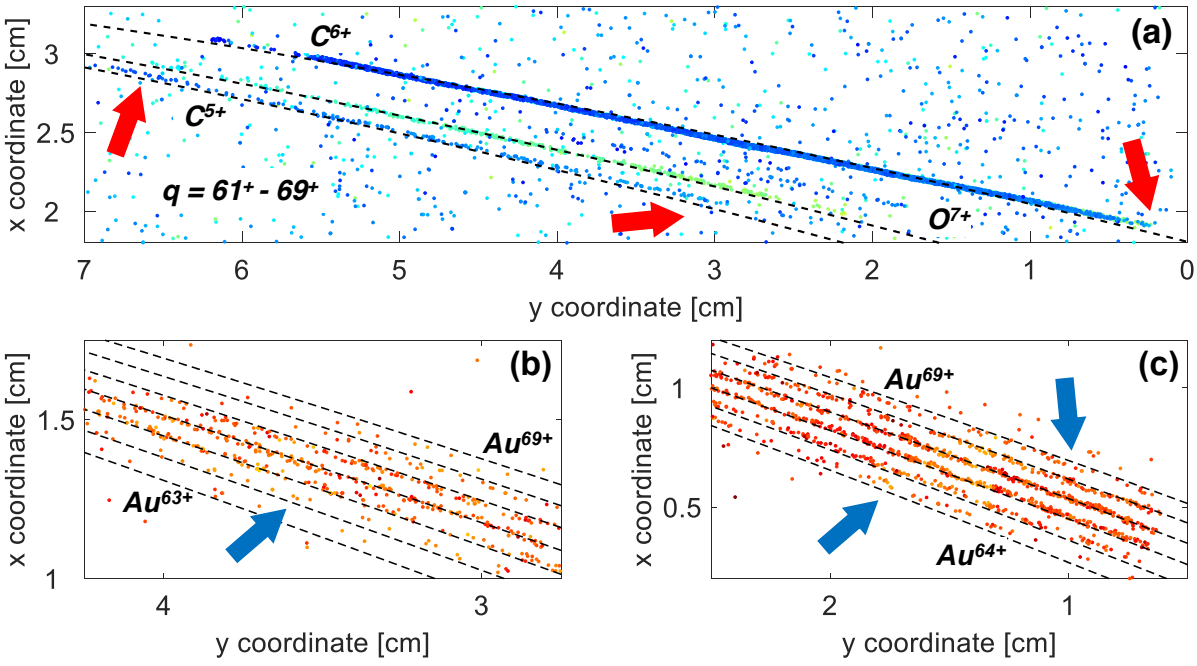

Figure 4.32: Reconstructed curves for the assignment of the manually traced curves to the charge state range of $61^+ - 69^+$, which does not fit the measured data sufficiently well, as is highlighted at prototypical cases by the red and blue arrows. (a) shows the light ion data only, (b) and (c) show heavy ion data.

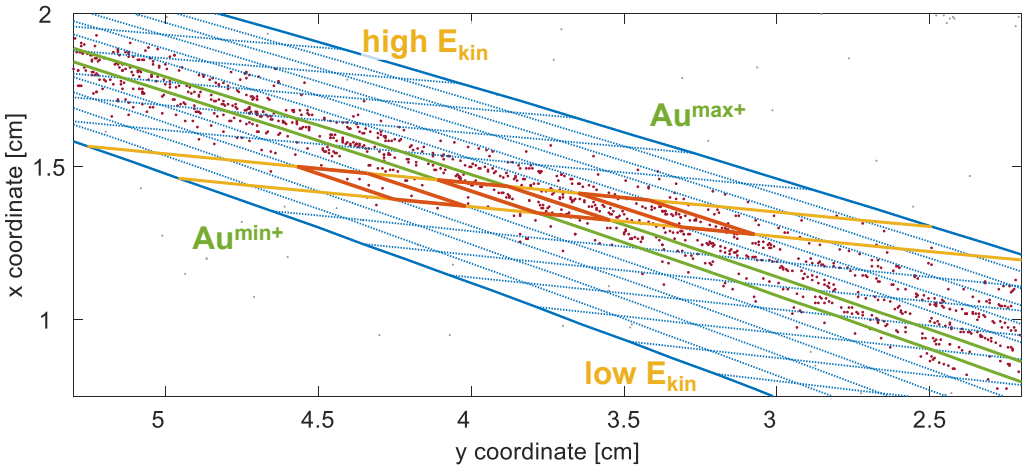

Figure 4.33: Superposition of the iso-charge-state, iso-energy mesh in blue with the raw data corresponding to the shot on the unheated, 500 nm thick gold foil. For reasons of clarity, only a part of the total image is shown. The green lines exemplarily enclose an ion curve corresponding to a distinct charge state. The summation of the signal within the green lines delivers the total ion number with the respective charge state, that has been detection in the applied diagnostics, independent of their kinetic energy. The yellow lines exemplarily enclose the ion signal within a specific energy interval. The summation of the signal within the yellow lines delivers the total ion number with kinetic energies within this interval, independent of their charge state. The orange tetragons visualize how the signal has been summed up and stored for the data analysis: the ions corresponding to a specific charge state have been counted in dependency of their energy.

distribution, this can be further transformed to pairs of $(q \,|\, \mathrm{E_{kin}})$. Summing up the respective signal on the detector delivers the desired gold ion energy spectra as a function of the charge states.

Fig. 4.33 shows a part of the iso-energy, iso-charge-state mesh in blue, which is generated based on the reconstructed ion traces from the preceding section. It was overlaid with the corresponding heavy ion data from the CR-39 detectors. For the analysis, only data points close to the ion curves have been considered, as the data points outside this region are most likely noise and would falsify the result. The discarded data points are drawn in grey in Fig. 4.33. The green lines visualize exemplarily two lines, that enclose an ion curve with a specific charge state. These lines are the centerlines between two adjacent reconstructed ion curves, as shown in Fig. 4.30. The summation of the signal within these green lines delivers the total number of ions with the corresponding charge state, that has been detected on the detection screen, independent of the kinetic energy. The yellow lines enclose the ion signal within a specific energy interval. The summation of the signal within the yellow lines delivers the total number of ions with kinetic energies within this energy interval,

that has been detected in the applied diagnostics, independent of their charge state. The width of the energy steps is defined by the size of the entrance pinhole projection onto the detector. The ion signal corresponding to a specific charge state is saved in dependency of the kinetic energy for the later data analysis, as visualized by the orange tetragons, within which the signal is summed up. The final energy spectrum, which will be shown below, is shown as integral over all charge states.

Three sources of experimental uncertainties have been identified in the previous sections: (i) the determination of the calibration factor b to be applied to the magnetic field, as discussed in Sec. 4.2.3, (ii) the charge state range corresponding to the measured gold ion traces, and (iii) the correct overlay of the iso-energy, iso-charge-state mesh with the measured CR-39 data, depending both on the position of the 19.92 MeV proton cutoff, as discussed in Sec. 4.2.3, and the superposition of CR-39 and IP data, which was addressed in Sec. 4.2.2. Additionally, the intrinsic energy uncertainty of the magnetic spectrometer has to be considered: each point in the spectrum is calculated by summation of all ions within a corresponding energy interval, whose width is depending on the projection of the TPS entrance pinhole onto the detection screen. The influence of these four sources of uncertainties was calculated separately and is depicted in Fig. 4.34.

The error margin in Fig. 4.34(a) shows the uncertainty due to the magnetic field calibration factor $b = 0.903^{+0.040}_{-0.007}$. As mentioned in Sec. 4.2.3, the y positions, at which gold ions with a certain charge state and energy would impinge, have been calculated for the two extremal values of the calibration factor given by the uncertainty. This is transformed into energy values by calculating the energy of the ions, that would arrive at these lower and upper y positions, when using b and the proton energy cutoff point, which also serves as fix point for the superposition of the iso-energy, iso-charge-state mesh with the detectors. The here described energy error margin is charge dependent: the lower the charge, the higher the uncertainty. The shown spectrum is a summation over all charge states. Hence, the corresponding energy error has been averaged over all occurring charge states in an energy interval. The uncertainty of the calibration factor is especially relevant for higher energies, as expected for magnetic spectrometers. The error margin shows the typical behaviour for magnetic spectrometers and increases strongly with the energy. Fig. 4.34(b) shows the limitation due to the energy resolution of the spectrometer, as discussed above. In Fig. 4.34(c), the error margin was determined by calculating the energy spectrum for the extreme cases of the possible charge state range. As deduced in Sec. 4.2.4, the uncertainty for the charge state range for this example of the unheated, 500 nm thick gold

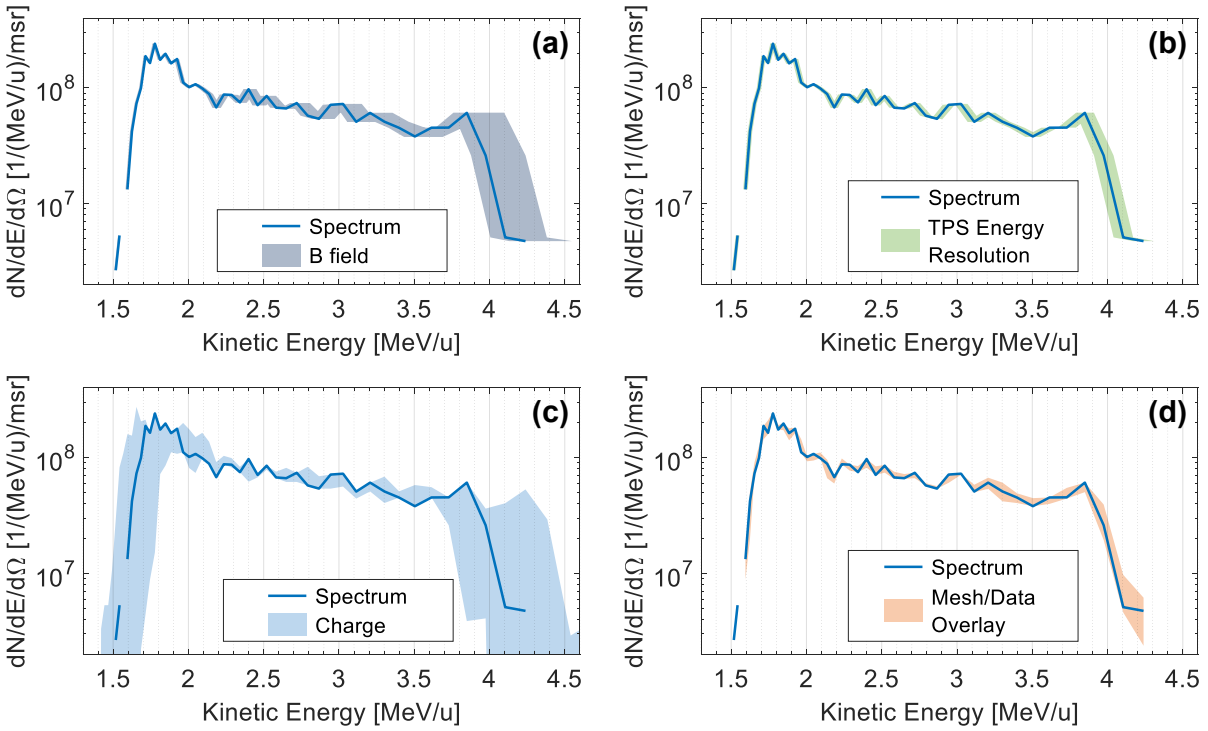

Figure 4.34: The gold ion energy spectrum is shown for a shot onto an unheated, 500 nm thick gold foil with four individual sources for experimental uncertainties, which have been identified during the data analysis: (a) the uncertainty due to the determination of the magnetic field calibration factor, (b) the intrinsic energy resolution of the TPS, (c) the uncertainty due to the assignment of the gold ion traces to a charge state range and (d) the uncertainty due to the superposition of the iso-energy, iso-charge-state mesh with the ion traces on the CR-39 detectors.

foil is $\Delta q = ^{+3}_{-2}$. For these calculations, the same reconstructed ion curves and, thus, the same iso-energy, iso-charge-state mesh have been used as for the spectra calculation in the ideal case, but the respective ion curves have been differently assigned to the shifted charge state range. The error margin shown in Fig. 4.34(d) is due to the superposition of the iso-energy, iso-charge-state mesh with the gold ion traces measured on CR-39 detectors, which has two contributions: first, the mesh is superimposed with the IP detectors by aligning the intersection point of the 19.92 MeV proton trajectory with the detection plane with the respective energy cutoff point on the IP from the calibration shot, as outlined in Sec. 4.2.3. This energy cutoff point could be determined with an uncertainty of ±5 pixels along the energy-dependent y dimension. Second, the data from the CR-39 detectors need to be overlaid with the IPs. This was done by aligning the ion traces along the circular geometric cutoff, which was visible on both CR-39 sheets and IPs. The precision of this alignment was estimated to be within ±5 pixels as well, which delivers a total uncertainty

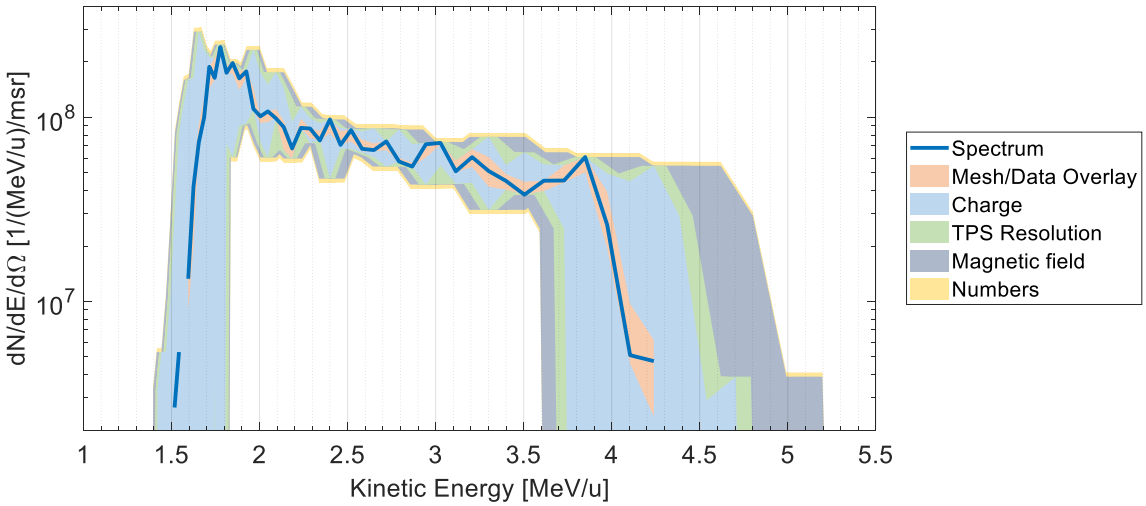

Figure 4.35: The final kinetic gold ion energy spectrum of the shot onto an unheated, 500 nm thick gold foil is shown with the sum of all sources of uncertainty in order to obtain a conservative estimate of the error margins. Additionally, an uncertainty of 5% has been allowed for the registered number gold ions, which is shown in yellow, to account for possible counting errors in the SAMAICA software.

of ±10 pixels for the superposition. Again, the spectra for the extreme cases have been determined, in this case by shifting the CR-39 sheet for ±10 pixels along y, in order to obtain an estimate for the largest possible error.

All these error sources have been added up for the final error margin in order to achieve a very conservative estimate of the spectrum's uncertainty. The result is shown in Fig. 4.35. Additionally to the four previously discussed errors, an uncertainty of 5% was allowed for the particle numbers to account for possible counting errors in the pattern recognition software SAMAICA. These happen, for example, if two gold ions are too close to each other and are therefore counted as a single gold ion ('clustering') or if structures appear on the CR-39, that are accidentally mistaken as gold ions, for instance dust particles of similar size and shape as the gold ion pits on the CR-39. This additional error is illustrated in yellow. It is obvious that the determination of the calibration factor for the magnetic field and the assignment of the measured gold ion traces to a certain charge state range have the greatest impact, while the other three sources of uncertainty show only a minor influence. In the presentation of the results in Sec. 4.2.7, the individual error sources will not be distinguished anymore by the choice of different colours.

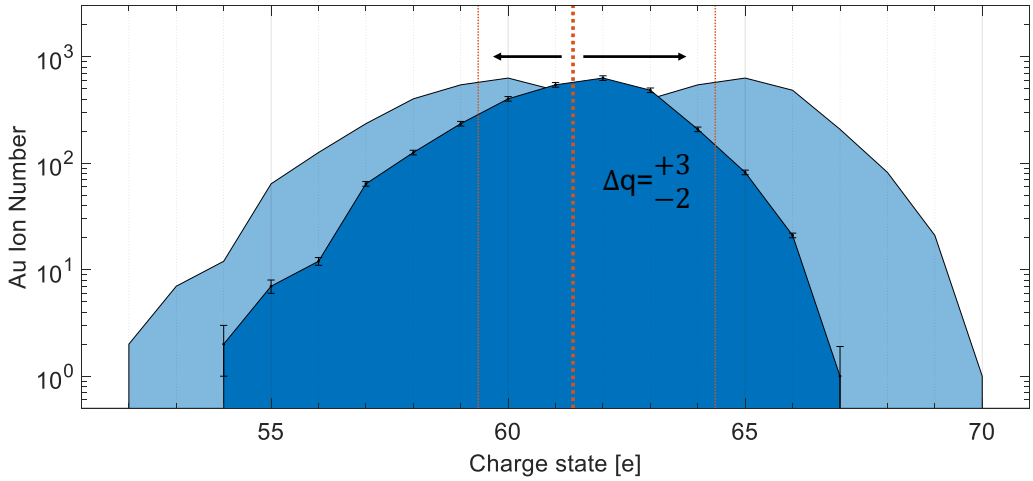

Figure 4.36: Gold ion charge distribution, integrated over all kinetic energies, for the shot on a 500 nm thick, unheated gold foil. The dark blue region shows the charge distribution including an uncertainty of either 1 ion count or $\pm 5\,\%$ of the gold ion number (whatever is bigger). Due to the uncertainty of the identification of the charge state region (see Sec. 4.2.4), this distribution might also be shifted – in this case for $\Delta q =^{+3}_{-2}$ – as shown by the light blue distributions. The thick, dotted orange line represents the mean charge state of the total distribution. The thin, dotted orange lines show the respective mean charge states of the shifted distributions.

4.2.6 Investigation of the Gold Charge State Distribution

As discussed above, the here presented gold ion energy spectra are integrated over all charge states, which is exemplarily shown for a single energy interval by the yellow lines in Fig. 4.33(a). Likewise, it is possible to present the total charge distribution, integrated over all energies, when summing up along the second dimension, visualized by the green lines in the mentioned figure. The resulting charge distribution for the shot on an unheated, 500 nm thick gold foil is shown in dark blue in Fig. 4.36. In this case, a logarithmic scale was chosen for the ordinate, which facilitates the determination of the width of the charge state distribution. The corresponding mean charge state is marked by the thick, dotted orange line. As the charge state region can only be identified within an uncertainty – in this case $\Delta q =^{+3}_{-2}$ – this distribution may also be shifted along the abscissa. The two extreme cases of distributions shifted to the outer margins of the error range are drawn in light blue with their corresponding mean charge states indicated by the thin dotted orange lines.

While the shown charge state distribution from this shot on an unheated, 500 nm gold foil might be shifted, its overall shape does not change, as the gold ion traces, each corresponding to a distinct charge state, were separable for all energy values. However, this turns out to be an exception, as the gold traces of the other investigated shots blur

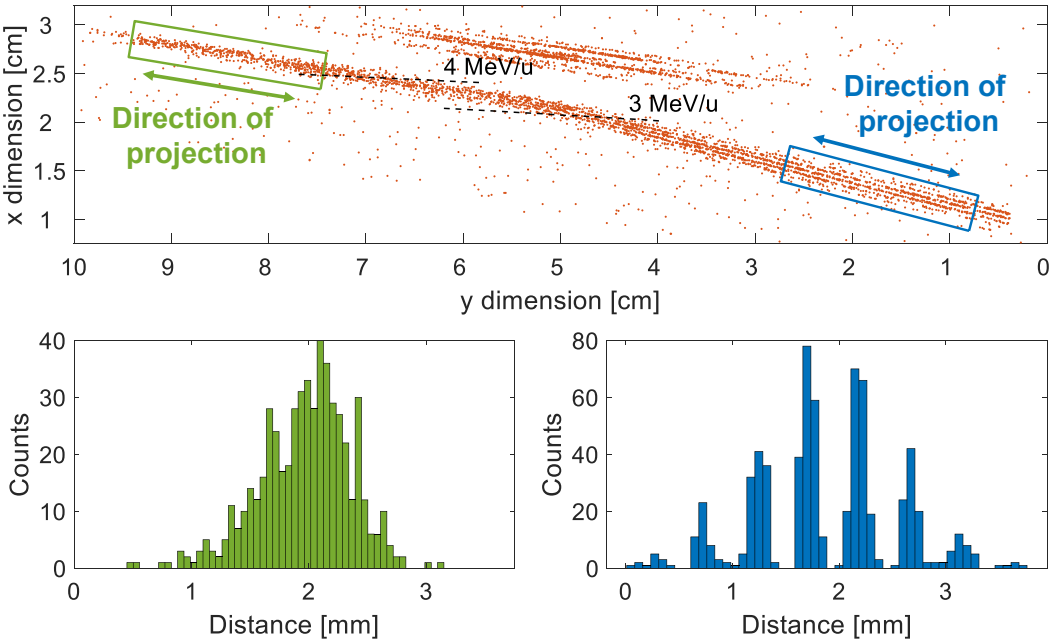

Figure 4.37: Top: Raw data from a shot on a heated, 300 nm thick gold foil. In the high (green) and low (blue) energy regions, projections along the ion traces were taken and are shown in the bottom. Clearly, the charge state resolution of the TPS is energy dependent, as the traces from the low energy region can be easily separated, while the traces from the high energy region are not resolvable.

when reaching higher energies and cannot be distinguished anymore. Fig. 4.37 shows this for the example of a heated shot on a 300 nm thick gold foil. The projection along the gold ion traces in the low energy region well below 3 MeV/u (blue) proves that the individual curves can be well separated. However, the same projection in the high energy region above 4 MeV/u (green) does not result in a resolvable structure. Thus, as expected for a TPS, the charge resolution degrades towards higher energies.

In Fig. 4.38, the charge state distribution is examined as a function of the kinetic energy. Each panel shows the number of gold ions within the stated energy interval as a function of their charge states. Here, the ordinate is linearly scaled, which facilitates the investigation of the shape of the ion distribution rather of its width. The ion number was normalized to the maximum of the respective distribution, which is declared in each panel ('norm = X'). The kinetic energy increases from the bottom to the top, which is also visualized by the face colours of the single distributions (blue means low energy, red means high energy). The respective mean value has been marked by an asterisk (*) for each charge state distribution. The error bars in the four topmost panels indicate the charge

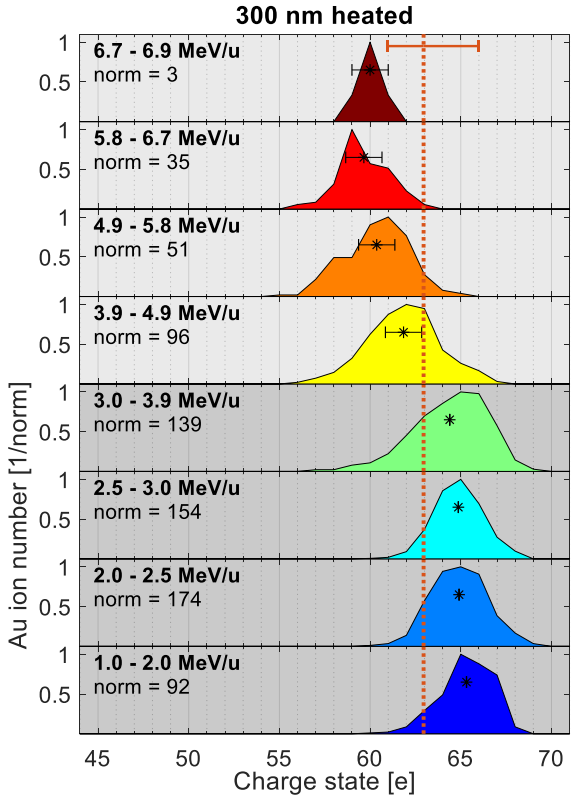

Figure 4.38: Energy dependent gold ion charge state distributions for a shot on a heated, 300 nm thick gold foil. The energies of the energy intervals in which the ion signal was integrated are increasing from the bottom to the top, which is also visualized by the face colours of the distributions (blue means low, red means high energy). The ion numbers of each distribution were normalized to their respective maximum, which is stated for each panel individually ('norm = X'). The respective mean value has been marked by an asterisk (*) for each charge state distribution. The error bars in the four topmost panels indicate the charge state resolution within the shown distribution. The total charge state mean value, averaged over all kinetic energies, is indicated by the dotted, orange line. In the topmost plot, the uncertainty of the charge state range itself is indicated by the orange error bar surrounding the total mean charge state.

state resolution within the shown distributions. For the energy intervals of the remaining panels, the individual gold ion traces were separable. Hence, the overall shape and width of these charge state distributions are known very precisely, while the shape and width of the four topmost distributions could be slightly different in reality, as the charge states of the gold ions could only be determined with an accuracy of $\Delta q = \pm 1$. The criterion for the resolution of single ion traces within an energy interval was, that the separation of the ion curves had to be at least as large as the size of the projection of the pinhole on the detection screen. The total charge state mean value, averaged over all kinetic energies, is

indicated by the dotted, orange line. In the topmost plot, the uncertainty of the charge state range, which has been discussed in Sec. 4.2.4, is indicated by the orange error bar surrounding the total mean charge state. This uncertainty would only cause a shift of the charge state range towards higher or lower charge states, but not change the overall shape and width of the individual charge state distributions, especially where single ion traces were separable.

4.2.7 Experimental Results and Discussion

In total, the accelerated ions from six laser shots on gold foils with varying thickness have been detected on CR-39 sheets. The raw data of these detectors are shown in Fig. 4.39 after they have been digitized and processed as described in Sec. 4.2.2. The orange points correspond to pits, which have been assigned to heavy ions due to their size. The blue points have been identified as light ions like carbon or oxygen ions. The red dashed circularly curved line on the right side of the raw data images depicts the geometric cutoff line, which has been used for the alignment of the CR-39 detectors along the y-axis (see Fig. 4.23). In each image, the iso-energy lines starting from 2 MeV/u up to 7 MeV/u (depending on the achieved energy for the respective shot) are indicated by black dotted lines.

For all six shots, heavy ion traces have been detected in the light ion region. The numbers of heavy ion pits in this region vary from shot to shot and show neither a clear dependency on the foil thickness nor on a preceding removal of hydrocarbon surface contaminants by cleaning the target foil with the heating laser. The curvature and overall shape of these ion traces agree very well with that of the adjacent light ion curves. Therefore, it is assumed that they do not originate from a different source position in the target and that they did not enter the spectrometer through a second, potentially unnoticed pinhole. In all shots, heavy ion traces have been observed between the C^{6+} and the O^{7+} lines (the two topmost blue curves in the raw data images), requiring a mass-to-charge ratio of at least 2.3. The shots on the 300 and 500 nm thick gold foils show heavy ions traces close to or even overlapping with the C^{6+} line, having a mass-to-charge ratio of 2. In none of the shots, heavy ion traces have been detected in the unphysical region below a mass-to-charge ratio of 2. This and the clear, narrow shape of the traces, similar to the identified real TPS curves, allow to argue against scattering of heavy ions in the entrance pinhole, as a broad, blurred structure would be expected in this case that would not necessarily show a sharp boundary at a mass-to-charge ratio of 2 and could extend into lower mass-to-charge ratio regions. A misinterpretation of light isotopes of carbon, nitrogen or oxygen as heavy

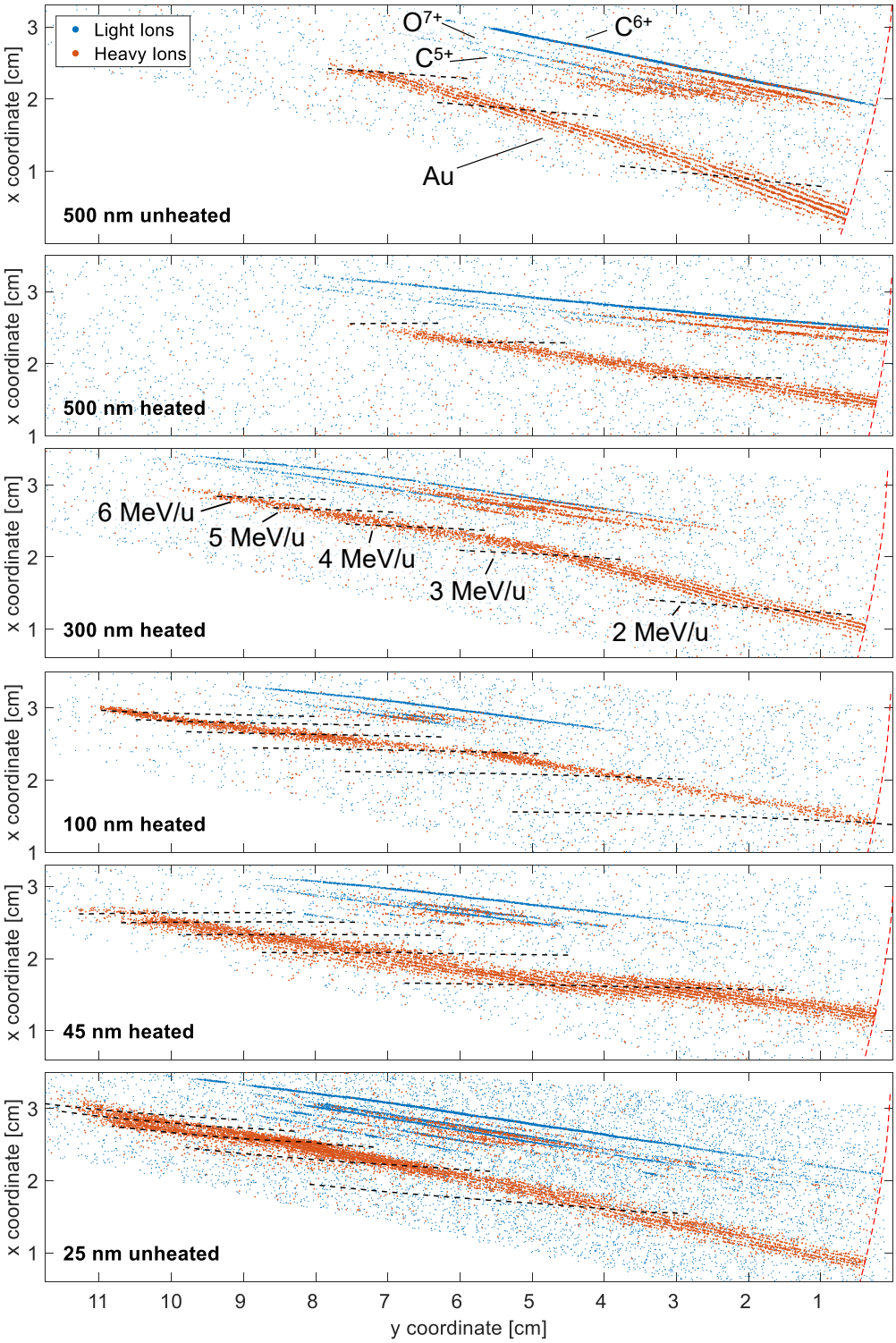

Figure 4.39: CR-39 raw data after filtration of the background, as described in Sec. 4.2.2, for shots on gold foils with different thickness. In all images, the iso-energy lines starting from 2 MeV/u up to 7 MeV/u are indicated by black dotted lines. These lines are exemplarily labelled for the shot on the 300 nm gold foil. The red circularly curved dashed line depicts the curve, which was used for the alignment of the CR-39 detectors along the y-axis, as described in Sec. 4.2.2.

ion impacts is very unlikely, as the individual traces are very close to each other. If these heavy ion pits originate from one species, the ion mass has to be very high in order to allow for such slight differences in the mass-to-charge ratio (as the ion charge is discrete). Moreover, no light isotopes were found whose traces could be superimposed to all of the measured curves. Concluding, many causes can be excluded, however, an explanation for these detected heavy ion traces still has to be found.

The resulting gold ion energy spectra (integrated over all charge states) for all six shots are shown in Fig. 4.40. The grey error margin includes all sources of uncertainty that have been discussed in Sec. 4.2.5. While from the thickest targets (500 nm) gold ions have been accelerated up to kinetic energies around 4 MeV/u, shots on all other foils have reliably delivered maximum gold ion energies above 6 MeV/u. The best results come from the shots on foils with a thickness of 100 nm and 25 nm, for which the energy barrier of 7 MeV/u for the fission-fusion reaction mechanism has most likely been achieved. Thus, the realized kinetic gold ion energies of around 5 MeV/u from the beamtime at the TPW (see Sec. 4.1.4) have been exceeded and a main goal of this thesis – the demonstration of laser-accelerated gold ions around 7 MeV/u in preparation for the fission-fusion reaction mechanism – has been accomplished.

The target heating process, with a simultaneous radiative heating of the front and rear side of the target (see Sec. 4.2.1), can be judged as similarly or slightly more effective than what was achieved during the TPW beamtime. Again, the potential for further improvements has been identified, as will be discussed in Sec. 4.2.8. Nevertheless, the proton signal was significantly reduced for all heated cases. For the shots on the heated foils with a thickness of 300 and 500 nm, even no proton signal at all was detected on the IPs. However, in contrast to the findings of the TPW experiment and further former experiments (e.g. [144, 145, 148]), no positive influence of the target foil cleaning on the gold ion energies could be observed. In fact, the highest energies were achieved for the shot on the unheated, 25 nm thick gold foil. The only available thickness which allows for a direct comparison of heated and unheated shots is 500 nm. Both shots on foils of this thickness delivered gold ions with the same kinetic energies, with a slight tendency – if any – towards higher energies for the unheated shot.

A similar result for the effect of target cleaning on the maximum gold ion energies is presented in a recent simulation paper [49]. The authors simulated the interaction of a PHELIX-like laser pulse (500 fs pulse duration, 60 J laser energy and a peak intensity of 2.4×10^{20} W/cm^2) with gold foils of the same thickness (500 nm) as the discussed shots

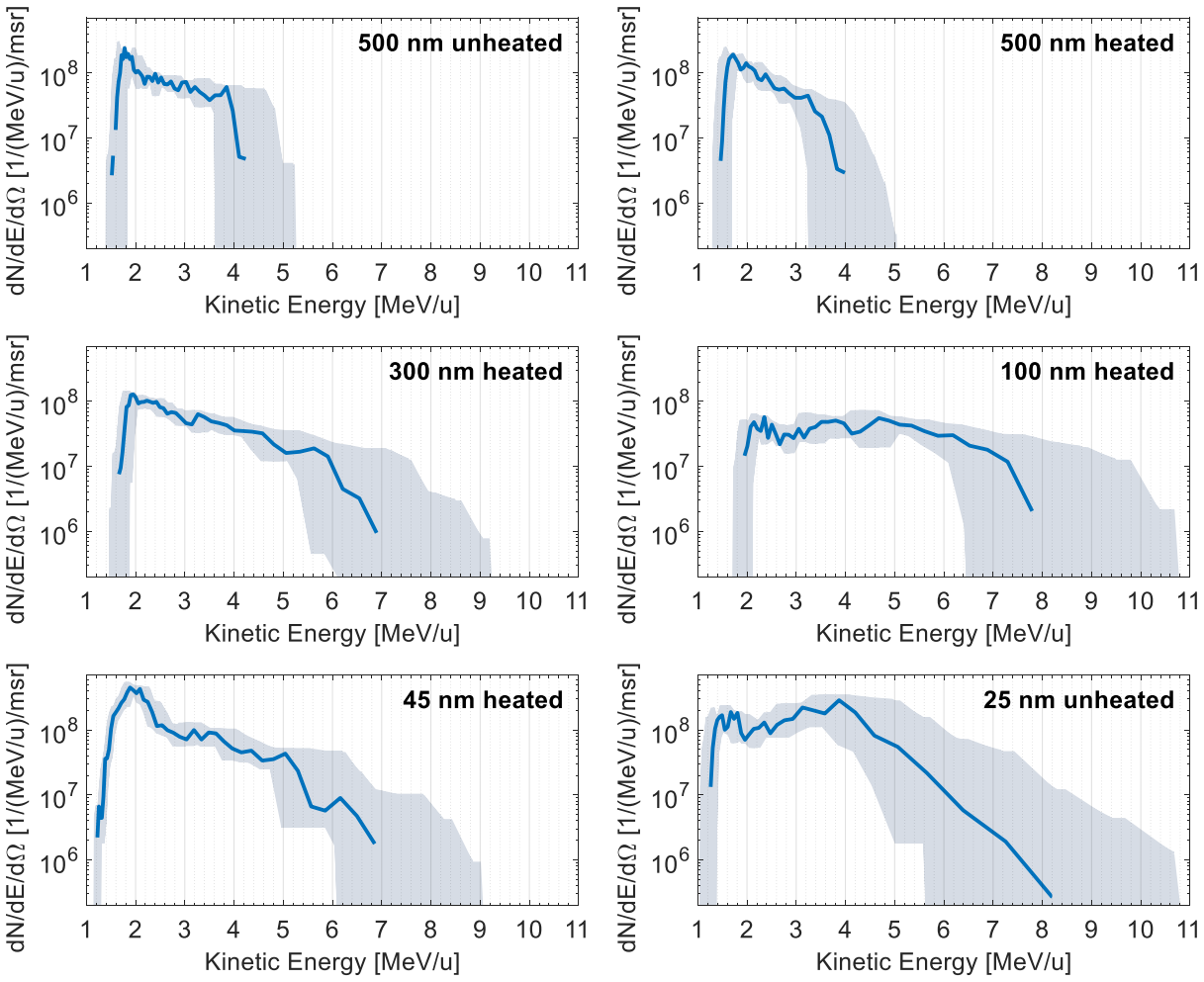

Figure 4.40: Gold ion energy spectra for shots on gold foils with varying thickness, integrated over all charge states. The grey error margin includes all sources for uncertainties from Sec. 4.2.5.

above, with and without a hydrogen contamination layer. Similar to our results, they also ended up with maximum gold ion energies that were equal or even slightly higher for the unheated, contaminated foil. However, they predict a significantly lower mean energy for the unheated shot, which is obviously not the case in the here presented spectra from the 500 nm thick gold foils, as the gold energy spectrum from the heated shot drops faster and has a lower ion number at high energies than that from the unheated shot. The reason for the contradicting finding in the simulations lies in the charge state distribution, which in this case exhibits a very prominent peak at 51^+ for the heated case (this distribution is shown in Fig. 4.42(b)) and a rather broad distribution peaking around $25^+ - 30^+$ for the unheated case. The difference in their resulting mean gold ion energies is thus not surprising.

This example reveals the necessity of a deeper understanding of the underlying ionization dynamics, as the strength of the acceleration (caused by the Lorentz force) obviously depends on the particle charge. Additionally, the charge separation field is built up by the electrons which have been removed from the target atoms. Thus, the number and position of ionization events substantially influence the magnitude and distribution of this field and thus also the ion acceleration. The gain in knowledge about the involved ionization mechanisms requires the availability of a sufficiently large pool of experimental data. The here presented experiment at the PHELIX laser delivers for the first time data from laser-accelerated heavy ions in the mass range of $A \approx 200$ with a very high charge state resolution, up to the possible discrimination of single charge states. Fig. 4.41 shows the charge state distributions for the six analyzed shots. Both the distribution with the blue face colour and the red curve show the same charge state distribution, once on a logarithmic and once on a linear scale. The width of the charge state distribution increases towards thinner targets. The lowest measured charge state is $(36^{+2}_{-3})^+$ for a foil thickness of 25 nm, while the highest is $(74^{+2}_{-3})^+$ from a 100 nm thick gold foil, which reaches the recently published record ionization value of 72^+, being the highest charge state of gold that has been realized in experiments [170]. A significant difference between the charge state distributions from heated and unheated foils, as found in the previously mentioned simulation paper [49], is not observed. Striking is that each of the charge state distributions – even the broad ones for thinner target foils – has a clear maximum, which becomes particularly visible on the linear scale. Prominent peaks are also visible at individual charge states in the respective distributions of the relevant simulation works [46, 47, 49] and can be attributed to large steps in the ionization potential.

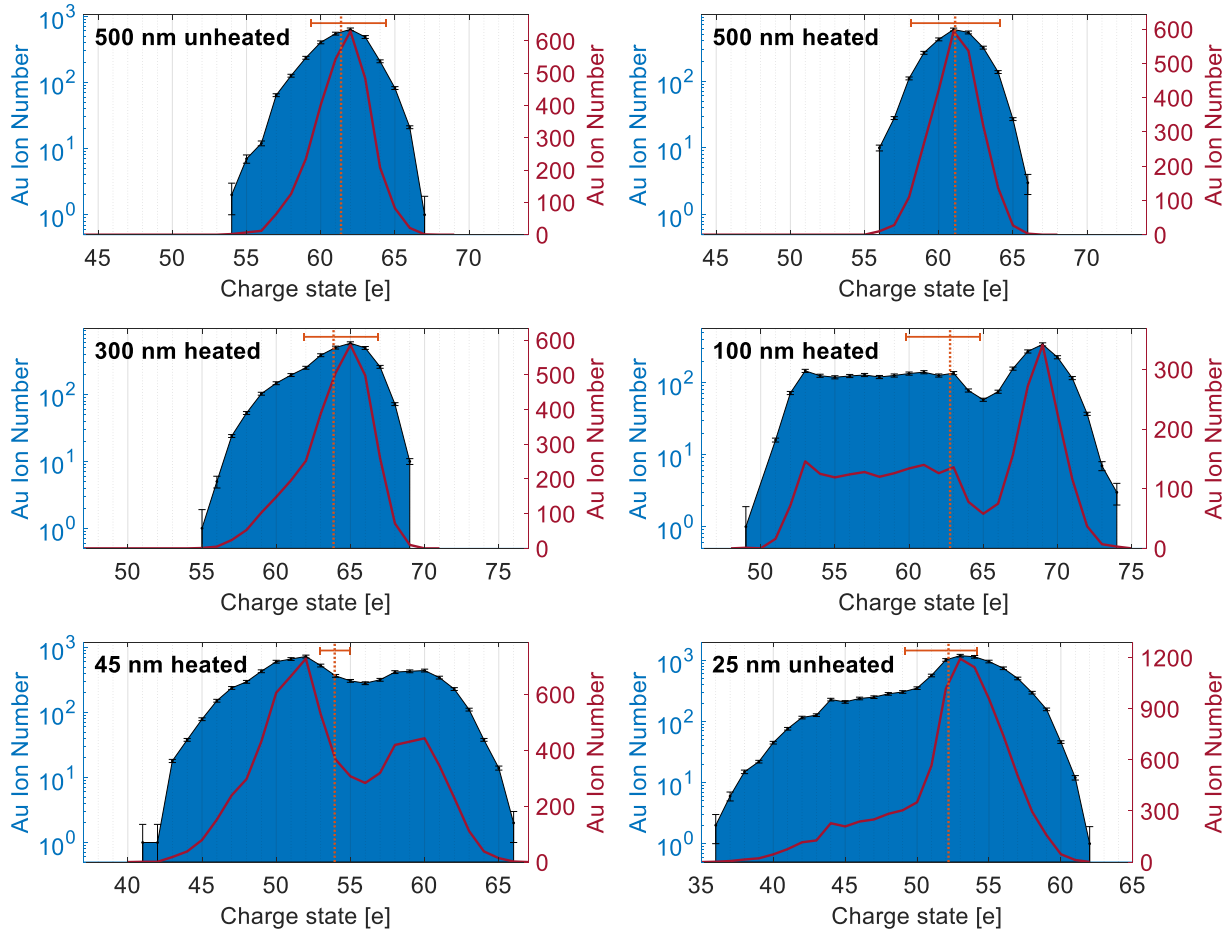

Figure 4.41: Gold ion charge distributions for shots on gold foils with varying thickness. The curve with the blue face colour is logarithmically scaled with the corresponding ordinate on the left side, while the red curve are the same values in linear scale with the ordinate on the right side. The dotted orange line shows the mean charge state of the total distribution with the error bars denoting the overall uncertainty for the charge state range.

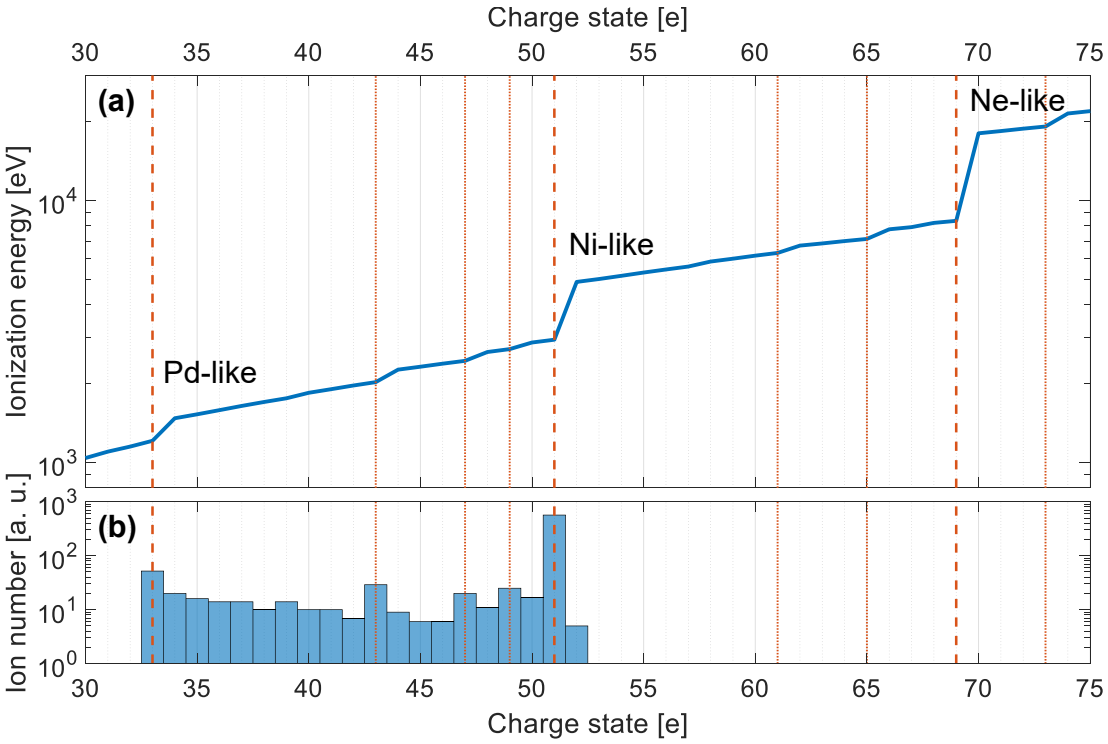

Figure 4.42: (a) Ionization energies for the sequential ionization of gold, taken from reference [60]. The thick, dashed orange lines show charge states with large steps in the ionization potential, which are associated with closed atomic shells, as already introduced in Fig. 2.2: 33^+ is palladium-like with a closed 4d shell ([Kr].4d10), 51^+ is nickel-like with a closed 3d shell ([Ar].3d10) and 69^+ is like the noble gas neon with a closed 2p shell. The thin, dotted orange lines visualize charge states, where the energy for further ionization is slightly higher (at least a factor of 2) than for the surrounding charge states.
(b) Charge state distribution from the simulation presented in reference [49] for the interaction of a PHELIX-like laser pulse with an uncontaminated, 500 nm thick gold foil. The distribution peaks at the steps in the ionization potential with a predominant occupation of the charge state 51^+.

The ionization potentials for the sequential ionization of gold [60] have already been introduced in Sec. 2.1.1 and are shown once more in Fig. 4.42(a). The thick, dashed orange lines show charge states related to closed atomic shells, which result in large steps in the ionization potential, as already shown in Fig. 2.2. Additionally in this figure, the thinner, dotted orange lines visualize smaller steps in the ionization potential with step sizes (differences between ionization energies at charge states $z+1$ and z) that are at least a factor of 2 higher than the sizes of the surrounding steps. In Fig. 4.42(b), the already mentioned charge state distribution from reference [49] for the simulation of a PHELIX-like laser interacting with an uncontaminated (heated), 500 nm thick gold foil is presented on a logarithmic scale (contrary to the usual presentation of charge state distributions in

linear scale in simulation papers). The relevance of the charge state 51^+ is evident at first sight, as the corresponding ion number is at least one magnitude higher than for the other appearing charge states. However, also the smaller steps in the ionization potential show an effect on the population of the charge states in the simulation, as peaks in the charge state distribution occur at all of the dotted lines, which becomes evident by the logarithmic presentation. All mentioned simulations of laser-driven gold ion acceleration show charge state distributions with peaks at these small steps in the ionization potential and a predominant occupation of the charge state 51^+.

This motivates a comparison of the peak positions of the here presented gold charge state spectra with the steps in the ionization potentials, which is done in Fig. 4.43. The distributions in blue show the ion numbers integrated over all energies for one charge state, while for the distributions in green the ions have been integrated between 1.8 and 3.9 MeV/u, where individual ion charge states could be resolved for the majority of the shots. Despite this single-charge-state resolution, the peaks in the measured distributions are not as sharp as in the simulations, where distinct charge states stand out compared to the neighboring charge states. Instead, the measured maxima are broadened and distributed over a width of at least three to four charge states. Nevertheless, these peaks coincide – within the allowed uncertainties for the charge state range – very well with the positions of the steps in the ionization potential and show a remarkable thickness dependency: the charge state distributions of gold ions from thinner foils (< 50 nm) peak around the charge state 51^+ with a rather broad underlying charge state distribution, while the gold ions from thicker foils are quite closely spread around maxima at much higher charge states. The distributions for the two shots on 500 nm thick gold foils are in excellent agreement with each other and the highest populated charge state lies around 61^+ for both cases. For decreasing gold foil thicknesses, the widths of the charge state distributions increase and their peak positions move towards higher values, all coinciding with larger steps in the ionization energies (around 65^+ for 300 nm and 69^+ for 100 nm). At a gold foil thickness of 100 nm, a uniform distribution at lower charge states between 51^+ and 65^+ arises additionally to the peak at 69^+. This appears to be the onset of a transition to the charge state spectra from thinner gold foils with thicknesses of 45 and 25 nm, which are relatively broad compared to the thicker foils and located at much lower charge states.

The exact interplay of the ionization mechanisms, which are responsible for the production of these high heavy ion charge states, is yet unknown. The two processes presented in Sec. 2.1, tunnel ionization and collisional electron impact ionization, are expected to be

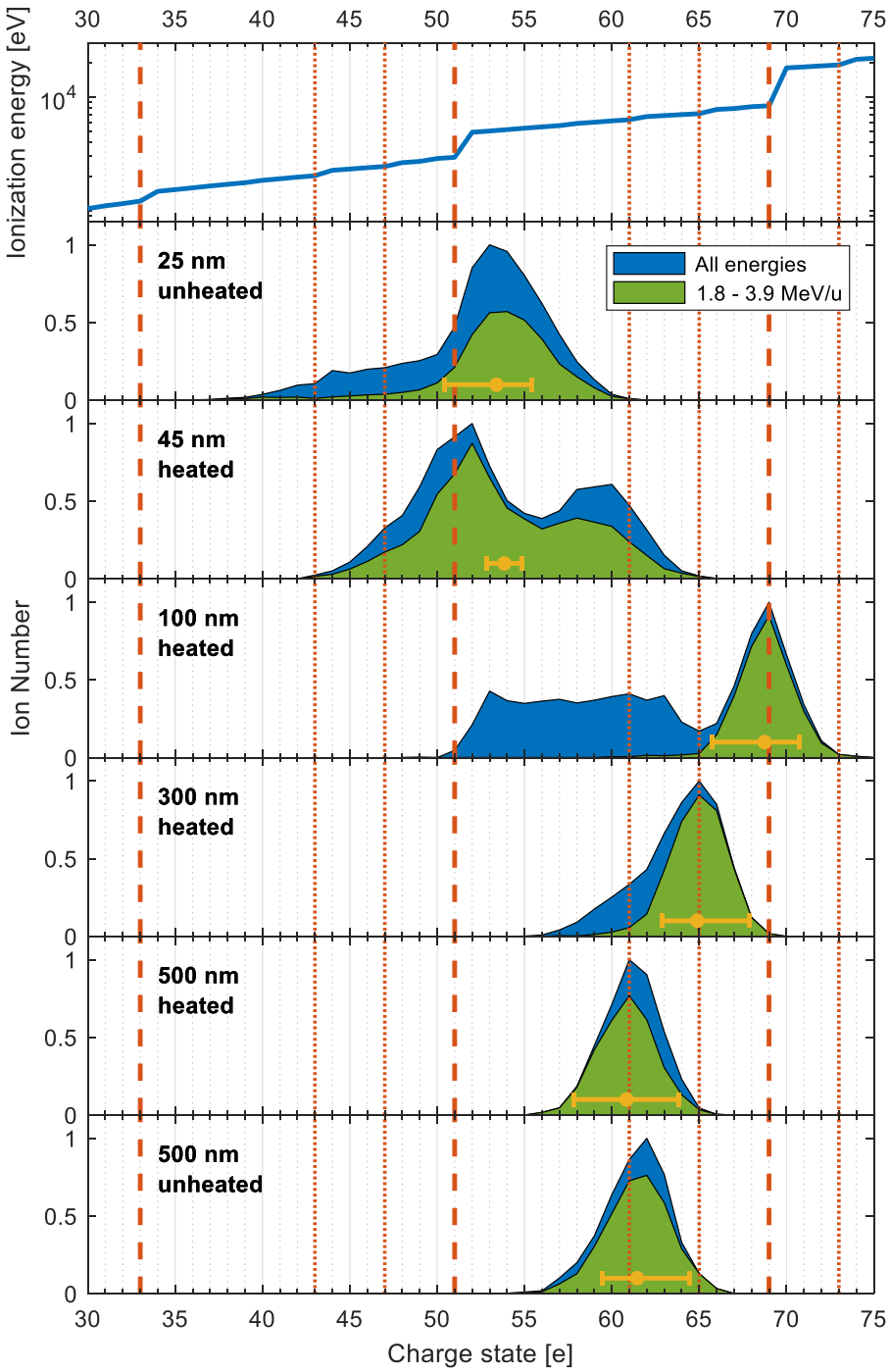

Figure 4.43: Comparison of the measured gold ion charge states from shots on gold foils with varying thickness with the positions of steps in the gold ionization energy. The blue distributions show the gold ion numbers for each charge state integrated over all energies. The green distributions display the number of gold ions integrated between 1.8 and 3.9 MeV/u, for which the individual charge states were resolvable for most of the shots. The yellow point depicts the mean charge state of the green distribution with an error bar showing the uncertainty of the total charge state range. The distributions are normalized to the respective maximum of the blue curves.

dominant. There is growing evidence from the still sparsely available experimental data that the occurrence of collisional ionization could depend on the target thickness. Braenzel et al. [45] and Wang et al. [51] have focused short-pulsed Ti:sapphire lasers on thin gold foils with a thickness of 14 nm and 150 nm, respectively. Both did not find evidence for collisional ionization and could explain their measured charge states with optical field ionization. Nishiuchi et al. [50] accelerated silver ions from silver foils with thicknesses ranging from 50 to 500 nm with a Ti:sapphire laser. They deduced that optical field ionization is only of relevance for thinner targets, as the laser field cannot penetrate through a thicker target and does not reach its rear side. The authors state that the ionization for thick targets is thus dominated by electron impact ionization, caused not by the laser-heated hot electron plasma but by the electrons in the neutralizing return current. Hollinger et al. [170], who demonstrated the above mentioned record ionization for gold, used a short-pulsed Ti:sapphire laser as well, which was focused on a gold foil with a thickness of the order of μm. They also attributed their high charge states to collisional ionization processes.

The laser intensity thresholds for optical field ionization of gold atoms have been plotted in Fig. 2.2. As can be seen in the figure, gold ion charge states up to 51^+ can be reached with the peak intensity of 4×10^{20} W cm^{-2}, which has been realized in our experiment. Hence, none of our charge state distributions could be explained by tunneling ionization, as all exhibit charge states above this value. However, the here expressed peak intensity is the cycle-averaged peak intensity,

$$I = c\epsilon_0 E^2 \cdot \underbrace{\frac{1}{T}\int_0^T \cos^2\left(2\pi\frac{t}{T}\right) \mathrm{d}t}_{=1/2}, \tag{4.7}$$

which is in reality a factor of 2 lower than the instantaneous peak value. Furthermore, considering the long laser pulse duration, it is possible that the target foil surface expands and becomes relativistically transparent before the laser pulse has ended. In this case, the laser penetrates the foil until it faces deeper target layers with densities above the critical value, at which the laser is reflected back. As a consequence of the superposition of the in- and outcoming wave, a standing wave is formed with an electric field amplitude twice as high as the original one, which could further push the laser intensity up to a factor of 4. With that, the real laser peak intensity potentially reaches values up to 3×10^{21} W cm^{-2}, which would already be sufficient to ionize gold up to charge states of 61^+ to 65^+.

When the target density drops down to below or near the critical density, relativistic self-focusing of the laser pulse in the plasma becomes conceivable [171–173]. This effect can be understood considering the relativistic mass increase of the electrons, $m_e = \gamma m_{e0}$, which leads to a modification of the refractive index, $n_\mathrm{r} = \sqrt{1 - n_e/\gamma n_{cr}}$ (see Sec. 2.2). As the Lorentz factor γ is increasing with the laser intensity, the refractive index of the plasma rises towards the center of the laser focus, which leads to further focusing of the laser. If this mechanism occurs, the peak laser intensity could be tremendously enhanced and the ionization of gold via the laser field up to charge states of 69^+, requiring an intensity of about 7×10^{21} W cm^{-2}, and even above becomes viable.

For the assessment of the relevance of collisional ionization, the estimated cross sections σ for the electron impact ionization from Fig. 2.3 are used. Based on these estimations, the probability of an ionization event can be evaluated,

$$P = \frac{N_e \sigma}{A}, \tag{4.8}$$

with N_e being the number of available electrons and A the irradiated area, which is assumed to be the FWHM area of the laser focus given in Sec. 4.2.1, $A_\mathrm{FWHM} = 15\,\mu$m. Both electron numbers and cross sections are depending on the energy. Therefore, the product $N_e\sigma$ is integrated over the whole energy range with the values for σ from Fig. 2.3. An exponential distribution is crudely assumed for the electron number,

$$N_e(E) = \frac{N}{E_{pon}} \cdot \exp\left(-\frac{E}{E_{pon}}\right), \tag{4.9}$$

with N being the total electron number and $E_{pon} = 6$ MeV the ponderomotive potential, which has been calculated using Eq. (2.13) and is taken as the mean electron energy [69,70]. The total number N of electrons has been estimated by the available number of free electrons in the foil contained by the FWHM spot of the laser

$$N = Z \cdot \frac{m_\mathrm{Au}}{M_\mathrm{Au}} = Z \cdot \frac{V \rho_\mathrm{Au}}{M_\mathrm{Au}}, \tag{4.10}$$

where it is assumed that all atoms have been Z-fold ionized and with the foil volume $V = A_\mathrm{FWHM} \cdot d$ with d being the gold foil thickness, ρ_Au and M_Au the mass density and atomic mass of gold, respectively. Assuming a gold foil thickness of 500 nm, we derive an total electron number of $N = Z \cdot 4.4 \times 10^{11}$ and end up in a probability of about 4 % for the

ionization from 51^+ to 52^+ and about 0.6 % for the ionization from 69^+ to 70^+[17]. Of course, these results have to be regarded as very unprecise, as neither the cross sections nor the electron numbers (including their energetic distribution) are known very well. Furthermore, the influence of a possible return current from regions surrounding the focal spot, which could potentiate the number of contributing electrons and thus the ionization probabilities, has not been considered. Nevertheless, these estimates demonstrate that ionization of gold atoms to these high charge states via electron impacts is certainly possible.

Thus, both of the presumably dominating ionization mechanisms have the potential to ionize gold atoms up to the measured high charge states. However, neither the remarkable thickness dependency nor the narrow width of the charge state distributions for thicker gold foils can be explained in a straight-forward way by these ionization processes. Therefore, this data certainly is a valuable input for further theoretical investigations to analyze the exact contributions of different ionization mechanisms in laser-generated plasmas.

Figs. 4.44 and 4.45 present the gold ion charge state distributions as a function of the kinetic energy of the ions. It is striking that the gold ion charge states decrease with increasing kinetic energy, especially for energies exceeding 4 MeV/u. At a first glance, this appears counterintuitive, as ions with lower mass-to-charge ratio are generally exposed to higher acceleration forces. Consequently, ions with higher charge states should actually end up with higher kinetic energies after the same acceleration time. However, the authors of reference [49] have observed in their simulations a similar behaviour of their ion bunches compared to our measurements and found as well higher kinetic energies from ions with lower charge states. They explained their finding by the sequential nature of the ionization dynamics in combination with the relatively long laser pulse: initially, all ions in the high laser field region are similarly ionized. However, faster particles leave the high-ionizing-field area relatively early and thus keep their lower charge state during their acceleration, while slower particles remain in the high-field region, where they get further ionized to higher charge states. Despite their more efficient acceleration, these particles cannot catch up with the lowly charged particles due to the limited remaining acceleration time. Certainly, this is a reasonable explanation for the results of this experiment showing highest energies from lower ion charge states. However, further simulations would be desirable in order to find a sound answer to this issue.

A comparison of some general thickness-dependent trends from the beamtime at the PHELIX laser with the earlier experiment at the TPW is drawn in Fig. 4.46. In panel (a),

[17] The probability is linearly dependent on the foil thickness and accordingly smaller for thinner foils.

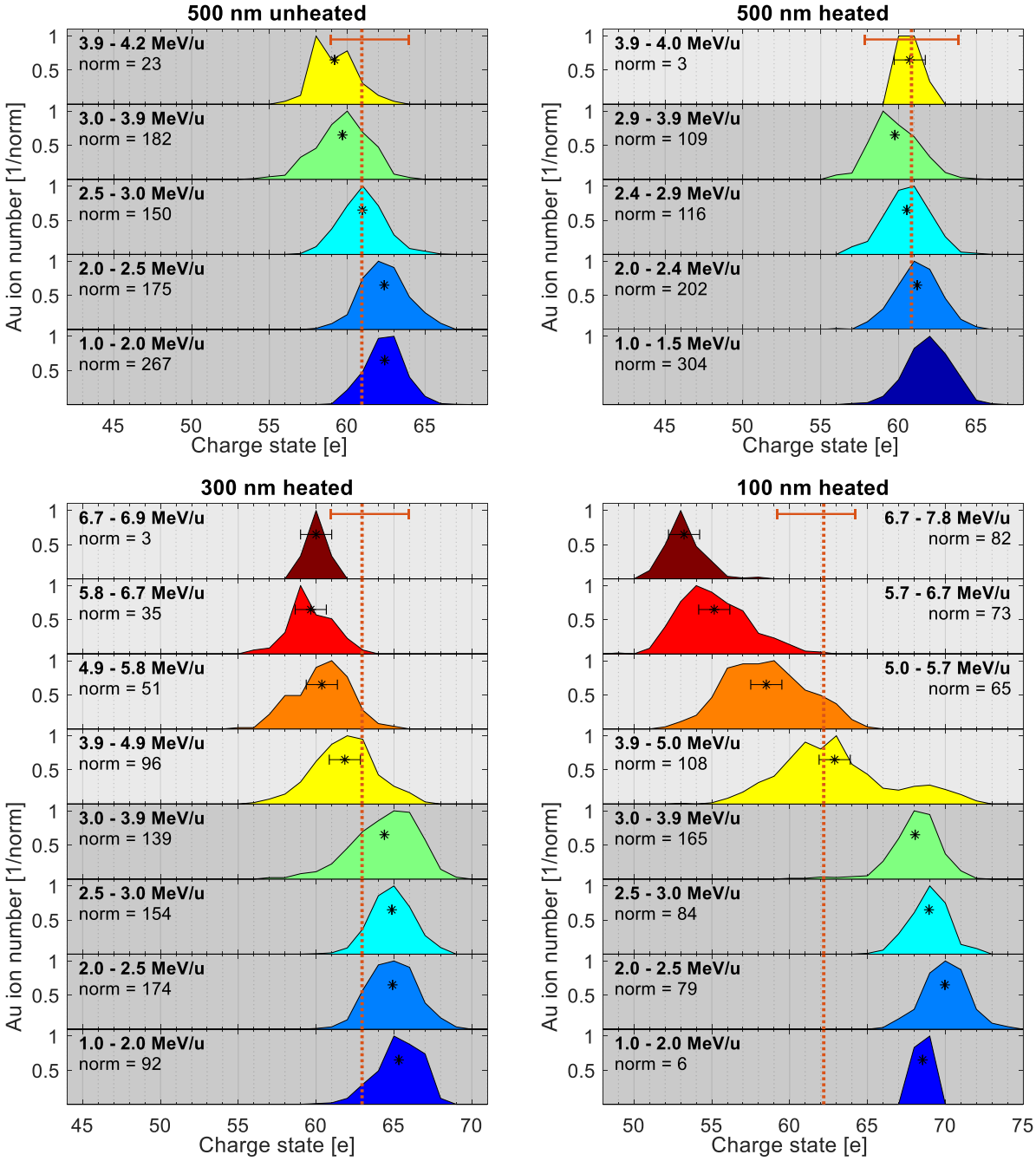

Figure 4.44: Energy dependent gold ion charge state distributions for shots on gold foils of varying thickness. The ion numbers of each distribution were normalized to their respective maximum, which is stated for each panel individually ('norm = X'). The respective mean value has been indicated as an asterisk (*) for each charge state distribution. The error bars in the four topmost panels indicate the charge state resolution within the shown distribution. The total charge state mean value, averaged over all kinetic energies, is indicated by the dotted, orange line. The uncertainty of the charge state range itself is indicated by the orange error bar surrounding the total mean charge state in the topmost plot.

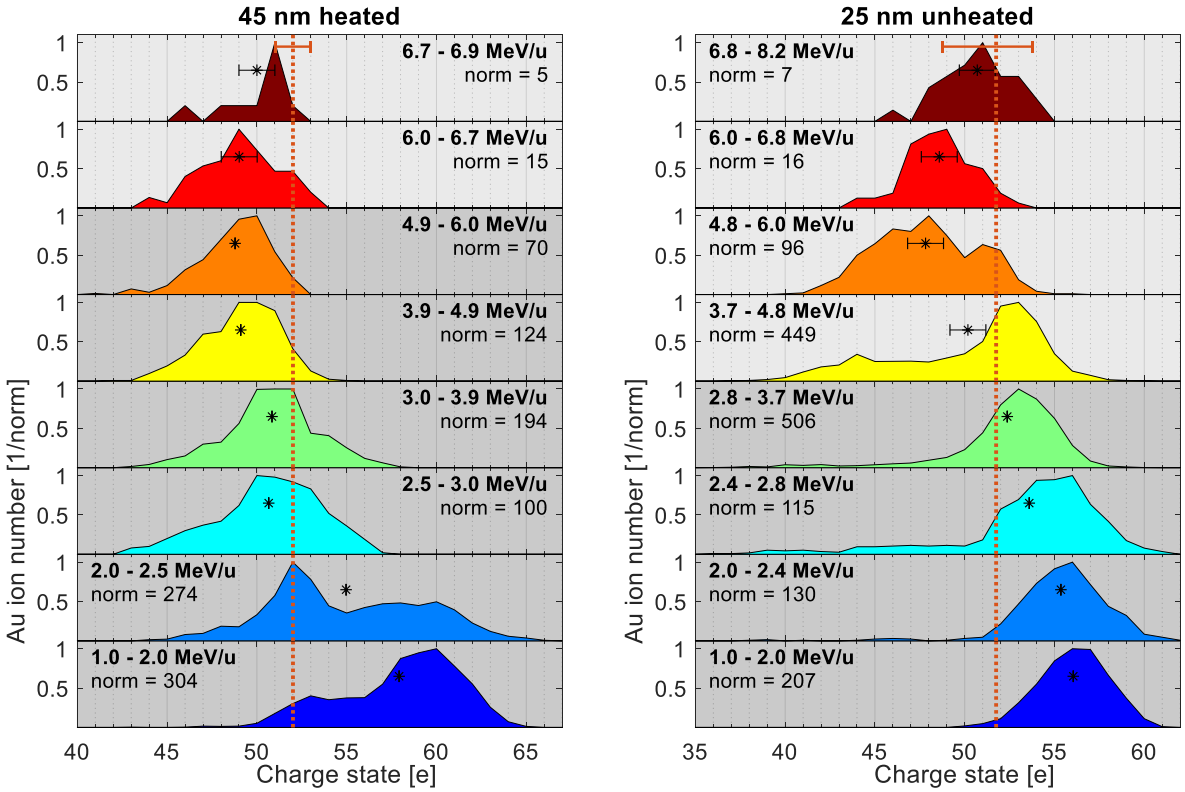

Figure 4.45: Energy dependent gold ion charge state distributions for shots on gold foils of varying thickness. The ion numbers of each distribution were normalized to their respective maximum, which is stated for each panel individually ('norm = X'). The respective mean value has been indicated as an asterisk (*) for each charge state distribution. The error bars in the four topmost panels indicate the charge state resolution within the shown distribution. The total charge state mean value, averaged over all kinetic energies, is indicated by the dotted, orange line. The uncertainty of the charge state range itself is indicated by the orange error bar surrounding the total mean charge state in the topmost plot.

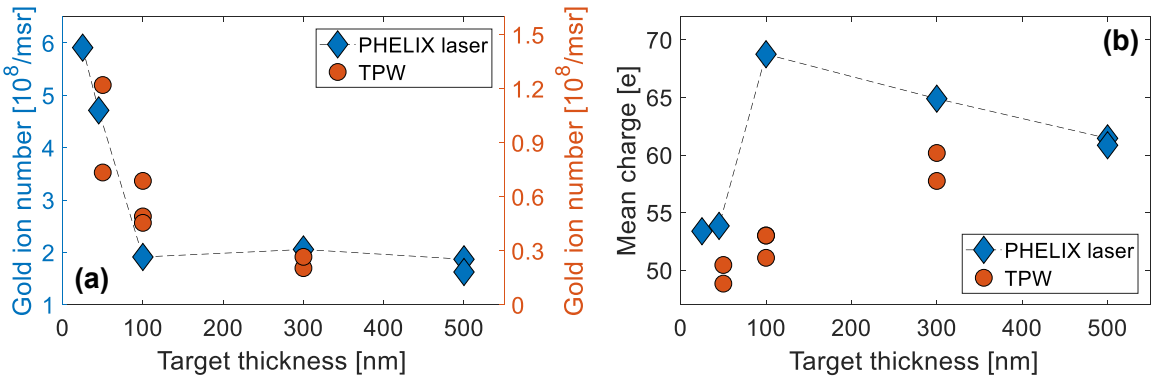

Figure 4.46: (a) Number of gold ions that have been accelerated in target normal direction for the experiment at the PHELIX laser (blue, left ordinate) and the TPW beamtime (orange, right y-axis), plotted versus the target thickness. The ion numbers have been normalized to the respective solid angle that was accepted by the TPS: 1.51×10^{-5} msr for the PHELIX laser and 2.25×10^{-5} msr for the TPW. (b) Mean charge state of detected gold ions that have been accelerated in target normal direction, plotted versus the target thickness.

the number of gold ions detected in target normal direction (normalized to their solid angle) is plotted against the target thickness. The data from the experiment at the PHELIX laser is displayed in blue (left ordinate), while the results from the TPW beamtime are plotted in orange (right ordinate). The ion number values on the right y-axis are about four times lower than these from the left ordinate, which means that the number of detected gold ions was accordingly higher for the experiment at the PHELIX laser. As can be seen, the general trend of an increasing ion number within the target normal direction for thinner targets can be confirmed for target foil thicknesses below 100 nm, while the ion number remains pretty much on the same level for the remaining foil thicknesses. In panel (b) of Fig. 4.46, the mean charge states of the ions with energies between 1.8 and 4 MeV/u (yellow points in the green distributions in Fig. 4.43) have been plotted against the target thickness, showing the thickness dependency discussed above. As a comparison, the mean charge states from the TPW data are displayed in orange. A fair comparison is of course not valid due to the lack of charge state resolution in the TPW experiment. However, in both experiments is observed that the foils with thicknesses below 100 nm show the lowest mean charge states.

4.2.8 Concluding Remarks

After the beamtime at the TPW, which was presented in Sec. 4.1, this beamtime at the PHELIX laser was the second experiment of our group aiming at the study of laser-driven

acceleration of gold ions. The success of this campaign can be summarized in two major results: first, the maximum hitherto published gold ion energies could be further increased from 5 MeV/u at the TPW and 6.1 MeV/u in reference [51] to beyond 7 MeV/u. The required energy barrier for the fission-fusion reaction mechanism has been reached for the first time with laser-accelerated heavy ions. Second, the charge state distribution of laser-accelerated gold ions could be measured experimentally with an unprecedented resolution. However, the distributions of the charge states cannot easily be explained with the known ionization mechanisms, which motivates further theoretical simulations in order to acquire a deeper understanding of the underlying ionization and acceleration mechanisms.

The drawbacks that have been identified in the setup of the experiment at the TPW, as outlined in Sec. 4.1.5, have been significantly improved. Most importantly, both energy and charge state resolution have been enhanced in the heavy ion diagnostics. However, the design goal (see Sec. 3.3.3) was not fully reached for both parameters. The energy resolution suffers especially from the unprecise calibration method for the magnetic field, which deteriorates the intrinsic energy resolution of the TPS considerably (compare panels (a) and (b) in Fig. 4.34). Originally, it was intended to apply the same calibration method as for the TPW experiment using the zero point and the proton energy cutoff after the 1 mm thick CR-39 layer on the IP. However, both points were not visible on the IPs. Contrary to the experiment design, the trajectory with the respective proton cutoff energy clipped at the drift tube connecting the main vacuum chamber with the extension chamber for the ion detector. And the zero point has not been detected, although a free optical path from the TPS pinhole to the detection screen was ensured. In future beamtimes, more time should be allowed for the zero point measurement and to deal with unexpected geometric restrictions, which hindered the measurement of the proton cutoff point behind the CR-39 layer in this experiment.

Another issue related to this campaign's TPS was the electric field, which collapsed after each shot. As a result, the gold ion charge states could only be identified within specific uncertainties, which varied from shot to shot due to the uncontrollable breakdown of the electric field. Though the determination of the relative charge distribution was hardly affected, the absolute charge states could not be ascertained with the intended accuracy of ≤ 1. As shown in Fig. 4.34(c), this had as well a severe impact on the energy resolution of the applied TPS, depending on the shot-specific uncertainty of the charge state range, as the particle deflection due to the Lorentz force in the magnetic field is depending not only on the kinetic energy, but also on the charge. The most likely reason for the collapse of the

electric field lies in the EMP accompanying the laser target interaction. The high voltage supplies were placed outside, but still close to the vacuum chamber and have not been encased by a Faraday cage and thus could have been affected by the EMP. An appropriate housing for the high voltage supplies has to be designed for future experiments. Shielding of the electrodes (respective the whole TPS dipole magnet including electrodes) and the cables in vacuum should be considered as well.

Compared to the TPW experiment, a more effective target heating has been realized: in two shots the complete proton signal in the energy range detectable by the TPS was removed. The surveillance of the target surface by a camera throughout the heating process was enabled by the simultaneous usage of the optical path for the temperature measurement and the focus diagnostics employing a flippable, remotely controllable mirror. As supposed after the beamtime at the TPW (see Sec. 4.1.5), it was observed that the target foil indeed deforms and moves slightly out of the focus during the heating. Thus, the position of the target along the laser axis had to be corrected for several tens of μm as a consequence of the foil deformation due to the heating process. However, the heating procedure and temperature control still allow for improvement. The heating setup needed to be adapted and advanced during the beamtime, until satisfying target cleaning results have been achieved. A reliable calculation of the target temperature from the thermal spectrum was not feasible. Thus, more knowledge about the heating characteristics and the temperature determination has to be gained to ensure an effective, controlled and reproducible target cleaning in future experimental campaigns, which was addressed by a subsequent master thesis work [157], which was still in preparation at the time of finishing this dissertation.

Chapter 5

Conclusion and Outlook

The availability of data regarding laser-driven acceleration of heavy ions in the mass range of $A \approx 200$ was very sparse at the beginning of this dissertation. The necessity of such high-density, laser-accelerated heavy ion bunches for the realization of the fission-fusion reaction mechanism motivated this thesis work with the declared goal of substantial progress towards the required bunch properties. In this dissertation, two experimental campaigns have been presented which pushed the heavy ion energies into the regime relevant for the fission-fusion reaction mechanism (≈ 7 MeV/u). The first one at the Texas Petawatt laser at the University of Texas at Austin, USA, resulted in kinetic gold ion energies of 5 MeV/u, being a factor of 2.5 higher than the maximum measured heavy ion energies which had been published back then. The gold ions generated during the second campaign, performed at the PHELIX laser of the GSI in Darmstadt, Germany, exceeded the energy barrier of 7 MeV/u, which is the first experimental proof of kinetic laser-accelerated heavy ion energies in the required range for the fission-fusion reaction mechanism. Furthermore, the gold ion charge state distributions have been measured with a very high resolution, which enabled the distinction of individual charge states of laser-accelerated heavy ions for the first time. The standard ionization mechanisms, which are expected to be dominant, do not deliver a straight-forward answer to the recorded charge state distributions. Therefore, the measured data raise new questions and are a valuable input for further theoretical investigations regarding the ionization dynamics in laser-generated plasmas.

With the laser-driven acceleration of heavy ions to kinetic energies above 7 MeV/u, a first major milestone towards the realization of the fission-fusion reaction mechanism has been accomplished. Starting from here, further studies are required in preparation for the pursued generation of neutron-rich r-process isotopes applying this reaction scheme. First,

the laser-driven heavy ion source needs to be advanced. A central goal is the realization of the acceleration in the RPA regime, as this results in a more efficient energy transfer to the heavy ions and, in particular, in a narrow-bandwidth energy distribution, which potentially could be tuned to be located around the fission-fusion barrier. This is essential, as only a small fraction of the exponentially decaying TNSA-like spectra is above this barrier. This substantially affects the fission-fusion yield, as the bulk of the laser-accelerated ions does not contribute. Further, the acceleration of heavy ions, which has been practiced with gold in this dissertation due to its ease of use, needs to be adapted to radioactive thorium targets, which need special care with respect to radioprotection measures. However, the relative mass difference between thorium and gold ions is rather low, which is why a similar acceleration dynamics may be expected, although the target cleaning will gain in importance regarding the high degree of oxidation at thorium surfaces.

Second, the fission of laser-accelerated heavy ions at light target ions and fission of heavy target ions induced by laser-accelerated light ions has to be investigated. The first proof-of-principle experiment showing the latter has recently been published in reference [174]. The authors induced fission of uranium ions by laser-accelerated protons and extracted the fission products using a fast gas-flow transport system. This technology needs to be adopted and further advanced in preparation for the measurement of laser-induced fission products and, later on, fission-fusion products. The demonstration of fission of laser-accelerated heavy ions at light target ions requires first the development of the laser-based acceleration of ions heavier than gold (e.g. thorium), as the fission barrier of gold is around $22 - 23$ MeV/u [175], which is still far above the results achieved in this thesis.

Third, the influence of collective effects needs to be investigated that potentially accompany the interaction of the laser-accelerated, ultra-dense ion bunch with the target material. Habs et al. assumed in reference [26] an ion range enhancement by a factor of 100 due to a reduced stopping power of such a ion bunch impinging on a solid foil, which would allow for a 100 times thicker reaction target, possibly resulting in a fission-fusion yield increased by four orders of magnitude. On the other hand, if these ultra-dense particle bunches interact with gaseous targets, the stopping power could be enhanced by some orders of magnitude due to collective deceleration by resonantly driven plasma wake fields, which could lead to a significant reduction of the size and costs of beam dumps [176].

At the Centre for Advanced Laser Applications (CALA) in Garching near Munich, the "High Field" (HF) beamlime has recently started operation. This beamline is dedicated to research towards the realization of the fission-fusion reaction mechanism and will tackle

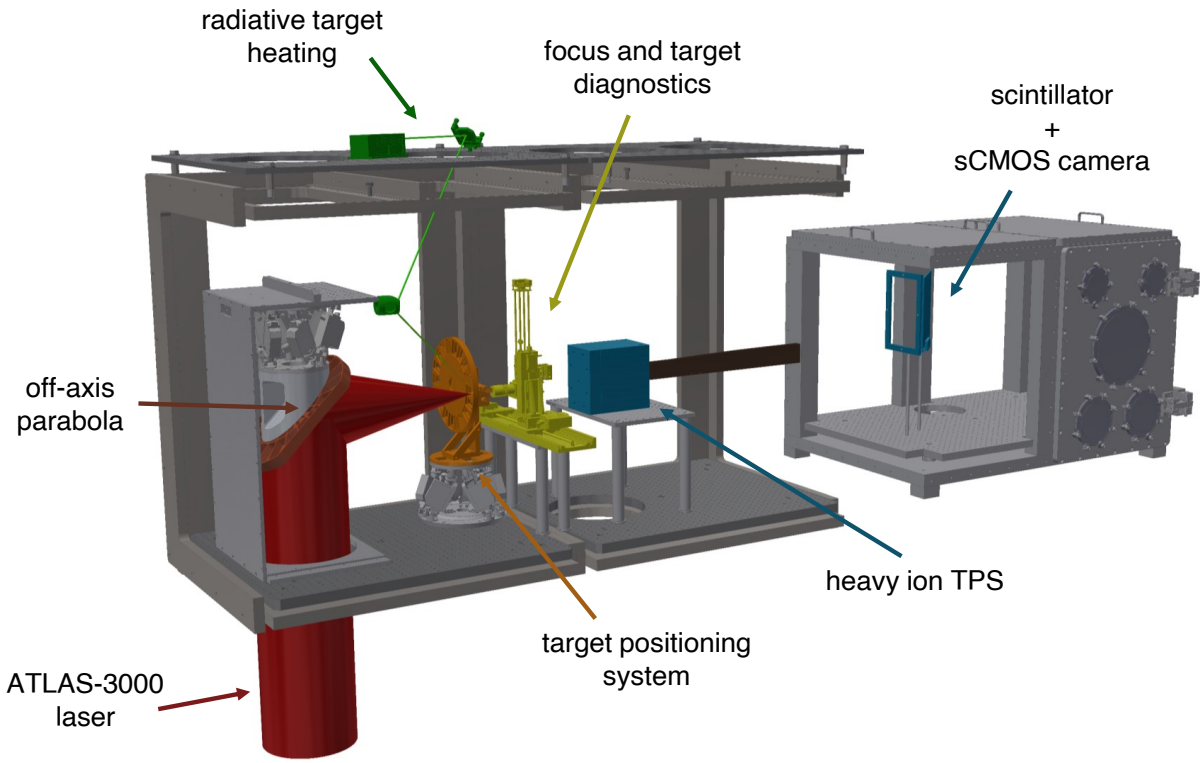

Figure 5.1: Experimental setup at the HF beamline at CALA with technology based on reference [17]. The ATLAS-3000 is focused by an off-axis parabolic mirror onto heavy ion target foils, positioned by a nano-foil target positioning system (orange) [177]. The laser focus is diagnosed and overlaid with the target by an optical microscope (yellow). Surface contaminants can be radiatively removed by a green cw laser (green), as described in Sec. 3.4. As ion diagnostics, the heavy ion TPS introduced in Sec. 3.3.3 will be used, together with the scintillator/sCMOS camera combination presented in Sec. 3.2.4.

the outlined topics. The basic experimental setup at this beamline has been substantially advanced during this thesis work and is sketched in Fig. 5.1, combining the technological improvements required for laser-driven heavy ion acceleration, as elucidated in Chapter 3. At this beamline, the technology for the production and measurement of the fission-fusion products will be developed, before it will be applied at the new 2×10 PW high power laser at the Extreme Light Infrastructure – Nuclear Physics (ELI-NP) in Măgurele near Bucharest with envisaged intensities of up to 10^{23} W/cm^2 [178]. These high intensities are expected to be favourable for the RPA-based acceleration of heavy ions, promising the successful application of the fission-fusion reaction mechanism with the generation of the desired neutron-rich r-process isotopes.

Index of Abbreviations

ADK	Ammosov Delone Krainov
ADU	analog-to-digital unit
ATLAS	Advanced Ti:Sapphire Laser
ATLAS-300	Advanced Ti:Sapphire Laser 300 Terawatt
ATLAS-3000	Advanced Ti:Sapphire Laser 3000 Terawatt
BSI	barrier-suppression ionization
CALA	the Centre for Advanced Laser Applications
CMOS	complementary metal oxide semiconductor
CPA	chirped pulse amplification
CR-39	Columbia Resin #39
cw	continuous-wave
DPSSL	diode-pumped solid-state laser
ELI-NP	Extreme Light Infrastructure – Nuclear Physics
EMP	electromagnetic pulse
GSI	GSI Helmholtzzentrum für Schwerionenforschung
HF	High Field
IP	imaging plate
LEX Photonics	the Laboratory for Extreme Photonics
NaOH	sodium hydroxide solution
NIR	near infrared
OPA	optical parametric amplifier
OPCPA	optical parametric chirped pulse amplification

PHELIX laser	Petawatt High Energy Laser for heavy Ion eXperiments
PSL	photostimulated luminescence
RPA	radiation pressure acceleration
SSNTD	solid-state nuclear track detector
TC	target chamber
Ti:sapphire	titanium-sapphire
Ti:sapphire laser	titanium-sapphire laser
TNSA	target normal sheath acceleration
TPS	Thomson parabola spectrometer
TPW	Texas Petawatt laser
WASP	wide-angle spectrometer

List of Scientific Contributions

Peer-reviewed Publications

2017

- **F.H. Lindner**, D. Haffa, J.H. Bin, F. Englbrecht, Y. Gao, J. Gebhard, J. Hartmann, P. Hilz, C. Kreuzer, S. Lehrack, T.M. Ostermayr, T.F. Rösch, M. Speicher, M. Würl, K. Parodi, J. Schreiber, P.G. Thirolf. *"Towards swift ion bunch acceleration by high-power laser pulses at the Centre for Advanced Laser Applications (CALA)."* Nuclear Instruments and Methods in Physics Research Section B: Beam Interactions with Materials and Atoms 402, 354-357 (2017)

- Y. Gao, J.H. Bin, D. Haffa, C. Kreuzer, J. Hartmann, M. Speicher, **F.H. Lindner**, T.M. Ostermayr, P. Hilz, T.F. Rösch, S. Lehrack, F. Englbrecht, S. Seuferling, M. Gilljohann, H. Ding, W. Ma, K. Parodi, J. Schreiber. *"An automated, 0.5 Hz nano-foil target positioning system for intense laser plasma experiments."* High Power Laser Science and Engineering 5, e12 (2017)

2018

- **F.H. Lindner**, J.H. Bin, F. Englbrecht, D. Haffa, P.R. Bolton, Y. Gao, J. Hartmann, P. Hilz, C. Kreuzer, T.M. Ostermayr, T.F. Rösch, M. Speicher, K. Parodi, P.G. Thirolf, J. Schreiber. *„A novel approach to electron data background treatment in an online wide-angle spectrometer for laser-accelerated ion and electron bunches."* Review of Scientific Instruments 89, 013301 (2018)

- P. Hilz, T.M. Ostermayr, A. Huebl, V. Bagnoud, B. Borm, M. Bussmann, M. Gallei, J. Gebhard, D. Haffa, J. Hartmann, T. Kluge, **F.H. Lindner**, P. Neumayr, C.G. Schaefer, U. Schramm, P.G. Thirolf, T.F. Rösch, F. Wagner, B. Zielbauer, J.

Schreiber. *"Isolated Proton Bunch Acceleration by a Peta-Watt Laser Pulse."* Nature Communications 9(1), 423 (2018)

- F.S. Englbrecht, M. Würl, F. Olivari, A. Ficorella, C. Kreuzer, **F.H. Lindner**, M. Dalla Palma, L. Pancheri, G.F. Dalla Betta, J. Schreiber, A. Quaranta, K. Parodi. *"An online, radiation hard proton energy-resolving scintillator stack for laser-driven proton bunches."* Radiation Protection Dosimetry 180(1-4), 291-295 (2018)

- M. Speicher, D. Haffa, M.A.O. Haug, J.H. Bin, Y. Gao, J. Hartmann, P. Hilz, C. Kreuzer, **F.H. Lindner**, T.M. Ostermayr, T. F. Rösch, R. Yang, J. Schreiber. *„Integrated double-plasma-mirror targets for contrast enhancement in laser ion acceleration."* Journal of Physics: Conference Series 1079, 012002 (2018)

- M. Würl, F.S. Englbrecht, S. Lehrack, C. Gianoli, **F.H. Lindner**, T.F. Rösch, D. Haffa, F. Olivari, M. Petasecca, M.L.F. Lerch, A. Pogossov, L.T. Tran, W. Assmann, J. Schreiber, A.B. Rosenfeld, K. Parodi. *"Time-of-Flight Spectrometry of Ultra-Short, Polyenergetic Proton Bunches."* Review of Scientific Instruments 89, 123302 (2018)

2019

- **F.H. Lindner**, E. McCary, X. Jiao, T.M. Ostermayr, R. Roycroft, G. Tiwari, B.M. Hegelich, J. Schreiber, P.G. Thirolf. *"En-route to the fission-fusion reaction mechanism: a status update on laser-driven heavy ion acceleration."* Plasma Physics and Controlled Fusion 61, 055002 (2019)

- D. Haffa, R. Yang, J.H. Bin, S. Lehrack, H. Ding, F.S. Englbrecht, Y. Gao, J. Gebhard, J. Goetzfried, M. Gilljohann, J. Hartmann, S. Herr, P. Hilz, C. Kreuzer, **F.H. Lindner**, E. Ridente, T.F. Rösch, G. Schilling, M. Speicher, D. Taray, T.M. Ostermayr, M. Würl, W. Assmann, S. Karsch, K. Parodi, J. Schreiber. *"Ion Bunch Energy Acoustic Tracing (I-BEAT)."* Scientific Reports 9, 6714 (2019)

2020

- T.F. Rösch, Z. Szabó, D. Haffa, J.H. Bin, S. Brunner, F.S. Englbrecht, A.A. Friedl, Y. Gao, J. Hartmann, P. Hilz, C. Kreuzer, **F.H. Lindner**, T.M. Ostermayr, R. Polanek, M. Speicher, E.R. Szabó, D. Taray, T. Tőkés, M. Würl, K. Parodi, K. Hideghéty,

J. Schreiber. *"A feasibility study of embryo irradiation with laser-accelerated protons"* Review of Scientific Instruments 91, 063303 (2020)

- F.S. Englbrecht, A. Döpp, J. Hartmann, **F.H. Lindner**, M.L. Groß, H.-F. Wirth, P.G. Thirolf, S. Karsch, J. Schreiber, K. Parodi, G. Dedes. *"Radiation protection modelling for 2.5 Petawatt-laser production of ultrashort x-ray, proton and ion bunches: Monte Carlo model of the Munich CALA facility"* Journal of Radiological Protection 40, 1048 (2020)

Other Publications

- T.F. Rösch, P. Hilz, J.H. Bin, F. Englbrecht, Y. Gao, D. Haffa, J. Hartmann, S. Herr, **F.H. Lindner**, M. Speicher, M. Würl, K. Parodi, J. Schreiber. *"Considerations on employing a PMQ-doublet for narrow and broad proton energy distributions"* Current Directions in Biomedical Engineering 3(2), 339-342 (2017)

- F.S. Englbrecht, F. Balling, T.F. Rösch, M. Würl, **F.H. Lindner**, K. Parodi, J. Schreiber. *"Characterization of online high dynamic range imaging for laser-driven ion beam diagnostics using visible light"* Current Directions in Biomedical Engineering 3(2), 343-346 (2017)

Conference Contributions

- **Oral:** *"Swift Ion Bunch Acceleration by High Power Laser Pulses."* 7$^{\text{th}}$ International Conference Charged & Neutral Particles Channeling Phenomena, Sirmione - Desenzano del Garda, Italy (2016)

- **Oral:** *"Laser-driven acceleration of gold ions in preparation of the fission-fusion reaction scheme."* Nuclear Photonics, Brașov, Romania (2018)

- **Poster:** *"Progress on Laser Driven Heavy Ion Acceleration in the Light of the Fission Fusion Reaction Mechanism"* The 3$^{\text{rd}}$ International Conference on Extreme Light, Prague, Czech Republic (2019)

Bibliography

[1] Strickland, D. and Mourou, G. *Optics Communications* **56**(3), 219–221 (1985).

[2] Hatchett, S. P., Brown, C. G., Cowan, T. E., Henry, E. A., Johnson, J. S., Key, M. H., Koch, J. A., Langdon, A. B., Lasinski, B. F., Lee, R. W., Mackinnon, A. J., Pennington, D. M., Perry, M. D., Phillips, T. W., Roth, M., Sangster, T. C., Singh, M. S., Snavely, R. A., Stoyer, M. A., Wilks, S. C., and Yasuike, K. *Physics of Plasmas* **7**(5), 2076–2082 (2000).

[3] Snavely, R. A., Key, M. H., Hatchett, S. P., Cowan, T. E., Roth, M., Phillips, T. W., Stoyer, M. A., Henry, E. A., Sangster, T. C., Singh, M. S., Wilks, S. C., MacKinnon, A., Offenberger, A., Pennington, D. M., Yasuike, K., Langdon, A. B., Lasinski, B. F., Johnson, J., Perry, M. D., and Campbell, E. M. *Physical Review Letters* **85**(14), 2945–2948 (2000).

[4] Daido, H., Nishiuchi, M., and Pirozhkov, A. S. *Reports on Progress in Physics* **75**(5), 056401 (2012).

[5] Macchi, A., Borghesi, M., and Passoni, M. *Reviews of Modern Physics* **85**(2), 751–793 (2013).

[6] Schreiber, J., Bolton, P. R., and Parodi, K. *Review of Scientific Instruments* **87**(7), 071101 (2016).

[7] Bolton, P. R., Parodi, K., and Schreiber, J., editors. *Applications of laser-driven particle acceleration*. CRC Press, Taylor and Francis Group, Boca Raton, FL (2018).

[8] Schmidhammer, U., Ma, J., and Mehran, M. In *Applications of laser-driven particle acceleration,* Bolton, P. R., Parodi, K., and Schreiber, J., editors, 111–128. CRC Press, Taylor and Francis Group, Boca Raton, FL (2018).

[9] Shikazono, N., Moribayashi, K., and Bolton, P. R. In *Applications of laser-driven particle acceleration,* Bolton, P. R., Parodi, K., and Schreiber, J., editors, 151–164. CRC Press, Taylor and Francis Group, Boca Raton, FL (2018).

[10] Bulanov, S., Esirkepov, T., Khoroshkov, V., Kuznetsov, A., and Pegoraro, F. *Physics Letters A* **299**(2-3), 240–247 (2002).

[11] Karsch, L., Beyreuther, E., Enghardt, W., Gotz, M., Masood, U., Schramm, U., Zeil, K., and Pawelke, J. *Acta Oncologica* **56**(11), 1359–1366 (2017).

[12] Kraft, S. D., Richter, C., Zeil, K., Baumann, M., Beyreuther, E., Bock, S., Bussmann, M., Cowan, T. E., Dammene, Y., Enghardt, W., Helbig, U., Karsch, L., Kluge, T., Laschinsky, L., Lessmann, E., Metzkes, J., Naumburger, D., Sauerbrey, R., Schürer, M., Sobiella, M., Woithe, J., Schramm, U., and Pawelke, J. *New Journal of Physics* **12**(8), 085003 (2010).

[13] Bin, J., Allinger, K., Assmann, W., Dollinger, G., Drexler, G. A., Friedl, A. A., Habs, D., Hilz, P., Hoerlein, R., Humble, N., Karsch, S., Khrennikov, K., Kiefer, D., Krausz, F., Ma, W., Michalski, D., Molls, M., Raith, S., Reinhardt, S., Röper, B., Schmid, T. E., Tajima, T., Wenz, J., Zlobinskaya, O., Schreiber, J., and Wilkens, J. J. *Applied Physics Letters* **101**(24), 243701 (2012).

[14] Zeil, K., Baumann, M., Beyreuther, E., Burris-Mog, T., Cowan, T. E., Enghardt, W., Karsch, L., Kraft, S. D., Laschinsky, L., Metzkes, J., Naumburger, D., Oppelt, M., Richter, C., Sauerbrey, R., Schürer, M., Schramm, U., and Pawelke, J. *Applied Physics B* **110**(4), 437–444 (2013).

[15] Masood, U., Bussmann, M., Cowan, T. E., Enghardt, W., Karsch, L., Kroll, F., Schramm, U., and Pawelke, J. *Applied Physics B* **117**(1), 41–52 (2014).

[16] Hofmann, K. M., Masood, U., Pawelke, J., and Wilkens, J. J. *Medical Physics* **42**(9), 5120–5129 (2015).

[17] Rösch, T. F., Szabó, Z., Haffa, D., Bin, J., Brunner, S., Englbrecht, F. S., Friedl, A. A., Gao, Y., Hartmann, J., Hilz, P., Kreuzer, C., Lindner, F. H., Ostermayr, T. M., Polanek, R., Speicher, M., Szabó, E. R., Taray, D., Tőkés, T., Würl, M., Parodi, K., Hideghéty, K., and Schreiber, J. *Review of Scientific Instruments* **91**(6), 063303 (2020).

[18] Beyreuther, E., Brand, M., Hans, S., Hideghéty, K., Karsch, L., Leßmann, E., Schürer, M., Szabó, E. R., and Pawelke, J. *Radiotherapy and Oncology* **139**, 46–50 (2019).

[19] Schippers, J. M., Lomax, A., Garonna, A., and Parodi, K. *Seminars in Radiation Oncology* **28**(2), 150–159 (2018).

[20] Ostermayr, T. M., Kreuzer, C., Englbrecht, F. S., Gebhard, J., Hartmann, J., Huebl, A., Haffa, D., Hilz, P., Parodi, K., Wenz, J., Donovan, M. E., Dyer, G., Gaul, E., Gordon, J., Martinez, M., McCary, E., Spinks, M., Tiwari, G., Hegelich, B. M., and Schreiber, J. *Nature Communications* **11**, 6174 (2020).

[21] Passoni, M., Fedeli, L., and Mirani, F. *Scientific Reports* **9**(1), 9202 (2019).

[22] Roth, M., Jung, D., Falk, K., Guler, N., Deppert, O., Devlin, M., Favalli, A., Fernandez, J., Gautier, D., Geissel, M., Haight, R., Hamilton, C. E., Hegelich, B. M., Johnson, R. P., Merrill, F., Schaumann, G., Schoenberg, K., Schollmeier, M., Shimada, T., Taddeucci, T., Tybo, J. L., Wagner, F., Wender, S. A., Wilde, C. H., and Wurden, G. A. *Physical Review Letters* **110**, 044802 (2013).

[23] Higginson, D., Vassura, L., Gugiu, M., Antici, P., Borghesi, M., Brauckmann, S., Diouf, C., Green, A., Palumbo, L., Petrascu, H., Sofia, S., Stardubtsev, M., Willi, O., Kar, S., Negoita, F., and Fuchs, J. *Physical Review Letters* **115**(5), 054802 (2015).

[24] Favalli, A., Guler, N., Henzlova, D., Croft, S., Falk, K., Gautier, D. C., Ianakiev, K. D., Iliev, M., Palaniyappan, S., Roth, M., Fernandez, J. C., and Swinhoe, M. T. *Scientific Reports* **9**(1), 2004 (2019).

[25] Sóti, Z., Magill, J., and Dreher, R. *EPJ Nuclear Sciences & Technologies* **5**, 6 (2019).

[26] Habs, D., Thirolf, P. G., Gross, M., Allinger, K., Bin, J., Henig, A., Kiefer, D., Ma, W., and Schreiber, J. *Applied Physics B* **103**(2), 471–484 (2011).

[27] Beringer, J. et al. *Physical Review D* **86**(1), 010001 (2012).

[28] Coc, A. and Vangioni, E. *International Journal of Modern Physics E* **26**(8), 1741002 (2017).

[29] Olive, K. A. and Skillman, E. D. *The Astrophysical Journal* **617**, 29–49 (2004).

[30] Burbidge, E. M., Burbidge, G. R., Fowler, W. A., and Hoyle, F. *Reviews of Modern Physics* **29**(4), 547–650 (1957).

[31] Sneden, C. and Cowan, J. J. *Science* **299**(5603), 70–75 (2003).

[32] Cowan, J. J. and Thielemann, F.-K. *Physics Today* **57**(10), 47–53 (2004).

[33] Arnould, M., Goriely, S., and Takahashi, K. *Physics Reports* **450**(4-6), 97–213 (2007).

[34] Käppeler, F. et al. *Reviews of Modern Physics* **83**(1), 157–193 (2011).

[35] Thielemann, F.-K. et al. *Progress in Particle and Nuclear Physics* **66**(2), 346–353 (2011).

[36] Abbott, B. P. et al. *Physical Review Letters* **119**(16), 161101 (2017).

[37] Pian, E. et al. *Nature* **551**, 67–70 (2017).

[38] Kasen, D., Metzger, B., Barnes, J., Quataert, E., and Ramirez-Ruiz, E. *Nature* **551**(7678), 80–84 (2017).

[39] Horowitz, C. J. et al. *Journal of Physics G: Nuclear and Particle Physics* **46**(8), 083001 (2019).

[40] Bollen, G. *AIP Conference Proceedings* **1224**, 432–441 (2010).

[41] Okuno, H., Fukunishi, N., and Kamigaito, O. *Progress of Theoretical and Experimental Physics* **2012**(1), 03C002 (2012).

[42] Gutbrod, H., editor. *FAIR Baseline Technical Report, Volume 2 Accelerator and Scientific Infrastructure*. GSI Darmstadt (2006).

[43] Chen, S. N., Negoita, F., Spohr, K., d'Humières, E., Pomerantz, I., and Fuchs, J. *Matter and Radiation at Extremes* **4**(5), 054402 (2019).

[44] Clark, E. L., Krushelnick, K., Zepf, M., Beg, F. N., Tatarakis, M., Machacek, A., Santala, M. I. K., Watts, I., Norreys, P. A., and Dangor, A. E. *Physical Review Letters* **85**(8), 1654–1657 (2000).

[45] Braenzel, J., Andreev, A., Platonov, K., Klingsporn, M., Ehrentraut, L., Sandner, W., and Schnürer, M. *Physical Review Letters* **114**(12), 124801 (2015).

[46] Petrov, G. M., McGuffey, C., Thomas, A. G. R., Krushelnick, K., and Beg, F. N. *Physics of Plasmas* **23**(6), 063108 (2016).

[47] Petrov, G. M., McGuffey, C., Thomas, A. G. R., Krushelnick, K., and Beg, F. N. *Plasma Physics and Controlled Fusion* **59**(7), 075003 (2017).

[48] Lindner, F. H., McCary, E., Jiao, X., Ostermayr, T. M., Roycroft, R., Tiwari, G., Hegelich, B. M., Schreiber, J., and Thirolf, P. G. *Plasma Physics and Controlled Fusion* **61**(5), 055002 (2019).

[49] Domanski, J. and Badziak, J. *Journal of Instrumentation* **15**, C05037 (2020).

[50] Nishiuchi, M., Dover, N. P., Hata, M., Sakaki, H., Kondo, K., Lowe, H. F., Miyahara, T., Kiriyama, H., Koga, J. K., Iwata, N., Alkhimova, M. A., Pirozhkov, A. S., Faenov, A. Y., Pikuz, T. A., Sagisaka, A., Watanabe, Y., Kando, M., Kondo, K., Ditter, E. J., Ettlinger, O. C., Hicks, G. S., Najmudin, Z., Ziegler, T., Zeil, K., Schramm, U., and Sentoku, Y. *Physical Review Research* **2**(3), 033081 (2020).

[51] Wang, P., Gong, Z., Lee, S. G., Shou, Y., Geng, Y., Jeon, C., Kim, I. J., Lee, W., Yoon, J. W., Sung, J. H., Lee, S. K., Kong, D., Liu, J., Mei, Z., Cao, Z., Pan, Z., Choi, I. W., Yan, X., Nam, C. H., and Ma, W. *arXiv:2008.09358 [physics.plasm-ph]* (2020).

[52] Keldysh, L. V. *Soviet Physics JETP* **20**(5), 1307–1314 (1965).

[53] Chin, S. L. *Advances in Multi-Photon Processes and Spectroscopy* **16**, 249–271 (2004).

[54] Augst, S., Strickland, D., Meyerhofer, D. D., Chin, S. L., and Eberly, J. H. *Physical Review Letters* **63**(20), 2212–2215 (1989).

[55] Augst, S., Meyerhofer, D. D., Strickland, D., and Chint, S. L. *Journal of the Optical Society of America B* **8**(4), 858–867 (1991).

[56] Penetrante, B. M. and Bardsley, J. N. *Physical Review A* **43**(6), 3100–3113 (1991).

[57] Gibson, G., Luk, T. S., and Rhodes, C. K. *Physical Review A* **41**(9), 5049–5052 (1990).

[58] Landau, L. D. and Lifshitz, E. M. *Quantum mechanics: non-relativistic theory.* Number 3 in Course of theoretical physics. Pergamon Press, Oxford, 3rd edition (1977).

[59] Chang, B., Bolton, P. R., and Fittinghoff, D. N. *Physical Review A* **47**(5), 4193–4203 (1993).

[60] Kramida, A., Ralchenko, Y., Reader, J., and NIST-ASD-Team. *NIST Atomic Spectra Database (version 5.7.1)*. https://physics.nist.gov/asd [visited on 08.07.2020]. National Institute of Standards and Technology, Gaithersburg, MD, USA (2019).

[61] Ammosov, M. V. and Krainov, V. P. *Soviet Physics JETP* **64**(6), 1191–1194 (1986).

[62] Märk, T. D. and Dunn, G. H., editors. *Electron Impact Ionization*. Springer-Verlag Wien, Vienna (1985).

[63] Lotz, W. *Zeitschrift für Physik* **206**, 205–211 (1967).

[64] Lotz, W. *Journal of the Optical Society of America* **60**(2), 206–210 (1970).

[65] Lotz, W. *Zeitschrift für Physik* **232**, 101–107 (1970).

[66] Lotz, W. *Zeitschrift für Physik* **216**, 241–247 (1968).

[67] Chen, F. F. *Introduction to Plasma Physics and Controlled Fusion*. Springer International Publishing AG Switzerland, Cham Heidelberg New York Dortrecht London, 3rd edition (2016).

[68] Kittel, C. *Introduction to solid state physics*. John Wiley & Sons, Inc, Hoboken, NJ, 8th edition (2005).

[69] Wilks, S. C., Kruer, W. L., Tabak, M., and Langdon, A. B. *Physical Review Letters* **69**(9), 1383–1386 (1992).

[70] Malka, G. and Miquel, J. L. *Physical Review Letters* **77**(1), 75–78 (1996).

[71] Wilks, S. and Kruer, W. *IEEE Journal of Quantum Electronics* **33**(11), 1954–1968 (1997).

[72] Freidberg, J. P., Mitchell, R. W., Morse, R. L., and Rudsinski, L. I. *Physical Review Letters* **28**(13), 795–799 (1972).

[73] Forslund, D. W., Kindel, J. M., and Lee, K. *Physical Review Letters* **39**(5), 284–288 (1977).

[74] Kruer, W. L. *The physics of laser plasma interactions.* Frontiers in physics. CRC Press, Taylor and Francis Group, Boca Raton, FL (2003).

[75] Brunel, F. *Physical Review Letters* **59**(1), 52–55 (1987).

[76] Kruer, W. L. and Estabrook, K. *The Physics of Fluids* **28**, 430–432 (1985).

[77] Wilks, S. C., Langdon, A. B., Cowan, T. E., Roth, M., Singh, M., Hatchett, S., Key, M. H., Pennington, D., and Snavely, R. A. *Physics of Plasmas* **8**(2), 542–549 (2001).

[78] Cowan, T. E., Fuchs, J., Ruhl, H., Kemp, A., Audebert, P., Roth, M., Stephens, R., Barton, I., Blazevic, A., Brambrink, E., Cobble, J., Fernández, J., Gauthier, J.-C., Geissel, M., Hegelich, M., Kaae, J., Karsch, S., Le Sage, G. P., Letzring, S., Manclossi, M., Meyroneinc, S., Newkirk, A., Pépin, H., and Renard-LeGalloudec, N. *Physical Review Letters* **92**(20), 204801 (2004).

[79] Nürnberg, F., Schollmeier, M., Brambrink, E., Blažević, A., Carroll, D. C., Flippo, K., Gautier, D. C., Geißel, M., Harres, K., Hegelich, B. M., Lundh, O., Markey, K., McKenna, P., Neely, D., Schreiber, J., and Roth, M. *Review of Scientific Instruments* **80**(3), 033301 (2009).

[80] Bin, J. H., Ma, W. J., Allinger, K., Wang, H. Y., Kiefer, D., Reinhardt, S., Hilz, P., Khrennikov, K., Karsch, S., Yan, X. Q., Krausz, F., Tajima, T., Habs, D., and Schreiber, J. *Physics of Plasmas* **20**(7), 073113 (2013).

[81] Rösch, T. F., Hilz, P., Bin, J., Englbrecht, F., Gao, Y., Haffa, D., Hartmann, J., Herr, S., Lindner, F. H., Speicher, M., Würl, M., Parodi, K., and Schreiber, J. *Current Directions in Biomedical Engineering* **3**(2), 339–342 (2017).

[82] Esirkepov, T., Borghesi, M., Bulanov, S. V., Mourou, G., and Tajima, T. *Physical Review Letters* **92**(17), 175003 (2004).

[83] Macchi, A., Cattani, F., Liseykina, T. V., and Cornolti, F. *Physical Review Letters* **94**(16), 165003 (2005).

[84] Henig, A., Steinke, S., Schnürer, M., Sokollik, T., Hörlein, R., Kiefer, D., Jung, D., Schreiber, J., Hegelich, B. M., Yan, X. Q., Meyer-ter Vehn, J., Tajima, T., Nickles, P. V., Sandner, W., and Habs, D. *Physical Review Letters* **103**(24), 245003 (2009).

[85] Kar, S., Kakolee, K. F., Qiao, B., Macchi, A., Cerchez, M., Doria, D., Geissler, M., McKenna, P., Neely, D., Osterholz, J., Prasad, R., Quinn, K., Ramakrishna, B., Sarri, G., Willi, O., Yuan, X. Y., Zepf, M., and Borghesi, M. *Physical Review Letters* **109**(18), 185006 (2012).

[86] Thirolf, P. G. In *The Euroschool on Exotic Beams - Vol. 5,* Scheidenberger, C. and Pfützner, M., editors, volume 948 of *Lecture Notes in Physics*, 255–292. Springer International Publishing, Cham (2018).

[87] Brenner, C. M., Robinson, A. P. L., Markey, K., Scott, R. H. H., Gray, R. J., Rosinski, M., Deppert, O., Badziak, J., Batani, D., Davies, J. R., Hassan, S. M., Lancaster, K. L., Li, K., Musgrave, I. O., Norreys, P. A., Pasley, J., Roth, M., Schlenvoigt, H.-P., Spindloe, C., Tatarakis, M., Winstone, T., Wolowski, J., Wyatt, D., McKenna, P., and Neely, D. *Applied Physics Letters* **104**(8), 081123 (2014).

[88] Andreyev, A. N., Nishio, K., and Schmidt, K.-H. *Rep. Prog. Phys.* **81**, 016301 (2018).

[89] Thirolf, P. G. *AIP Conference Proceedings* **1645**, 210–218 (2015).

[90] Lindner, F. H., Haffa, D., Bin, J., Englbrecht, F., Gao, Y., Gebhard, J., Hartmann, J., Hilz, P., Kreuzer, C., Lehrack, S., Ostermayr, T. M., Rösch, T. F., Speicher, M., Würl, M., Parodi, K., Schreiber, J., and Thirolf, P. G. *Nuclear Instruments and Methods in Physics Research Section B: Beam Interactions with Materials and Atoms* **402**, 354–357 (2017).

[91] Kreuzer, C. *Technological developments for Laser Ion Acceleration.* PhD thesis, Ludwig-Maximilians-Universität München (2018).

[92] Eliezer, S. *The interaction of high-power lasers with plasmas.* Series in plasma physics. Institute of Physics Publishing, Bristol (2002).

[93] Saleh, B. and Teich, M. *Fundamentals of Photonics.* John Wiley & Sons, Inc, Hoboken, NJ, 3rd edition (2019).

[94] Martinez, M., Gaul, E., Ditmire, T., Douglas, S., Gorski, D., Henderson, W., Blakeney, J., Hammond, D., Gerity, M., Caird, J., Erlandson, A., Iovanovic, I., Ebbers, C., and Molander, B. *Proceedings of SPIE* **5991**, 59911N (2006).

[95] Bagnoud, V., Aurand, B., Blazevic, A., Borneis, S., Bruske, C., Ecker, B., Eisenbarth, U., Fils, J., Frank, A., Gaul, E., Goette, S., Haefner, C., Hahn, T., Harres, K., Heuck, H.-M., Hochhaus, D., Hoffmann, D. H. H., Javorková, D., Kluge, H.-J., Kuehl, T., Kunzer, S., Kreutz, M., Merz-Mantwill, T., Neumayer, P., Onkels, E., Reemts, D., Rosmej, O., Roth, M., Stoehlker, T., Tauschwitz, A., Zielbauer, B., Zimmer, D., and Witte, K. *Applied Physics B* **100**(1), 137–150 (2010).

[96] Website Texas Petawatt laser. http://texaspetawatt.ph.utexas.edu/ (last accessed on 20.10.2020).

[97] Butkus, R., Danielius, R., Dubietis, A., Piskarskas, A., and Stabinis, A. *Applied Physics B* **79**(6), 693–700 (2004).

[98] Akhmanov, S., Kovrigin, A., Piskarskas, A., Fadeev, V., and Khokhlov, R. *JETP Letters* **2**(7), 191–193 (1965).

[99] Website PHELIX laser facility. https://www.gsi.de/en/work/research/appamml/plasma_physicsphelix/phelix.htm (last accessed on 20.10.2020).

[100] Wagner, F., João, C. P., Fils, J., Gottschall, T., Hein, J., Körner, J., Limpert, J., Roth, M., Stöhlker, T., and Bagnoud, V. *Applied Physics B* **116**(2), 429–435 (2014).

[101] Groening, L., Adonin, A., Du, X., Hollinger, R., Jaeger, E., Jäger, E., Maier, M. T., Mickat, S., Rubin, A., Schlitt, B., Schreiber, G., Vormann, H., Xiao, C., Yakushev, A., and Zhang, C. *Proceedings IPAC'16* , 880–882 (2016).

[102] Baumhacker, H., Böswald, A., Haas, H., Witte, K., Andiel, U., Bayerl, J., Dong, X., Dreher, M., Eidmann, K., Fischer, M., Hegelich, M., Kaluza, M., Karsch, S., Keller, G., Pretzler, G., Stehbeck, H., and Tsakiris, G. *Advanced Titanium Sapphire Laser ATLAS.* MPQ-Report 272, Max-Planck-Institut für Quantenoptik, Garching bei München, (2002).

[103] Mead, M. J., Neely, D., Gauoin, J., Heathcote, R., and Patel, P. *Review of Scientific Instruments* **75**(10), 4225–4227 (2004).

[104] Poyé, A., Hulin, S., Bailly-Grandvaux, M., Dubois, J.-L., Ribolzi, J., Raffestin, D., Bardon, M., Lubrano-Lavaderci, F., D'Humières, E., Santos, J. J., Nicolaï, P., and Tikhonchuk, V. *Physical Review E* **91**(4), 043106 (2015).

[105] Miyahara, J., Takahashi, K., Amemiya, Y., Kamiya, N., and Satow, Y. *Nuclear Instruments and Methods in Physics Research Section A* **246**(1-3), 572–578 (1986).

[106] Scheibe, B. GE Healthcare Europe GmbH. Private Communication, (2020).

[107] Takahashi, K. *Journal of Luminescence* **100**(1-4), 307–315 (2002).

[108] Ohuchi, H., Yamadera, A., and Nakamura, T. *Nuclear Instruments and Methods in Physics Research Section A* **450**(2-3), 343–352 (2000).

[109] Fleischer, R. L., Price, P. B., and Walker, R. M. *Journal of Applied Physics* **36**(11), 3645–3652 (1965).

[110] Bruneni, J. L. *More Than Meets The Eye. The Stories Behind the Development of Plastic Lenses*. PPG Industries, Inc., Pittsburgh, PA (1997).

[111] Cartwright, B., Shirk, E., and Price, P. *Nuclear Instruments and Methods* **153**(2-3), 457–460 (1978).

[112] Gaillard, S., Fuchs, J., Renard-Le Galloudec, N., and Cowan, T. E. *Review of Scientific Instruments* **78**(1), 013304 (2007).

[113] Adams, J. H. *Nuclear Tracks* **4**(2), 67–76 (1980).

[114] Khan, H. A., Brandt, R., Khan, N. A., and Jamil, K. *Nuclear Tracks and Radiation Measurements (1982)* **7**(3), 129–139 (1983).

[115] Jeong, T. W., Singh, P. K., Scullion, C., Ahmed, H., Hadjisolomou, P., Jeon, C., Yun, H., Kakolee, K. F., Borghesi, M., and Ter-Avetisyan, S. *Scientific Reports* **7**(1), 2152 (2017).

[116] Rad-icon Imaging Corp. *RadEye1. Large Area Image Sensor*. Santa Clara, CA (2008).

[117] Graeve, T. and Weckler, G. P. *Proceedings of SPIE* **4320**, 68–76 (2001).

[118] Bigas, M., Cabruja, E., Forest, J., and Salvi, J. *Microelectronics Journal* **37**(5), 433–451 (2006).

[119] Reinhardt, S. *Detection of laser-accelerated protons*. PhD thesis, Ludwig-Maximilians-Universität München (2012).

[120] Reinhardt, S., Draxinger, W., Schreiber, J., and Assmann, W. *Journal of Instrumentation* **8**(03), P03008 (2013).

[121] Lindner, F. H., Bin, J. H., Englbrecht, F., Haffa, D., Bolton, P. R., Gao, Y., Hartmann, J., Hilz, P., Kreuzer, C., Ostermayr, T. M., Rösch, T. F., Speicher, M., Parodi, K., Thirolf, P. G., and Schreiber, J. *Review of Scientific Instruments* **89**(1), 013301 (2018).

[122] Englbrecht, F., Balling, F., Rösch, T. F., Würl, M., Lindner, F. H., Parodi, K., and Schreiber, J. *Current Directions in Biomedical Engineering* **3**(2), 343–346 (2017).

[123] Englbrecht, F. S., Würl, M., Olivari, F., Ficorella, A., Kreuzer, C., Lindner, F. H., Palma, M. D., Pancheri, L., Betta, G.-F. D., Schreiber, J., Quaranta, A., and Parodi, K. *Radiation Protection Dosimetry* **180**(1-4), 291–295 (2018).

[124] Draxinger, W. *Entwicklung und Charakterisierung eines Pixeldetektors für laserbeschleunigte Ionen*. Diploma thesis, Ludwig-Maximilians-Universität München (2012).

[125] Metzkes, J., Karsch, L., Kraft, S. D., Pawelke, J., Richter, C., Schürer, M., Sobiella, M., Stiller, N., Zeil, K., and Schramm, U. *Review of Scientific Instruments* **83**(12), 123301 (2012).

[126] Green, J. S., Borghesi, M., Brenner, C. M., Carroll, D. C., Dover, N. P., Foster, P. S., Gallegos, P., Green, S., Kirby, D., Kirkby, K. J., McKenna, P., Merchant, M. J., Najmudin, Z., Palmer, C. A. J., Parker, D., Prasad, R., Quinn, K. E., Rajeev, P. P., Read, M. P., Romagnani, L., Schreiber, J., Streeter, M. J. V., Tresca, O., Wahlström, C.-G., Zepf, M., and Neely, D. *Proceedings of SPIE* **8079**, 807919 (2011).

[127] Schwind, K. M., Aktan, E., Prasad, R., Cerchez, M., Eversheim, D., Willi, O., and Aurand, B. *Review of Scientific Instruments* **90**(5), 053307 (2019).

[128] Xu, M.-H., Li, H.-W., Liu, B.-C., Liu, F., Su, L.-N., Du, F., Zhang, L., Zheng, Y., Ma, J.-L., Neely, D., McKenna, P., Wang, Z.-H., Wei, Z.-Y., Yan, X.-Q., Li, Y.-T., Li, Y.-J., and Zhang, J. *Chinese Physics Letters* **28**(9), 095203 (2011).

[129] Ponnath, L. *Development of Diagnostics Components for Laser-Accelerated Heavy Ions*. Master's thesis, Ludwig-Maximilians-Universität München (2018).

[130] Princeton Instruments, Inc. *KURO - Back-illumated scientific CMOS camera. Datasheet (revA2.3)*. (2017).

[131] TAMRON Europe GmbH. *Lens Catalogue*. Cologne (2019).

[132] Saint-Gobain Ceramics & Plastics, Inc. *BC-400,BC-404,BC-408,BC-412,BC-416. Premium Plastic Scintillators*. (2018).

[133] Ziegler, J. F., Ziegler, M., and Biersack, J. *Nuclear Instruments and Methods in Physics Research Section B: Beam Interactions with Materials and Atoms* **268**(11-12), 1818–1823 (2010).

[134] Leo, W. R. *Techniques for Nuclear and Particle Physics Experiments. A How-to Approach*. Springer-Verlag, Berlin Heidelberg, 2nd edition (1994).

[135] Mora, P. *Physical Review Letters* **90**(18), 185002 (2003).

[136] Schreiber, J., Bell, F., Grüner, F., Schramm, U., Geissler, M., Schnürer, M., Ter-Avetisyan, S., Hegelich, B. M., Cobble, J., Brambrink, E., Fuchs, J., Audebert, P., and Habs, D. *Physical Review Letters* **97**(4), 045005 (2006).

[137] Tampo, M., Awano, S., Bolton, P. R., Kondo, K., Mima, K., Mori, Y., Nakamura, H., Nakatsutsumi, M., Stephens, R. B., Tanaka, K. A., Tanimoto, T., Yabuuchi, T., and Kodama, R. *Physics of Plasmas* **17**(7), 073110 (2010).

[138] Berger, M., Coursey, J., Zucker, M., and Chang, J. *ESTAR, PSTAR, and ASTAR: Computer Programs for Calculating Stopping-Power and Range Tables for Electrons, Protons, and Helium Ions (version 2.0.1)*. National Institute of Standards and Technology, Gaithersburg, MD. http://physics.nist.gov/Star. Visited on 02.02.2020.

[139] Lindner, F. H. *Online Diagnostics for Laser Accelerated Ions and Electrons*. Master's thesis, Ludwig-Maximilians-Universität München (2015).

[140] Tanaka, K. A., Yabuuchi, T., Sato, T., Kodama, R., Kitagawa, Y., Takahashi, T., Ikeda, T., Honda, Y., and Okuda, S. *Review of Scientific Instruments* **76**(1), 013507 (2005).

[141] Glinec, Y., Faure, J., Guemnie-Tafo, A., Malka, V., Monard, H., Larbre, J. P., De Waele, V., Marignier, J. L., and Mostafavi, M. *Review of Scientific Instruments* **77**(10), 103301 (2006).

[142] Thomson, J. *The London, Edinburgh, and Dublin Philosophical Magazine and Journal of Science* **21**(122), 225–249 (1911).

[143] Jung, D., Hörlein, R., Kiefer, D., Letzring, S., Gautier, D. C., Schramm, U., Hübsch, C., Öhm, R., Albright, B. J., Fernandez, J. C., Habs, D., and Hegelich, B. M. *Review of Scientific Instruments* **82**(1), 013306 (2011).

[144] Hegelich, M., Karsch, S., Pretzler, G., Habs, D., Witte, K., Guenther, W., Allen, M., Blazevic, A., Fuchs, J., Gauthier, J. C., Geissel, M., Audebert, P., Cowan, T., and Roth, M. *Physical Review Letters* **89**(8), 085002 (2002).

[145] McKenna, P., Ledingham, K. W. D., Yang, J. M., Robson, L., McCanny, T., Shimizu, S., Clarke, R. J., Neely, D., Spohr, K., Chapman, R., Singhal, R. P., Krushelnick, K., Wei, M. S., and Norreys, P. A. *Physical Review E* **70**(3), 036405 (2004).

[146] Hegelich, B. M., Albright, B., Audebert, P., Blazevic, A., Brambrink, E., Cobble, J., Cowan, T., Fuchs, J., Gauthier, J. C., Gautier, C., Geissel, M., Habs, D., Johnson, R., Karsch, S., Kemp, A., Letzring, S., Roth, M., Schramm, U., Schreiber, J., Witte, K. J., and Fernández, J. C. *Physics of Plasmas* **12**(5), 056314 (2005).

[147] Jung, D., Yin, L., Gautier, D. C., Wu, H.-C., Letzring, S., Dromey, B., Shah, R., Palaniyappan, S., Shimada, T., Johnson, R. P., Schreiber, J., Habs, D., Fernández, J. C., Hegelich, B. M., and Albright, B. J. *Physics of Plasmas* **20**(8), 083103 (2013).

[148] Safronov, K. V., Gorokhov, S. A., Flegentov, V. A., Potapov, A. V., Gavrilov, D. S., Kakshin, A. G., Loboda, E. A., and Vikhlyaev, D. A. *Physics of Plasmas* **25**(10), 103114 (2018).

[149] Kondo, K., Nishiuchi, M., Sakaki, H., Dover, N. P., Lowe, H. F., Miyahara, T., Watanabe, Y., Ziegler, T., Zeil, K., Schramm, U., Ditter, E. J., Hicks, G. S., Ettlinger, O. C., Najmudin, Z., Kiriyama, H., Kando, M., and Kondo, K. *Crystals* **10**(9), 837 (2020).

[150] Hegelich, B. M., Albright, B. J., Cobble, J., Flippo, K., Letzring, S., Paffett, M., Ruhl, H., Schreiber, J., Schulze, R. K., and Fernández, J. C. *Nature* **439**(7075), 441–444 (2006).

[151] Schwoerer, H., Pfotenhauer, S., Jäckel, O., Amthor, K.-U., Liesfeld, B., Ziegler, W., Sauerbrey, R., Ledingham, K. W. D., and Esirkepov, T. *Nature* **439**(7075), 445–448 (2006).

[152] Fernández, J. C., Hegelich, B. M., Cobble, J. A., Flippo, K. A., Letzring, S. A., Johnson, R. P., Gautier, D. C., Shimada, T., Kyrala, G. A., Wang, Y., Wetteland, C. J., and Schreiber, J. *Laser and Particle Beams* **23**(03), 267–273 (2005).

[153] Sommer, P., Metzkes-Ng, J., Brack, F.-E., Cowan, T. E., Kraft, S. D., Obst, L., Rehwald, M., Schlenvoigt, H.-P., Schramm, U., and Zeil, K. *Plasma Physics and Controlled Fusion* **60**(5), 054002 (2018).

[154] Hoffmeister, G., Bellei, C., Harres, K., Ivanov, D., Kraus, D., Pelka, A., Rethfeld, B., Schaumann, G., and Roth, M. *Physical Review Special Topics - Accelerators and Beams* **16**(4), 041304 (2013).

[155] Allen, M., Patel, P. K., Mackinnon, A., Price, D., Wilks, S., and Morse, E. *Physical Review Letters* **93**(26), 265004 (2004).

[156] Loebich, O. *Gold Bulletin* **5**(1), 2–10 (1972).

[157] Weiser, M. Master's thesis, Ludwig-Maximilians-Universität München (2021). In preparation.

[158] Planck, M. *Verhandlungen der Deutschen Physikalischen Gesellschaft* **2**, 237–245 (1900).

[159] Andrews, D. G. *An Introduction to Atmospheric Physics*. Cambridge University Press, Cambridge, 2nd edition (2010).

[160] Ocean Optics, Inc. (now: Ocean Insight). *NIRQuest Installation and Operation Manual*. (2010).

[161] Arganda-Carreras, I., Kaynig, V., Rueden, C., Eliceiri, K. W., Schindelin, J., Cardona, A., and Sebastian Seung, H. *Bioinformatics* **33**(15), 2424–2426 (2017).

[162] Holmes, G., Donkin, A., and Witten, I. *Proceedings of ANZIIS '94 - Australian New Zealnd Intelligent Information Systems Conference* , 357–361 (1994).

[163] Schreiber, J., Kaluza, M., Grüner, F., Schramm, U., Hegelich, B., Cobble, J., Geissler, M., Brambrink, E., Fuchs, J., Audebert, P., Habs, D., and Witte, K. *Applied Physics B* **79**(8), 1041–1045 (2004).

[164] Steinke, S., Hilz, P., Schnürer, M., Priebe, G., Bränzel, J., Abicht, F., Kiefer, D., Kreuzer, C., Ostermayr, T., Schreiber, J., Andreev, A. A., Yu, T. P., Pukhov, A., and Sandner, W. *Physical Review Special Topics - Accelerators and Beams* **16**(1), 011303 (2013).

[165] Yu, T. P., Yin, Y., Zou, D. B., Ge, Z. Y., Yang, X. H., Zhuo, H. B., Ma, Y. Y., Shao, F. Q., and Pukhov, A. *Optics Express* **21**(19), 22558 (2013).

[166] Zielbauer, B. GSI Darmstadt. Private Communication, (2020).

[167] Ziener, C., Foster, P. S., Divall, E. J., Hooker, C. J., Hutchinson, M. H. R., Langley, A. J., and Neely, D. *Journal of Applied Physics* **93**(1), 768–770 (2003).

[168] Ziegler, J., Biersack, J., and Ziegler, M. *SRIM, the Stopping and Range of Ions in Matter*. SRIM Company, Chester, Maryland (2008).

[169] Fahrmeir, L., Heumann, C., Künstler, R., Pigeot, I., and Tutz, G. *Statistik. Der Weg zur Datenanalyse.* Springer-Lehrbuch. Springer-Verlag, Berlin, Heidelberg (2016).

[170] Hollinger, R., Wang, S., Wang, Y., Moreau, A., Capeluto, M. G., Song, H., Rockwood, A., Bayarsaikhan, E., Kaymak, V., Pukhov, A., Shlyaptsev, V. N., and Rocca, J. J. *Nature Photonics* **14**(10), 607–611 (2020).

[171] Sun, G.-Z., Ott, E., Lee, Y. C., and Guzdar, P. *The Physics of Fluids* **30**, 526–532 (1987).

[172] Pukhov, A. and Meyer-ter Vehn, J. *Physical Review Letters* **76**(21), 3975–3978 (1996).

[173] Bin, J., Ma, W., Wang, H., Streeter, M., Kreuzer, C., Kiefer, D., Yeung, M., Cousens, S., Foster, P., Dromey, B., Yan, X., Ramis, R., Meyer-ter Vehn, J., Zepf, M., and Schreiber, J. *Physical Review Letters* **115**(6), 064801 (2015).

[174] Boller, P., Zylstra, A., Neumayer, P., Bernstein, L., Brabetz, C., Despotopulos, J., Glorius, J., Hellmund, J., Henry, E. A., Hornung, J., Jeet, J., Khuyagbaatar, J., Lens, L., Roeder, S., Stoehlker, T., Yakushev, A., Litvinov, Y. A., Shaughnessy, D., Bagnoud, V., Kuehl, T., and Schneider, D. H. G. *Scientific Reports* **10**(1), 17183 (2020).

[175] Möller, P., Sierk, A. J., Ichikawa, T., Iwamoto, A., Bengtsson, R., Uhrenholt, H., and Åberg, S. *Physical Review C* **79**(6), 064304 (2009).

[176] Wu, H.-C., Tajima, T., Habs, D., Chao, A. W., and Meyer-ter Vehn, J. *Physical Review Special Topics - Accelerators and Beams* **13**(10), 101303 (2010).

[177] Gao, Y., Bin, J., Haffa, D., Kreuzer, C., Hartmann, J., Speicher, M., Lindner, F. H., Ostermayr, T. M., Hilz, P., Rösch, T. F., Lehrack, S., Englbrecht, F., Seuferling, S., Gilljohann, M., Ding, H., Ma, W., Parodi, K., and Schreiber, J. *High Power Laser Science and Engineering* **5**, e12 (2017).

[178] Gales, S., Tanaka, K. A., Balabanski, D. L., Negoita, F., Stutman, D., Tesileanu, O., Ur, C. A., Ursescu, D., Andrei, I., Ataman, S., Cernaianu, M. O., D'Alessi, L., Dancus, I., Diaconescu, B., Djourelov, N., Filipescu, D., Ghenuche, P., Ghita, D. G., Matei, C., Seto, K., Zeng, M., and Zamfir, N. V. *Reports on Progress in Physics* **81**(9), 094301 (2018).

Acknowledgements

Diese Arbeit könnte es in dieser Form nicht geben, wäre da nicht diese große Zahl an Personen, die mir in den vergangenen Jahren stets zur Seite standen und mich immer mit Rat und Tat unterstützt haben.

Mein zuvordester Dank gebührt meinem Doktorvater *Prof. Dr. Peter G. Thirolf* für die Gelegenheit, meine Doktorarbeit in seiner Arbeitsgruppe anfertigen zu dürfen. Vielen Dank für Deine kompetente Anleitung, die jederzeit großartige Unterstützung und die vielen kritischen, aber durchaus notwendigen Nachfragen, durch die mir die Bedeutsamkeit selbst kleinster Details erst bewusst wurden. Unsere unzähligen Gespräche und Diskussionen, die nicht nur meinen physikalischen Sachverstand förderten, werden mir stets in positiver Erinnerung bleiben.

Weiter möchte ich mich ganz besonders bei *Prof. Dr. Jörg Schreiber* bedanken, über den ich erst auf das Thema meiner Doktorarbeit gestoßen bin. Auch nach Abschluss meiner Masterarbeit war ich stets in seiner Arbeitsgruppe willkommen und konnte ich mich immer auf seine fachliche wie auch persönliche Betreuung stützen. Vielen Dank für die vielen Diskussionen, den physikalischen Input und dass Du immer mehr in meinen Daten gesehen hast, als ich zunächst erkennen wollte.

Danke an all die wunderbaren Kollegen, mit denen ich im Laufe der Jahre zusammenarbeiten durfte. Dabei denke ich insbesondere zurück an die Strahlzeiten an LEX Photonics, bei denen ich das experimentelle Handwerkszeug von meinen älteren Kollegen erlernen durfte, insbesondere von *Prof. Dr. Jianhui Bin*, *Dr. Daniel Haffa*, *Dr. Peter Hilz*, *Dr. Christian Kreuzer* und *Dr. Tobias M. Ostermayr*. Danke natürlich auch an alle anderen Teilnehmer dieser Strahlzeiten, die sich durch Euch nahezu familiär anfühlten: *Franz Englbrecht*, *Dr. Ying Gao*, *Jens Hartmann*, *Thomas Rösch*, *Martin Speicher*, *Dr. Matthias Würl* und alle, die ich unberechtigterweise in dieser Aufzählung vergessen haben sollte.

Thank you to the people at the University of Texas at Austin for the collaboration which lead to my first publication about laser-driven gold ion acceleration. Special thanks goes to *Eddie McCary*, but also to the other members of the experimental team: *Xuejing*

Jiao, *Rebecca Roycroft* and *Ganesh Tiwari*. Thank you to *Prof. Dr. Manuel Hegelich* for inviting me to join this experimental campaign and to the facility staff at the TPW for operating the laser and all the support during the beamtime. Vielen Dank an *Dr. Tobias M. Ostermayr* für die Unterstützung bei der CR-39-Datenauswertung.

Ein ganz herzlicher Dank geht an diejenigen, die mich auf die Strahlzeit am PHELIX-Laser an der GSI begleitet haben und ohne die ich die zentralen Daten meiner Doktorarbeit nicht hätte generieren können: *Erin Grace Fitzpatrick*, *Dr. Daniel Haffa*, *Anna-Katharina Schmidt*, *Martin Speicher* und *Prof. Dr. Peter G. Thirolf*. Ein besonderes Dankeschön gebührt *Dr. Bernhard Zielbauer* für seine großartige und lösungsorientierte Unterstützung bei der Vorbereitung und Durchführung der Strahlzeit. Danke an das PHELIX-Team unter der Leitung von *Dr. Stefan Götte* für die zuverlässige Bereitstellung des Lasers.

Vielen Dank an alle, die EG und mir beim Aufbau des HF-Caves in CALA geholfen haben, wobei ich insbesondere die Unterstützung durch *Lenny Doyle*, *Jens Hartmann* sowie *Thomas Rösch* hervorheben möchte. Herzlichen Dank an meine beiden Masterstudenten *Lukas Ponnath* und *Max Weiser* sowie meinem Bachelorstudenten *Leopold Brünnig*, welche die erforderlichen technischen Entwicklungen für die erfolgreiche Schwerionenbeschleunigung und -messung substanziell vorantrieben. Ein ganz besonderes Dankeschön geht an *Oliver Gosau* und *Nik Gjotev*, auf deren Hilfsbereitschaft und technische Unterstützung man sich immer verlassen konnte. Bedanken darf ich mich auch bei den Mitarbeitern der mechanischen Werkstatt der LMU in Garching unter der Leitung von *Rolf Öhm*, die immer eine hervorragende Arbeit gemacht haben. Danke auch an *Dr. Jerzy Szerypo* und *Simon Stork* für die Fertigung der Folientargets für meine Strahlzeiten.

Vielen Dank auch an alle Kollegen, die zu Freunden wurden. Mein ganz besonderer Dank gebührt hier *Johannes Gebhard* und *Thomas Rösch*, die mich durch alle Hoch- und Tiefphasen meiner Doktorarbeit freundschaftlich begleitet haben, Rückschläge erträglicher machten und so meinen erfolgreichen Abschluss erst ermöglichten. Danke auch an alle meine Münchner Freunde außerhalb der Arbeitsgruppe, die daran ebenso ihren Anteil haben, ganz besonders *Felix*, *Theresa*, *Flo*, *Sebastian* und *alle trinkfesten Stammtisch- und Vorstandskollegen von MünchenKlang*. Und natürlich an meine Plößberger Freunde, insbesondere *Sabi*, *Matze*, *Andi* und *Flo*, die meinen Weg schon sehr lange treu begleiten.

Mein tiefster und aufrichtigster Dank gebührt allerdings *meinen Geschwistern* und noch viel mehr *meinen Eltern*, die immer bedingungslos zu mir standen und mich bei all meinen Entscheidungen und in jeder Lebenslage unterstützten. Danke, dass ihr den Menschen aus mir gemacht habt, der ich heute bin!